Synchrotron X-ray and Electrochemical Studies of Pitting Corrosion of Iron

by

Weichen Xu

A thesis submitted to the University of Birmingham for the degree of DOCTOR OF PHILOSOPHY

School of Metallurgy and Materials

University of Birmingham

2014

Abstract

Pitting corrosion of iron has been studied via artificial pits. Solid corrosion products have been observed in the pit solution, which have been characterised as disordered carbon and Fe_3C (known as both cementite and cohenite) using *in-situ* synchrotron XRD and *ex-situ* Raman spectroscopy. These corrosion products were found to act as diffusion barriers for metal ions and to give a small increase in the solution resistance. The formation of carbon-containing corrosion products depends upon the interfacial potential. The potential dependence suggests that Fe_3C may be protected from dissolution by a carbon layer.

High purity iron was used to calculate an effective diffusion coefficient for metal ions (a combination of self-diffusion and electrical migration) in different $MgCl_2$ concentrations during diffusion-limited dissolution. The contribution of self-diffusion increases with increasing $MgCl_2$ concentration if the depletion of Mg^{2+} in the pit is considered. The Tafel kinetics of iron dissolution in solutions saturated in Fe^{2+} has been studied in different $MgCl_2$ concentrations. The Tafel slope (56 to 70 mV/decade) was independent of $MgCl_2$ and $FeCl_2$ concentration when $FeCl_2$ is saturated.

The effect of nitrate on the composition and structure of salt layers has been characterised using *in-situ* synchrotron XRD. The salt layer has been found to be composed of $FeCl_2.4H_2O$ in chloride with and without trace nitrate, and $Fe(NO_3)_2.6H_2O$ in nitrate with trace chloride. The salt layer is isotropic in HCl and anisotropic in HCl with trace nitrate.

The dissolution behaviour of iron in HCl and chloride/nitrate solutions has been studied using *in-situ* synchrotron X-ray radiography. It has been found that dissolution is relatively uniform in the presence of salt layers, but crevice formation and surface roughening can take place on salt-free surfaces. The potentiodynamic measurements on iron in nitrate/chloride solutions

induce abrupt transitions between dissolution and passivation, resulting in deep and localised attack.

Acknowledgements

I really appreciate all the people who have helped me for my PhD research.

First of all, I would like to sincerely thank my supervisor Professor Alison J. Davenport for her invaluable guidance and advice on my PhD project. Starting as a student without much experience on research, I will never make it without her help, criticism, patience and support. It is definitely precious experience that I can benefit from for my future life and career.

I would like to give my heartfelt gratitude to my co-supervisor Professor Trevor Rayment (Diamond Light Source, UK), who has also given me invaluable advice and encouragement, and helped me so much on my research, especially on the synchrotron work.

I am grateful to China Scholarship Council and School of Metallurgy and Materials (University of Birmingham) for their financial support, and the beam scientists of Beamline I18 and I13 in Diamond Light Source: Professor Fred Mosselmans, Dr Paul Quinn, Dr Christoph Rau, Dr Joan Vila-Comamala, and all the other scientists and staff in these beamlines. Also, I would like to thank Scott Greenwell (University of Bristol) for all his generous help on the Raman measurement.

Last but not least, I would like to thank my dear family and, of course, all my lovely friends who are or were in the corrosion group: Steven and Mahrez (helped me a lot on synchrotron work), Mehdi and April (helped me a lot on electrochemistry, starting with making samples), Fei, Liya, Sophie, Andrew dP, Andrew C, Sarah, Angus, Haval, Gavin, Majid, Georgia, Joshua, Ali, Lorna, Aaron, Juan, Yehia... You have given the most generous help and made my PhD life here enjoyable. I wish all the best for you guys!

Dedicated to

my grandfather Chengtian Xu and my grandmother Chengfang Sun...

Contents

List of symbols and definition

Symbol	Definition
A	Area of electrode surface
b_a	Anodic Tafel slope
C	Concentration
C_{sat}	Saturation concentration of metal ions
ΔC	Difference of metal ion concentration between pit bottom and pit mouth
D	Diffusion coefficient
D_{eff}	Effective diffusion coefficient
E	Potential
E_{corr}	Open circuit potential
E_{app}	Applied potential
E_{int}	Interfacial (*IR*-corrected) potential
E_T	Transition potential
E_p	Pitting potential
E_{rp}	Repassivation potential
f	Frequency of ac signal
F	Faraday's constant
i	Current density
i_{lim}	Diffusion-limited current density
i_{peak}	Maximum current density in the metal ion supersaturation process
ix	Pit stability product of 1D artificial pit
i_{corr}	Current density at open circuit potential
i_{crit}	Critical current density at the active-passive transition of certain alloys
I	Current
I_a	Anodic current
I_{corr}	Current at open circuit potential
I_{lim}	Diffusion-limited current
IR	Potential drop (*IR* drop)
m	Weight of metal
M	Molar mass of metal
n	Average valence of metal ions
Q	Transferred charge
R_s	Resistance of solution (solution of pit interior and exterior)
R_{ext}	Resistance in the bulk solution
R_{total}	Resistance of solution and salt layer
R	Gas constant
t	Time
T	Temperature
x	Depth of artificial pit
α	Charge transfer coefficient
η	Overpotential
ρ	Density of metal
ρ_s	Average resistivity of solution in an artificial pit

1. INTRODUCTION

For the management of radioactive waste storage, especially the high level waste (HLW), deep geological disposal is required after interim storage, which has been proposed at the present stage and may last for 100 years or even more [1]. Carbon steel is under consideration for use as the container material for the storage of high level waste (HLW) in deep repositories [2], and for the tanks used for the temporary storage of high-level liquid radioactive waste before vitrification and permanent disposal [3].

However, localised corrosion issues have been reported on carbon steel storage tanks, including pitting [3] and stress corrosion cracking [4], which are due to the presence of acidic and concentrated chloride/nitrate in the liquid radioactive wastes (LRWs) [5, 6]. For example, the leakage of radioactive waste into the surrounding environment has been reported on 67 out of 149 carbon steel tanks at the Hanford site, US [3]. Double-shell storage tanks have been used with video surveillance in the annulus, but which cannot manage the corrosion issue. Nitrate species has been generally regarded as an inhibitor for metal dissolution [7], and the mechanism of the reported localised failure is still not clear enough, so it is essential to fully understand the mechanism of localised corrosion of steels in acidified chloride and/or nitrate solutions. In addition to the carbon steel tanks for interim storage, localised attack on carbon steel materials used for permanent deep disposal can also occur in aerobic or aerobic/anaerobic transition conditions, despite the good corrosion resistance of carbon steel containers in the expected repository environment [2, 8].

In order to understand the localised corrosion of carbon steel in chloride and/or nitrate solutions, pitting corrosion of iron, including the effect of carbon, has been investigated via iron artificial pit electrodes in the present work. The influence of corrosion products within a

pit on the electrochemical behaviour has been characterised. The diffusivity of metal ions and the Tafel kinetics of iron dissolution have been obtained from dynamically growing pits in a wide range of chloride concentrations.

Furthermore, during the high-rate dissolution, the concentrations of metal ions at the pit bottom can reach a certain supersaturation ratio, which leads to the precipitation of a salt layer at the metal/solution interface. *In-situ* synchrotron XRD has been applied to characterise the composition and structure of the salt layer and corrosion products within iron artificial pits in different concentrations of chloride/nitrate solutions, and the dissolution behaviour of the artificial pits has also been investigated using synchrotron X-ray radiography.

2. LITERATURE REVIEW

2.1 Pitting corrosion

Pitting corrosion takes place when there is localised corrosion attack on a surface that is otherwise protected from corrosion by the presence of a passive oxide film. It takes place where there is breakdown of the passive film, typically at local heterogeneities including flaws, inclusions, or second-phase particles. It is induced by aggressive anionic species, usually chloride owing to its high diffusivity, its ability to form strong acids with protons, and its ubiquitousness [9-11]. Theories of pit initiation include passive film penetration, passive film breaking and adsorption of chloride [12].

Inside a pit on iron, the anodic dissolution process is

$$Fe \rightarrow Fe^{2+} + 2e^{-} \qquad \text{Equation 2-1}$$

Pitting corrosion is considered to be an autocatalytic process: once a pit initiates and starts growing, the local pH undergoes significant changes mainly via hydrolysis reactions of metal ions [13]:

$$Fe^{2+} + H_2O \rightarrow FeOH^{+} + H^{+} \qquad \text{Equation 2-2}$$

Chloride ions are drawn to the pit cavity to maintain charge neutrality, making the pit solution more aggressive and promoting further pit propagation and growth [9]. The stability of a pit depends on the metal dissolution rate and the metal ion diffusion rate: if the dissolution rate is not high enough to replenish the metal ions lost by diffusion, the pit environment may lose aggressiveness as H^{+} and Cl^{-} are both maintained by the local concentration of metal ions [9].

Figure 2-1 shows a schematic diagram of the pitting process for a metal in NaCl, where the oxygen reduction reaction (ORR) is the cathodic reaction at an otherwise passive surface:

$$O_2 + 2H_2O + 4e^- \rightarrow 4OH^- \qquad \text{Equation 2-3}$$

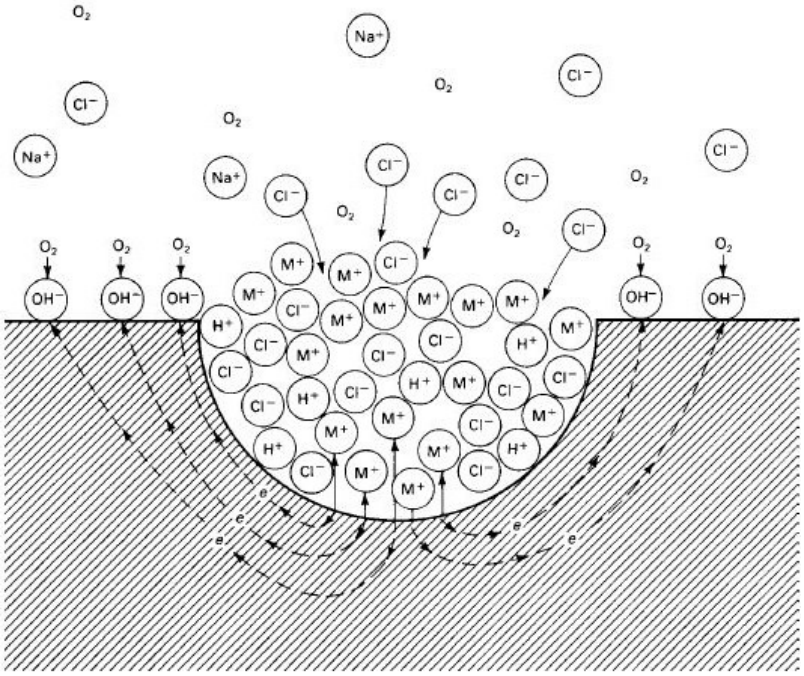

Figure 2-1. A schematic diagram of the autocatalytic process of pitting in aerated NaCl solution, metal dissolution as anodic reaction, oxygen reduction as cathodic reaction [10]

Due to the accumulation of metal ions in a pitting area, the local concentrations of H^+ and Cl^- within the pit differ significantly from the bulk solution. Wilde and Williams [14] reported that a low pH developed within the pit cavity of stainless steel 304L (pH value 0 to 3 depending on exposure time in neutral 1 M NaCl). Furthermore, Suzuki [15] found that the chloride concentration within a stainless steel pit in 0.5 M NaCl was between 3.78 to 6.47 M, and the pH was between -0.13 and 0.8; the low pH was mainly attributed to hydrolysis of Cr/Mo ions, but the pH did not agree well with the hydrolysis thermodynamic calculations, which was believed to be ascribed to the presence of hydroxyl-chloro complexes of metal ions and high chloride concentrations. Mankowski [16] studied the pit solution frozen with solid

CO_2 in the end of the experiment in 0.5 M NaCl with less than 0.1 M H_2SO_4: it was found that the pH could be as low as 0 and chloride concentration could be up to 12 M. The low pH was believed to result from increased proton activity due to metal ion hydrolysis and high chloride concentrations; the measured pH values agreed with Suzuki [15].

There are three key aspects to control pitting corrosion: firstly the local chemistry should be sufficiently aggressive to destroy passivity, secondly the anode and cathode (connected via ionic/electrical communication) should be physically separated, and thirdly a high rate dissolution must be stabilised [17]. The parameters used to describe pitting corrosion are pitting potential E_p and repassivation potential E_{rp}. The concept of "critical current density" i_{crit} at the active/passive transition for certain alloys has also been defined [11], and they are shown in a typical current-voltage diagram (Figure 2-2). Pitting susceptibility can be related to the difference between E_p and E_{rp} [10], since a stable pit occurs above E_p, and an active pit repassivates below E_{rp}. A conservative criterion is that pitting corrosion is possible above E_{rp} (the metastable pit has a chance to either passivate or keep growing), and should not occur in the region more than 100 mV below E_{rp} [18].

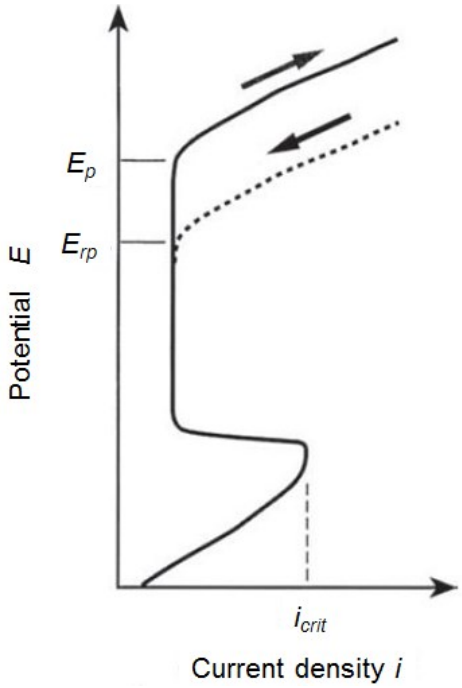

Figure 2-2. A polarisation curve showing critical pitting potential E_p, repassivation potential E_{rp} and critical current density i_{crit} in a potential sweep measurement [11]

2.2 Artificial pits

Simulated pits have frequently been studied because of the difficulty of characterising a real growing pit. For example, Suzuki [19] used a simulated pit, which was a hemispherical cavity drilled into a stainless steel plate and covered with Teflon sheet, in which there was a small hole for the diffusion of metal ions. The one dimensional artificial pit is a more simplified pitting geometry, and has been used widely for investigation on pit growth. The idea is to embed a thin metal wire or foil by insulator mounting (resin), such that the cross section area is exposed in the electrolyte, so a pit forms after the metal surface recedes. When the artificial pit is deep enough, mass transport is essentially one dimensional, parallel to the axis of the "cavity". This geometry is often called "lead in pencil" [20-22]. The artificial pit usually faces upwards to minimise natural convection effects [21, 23]. Figure 2-3 shows the setup of an electrochemical experiment with a one dimensional artificial pit; the metal is the working

electrode connected to a potentiostat. The current-voltage characteristics in an artificial pit are described in Section 2.3.2.

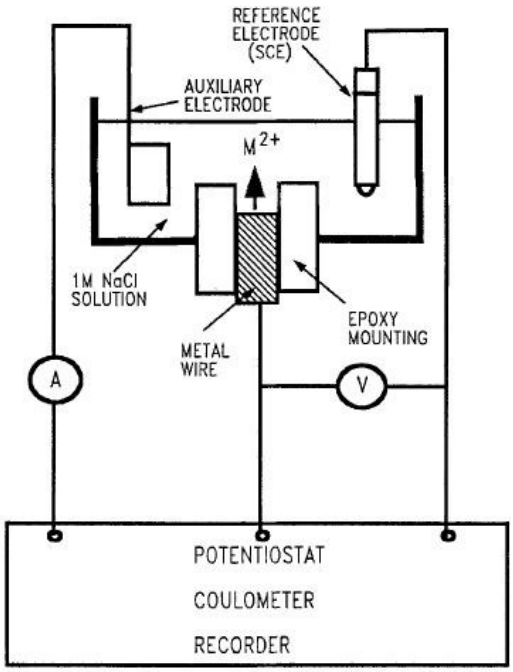

Figure 2-3. A schematic diagram of an electrochemical experimental setup using the one dimensional artificial pit [20]

2.3 Salt layers

In 1950, Hoar [24] observed powdery and white crystals on a Ni anode dissolving in sulphuric acid, and related this observation to the earlier reported "loose layer of solid corrosion products", which formed through salt precipitation from saturated solution. Hoar [25] suggested that a "compact solid film" could form under steady state conditions, allowing metal cations to enter and leave it at the same rate. Since the 1960s, the salt layer has been extensively studied on its properties and effects on dissolution.

2.3.1 Salt layer precipitation and dissolution

Salt layer precipitation is due to high rate anodic dissolution, resulting in a local solution that is supersaturated in metal chloride [26]. The supersaturation ratio was found to range from 1:1.8 to 1:5 in different circumstances [23, 27-29]. However, in the presence of convection, e.g. in Kuo and Landolt's study on an Fe rotating disc electrode in chloride media, the saturation concentration was reached, but supersaturation was negligible, so salt layer precipitation was prevented [30]. Salt precipitation can be very fast if the current density is high enough. Alkire [23] reported that the time for salt precipitation was in milliseconds when current density was ~10^2 A/cm^2. Beck and Alkire [31] also calculated the time to saturate the solution and deposit several layers of salt molecules, and found that it could be as fast as 10^{-4} s when current density was 10^3 to 10^6 A/cm^2, which indicates that the salt precipitation may occur at a very early stage of pitting when the current density is very high.

The salt layer dissolves if a high rate of metal dissolution is not maintained and the solution becomes diluted. Danielson [32] studied a Ni artificial pit in 0.5 M HCl and reported that the time for salt dissolution was directly proportional to its thickness and/or pit depth; the dissolution time was 1.93 s when the current density was 66 mA/cm^2. Steinsmo and Isaacs [20] also found that the rate of salt dissolution depended on the pit depth, consistent with Danielson [32]. These studies indicate that a salt layer is only present in a dynamically dissolving pit, and that the precipitation and dissolution are both very fast processes.

Novakovski and Sorokina [26] studied pitting corrosion using an artificial pit (18% Cr, 9% Ni, 0.1% C, Ti), and found that the dissolution rate is linear with the inverse pit depth, which indicates that the current density is regulated by diffusion/migration. Salt precipitation was observed on the electrode surface, and it was assumed that the salt layer acted as a self-

regulating resistance due to its lower ionic conductivity compared to the pit solution. When a higher potential was applied, the salt layer was expected to become thicker and consumed the excess potential.

It is agreed by Isaacs [33], who found a resistive layer on the electrode surface of a stainless steel 304 artificial pit via impedance measurement. The resistance of the layer was found to increase with increasing applied potential while the current was independent of potential, which indicates that the system is self-regulated. It was also suggested that the thickness of the resistive layer depended on the potential and diffusion rate of metal ions, and the layer would adjust its thickness/resistance to keep the current constant. Furthermore, Tester and Isaacs [34] studied artificial pits of both stainless steel 304 and Ni, and also reported that the current was independent of applied potential in a potential step measurement, which indicates the self-regulating property of salt layer via adjustment of the layer resistance/thickness. The thickness and resistance of a salt layer have been found to increase with applied potential by Issacs et al. [21] (using *in-situ* XRF microprobe in a stainless steel artificial pit) and Danielson [32] (using ac impedance method in a Ni artificial pit) respectively, both of which have supported the self-regulating property of a salt layer.

Based on the self-regulating property of a salt layer described above, Newman and Ajjawi [35] assumed that the interfacial potential would not change much with the applied potential, since the salt layer should consume most of the potential, as suggested by Isaacs [33]. However, Grimm and Landolt [36] studied an Fe rotating disc electrode using ac impedance method, and found that both the resistance of the salt layer and the *IR*-corrected potential increased with increasing applied potential, with the current limited at a constant value. Figure 2-4 shows the Nyquist plots of the system without (a) and with (b) salt layers. The total resistance values between the metal and reference electrode (the resistance of any salt layer and solution

resistance) are indicated by the arrows in the figures, where the capacitance (represented by the imaginary part) is close to zero; the increase of the total resistance with increasing potential (Figure 2-4b) was ascribed to the increase of salt layer resistance. The *IR*-corrected potential was thus obtained (applied potential subtracted *IR* drop), which was also found to increase with the increasing applied potential. In addition, the current increased drastically when the *IR*-corrected potential exceeded ca. 0.6 V(SCE), which they correlated with the Fe^{2+}/Fe^{3+} redox potential.

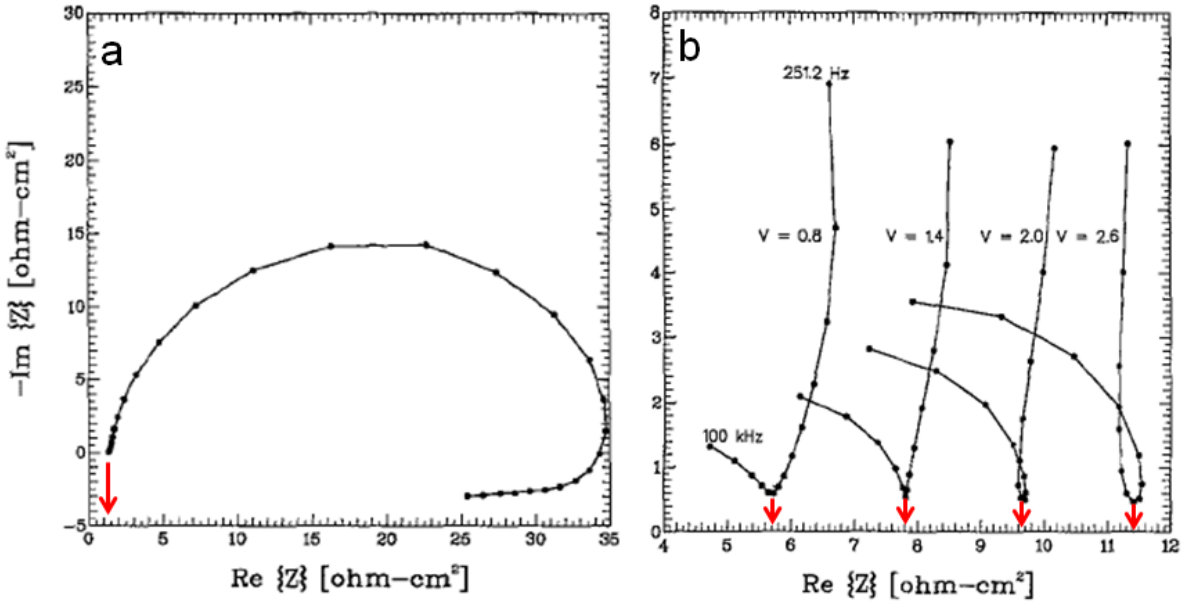

Figure 2-4. Nyquist plots obtained from an iron rotating disc electrode (rotating speed 200 rpm) in 4 M $FeCl_2$ (a) at the open circuit potential for the measurement of solution resistance without salt layers (100 kHz to 0.1 Hz), and (b) at different applied voltages in the presence of salt layers. The frequency for each curve in (b) is between 100 kHz and 251.2 Hz, amplitude 10 mV [36]. The arrows added into the figures indicate the values of the resistance including the solution and salt layer (if any) resistance.

2.3.2 Current-voltage characteristics in an artificial pit

At the very early stage of dissolution of an artificial pit, only part of the metal surface is active. The current increases with the increasing area of active dissolution until the dissolution of the whole cross section area is activated. At a later stage, the current is controlled by diffusion,

because the driving force for diffusion (concentration gradient) reaches the upper limit [34]. The relationship between current and overpotential is described in [37] as shown in Figure 2-5.

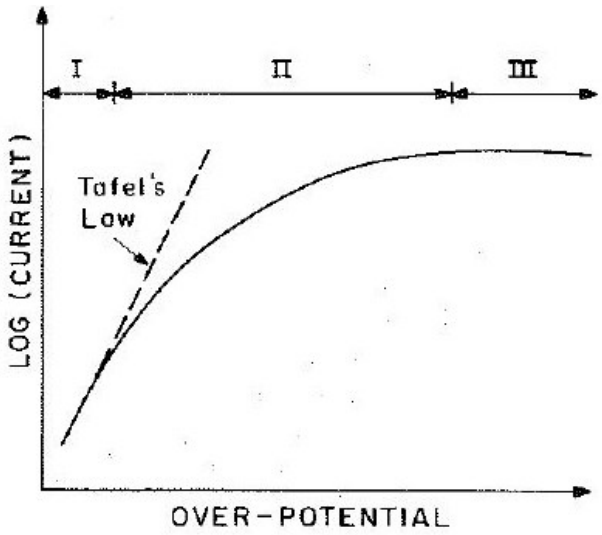

Figure 2-5. Schematic diagram of current vs. overpotential: I. activation-controlled region; II. *IR*-controlled region; III. diffusion-controlled region [37].

In region I, the current is very low, and all of the potential is consumed at the metal/solution interface. Equation 2-4 is valid,

$$\eta = a \ln i + b \qquad \text{Equation 2-4}$$

where a and b are constants, and η is the overvoltage. In region II, with the increase of current, the potential drop in the solution cannot be ignored, and the potential drop may be described by Equation 2-5,

$$\eta = a \ln i + b + IR_s \qquad \text{Equation 2-5}$$

where a, b are constants, η is the overvoltage, and R_s is the solution resistance; in region III, metal ion supersaturation may occur which results in the precipitation of a salt layer on the metal surface, and the dissolution is limited by diffusion and independent of potential [20, 27, 32, 34, 37].

To describe the current-voltage characteristics and the effect of a salt layer, a cyclic voltammetry measurement on an artificial pit is described by Tang and Davenport [38]. In Figure 2-6, on the forward potential scan, from point A to B, dissolution is under ohmic-control, and the current increases linearly with potential until point C is reached, where a salt layer starts to precipitate at the metal/solution interface since the supersaturation ratio has exceeded a certain value. The current then deceases rapidly to point D, because the salt layer acts as a resistive layer. The salt layer then becomes thinner, since the layer undergoes a self-regulating process (Section 2.3.1) and the dissolution eventually reaches a steady-state, limited by diffusion. The current is called diffusion limited current I_{lim}, which is independent of potential.

On the reverse potential scan, dissolution is still diffusion-limited through the self-regulating salt layer until point F is reached (the salt layer keeps thinning), where the overpotential is not enough to maintain the dissolution rate for metal ions to be saturated, and the salt layer starts to dissolve. The potential where the current drops just at the value of I_{lim}, is called the transition potential E_T as defined in [39], which is regarded as the transition from diffusion-control to ohmic-control dissolution as shown in Figure 2-6. Laycock and Newman [39] suggested that the pit surface became salt-free at potentials less than E_T.

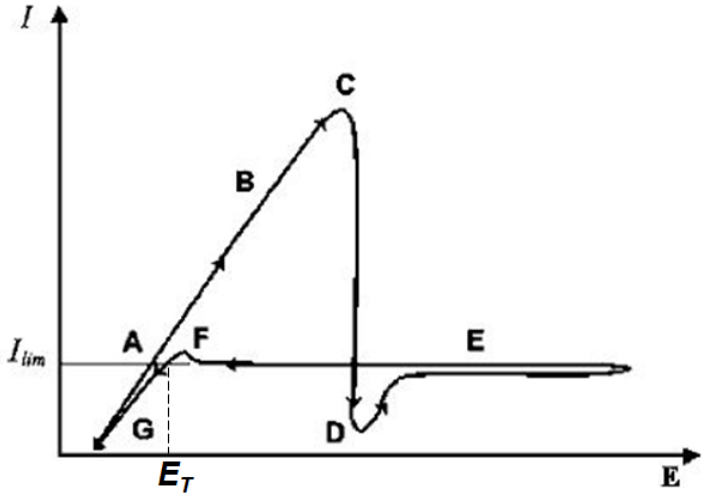

Figure 2-6. Current-voltage characteristics of a potential sweep on an artificial pit [38] with transition potential E_T marked [39]. In the forward sweep, points A and B are in the ohmic-control region in the absence of a salt layer, and metal ions are supersaturated at point B; point C is at the maximum current during the metal ion supersaturation process; a salt layer precipitates at point D due to the metal ion supersaturation; point E is in the diffusion-control region in the presence of a salt layer, and the thickness increases with increasing potential. In the reverse sweep, point F is in the diffusion-control region, but the salt layer starts to dissolve; point G is in the ohmic-control region in the absence of a salt layer.

2.3.3 Salt layer thickness and structure

Isaacs [33] assumed that the chloride salt layer on the anode was only 2 to 10 nm thick with a resistivity of ~10^8 ohm.cm. However, Alkire [23] suggested that salt layer thickness was between 2 and 25 μm, which was calculated with supersaturation ratio and current density; and Hunkeler [40] reported that the salt layer resistivity was only ~10^4 ohm.cm, and the ohmic drop across the salt layer increased with pit depth and potential. Danielson [32] used potential step and ac impedance methods to measure the resistance of the solution and salt layer in a Ni artificial pit, and found that the salt resistivity was 5600 ohm.cm, and the electric field across the layer was ~400 V/cm, which indicates that the ionic transport across the salt layer is through low electric field and ohmic migration; the salt layer was 1 to 15 μm thick, and the thickness increased with applied potential and pit depth, and it was proposed that

higher chloride concentrations also resulted in thicker salt layer. This thickness was much greater than that estimated by Isaacs [33].

Furthermore, a direct measurement was carried out by Isaacs et al. [21], who measured the thickness of the salt layer on stainless steel in acidic NaCl using an *in-situ* X-ray microprobe (fluorescence), it was found that the layer was 5.5 μm thick at applied voltage 1 V(SCE) in an artificial pit deeper than 1.6 mm; the electric field across the salt layer was 2100 V/cm.

Vetter [41] assumed that the salt layer on iron in chloride and sulphate solutions was non-porous. However, Danielson [32] estimated that the porosity of the nickel chloride salt layer was ~0.1% ($A_{pore}/A_{geometrical}$), which was calculated using the salt resistance measured via an ac impedance method and the theoretical resistivity of saturated chlorides (in the pores of the salt layer). West et al. [42] also calculated the porosity of the salt layer to be 0.24% or 0.90% using two different models, which were in the same magnitude as Danielson [32].

Landolt and co-workers used ac impedance to characterise the salt layer structure using a duplex model. For example, Clerc and Landolt [43] studied a Ni artificial pit in nearly neutral chloride solution (10 M LiCl + 0.01 M HCl), and suggested that the salt layer consisted of a compact semiconducting inner film (~10 nm thick) with high electric field and an porous outer film with low electric field. Similar results were reported in other work of Landolt et al. [36, 42, 44] on Fe and Fe-Cr alloys in deaerated 4 M $FeCl_2$; the model is described in Figure 2-7. Another impedance study reported by Sridhar and Dunn [45] suggested a similar duplex structure of salt layer on Ni in 0.5 M HCl.

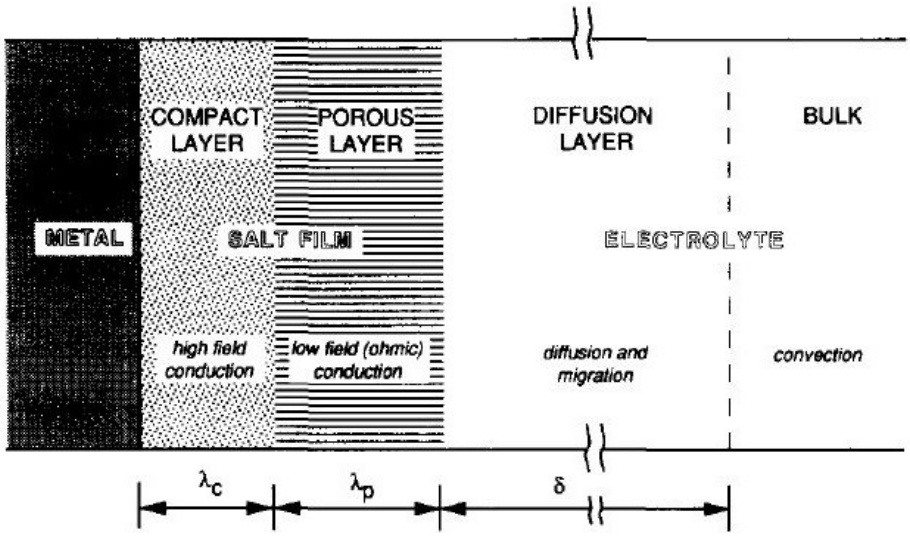

Figure 2-7. Schematic diagram of a duplex model of a salt layer from ac impedance study [44]

A similar duplex structure is also proposed for the electrochemical machining (ECM) process of Fe in $NaNO_3$. Lohrengel and co-workers [46-48] proposed a duplex salt layer in the transpassive regime (potential above 2 V, current density ~10^2 A/cm^2), with a supersaturated $Fe(NO_3)_3.9H_2O$ and/or $Fe(NO_3)_2.6H_2O$ outer layer (viscous solution or molten salt due to Joule heating at high current, as the melting point of these salts are below 60 °C) and an inner oxide layer. Rosenkranz [49] believed that the water activity in this salt layer was low enough to suppress oxygen evolution.

2.3.4 Salt layer composition

Although the salt layer has been observed in the corrosion processes in [23, 24, 26, 28], among which Hoar and Mowat [24] characterised the white crystals on Ni anode in H_2SO_4 as $NiSO_4/NiSO_4.H_2O$ with X-ray analysis (details of the analysis were not given), the composition of the salt was not studied in the other work. The *in-situ* XRF technique (synchrotron X-ray probe) has been used for the first time by Isaacs et al. to characterise the salt layer composition of a stainless steel artificial pit, and it was found that the salt layer was

rich in iron with little nickel and very small amount of chromium [21], and an addition of Mo (2.1%wt.) has little effect on the composition of the salt layer [50].

Since solid salt and saturated solution can be distinguished by Raman spectroscopy, Sridhar and Dunn [45] used *in-situ* Raman measurements on a Ni artificial pit and characterised the salt layer as $NiCl_2.6H_2O$. A more recent work carried out by Rayment et al. [51] employed *in-situ* synchrotron X-ray diffraction to study Ni, Fe and stainless steel 316L artificial pits in 1 M HCl, and found that $NiCl_2.6H_2O$ and $FeCl_2.4H_2O$ were the dominant phase for salt layers on Ni and Fe/stainless steel anodes, respectively. This was also reported in another *in-situ* X-ray study of Hammons et al. [52]. Furthermore, while comparing 2D diffraction images, Rayment et al. [51] suggested that, for iron, the ferrous salt was finer with randomly-oriented/isotropic crystallites (diffraction rings smooth and continuous), while for stainless steel 316L, the salt layer was coarser with fewer but larger crystallites (diffraction rings discontinuous) as shown in Figure 2-8.

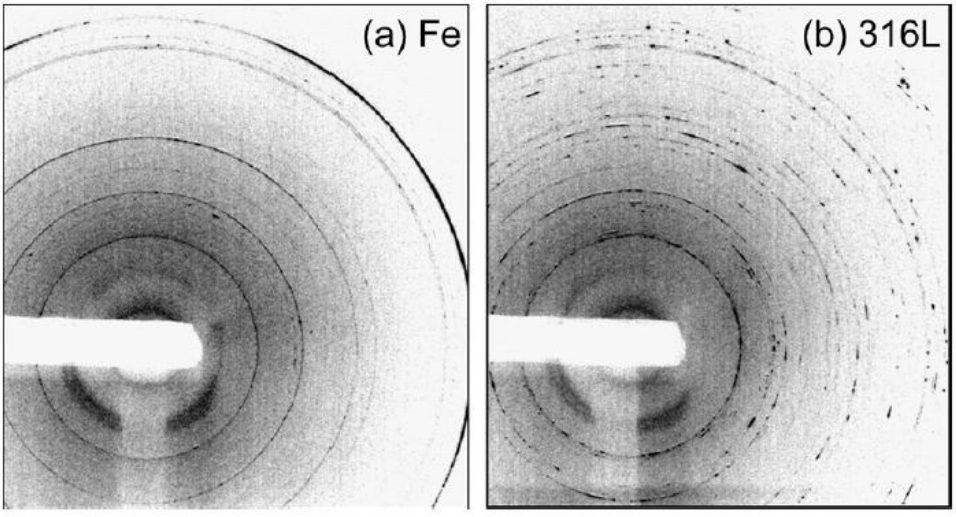

Figure 2-8. *In-situ* X-ray diffraction images of the salt layer on (a) iron and (b) stainless steel 316L in 1 M HCl [51]

2.4 Mass transport in artificial pits

It is difficult to make quantitative studies of the electrochemistry in real pits, so 1D artificial pits (see Section 2.2) have been used widely to investigate mass transport and metal ion concentration inside pits.

2.4.1 Assumptions made for mass transport studies of artificial pits

A number of assumptions are commonly made in studies of mass transport in artificial pits:

(1) In alloys, the metal ions are regarded as a single hypothetical species M^{n+} [20, 33, 34, 37, 53].

(2) Transport of hydrolysis products in the pit solution is ignored [23, 37].

(3) The diffusion length is the artificial pit depth after the pit reaches a minimum depth [20, 34, 37, 53, 54], where the diffusion from the pit mouth can be neglected. This is valid when the current-pit depth product "*ix*" is a constant [37, 53], i.e. i is linear with $1/x$, and the effects of diffusion in the bulk solution are negligible. Gaudet et al. [37] determined this minimum pit depth by a plot of current vs. inverse pit depth.

(4) Under conditions of diffusion-limited dissolution of Fe-alloys in chlorides, at the pit bottom, the concentration of metal ions is usually regarded as the saturation concentration of $FeCl_2$ [20, 30, 37, 39, 53, 55], and at the pit mouth the concentration of metal ions is zero [13, 20, 33, 34, 37, 53, 54, 56].

2.4.2 Diffusion and metal ion concentration

Novakovski and Sorokina [26] found the reciprocal of the current as a linear relationship with diffusion length in a 18-8 stainless steel artificial pit. Isaacs [33] suggested that diffusion current was determined by Fick's first law (Equation 2-6) for diffusion-limited dissolution,

$$I = \frac{nFD(C_s - C)A}{x + \Delta} \qquad \text{Equation 2-6}$$

where n is the average valence of metal ions, F is Faraday's constant (96500 C/mol), D is the average diffusion coefficient of dissolving metal ions (assumed to be ~0.5×10^{-5} cm^2/s in a stainless steel 304 artificial pit in 1 M NaCl), C_s is the saturation concentration of metal ions (6 M based on the assumed "D") at metal/solution interface, C is the concentration of metal ions in the bulk solution, A is the cross-section area of the electrode, x is the diffusion length (pit depth), and Δ can be regarded as an additional diffusion path in the bulk solution. If it is assumed that the metal in the pit is dissolving without any other reactions, the diffusion length/pit depth x is given by Faraday's law [33] (Equation 2-7),

$$x = \int_0^t \frac{M_w}{AnF\rho} I dt \qquad \text{Equation 2-7}$$

where M_w and ρ are the molar mass and density of the metal.

Furthermore, Pickering and Frankenthal [57] proposed a model for ion transport, which took into account both diffusion and electrical migration, but ignored ionic interactions. This model was also applied by Galvele [13] in the circumstances with various concentrations of aggressive anions, and a pit stability product "ix" (termed by Pistorius and Burstein [55]) was used to determine whether a pit would grow or passivate (x is pit depth, i is the current density). Tester and Isaacs [34] developed the mass transport model described in Equation 2-6 using the Nernst-Einstein equation, where both diffusion and migration were taken into account (Equation 2-8),

$$\frac{I}{AnF} = D\left[\frac{\partial C}{\partial x} + C\frac{nF}{RT}\frac{\partial \Phi}{\partial x}\right] \qquad \text{Equation 2-8}$$

where T is the absolute temperature and R is the gas constant, the other symbols are the same as described in Equation 2-6. Tester and Isaacs [34] believed that chloride activity (a_{Cl^-}) was an important factor on the solubility of metal chloride, and viscosity effects had to be considered to correct the diffusion coefficient at high chloride concentrations.

Kuo and Landolt [30] studied an iron rotating disc electrode in concentrated chloride media and characterised Fe^{2+} as the diffusion-limiting species. The $FeCl_2$ saturation concentration in water was determined to be 4.25±0.05 M according to atomic adsorption analysis, and $FeCl_2$ concentration at the metal surface was equal to this saturation concentration when dissolution was diffusion-limited, and an "effective diffusion coefficient" (diffusion and migration taken into account) 0.85×10^{-5} cm^2/s was determined assuming that the self-diffusivity (electric migration excluded) was constant, and that the viscosity varied with chloride concentration to correct the coefficient.

Gaudet et al. [37] reported a constant effective diffusion coefficient 0.824×10^{-5} cm^2/s for stainless steel 304 in 1 M NaCl, which was derived from "*ix*" value in Equation 2-9,

$$ix = nFDC_{sat} \qquad \text{Equation 2-9}$$

with the assumption that C_{sat} was the saturation concentration of Fe^{2+} (saturation concentration of $FeCl_2$, 4.2 M) at the pit bottom and the concentration of Fe^{2+} at the pit mouth was zero. The effective diffusion coefficient is close to that determined by Kuo and Landolt [30]. Based on the same assumption, Ghahari [58] reported an effective diffusion coefficient 1.03×10^{-5} cm^2/s in an experiment on a 1D foil of stainless steel 304. Steinsmo and Isaacs [20] studied Fe-17.4Cr alloy artificial pit in 1 M NaCl and reported an effective diffusion coefficient 1.02×10^{-5} cm^2/s via the "*ix*" value in Equation 2-9, but since chromium chloride may also be present, the saturation concentration of $FeCl_2$ was assumed to be 3.5 M. Isaacs

[21] applied *in-situ* XRF to a Fe-17.7Cr-12.8Ni artificial pit in acidic 1 M chloride, the saturation concentrations of Fe^{2+}, Cr^{3+} and Ni^{2+} were found to be 3.46 M, 1.08 M, 0.48 M respectively. The effective diffusion coefficients were 0.64×10^{-5} cm^2/s, 0.56×10^{-5} cm^2/s and 0.8×10^{-5} cm^2/s, respectively. The total concentration of metal ions was 5.02 M. These diffusion coefficients and saturation concentrations are summarised in Table 2-1.

Table 2-1. Summary of metal ion diffusivity and saturation concentration in Fe-alloys 1D artificial pits (C_{sat}: metal ion saturation concentration; D_{eff}: effective diffusion coefficient)

authors	diffusivity (10^{-5} cm^2/s)	C_{sat} (M)	metal and solution	notes
Isaacs [33]	0.5 (assumed)	6	stainless steel 304, 1 M NaCl	electrical migration not considered
Kuo [30]	0.85	4.2 (measured)	iron, $FeCl_2$, NaCl or HCl	constant D_{eff}, viscosity varied with concentration
Gaudet [37]	0.824	4.2 [30]	stainless steel 304, 1 M NaCl	constant D_{eff} calculated with "*ix*" value
Steinstmo [20]	1.02	3.5 ($CrCl_3$ may reduce the solubility of $FeCl_2$)	Fe-17.4Cr, 1 M NaCl	constant D_{eff} calculated with "*ix*" value
Isaacs [21]	0.64	5.02 (metal ion concentration measured using XRF)	Fe-17.7Cr-12.8Ni, 0.5 M HCl + 0.5 M NaCl	constant D_{eff} determined with concentration gradients and current
Ghahari [58]	1.03	4.2 [30]	stainless steel 304, 1 M NaCl	constant D_{eff} by Faraday's law/Fick's first law

In addition, some authors have reported the presence of a surface layer (other than a salt layer) formed during steel dissolution, which was found to inhibit the diffusion of metal ions, e.g. in NaCl as carbides [59], in nitrates as carbon film [60] or carbides [61], in NaOH as carbon/magnetite [62], and in CO_2 saturated solutions as $FeCO_3$ [63] or $FeCO_3$ with trace

carbides [64, 65]. However, no quantitative characterisation on the effect of diffusion has been reported. Kawaley [66] observed the formation of a "black layer" within an iron artificial pit; Mi [67] also found a black layer in a stainless steel artificial pit, which slightly hindered the diffusion, but the composition was not characterised. Since the carbon contents in the materials may not be significant enough to inhibit diffusion, this effect was not considered in the work reported in Table 2-1.

2.5 Tafel kinetics in metal ion saturation solution

According to [68], Tafel slope is deduced from the Butler-Volmer equation

$$I = I_0[e^{\alpha nF\eta/RT} - e^{-(1-\alpha)nF\eta/RT}] \qquad \text{Equation 2-10}$$

where I_0 is the current at equilibrium, α is the charge transfer coefficient and the value is ~0.5, η is the overpotential ($\eta = E - E_{corr}$, where E_{corr} is the open circuit potential). When $\eta >> \frac{RT}{nF}$, the cathodic reaction is negligible, the Tafel equation for the anodic dissolution may be written as

$$\eta = \frac{2.303RT}{\alpha nF}\log(I_a / I_0) \qquad \text{Equation 2-11}$$

and anodic Tafel slope is defined as

$$b_a = d\eta / d\log I_a = \frac{2.303RT}{\alpha nF} \qquad \text{Equation 2-12}$$

where I_a is the anodic current. When the ohmic drop across the solution of an artificial pit during active dissolution is taken into account, the dissolution kinetics may be described as Equation 2-13 [37],

$$\eta = b_a \log I + IR_s + B \qquad \text{Equation 2-13}$$

where η is the applied overpotential, R_s is the solution resistance, b_a is the anodic Tafel slope, and B is a constant, which can be related to corrosion potential E_{corr}. Laycock and White [69] assumed that dissolution kinetics was identical for salt-covered and salt-free surfaces, so when the potential drop across a salt layer and pit solution were both taken into account, the dissolution kinetics could be described as

$$E_{app} = E_{corr} + b_a \log(i_a / i_0) + \Phi_s + \Phi_{sl} \qquad \text{Equation 2-14}$$

where Φ_s and Φ_{sl} are the potential drop in solution and across salt layer respectively. The anodic Tafel slope b_a can be obtained from the current-voltage characteristics if the applied potential is *IR*-corrected as "$E_{app} - (\Phi_s + \Phi_{sl})$". This b_a value describes the Tafel kinetics in a metal ion saturated solution, and three methods have been reported in literature to measure the Tafel slope for metal ions at saturation or near-saturation concentrations. The results of Tafel kinetics derived from these three methods are summarised in the following sections.

2.5.1 Potentiostatic/potential step method

Newman and Isaacs [54] applied a potential step methods from 200 mV(SCE) (salt-covered surface) to below -300 mV(SCE) (salt-free surface) to obtain active dissolution at near-saturation concentration of metal ions. The anodic Tafel slope of Fe-19Cr-10Ni alloy in 1 M NaCl was found to be about 60 mV/decade and 75 mV/decade for above and below -300 mV(SCE), respectively. The anodic Tafel slope for stainless steel 304L in 1 M NaCl was around 60 mV/decade above -250 mV(SCE). The potential was *IR*-corrected for both materials (Figure 2-9a). A similar potential step method was applied by Gaudet et al. [37], who found that the Tafel slope for stainless steel 304 in 1 M NaCl was 54 mV/decade

after *IR*-correction (Figure 2-9b). Steinsmo and Isaacs [20] also used a potential step method, where an imposed ac signal (10 kHz square wave with 10 mV amplitude) was used to measure the solution resistance for *IR*-correction. The anodic Tafel slope of Fe-17.4Cr alloy in 1 M NaCl was 108 mV/decade, almost twice as much as the Ni-containing alloys described above. Enerhaug et al. [53] used the same method for 12.3Cr-2.6Mo-6.5Ni (super martensitic) stainless steel in 1 M NaCl, and found that the Tafel slope was 57 mV/decade.

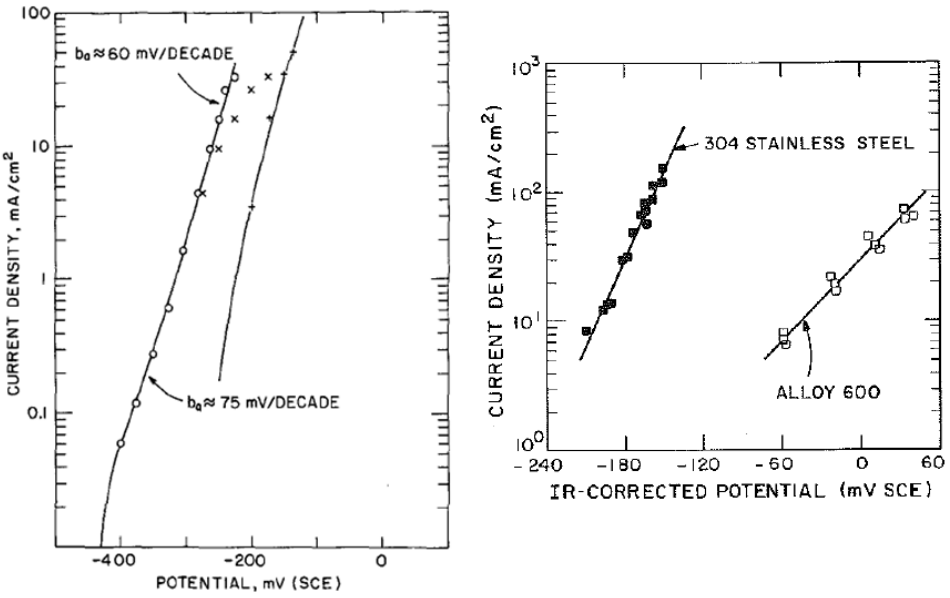

Figure 2-9. Anodic dissolution kinetics for metal ions at near-saturation concentrations. (a) Fe-19Cr-10Ni alloy (left) and stainless steel 304L (right) in 1 M NaCl [54]; (b) stainless steel 304 (left) and alloy 600 (right) in 1 M NaCl [37]

2.5.2 Transition potential method

As defined by Laycock and Newman [39], the transition potential E_T is the potential just between diffusion-controlled and ohmic-controlled dissolution. The pit is assumed at this point to be in a salt-free state but the solution is saturated in metal ions at the electrode. Equation 2-15 applies in this circumstance [39],

$$E_T = E_{corr} + \Delta E_{act} + IR_s \qquad \text{Equation 2-15}$$

where ΔE_{act} and IR_s represent the overpotential for the active dissolution reaction and the solution resistance, respectively. Laycock and Newman [39] assumed that the *IR* drop in pit solution was a constant for all pit depths, because I_{lim} was proportional to $1/x$ (inverse pit depth) according to Fick's first law (Equation 2-6), and the pit solution resistance was proportional to x (pit depth). Equation 2-15 can be rewritten as

$$E_T = E_{corr} + b_a \log(i_{lim} / i_{corr}) + I_{lim} R_s \qquad \text{Equation 2-16}$$

Since the *IR* drop in pit solution was assumed to be constant, only the potential drop of the pit exterior was subtracted from IR_s to give a linear-fit of E_T vs. $\log i_{lim}$. The Tafel slope was ~110 mV/decade for metal ion saturation solution for stainless steel 302 in 1 M NaCl (Figure 2-10). However, Mi [67] used the same method on stainless steel 304 and compared the *IR*-correction used by Laycock and Newman [39] with a full *IR*-correction, which subtracts both the interior (pit solution) and exterior (bulk solution) *IR* drop. This study reported values close to those of Laycock and Newman [39] if the *IR* drop of bulk solution was subtracted, but the Tafel slopes dropped to ca. 50 mV/decade if a full *IR*-correction was carried out. This indicates that the assumption of constant *IR* drop for the pit interior may not be valid, since I_{lim} was only proportional to $1/x$ after the pit depth reaches a certain value, as reported by Gaudet et al. [37].

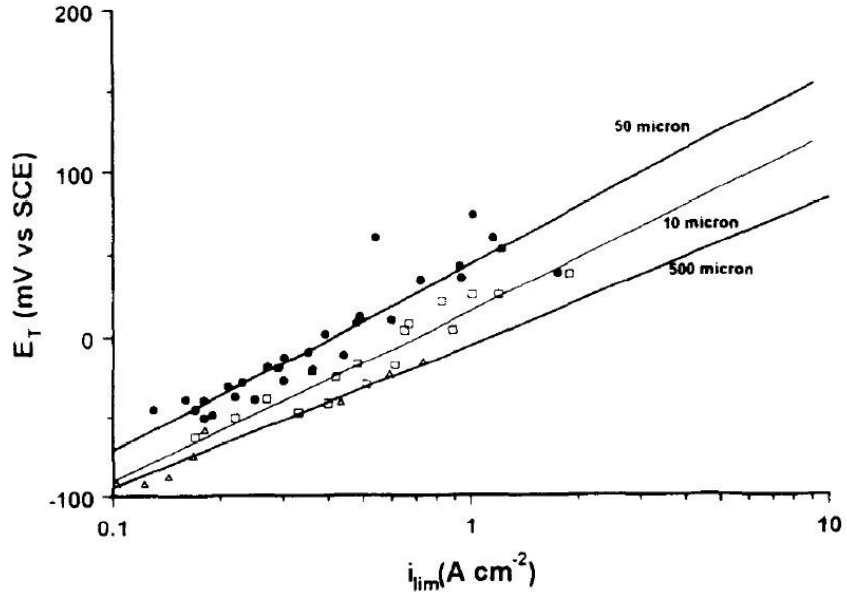

Figure 2-10. Transition potential E_T vs. logi_{lim} for stainless steel 302 wire artificial pits (10, 50, 500 μm diameter) in 1 M NaCl, *IR* drop of pit exterior was subtracted for the correction of E_T [39].

2.5.3 Potentiodynamic method in ohmic-control region

In the current-voltage plot shown in Figure 2-6, from point A to B, the dissolution is ohmic-controlled before salt precipitation [38], and the surface concentration of metal ions can be at saturation, near-saturation or supersaturation. Mi [67] studied an artificial pit of stainless steel 304 in 0.5 M $MgCl_2$, and the anodic Tafel slope was obtained from the linear-fit of the *IR*-corrected potential and current density (Figure 2-11) in the ohmic-control region. The solution resistance was measured using an imposed ac signal (frequency 100 kHz, amplitude 5 mV) on the applied potential, because the capacitive component was essentially zero at high frequencies. Thus the solution resistance and the current were measured concurrently (see Appendix). The Tafel slope was determined to be 51 to 56 mV/decade, and a faster potential sweep resulted in a slightly larger Tafel slope (sweep rate 2 to 10 mV/s).

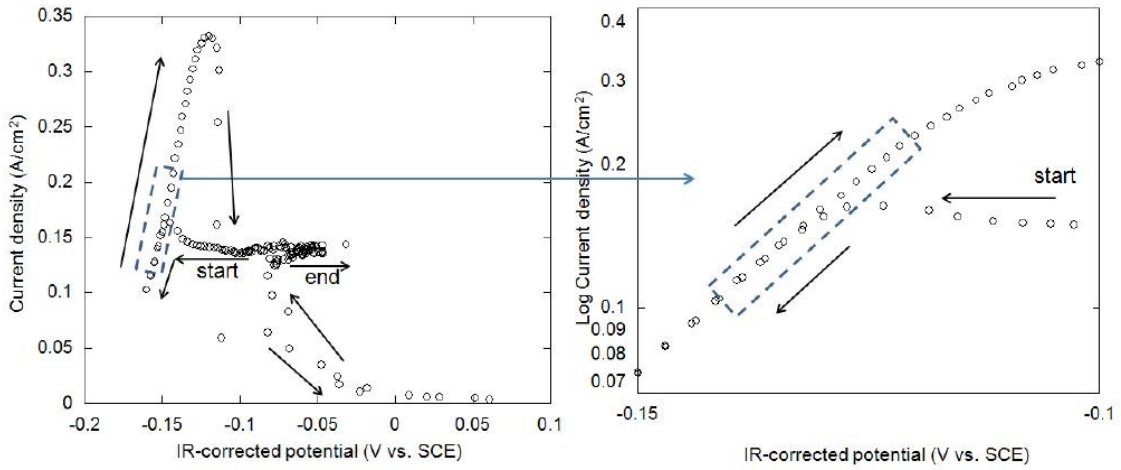

Figure 2-11. Current density vs. *IR*-corrected potential on a stainless steel 304 artificial pit in 0.5 M $MgCl_2$, potential scan rate 10 mV/s, the Tafel slope was obtained from the linear-fit of *IR*-corrected potential vs. current density in the ohmic-control region [67]

A summary of the results of Tafel slope measurements for metal ion saturation or near-saturation concentration is in Table 2-2.

Table 2-2. Summary of Tafel slope in metal ion saturation or near-saturation solutions

authors	Tafel slope (mV/decade)	metal and solution	metal ion concentration	notes
Newman and Isaacs [54]	60 and 75 for above and below -300 mV(SCE) respectively	Fe-19Cr-10Ni, 1 M NaCl	near-saturation	potential step method, IR_s corrected
Newman and Isaacs [54]	60 above -250 mV(SCE)	stainless steel 304L, 1 M NaCl	near-saturation	potential step method, IR_s corrected
Gaudet [37]	54	stainless steel 304, 1 M NaCl	near-saturation	potential step method, IR_s corrected
Steinsmo [20]	108	Fe-17.4Cr, 1 M NaCl	near-saturation	potential step method, IR_s corrected
Enerhaug [53]	57	super martensitic stainless steel, 1 M NaCl	near-saturation	potential step method, IR_s corrected
Laycock [39]	110	stainless steel 302, 1 M NaCl	saturation	E_T method, IR_{ext} corrected
Mi [67]	51 to 56 (depending on potential sweep rate)	stainless steel 304, 0.5 M $MgCl_2$	near-saturation	potentiodynamic method in ohmic-control region, IR_s corrected

2.6 Active/brightening dissolution

2.6.1 Hoar's work

Brightening/electropolishing dissolution is the anodic dissolution of an electrode surface, which may involve smoothing of rough surface or suppression of "etching figures" [24]. Hoar was the first to extensively study the etching/brightening dissolution. It was believed that a compact film of high ionic-conductivity was necessary for anodic brightening [25]. The diffusion layer above the ionic-conductive film is believed to be significant for brightening dissolution, which tends to limit the dissolution of the whole area to the same rate, i.e. ion diffusion would be faster at "asperities" and slower at "valleys", so a rough surface tends to

level [70]. Furthermore, Hoar [25] found that during electropolishing dissolution, higher potentials increased the pitting area and current simultaneously, but the current density over the pit surface was independent of potential, consistent with the presence of a self-regulating salt layer as described in Section 2.3.1.

Hoar [71] discussed several types of dissolution/ passivation, and a summary is given in a potential vs. concentration of corrosive anions in Figure 2-12, which describes the transition between passivation and several types of dissolution, this concept was further developed by Sato [72-74], whose studies are reviewed in Section 2.6.2.

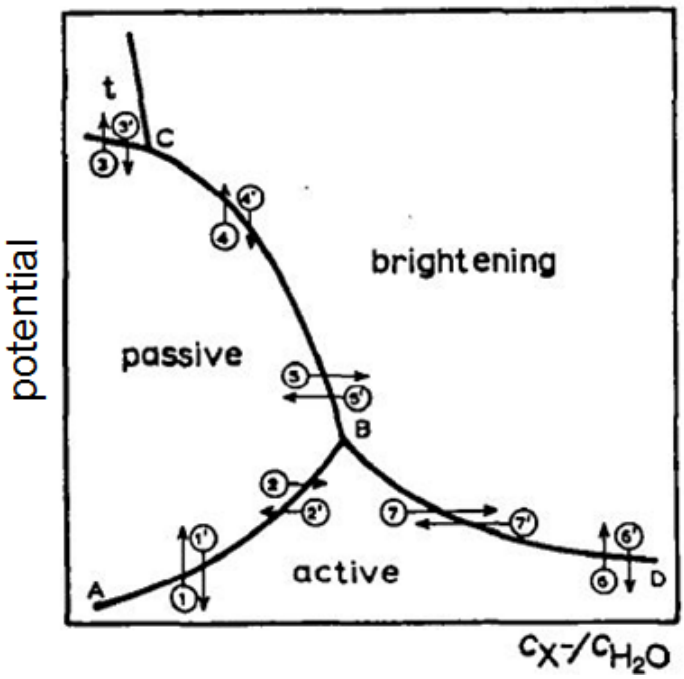

Figure 2-12. A schematic diagram of dissolution behaviour as a function of potential and concentration of corrosive anions (1 and 1′: passivation and active dissolution leading to etching morphology; 2 and 2′: passivation and etching dissolution activated by sufficient corrosive anions; 3 and 3′: passivation and transpassive brightening dissolution; 4 and 4′: passivation and brightening dissolution of pitting at high potentials; 5 and 5′: passivation and brightening dissolution of pitting by concentrated corrosive anions; 6 and 6′: etching/brightening dissolution by changing potential in corrosive solutions; 7 and 7′: etching/brightening dissolution by changing the concentration of corrosive anions, which was described in [70]) [71]

2.6.2 Effect of salt layer and potentials

Brightening dissolution has been reported to occur under a salt layer at high potentials. Schwenk [75] observed that an etched pit on stainless steel at low potentials (near the equilibrium potential) became isotropic at higher potentials. This observation was also reported by Ke and Alkire [76]. Similarly, Beck [22] linked the brightening of a titanium surface at high voltages (3 V to 6 V/SCE) and the crystallographic etching at lower voltages with the presence/absence of a salt layer. Beck [77] also reported that an active dissolution (salt-free) of aluminium resulted in a deeply etched surface. Frankenthal and Pickering [78] related the polishing morphology of an iron pit to the formation of a "rate-limiting film", and transition from etching to brightening was observed upon the formation of a ferrous salt layer, which was also reported by Beck and Alkire [31]. Frankel [10] also believed that a crystallographic etching morphology of a pit occurs at a low potential without a salt layer.

Sato [72] has suggested two modes of dissolution in concentrated solutions: firstly, active/etching dissolution (on bare metal surface at low potentials), and secondly, transpassive/brightening dissolution (at relatively high potentials). A critical concentration of aggressive anions at high potentials was determined above which brightening dissolution took place ($[Cl^-]>2$ M). Other work by Sato [73, 74] supported and further developed Hoar's model described in Figure 2-12. It was proposed that the electropolishing surface is usually salt-covered at high potentials, and an increase in the concentration of aggressive anions extends the "electropolishing potential" to lower potentials, while an increase in the concentration of H^+ extends the active/etching dissolution potential to higher potentials.

Sazou [79] studied the dissolution of iron in an artificial pit in H_2SO_4 with trace chloride, where brightening of electrode surface was observed above a critical applied potential

(0.7 V/SCE) and a critical chloride concentration (25 mM), and this coincided with the precipitation of a ferrous salt layer, consistent with the work of Sato [73, 74]. This was also reported in Sazou's other work on the $Fe/H_2SO_4/NaCl$ system [80, 81].

Electropolishing dissolution is important for electrochemical machining. Mao [82] ascribed the electropolishing surface to the precipitation of a salt layer during the ECM process on steel in $NaClO_3$, which was also reported for $NaNO_3$ electrolytes [83]. In addition, Mao [84] assumed a dual (salt and oxide) film to be the reason for electropolishing in the transpassive regime, the oxide film was compact and "contaminated" by adsorbed anions (as suggested by Hoar [25]), which was converted from a salt layer that precipitated at lower potentials. This dual structure is similar to the duplex salt layer structure described in Section 2.3.3.

Landolt [85] reviewed electropolishing/etching dissolution in pitting and electrochemical machining, and suggested that diffusion-controlled dissolution is the critical factor for electropolishing dissolution, and the presence of a salt layer often coincides with it. In contrast, the etching dissolution may result from the different dissolution rates of crystallographic planes [86] or preferential dissolution of certain planes [87]. Diffusion-control, although usually attributed to the transport of metal ions from the electrode to solution, could also be related to transport of other species such as water or Cl^- towards the electrode, as reviewed earlier by Kuo and Landolt [30].

2.7 Nitrates

2.7.1 Nitrate reduction mechanisms

Nitrate can act as an oxidising agent, and its reduction mechanism has been widely studied since the 1940s. Evans [88] found that the addition of nitrous acid into nitric acid increased the current density of cathodic reaction, while the removal of nitrous acid (by drawing air through the solution to oxidise nitrous acid) greatly reduced the current density of cathodic reaction, which indicates that the reduction of nitric acid is autocatalytic: the possible reduction products were HNO_2 and NO_2. In the 1950s and 1960s, two autocatalytic mechanisms in concentrated HNO_3 were proposed by Vetter and Schmid respectively, which were reviewed by Balbaud [89]:

(1). Vetter's mechanism.

NO_2 is the electroactive species on the electrode surface:

$$(HNO_2)_{ads.} + H^+ = (NO^+)_{ads.} + H_2O \qquad \text{Equation 2-17}$$

$$(NO_3^-)_{ads.} + (NO^+)_{ads.} = (N_2O_4)_{ads.} \qquad \text{Equation 2-18}$$

$$(N_2O_4)_{ads.} = 2(NO_2)_{ads.} \qquad \text{Equation 2-19}$$

$$(NO_2)_{ads.} + e^- = (NO_2)^-_{ads.} \qquad \text{Equation 2-20}$$

$$(NO_2)^-_{ads.} + H^+ = (HNO_2)_{ads.}; \qquad \text{Equation 2-21}$$

(2). Schmid's mechanism.

NO^+ is the electroactive species near the electrode surface in the solution:

$$HNO_2 + H^+ = NO^+ + H_2O \qquad \text{Equation 2-22}$$

$$NO^+ + e^- = NO \qquad \text{Equation 2-23}$$

$$2NO + NO_3^- + H^+ + H_2O = 3HNO_2. \qquad \text{Equation 2-24}$$

Either of these two mechanisms may proceed depending on the nitrate concentration. Balbaud [90] believed that, near the equilibrium potential of the nitrate reduction reaction, the major species was NO and NO_2 for less than 8 M HNO_3 and more than 8 M HNO_3, respectively. This was confirmed in [89], where NO_2 (red gas) evolution was observed from 8 M and 12 M HNO_3 at 0.4 V(SSE) and NO (colourless gas, assumed to be NO) evolution was observed from 4 M HNO_3 at 0.25 V(SSE) during the cathodic polarisation of a Pt electrode. It was also reported that HNO_2 may accelerate the cathodic reduction reaction of HNO_3, which was more noticeable for lower HNO_3 concentrations (agreed with the observation of Evans [88] described above). It indicates that HNO_3 is mostly reduced indirectly through an autocatalytic mechanism, and HNO_2 was regarded as the electroactive species. The reduction products were either NO or NO_2 depending on the applied potentials and the HNO_3 concentration [89]. The mechanism was proposed as follows [91]:

(1). $[HNO_3] > 8$ M:

$$(HNO_2)_{el.} + H^+ + e^- + s = (NO)_{ads.} + H_2O \qquad \text{Equation 2-25}$$

$$HNO_3 + (NO)_{ads.} = (HNO_2)_{el.} + (NO_2)_{ads.} \qquad \text{Equation 2-26}$$

$$2(NO_2)_{ads.} + H_2O = HNO_3 + (HNO_2)_{el.} + 2s \qquad \text{Equation 2-27}$$

$$(NO_2)_{ads.} = (NO_2)_{g.} + s \qquad \text{Equation 2-28}$$

$$(HNO_2)_{el.} = (HNO_2)_{sol.}; \qquad \text{Equation 2-29}$$

(2). $[HNO_3] < 8$ M:

$$(HNO_2)_{el.} + H^+ + e^- + s = (NO)_{ads.} + H_2O \quad \text{Equation 2-30}$$

$$HNO_3 + 2(NO)_{ads.} + H_2O = 3(HNO_2)_{el.} + 2s \quad \text{Equation 2-31}$$

$$(NO)_{ads.} = (NO)_{g.} + s \quad \text{Equation 2-32}$$

$$(HNO_2)_{el.} = (HNO_2)_{sol.} \quad \text{Equation 2-33}$$

("el." means at the electrode, "sol." means in the solution, "ads." means the species that adsorbed on the electrode, "s" means an available adsorption site on the electrode).

From this mechanism, Balbaud [91] believed that HNO_3 reduction is catalysed by its reduction products. This was demonstrated by other work. For example, Armstrong [92] found that NO and NO_2 catalysed/autocatalysed the nitrate reduction reaction on a stainless steel 304L electrode, increasing the current by 10 times, but N_2 and N_2O had no effect. The catalysing effect of NO_x was also reported by Takeuchi [93], who found that the accelerated corrosion rate was limited by the solubility of HNO_2. Fauvet [94] described this mechanism as shown in Figure 2-13 and pointed out the "ambivalent" effects of HNO_2, i.e. it thermodynamically inhibited the redox reaction according to Nernst equation, but kinetically catalysed the reaction.

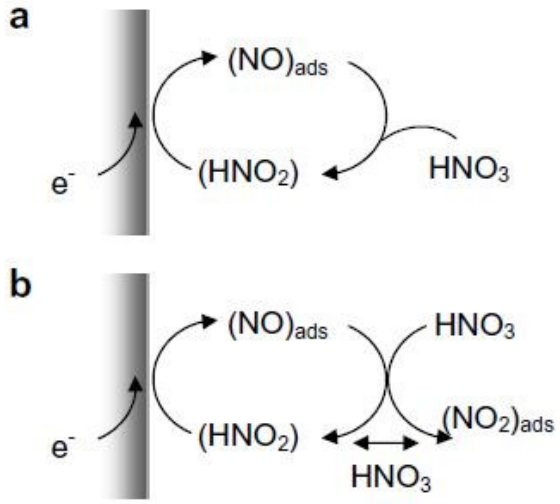

Figure 2-13. Sketch of HNO_3 reduction mechanism. (a) HNO_3 concentration < 6 M; (b) HNO_3 concentration > 8 M), "ads" indicates the species that are adsorbed on the electrode [94]. The mechanism (a) is identical to Equation 2-30 and Equation 2-31, the mechanism (b) is identical to Equation 2-25 and Equation 2-26.

2.7.2 Fe-alloys corrosion in nitrate-containing solutions

Anions can be classified as aggressive (depassivating) and inhibitive (passivating). Halide ions are the most important aggressive anions promoting the breakdown of local passivity, while inhibitive ions, such as nitrate, chromate, sulphate and phosphate, often exert the opposite effects [7].

2.7.2.1 Adsorption mechanism

Since chloride and nitrate ions can both adsorb on the metal surface during anodic dissolution [95], the adsorption mechanism has been discussed in various work. Schwenk [75] reported that the addition of $NaNO_3$ to NaCl suppressed pit propagation of stainless steel under potentiostatic conditions, and the suppression was enhanced with increasing nitrate concentration. It was claimed to be ascribed to an adsorption mechanism: in the pitting potential region of a certain electrolyte, activators (chloride/bromide ions) were preferentially adsorbed, while outside the potential region, passivators (nitrate/hydroxide ions) were

preferentially adsorbed. Uhlig and Gilman [96] also reported an inhibition effect of nitrate on the dissolution of stainless steel: the addition of nitrate to chloride solutions decreased the weight loss of stainless steel for a one day immersion compared to in the absence of nitrate; critical concentrations of chloride were determined for certain concentrations of nitrate. It was also ascribed to be a competitive adsorption mechanism between Cl^- and NO_3^-.

Leckie and Uhlig [97] reported that the addition of nitrate increased the pitting potential of stainless steel (Figure 2-14), which was attributed to the "competitive adsorption" between Cl^- and NO_3^-, i.e. both anions adsorbed at certain sites on the metal surface, in the presence of nitrate, a higher potential was required for sufficient Cl^- adsorption to destroy the local passivity. Equation 2-34 was proposed for the critical concentration of chloride for pitting,

$$\log[Cl^-] = 1.88\log[NO_3^-]+1.18 \qquad \text{Equation 2-34}$$

which agrees with Uhlig and Gilman [96]. "Safe" regions of $[Cl^-]/[NO_3^-]$ where pitting was completely suppressed were also determined for stainless steel 316L [98] and steel [6].

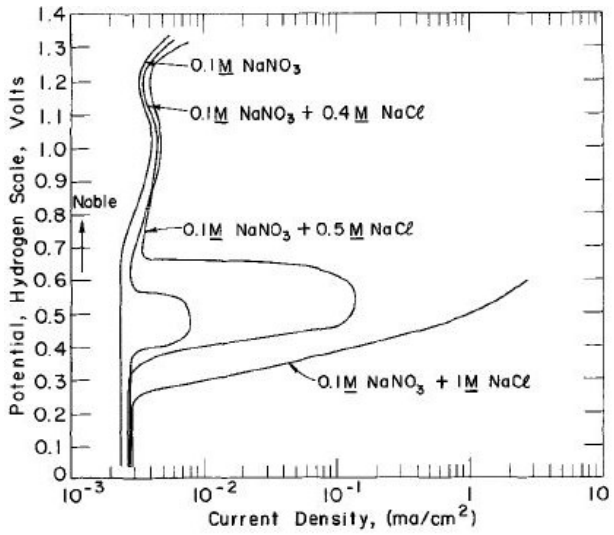

Figure 2-14. Polarization of stainless steel in 0.1 M $NaNO_3$ with different concentrations of NaCl, showing the inhibitive effect of nitrate on pitting corrosion [97]

Yang [99] proposed a model combining the Point Defect Model [100] and competitive adsorption between NO_3^- and Cl^- [97] for the oxygen vacancies within a passive film, and the pitting potential of stainless steel 316L was found to be linear with $-\log([Cl^-]/[NO_3^-])$.

Anderko [101] developed a model through the competitive adsorption mechanism. It is based on an assumption that the measureable current at the repassivation potential would include the contributions of active dissolution current (metal ions generated due to the adsorbed aggressive ions, i.e. Cl^-) and passive current (oxide film generated due to water and the adsorbed inhibitive ions, i.e. NO_3^-). It was found that nitrate caused a rapid increase of repassivation potential above a critical concentration of nitrate, which manifested another inhibitive effect of nitrate on pitting corrosion besides increasing the critical pitting potential.

Ramya [102] carried out a Raman measurement on the passive film of a corroded surface of nitrogen-alloyed stainless steel. It was found that the concentration of nitrate at pitted areas was much higher than the other regions. This was regarded as evidence of nitrate preferential adsorption. However, this conclusion may be doubtful since the detected nitrate may be the product of the nitrogen oxidation during the anodic dissolution, and an adsorption mechanism is not necessarily involved.

2.7.2.2 Nitrate reduction mechanism

Green and Parkins [60] studied mild steel corrosion in acidic nitrates and suggested that the cathodic reaction was NO_3^- reduction to NO_2^-. Bandy and Vanrooyen [103] regarded the reduction of NO_3^- to NH_4^+ as a proton-consuming reaction (see Equation 2-35), which can improve the pitting resistance of stainless steel by increasing pH,

$$NO_3^- + 10H^+ + 8e^- = 3H_2O + NH_4^+ \qquad \text{Equation 2-35}$$

Leckie and Uhlig [97] found that a higher potential above the pitting potential may lead to passivation again (Figure 2-14), which was attributed to the redox reaction between NO_3^- and Fe^{2+}: when potential increased above the pitting potential, the dissolved Fe^{2+} may consume NO_3^- at the surface via the redox reaction, but Fe^{2+} may be oxidised to Fe^{3+} if the potential was higher than the Fe^{2+}/Fe^{3+} redox potential, so nitrate consumption by Fe^{2+} was diminished. Thus the inhibitive effect of nitrate via competitive adsorption with chloride (see Section 2.7.2.1) became dominant again.

However, it has been noted that nitrate is reduced much more easily by Fe^0 than Fe^{2+}, especially under acidic conditions [104-109]. Alexander [110] applied UV spectroscopy to investigate the dissolved corrosion products of iron in deaerated acidic $NaNO_3$, and found NO_2^- with no NO_3^- or Fe^{3+} species after an immersion test of less than 30 min, indicating that NO_3^- was mostly reduced by Fe^0. Buresh [111] found that nitrate reduction by Fe^{2+} only occurred above pH 7 with Cu^{2+} as a catalyst, but would not take place in acidic solutions, which was also demonstrated by Huang [112]. Nevertheless, these findings are not necessarily contradictory to the importance of the redox reaction between NO_3^- and Fe^{2+}, which may take place more readily with low water activity, e.g. within a salt layer [7, 35].

Newman and Ajjawi [35] found that a salt-covered stainless steel artificial pit in NaCl was passivated by addition of certain amount of nitrate at a critical potential during a potential forward scan, which depended on the $[NO_3^-]/[Cl^-]$ ratio. Current fluctuation was also observed, followed by abrupt passivation (Figure 2-15). It was claimed that either nitrate electroreduction or a redox reaction between Fe^{2+} and NO_3^-, both of which consume H^+ and produce water, occur more readily at the metal/salt interface than in the pit solution. In addition, a thicker salt layer results in a less acidic internal (pore) environment, which may also favour passivation. This has been reported earlier by Beck [28], who proposed that

passivation of iron may take place under a salt layer, and the increase of pH was proportional to the *IR* drop across the salt layer.

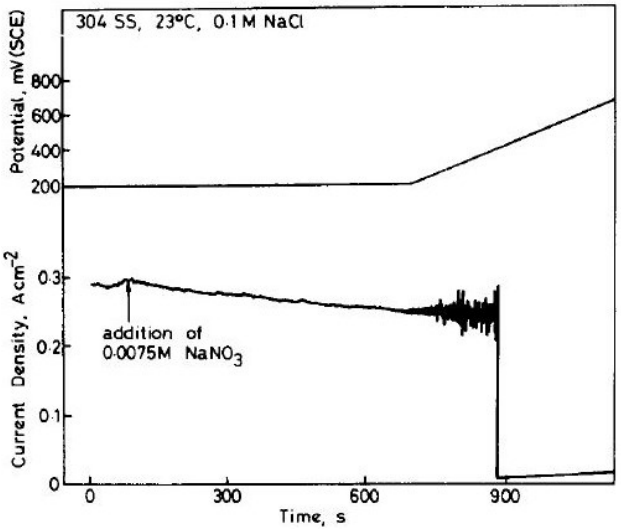

Figure 2-15. Addition of 7.5 mM $NaNO_3$ into 0.1 M NaCl in a stainless steel artificial pit during the diffusion-limited dissolution (salt-covered), passivation occurred above 440 mV(SCE) (pit depth 300 μm, pit diameter 50 μm) [35]

Sazou and Pagitsas [7] studied the $Fe/H_2SO_4/Cl^-/NO_3^-$ system and reported that nitrate stimulated pitting at low potentials; it was proposed that this occurred through the binding between NO_2^- (reduction product) and Fe^{2+}. However, it was found that nitrate led to passivation at high potentials: it was claimed that this occurred as a result of the redox reaction between NO_3^- and Fe^{2+}, when a salt layer may be present.

Kawaley [66] observed current oscillations during diffusion-limited dissolution of an iron artificial pit in 5 mM NaCl + 0.25 mM $NaNO_3$ (Figure 2-16a), and a dissolution/passivation transition at 0.7 V(SCE) in 5 mM NaCl+1.5 mM $NaNO_3$ (Figure 2-16b); bubbles were visible upon the addition of nitrate, but the cause was not clarified. Li [3] also observed bubbles in the vicinity of anodically polarised carbon steel in neutral $Cl^-/NO_3^-/NO_2^-$ solutions. Since the potential was higher than the thermodynamic potential of hydrogen evolution reaction, the

bubbles were ascribed to nitrate/nitrite reduction promoted by acidification through metal ion hydrolysis, and the gas was believed to be nitrogenous gas via nitrate reduction, consistent with other work [89, 91]. However, Brossia and Kelly [113] cast doubt on the possibility of nitrate reduction in the case of crevice corrosion of stainless steel in sulphate/nitrate solutions, since gaseous products were not observed, and neither NH_4^+ nor NO_2^- were detected.

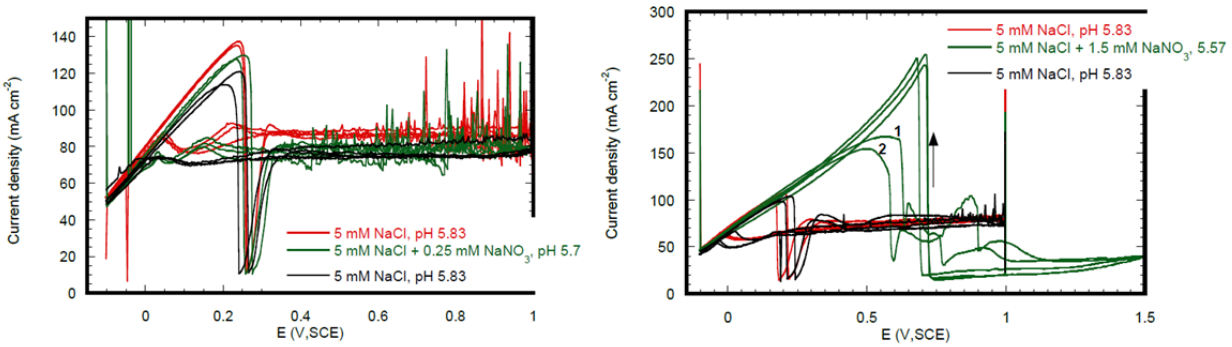

Figure 2-16. The current-voltage characteristics of Fe artificial pits in $NaCl/NaNO_3$ solutions, potential sweep in 3 mV/s, pit depth 1 mm. (a) 0.25 mM $NaNO_3$ + 5 mM NaCl; (b) 1.5 mM $NaNO_3$ + 5 mM NaCl [66]

Nitrate reduction to elemental nitrogen has also been proposed. Newman and Shahrabi [114] believed that anodic dissolution of stainless steel in nitrates could be blocked by the enrichment of elemental-nitrogen (via nitrate reduction), and this passivation was not through oxide formation. This was also proposed by Ortiz et al. [115] (according to the Pourbaix diagram of nitrogen), who found that NO_3^- was an efficient inhibitor for the crevice corrosion of Ni alloys.

Wexler and Galvele [116] detected N_2 after pitting of aluminium in $NaNO_3$, but no work has reported the detection of "elemental-nitrogen". Furthermore, Grabke [117] found that the elemental nitrogen in iron could be reduced to NH_4^+ in a wide range of potentials and pH. However, Raman measurements on nitrogen-alloyed steels demonstrated that nitrogen was

oxidised to NO_3^- at "pitting precursors" (where pit initiates at pitting potential) or after pitting (above pitting potential) [102, 118]. Yashiro [119] detected both NH_4^+ and NO_3^- after anodic polarisation of nitrogen-alloyed steels in chlorides. So the elemental nitrogen is very likely to be oxidised or reduced during the metal dissolution, and the metal surface is unlikely to be passivated by elemental-nitrogen.

Nitrate electroreduction can be manifested by the shift of corrosion potential. Uhlig and Cook [120] found that the addition of nitrate shifted the corrosion potential to more positive values, since the cathodic reaction was promoted by nitrate reduction. Kolman et al. [121] reported an active/passive transition during an immersion test of stainless steel in HNO_3/NaCl, it was believed that the OCP was shifted to the passive region by HNO_3 reduction, and it was demonstrated by the spontaneous passivation with NO/NO_2 injection, which catalysed this reaction (autocatalytic). The increase of the OCP via promoted nitrate reduction (cathodic reaction) has also been reported in the presence of catalysing NO_x [92, 93] or more concentrated HNO_3 [122]. A decrease in the OCP has also been found upon addition of chloride, which retards the nitrate reduction via competitive adsorption [122-125]. In addition, since nitrate reduction product NO_2^- is also prone to adsorb on the metal surface [126], the work reported in [122-126] indicate that the two mechanisms may operate simultaneously.

In summary, several models have been proposed to explain the effect of nitrate on corrosion of Fe-alloys [127]: competitive adsorption between NO_3^- and Cl^-, redox reaction between Fe^{2+} and NO_3^-, and electroreduction of NO_3^-. In addition, since nitrate-metal complex is stable only for nitrate/iron species [128], Ramya [102] suggested that iron chlorides or iron hydroxyl chlorides may form complexes with NO_3^-, which can inhibit the dissolution during pitting.

2.7.2.3 Current fluctuations

Newman and Ajjawi [35] reported current fluctuations for a stainless steel artificial pit in 0.1 M NaCl + 7.5 mM $NaNO_3$ just before passivation occurred (Figure 2-15). Zakeri and Moayed [129] also observed current fluctuations for a stainless steel artificial pit in 0.6 M NaCl + 0.02 M $NaNO_3$ in the diffusion-limited region (Figure 2-17). The current fluctuations were both ascribed to the presence of local passivation/reactivation beneath a salt layer, and the passivation was due to the nitrate reduction mechanism described in Section 2.7.2.2.

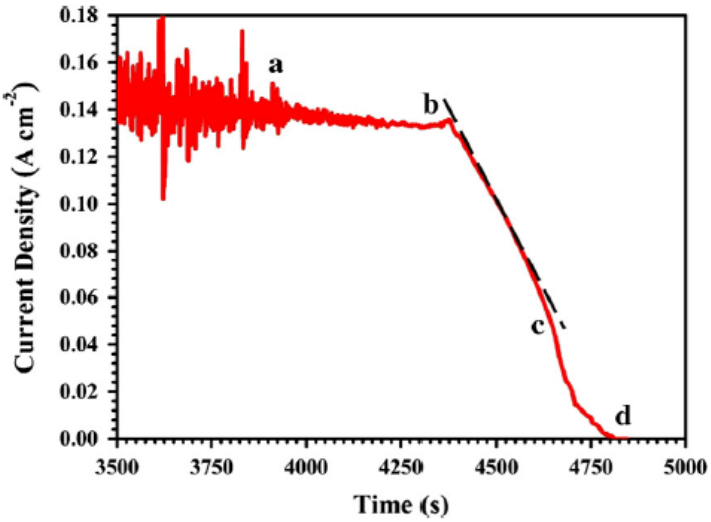

Figure 2-17. Current density vs. time of a duplex stainless steel 2205 artificial pit in 0.6 M NaCl + 0.02 $NaNO_3$ at 65 °C, potentiostatic test at 850 mV(SCE) before point "a", and potentiodynamic test (1 mV/s) from point "a" (at 850 mV/SCE) to point "d" at corrosion potential [129]

Ma [130] reported the development of current oscillations during iron dissolution in H_2SO_4/NaCl/$NaNO_3$ solutions, which was related to the susceptibility of pitting and was ascribed to the competition between "passivating" nitrate and "depassivating" chloride, resulting in the formation/dissolution of oxide film and ferrous salt layer.

Sazou and co-workers [79-81] have reported the potential-dependent current oscillations in Fe/H_2SO_4/NaCl systems, Figure 2-18a shows a "chaotic" oscillation with "aperiodic burst"

(due to the aperiodic activation/passivation transitions); Figure 2-18b shows an oscillation with almost even amplitude above and below a limited current. It was suggested that the oscillation in Figure 2-18b may be attributed to the cyclic dissolution/formation of a salt layer, since it is the same as the current oscillation reported in [131, 132], where an iron rotating electrode was dissolved in chlorides and the alternating formation/removal of a salt layer led to the current oscillation shown in Figure 2-19.

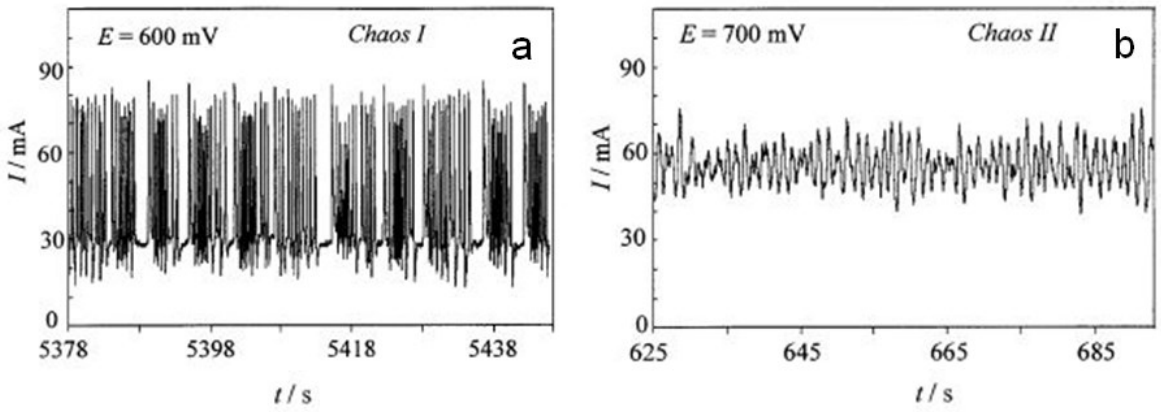

Figure 2-18. Current oscillations of an iron artificial pit in H_2SO_4 + 25 mM Cl^-. (a) chaos I due to the aperiodic activation/passivation; (b) chaos II due to the cyclic dissolution/formation of a salt layer [79]

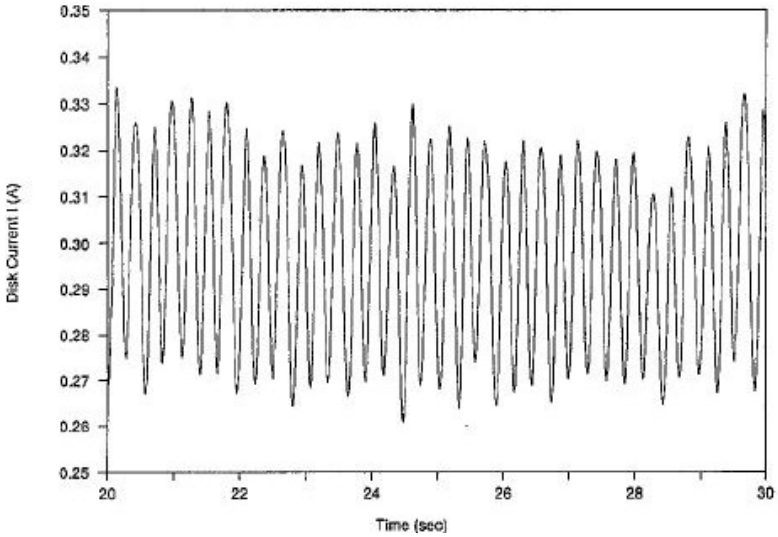

Figure 2-19. The current oscillation of an iron rotating electrode (200 rpm) in 4 M NaCl, applied potential 4 V(SCE) [132]

2.7.3 Fe^{3+} as a catalyst for nitrate reduction

Fe^{3+} has been reported to catalyse the nitrate reduction in concentrated HNO_3 (3 to 8 M). Arai et al. [133] found that 0.029 M Fe^{3+} accelerated nitrate reduction during cathodic polarisation of stainless steel in 8 M HNO_3 (Figure 2-20a); the evolution rate of gaseous products NO_x via HNO_3 reduction was substantially increased during free corrosion of stainless steel after the addition of 0.086 M Fe^{3+} (Figure 2-20b). Priya [134] reported that both Fe^{3+} and Cr^{6+} can catalyse the HNO_3 reduction and may increase the corrosion potential to the transpassive region. Other work [91, 93, 135] also agreed on that Fe^{3+} can catalyse the reduction of HNO_3, among which Takeuchi and Whillock [93] ascribed it to the coupling of Fe^{3+}/Fe^{2+}. However, no detailed mechanism has been proposed in these papers.

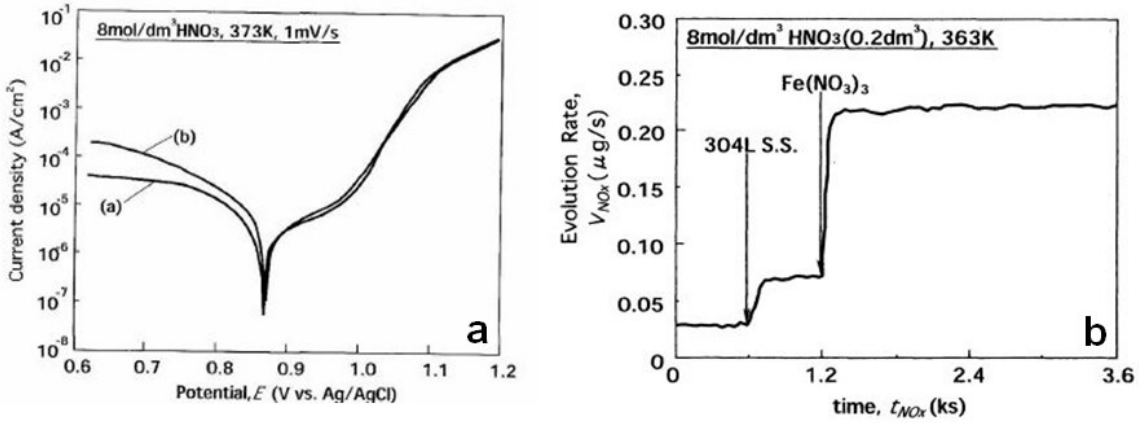

Figure 2-20. (a) polarisation of stainless steel 304L in 8 M HNO_3, potential sweep rate 1 mV/s at 100 °C (a. Fe^{3+} free; b. with 0.029 M Fe^{3+}); (b) evolution rate of NO_x vs. time in 8 M HNO_3 at 90 °C, stainless steel immersed at t=600 s, 0.086 M Fe^{3+} added at t=1200 s [133]

2.8 Synchrotron X-ray facilities

2.8.1 Introduction

Modern synchrotrons produce powerful beams of X-rays, which are highly parallel with high intensity. Figure 2-21 describes a synchrotron system consisting of five components: (1) a source of electrons with a linear accelerator (linac), (2) a booster ring to which the accelerated electrons are injected and further accelerated to relativistic speeds, (3) an evacuated storage ring to keep the electrons in an orbit with arrays of magnets (the bending magnets produce wide spectra of X rays; insertion devices/undulators produce intense X-rays), (4) radio frequency (RF) supply to replenish the energy loss due to radiation, (5) beamlines outside the storage ring along the tangent of bending magnets or straight insertion device. Energy is emitted as synchrotron light when the travelling direction of electrons is changed in a magnetic field [136-139].

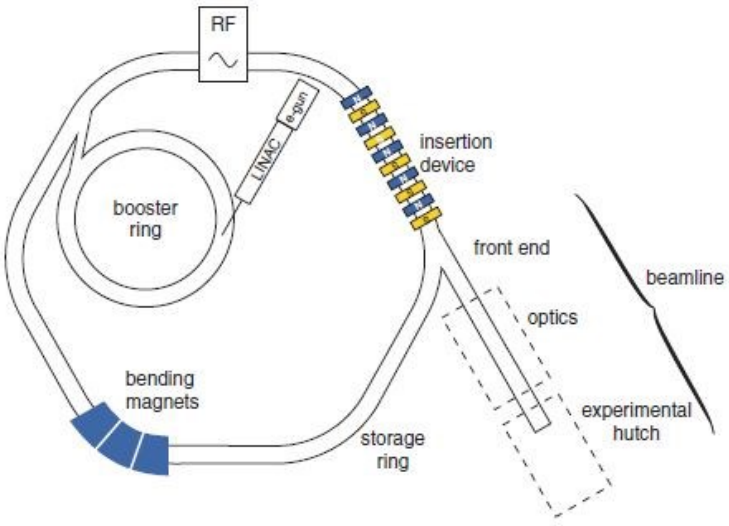

Figure 2-21. A schematic diagram of a modern synchrotron source [136]

2.8.2 X-ray diffraction on salt layer

A salt layer only precipitates on dynamically dissolving metal surface [51], and the removal of the potentials for this condition leads to salt dissolution, salt layers must therefore be studied *in-situ*.

This can be carried out with synchrotron X-rays, XRF techniques have been used in early work to investigate the salt layer [21, 50], but which does not give structural information. For the first time, Rayment et al. [51] has characterised the composition and structure of the salt layers on Ni, Fe and stainless steel with *in-situ* synchrotron XRD in artificial pits.

In-situ synchrotron X-ray diffraction has also been used in other corrosion research. Ingham et al.[63] studied the corrosion products of carbon steel in CO_2 saturated NaCl and identified siderite as the main phase; it was also found that the formation rate of the corrosion products increased with increasing temperature, while the crystallite size decreased with increasing temperature. Dowsett et al. [140] monitored and characterised the synthetic CuCl (nantokite) layer on copper surface in saturated $CuCl_2$ via time-lapse synchrotron XRD; it was proposed that the reported methods are applicable to the investigations of other corrosion processes.

2.8.3 X-ray radiography

The technique of X-ray radiography is based on penetration of X-rays through a specimen. X-ray illuminates the specimen, and the transmitted beam is attenuated depending on the properties of specimen according to Equation 2-36,

$$I = I_0 \exp(-\mu x) \qquad \text{Equation 2-36}$$

where I and I_0 are the intensity of incoming and transmitted X-ray respectively, x is the thickness of the specimen, μ is attenuation coefficient [141]. Ghahari [58, 142] and Laycock et al. [143] have applied *in-situ* synchrotron radiography to monitor 2D artificial pits of stainless steel and studied the dissolution kinetics of the pit growth, which has been characterised and modelled both in the width and depth directions of the pit. It was also used by Hammons et al. [52] on a Ni artificial pit to characterise the interfacial phenomena during high rate dissolution, it was found that salt nucleation caused obvious surface roughening upon reaching a critical supersaturation ratio, which was not observed at steady-state.

2.8.4 Effect of radiation in aqueous solutions

Intense radiation by synchrotron X-rays may produce beam damage on specimen surfaces in aqueous solutions. Nagy and You [144] reported the effect of radiolysis in a Pt/aqueous solution system in a synchrotron X-ray beam (12 keV, beam size 0.3×0.03 cm^2), and it was suggested that radiolytic products of water may include H_2 and H_2O_2, and the degree of radiolysis depended on the amount of solution, which could be minimised by flushing the solution. Other radiolytic products from the solutes were also possible [144, 145]. Mesu et al. [146] monitored the interaction between water and synchrotron X-rays (9 keV, beam size 0.03×0.2 mm^2), and the reactions described in Equation 2-37 were proposed; bubbles were observed in the solution, which were believed to be composed of H_2 (due to the reaction between water and hydrated electrons [147]) and O_2 (as a result of H_2O_2 breakdown, the H_2O_2 is due to the recombination of HO in Equation 2-37 [146]),

$$H_2O + h\nu_{(X\text{-}ray)} \xrightarrow{H_2O} H_2O^+ + e^-_{(dry)} \rightarrow H_3O^+ + HO + e^-_{(aq)} \qquad \text{Equation 2-37}$$

The $e^-_{(dry)}$ and $e^-_{(aq)}$ mean "dehydrated" and "hydrated" electrons respectively. These phenomena were accentuated by higher flux X-ray beam. An aluminium filter and large beam

size can be used to attenuate the effect of beam damage [51], but there is still scant investigation on this issue.

2.9 Summary

Pitting corrosion of Fe-alloys in chloride solutions has been extensively studied, however, some issues still remain unclear. There has been relatively little work characterising the nature of salt layers or other dissolution products within pits, or to examine in detail the diffusion of metal ions and iron dissolution kinetics, and the reported Tafel slopes for metal ion saturated solutions varied widely from 50 to 110 mV/decade. Several models have been proposed for iron dissolution in nitrate solutions, but the mechanism is still not clear for growing pits.

The present work demonstrates the use of *in-situ* synchrotron X-rays to investigate the pitting corrosion of iron in chloride/nitrate solutions, including the nature of salt layers, corrosion products and dissolution behaviour. Electrochemical measurements have been carried out to investigate the mass transport and dissolution kinetics of an iron pit in a wide range of chloride concentrations, the effective diffusion coefficient of metal ions has been compared with the self-diffusivity calculated with simulation software, and Tafel kinetics in metal ion saturation concentrations has been studied. Finally, a galvanodynamic method has been proposed as an alternative method for evaluating dissolution kinetics in artificial pits.

3. EXPERIMENTAL METHODS

3.1 Materials

Commercial purity and high purity iron were obtained from Goodfellow Cambridge Ltd. and Advent Research Materials Ltd., UK. Details are provided in Table 3-1. Carbon steel (carbon content ~0.75%) was provided by Tata Steel Ltd. and cut and ground into foils ~130 μm thick (SiC abrasive paper, P1200 grit).

3.2 Electrochemical cells

3.2.1 Foil artificial pit

The electrochemical cell used for artificial pit studies with foils is shown in Figure 3-1 and follows the design of Rayment et al. [51]. The foil artificial pit electrodes were made from ~2.5 cm long, 3 mm wide foils (~0.7 mm wide for radiography experiments), which were degreased with methanol and sandwiched in Araldite epoxy resin (non-crystalline). The epoxy-coated foil was attached with 25 mm wide adhesive silicone Kapton tapes (RS components, UK), to a cell constructed from a PVC tube (volume ~30 ml), the cut end of the foil faced upwards, and an artificial corrosion pit formed after the electrode surface receded. The electrochemical cell consisted of a Ag/AgCl reference electrode (3 M NaCl, BASi, UK, MF-2078) and a platinum wire as the auxiliary/counter electrode (surface area ca. 2 cm^2), the solution volume was 20 ml.

Table 3-1. Pure iron materials (the information on processing method is provided in [148])

type	thickness or diameter	suppliers	composition (from suppliers)	processing method	experiments
foils	25 µm	Goodfellow Cambridge Ltd. (catalogue No: FE000230)	Fe 99.99+%, Ag 1 ppm, Al 2 ppm, Ca 3 ppm, Cr 1 ppm, Cu 2 ppm, Mg 2 ppm, Mn 1 ppm, Ni 1 ppm, Si 3 ppm	as rolled	radiography, nitrate study, SEM
	50 µm	Advent Research Materials Ltd. (catalogue No: FE163818)	Fe 99.5%, C 1200 ppm, Mn 5000 ppm, S 500 ppm, P 500 ppm	work hardened	synchrotron diffraction, Raman, nitrate study, SEM/EBSD
	75 µm	Goodfellow Cambridge Ltd. (catalogue No: FE000292)	Fe 99.99+%, Ag 1 ppm, Al 2 ppm, Ca 3 ppm, Cr 1 ppm, Cu 2 ppm, Mg 2 ppm, Mn 1 ppm, Ni 1 ppm, Si 3 ppm	as rolled	black layer study
	100 µm	Goodfellow Cambridge Ltd. (catalogue No: FE000320)	Fe 99.5%, C 800 ppm, Mn 3000 ppm, Si 1000 ppm, P<400 ppm, S<500 ppm	work hardened	
wires	130 µm	Goodfellow Cambridge Ltd. (catalogue No: FE005125)	Fe 99.99+%, Ag 1 ppm, Al 2 ppm, Ca 3 ppm, Cr 1 ppm, Cu 2 ppm, Mg 2 ppm, Mn 1 ppm, Ni 1 ppm, Si 3 ppm	work hardened	diffusivity and Tafel kinetics
	250 µm	Goodfellow Cambridge Ltd. (catalogue No: FE005141/2)	Fe 99.99+%, Ag 1 ppm, Al 2 ppm, Ca 3 ppm, Cr 1 ppm, Cu 2 ppm, Mg 2 ppm, Mn 1 ppm, Ni 1 ppm, Si 3 ppm	annealed	
	250 µm	Advent Research Materials Ltd. (catalogue No: FE525618)	Fe 99.5%, C<1000 ppm, S<250 ppm, Mn<4000 ppm, P<200 ppm	annealed	black layer study

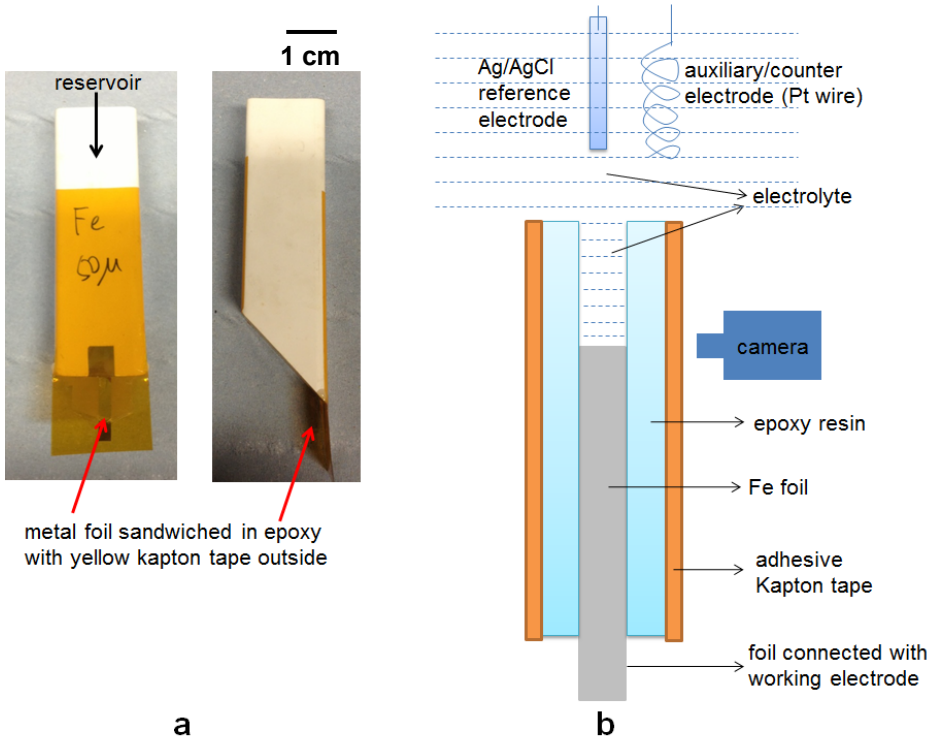

Figure 3-1. Fe foil artificial pit. (a) pictures of the electrochemical cell; (b) schematic diagram of electrochemical experiment setup (foil thickness 25 to 100 μm, epoxy thickness 50 to 100 μm, Kapton tape thickness 65 μm)

3.2.2 Wire artificial pit

Iron wires were degreased with methanol and connected with a ~15 cm long electrical cable. The Fe wire was wound around the stripped end of the cable and then silver paste was painted over the wound wire to make an electrical connection. The painted area was wrapped with thread seal tape (12 m×12 mm×0.075 mm, RS Components, UK), then the Fe wire along with the electrical cable was placed within an acrylic tube (outer diameter 6 mm, inner diameter 4 mm, Alternative Plastics Ltd., UK) and fixed by Araldite epoxy resin at the bottom of the tube, finally the wire was mounted in epoxy resin (EpoFix resin, Struers, UK), which was injected into the tube, and the resin cured for 1 day before use. A typical cell is shown schematically in Figure 3-2. Before each experiment, the cross-section surface was ground with SiC abrasive paper P800 grit.

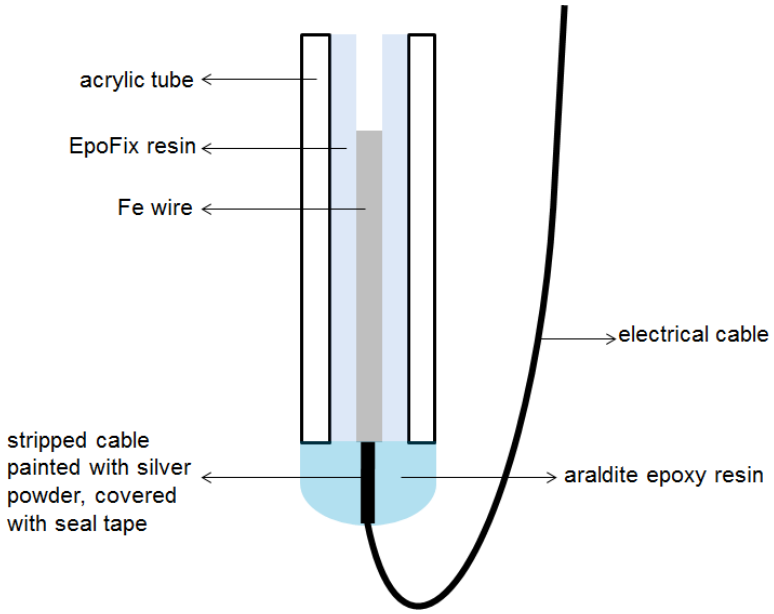

Figure 3-2. Schematic diagram of wire artificial pit electrode (wire thickness is 120 or 250 µm, acrylic tube internal diameter 4 mm, external diameter 6 mm, so the resin is 2 mm thick)

For the electrochemical cell, the electrode faced upwards and was fixed with a plastic sample holder into an uncovered plastic reservoir (volume ~120 ml), with an SCE reference electrode and a platinum wire as the auxiliary/counter electrode (Figure 3-3).

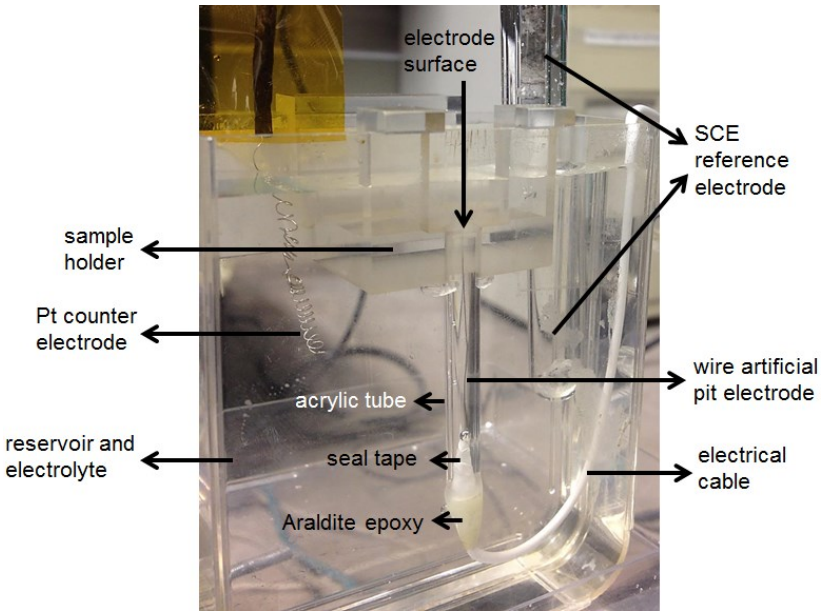

Figure 3-3. A picture of the setup of an Fe wire artificial pit electrochemical cell (the external diameter of the acrylic tube is 6 mm)

3.3 Electrolytes

HCl, $NaNO_3$, $MgCl_2$ and HNO_3 electrolytes were made with deionised water (resistivity 18 MΩ·cm, Millipore, UK) and details are provided in Table 3-2.

Table 3-2. Electrolytes for electrochemical experiments

solutes	concentration (M)	purity/original concentration (from suppliers)	suppliers	experiments
HCl	0.01, 0.05, 1	laboratory reagent, 32%	Fisher Scientific UK	black layer study, synchrotron study
$NaNO_3$	0.02, 0.05, 0.1	laboratory reagent	Fisher Scientific UK	nitrate study, synchrotron study
$MgCl_2.6H_2O$	0.01, 0.1, 0.5, 1, 2, 3	ACS reagent	Sigma-Aldrich, UK	diffusivity and Tafel kinetics
HNO_3	0.1	laboratory reagent, 70%	Fisher Scientific UK	synchrotron study

3.4 Electrochemical experiments

The electrochemical experiments were carried out using an ACM potentiostat (ACM instruments) and an Ivium CompactStat potentiostat (IVIUM Technologies, the Netherlands). The procedure for artificial pits for both foil and wire experiments was as follows. The electrode surface was fully immersed in the electrolyte, and then the following sequence of potentials was applied: 0 mV (for 300 s), 200 mV (300 s), 400 mV (300 s) and finally 600 mV or 1000 mV for steady-state dissolution. Potentials were imposed with respect to the Ag/AgCl and SCE scales, for foils and wires, respectively. After reaching a certain pit depth, potentiostatic, potentiodynamic, galvanostatic or galvanodynamic sequences were applied as required. Under some conditions, solid corrosion products formed inside the pits: these corrosion products could be removed by flushing the pits using a fine syringe connected to a

non-metallic needle (Microfil 28 gauge, World Precision Instruments, US). In laboratory-based experiments, an optical system was set up to monitor the pits, which was a horizontally placed microscope coupled to a CCD camera (5 mega pixel INFINITY 2 CCD, connected to a Mitutoyo 10x objective with a Navitar microscope extender arm, zoom to 40x).

During high-rate dissolution, the cell resistance was recorded concurrently using the IVIUM CompactStat by imposing a square wave ac signal at a fixed frequency with amplitude 10 mV on the applied potential. In this study, the appropriate frequency, at which the effect of capacitive component is negligible, was determined with an impedance spectrum (from 100 kHz to 10 Hz, amplitude 10 mV). It was found that, in the presence of a salt layer on the artificial pit, the appropriate frequency is at 30 to 50 kHz provided the effective ohmic resistance was less than ~10 kΩ; while in the absence of a salt layer, the pit solution resistance can be measured using a frequency between 100 kHz and 30 kHz. The approach used was based on that described in previous work [20, 32, 67].

Foil artificial pits were used in the study of nitrate effects on Fe corrosion. Ag/AgCl reference electrodes (RE) were used in nitrate-free and trace nitrate solutions. For mainly nitrate solutions, the Ag/AgCl RE was immersed in 3 M NaCl in a 2.5 ml syringe, connected to the cell via a 250 μm diameter non-metallic needle (Microfil 28 gauge, World Precision Instruments, US) as a Luggin capillary, an O-ring was used to fix the RE inside the syringe (Figure 3-4). This setup ensured that nitrate ions would not affect the precision of the reference electrode. Before each experiment, the bubbles and air gap at the bottom were removed to ensure a good ionic connection. This arrangement was calibrated against a standard reference electrode before and after each electrochemical experiment and the difference was found to be negligible.

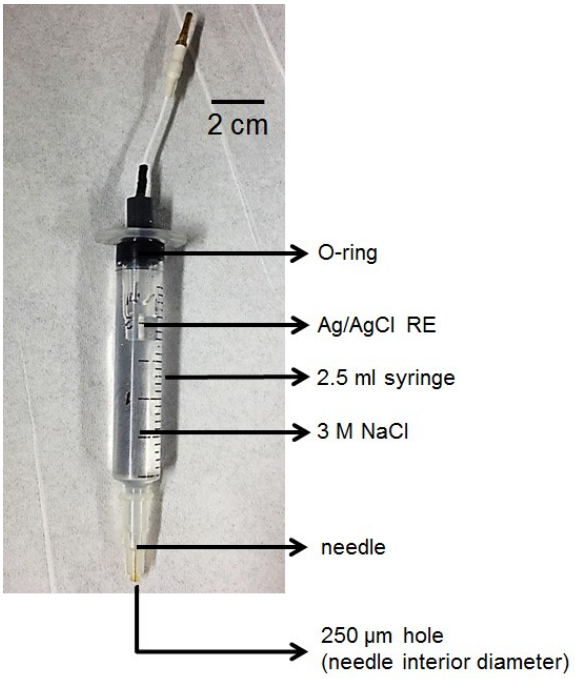

Figure 3-4. A setup of the Ag/AgCl reference electrode to avoid the effect of nitrate.

3.5 Calculation of solution properties

In studies of mass transport, Fe^{2+} or $FeCl^{+}$ diffusivities in electrolytes were derived from experimental data and compared with the theoretical calculations of OLI Analyser Studio v9.0 (OLI Systems Inc., USA), which is a commercial computer simulation software for aqueous chemical and physical properties [149]. It can be used to calculate conductivities of solutions (model studied in [150]), ion self-diffusivities (model studied in [151, 152]), pH and salt saturation concentrations (model studied in [153]).

In the present work, the units of the calculations were set as "Metric, molar concentration" in "Units Manager", and the databank was "AQ". "Precipitation point" in "Single Point" calculation was used to obtain a single parameter for a specific electrolyte, for example, the saturation concentration of $FeCl_2$ in 0.5 M $MgCl_2$. "Survey" was used to obtain a profile, for

example, self-diffusivity of Fe^{2+} vs. chloride concentrations. More information is available from OLI [154].

3.6 *In-situ* synchrotron X-ray diffraction

In-situ synchrotron X-ray diffraction experiments were carried out at Diamond Light Source, UK, using the microfocus spectroscopy Beamline I18 [155]. Powder diffraction patterns were recorded at 12 keV (X-ray wavelength 1.0332 Å) with a CCD detector (resolution 26 μm×26 μm/pixel). To avoid beam damage, the X-ray was attenuated by 0.75 mm of aluminium, and the X-ray spot size was ~2.5 μm (v)×15 μm (h). The data collection time for each diffraction image was 15 s. A sample stage was used to move the electrochemical cell to a position where X-ray beam was located above the electrode, then the cell was raised up in 2 μm increments, so that the X-ray beam probed from the electrolytes through any salt layers, into metals. For each electrochemical condition, five scans were carried out, as shown schematically in Figure 3-5. The diffraction data were then reduced to one dimensional powder diffraction patterns with the XDRUA [156] and Fullprof software package [157]. The materials and electrolytes used for the XRD measurements are in Table 3-1 and Table 3-2 respectively.

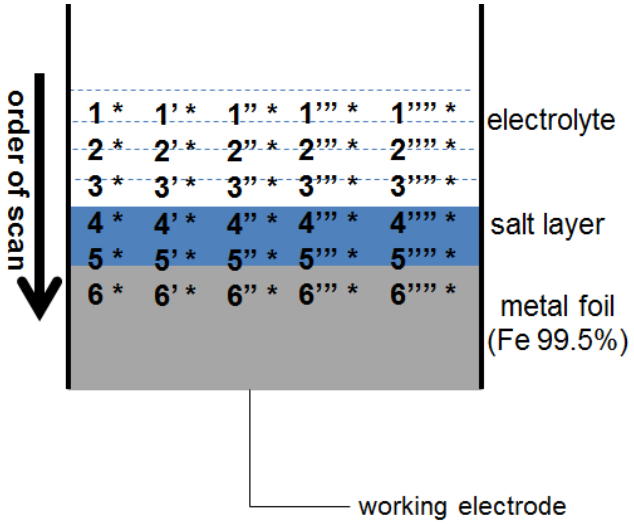

Figure 3-5. Schematic diagram of X-ray scans in an Fe foil artificial pit from electrolyte through salt layer, into the metal, the cell was raised in 2 µm increments, the numbers represent the order of one vertical scan, the asterisks (*) represent the position where X-ray probed.

3.7 *In-situ* synchrotron X-ray radiography

In-situ synchrotron radiography experiments were conducted at Diamond Light Source, UK (Beamline I13-imaging). The X-ray beam was attenuated by a combination of 2 mm aluminium, 0.2 mm aluminium and 0.2 mm graphite filters, and the energy was 15 keV. The CCD detector used 1×1 binning and a 10x objective (11 µm×11 µm/pixel), covering a maximum field of view of 2.2×2.2 mm^2, with a minimum pixel size of 1.1×1.1 μm^2. The exposure time was 40 ms and the interval for image collection was 1.05 to 1.1 s. 30 flat-fields and 30 dark-fields were collected before each measurement, and the analysed radiographs were corrected with averaged flat-fields and averaged dark-fields as "(data - dark field) / (flat field - dark field)".

3.8 Surface characterisation

Surface characterisation in the present work included scanning electron microscopy, electron backscatter diffraction and energy-dispersive X-ray spectroscopy, which were conducted on a

JEOL 7000 SEM (Japan Electron Optics Laboratory Co., Ltd.). The characterised surface was the cross-section area of the foil working electrode.

After an electrochemical experiment, the sandwiched foil was removed from the cell (Figure 3-1) and immersed in methanol for 2 hours, so that the resin could be easily peeled off. Then the foil was cleaned with methanol in ultrasonic bath and dried with warm air, and fixed onto an SEM sample stage with copper tape, with the cross-section area facing upwards (Figure 3-6a). The sample was stored in a desiccator before use.

For electron backscatter diffraction (EBSD), an as-received foil was cut to the same size of the foil used for electrochemical experiment, and mounted in Bakelite (~180 °C) with the cross-section area exposed (Figure 3-6b). The surface was subsequently ground with SiC abrasive paper from P240, P400, P800, P1200 to P4000 grit with water as lubricant, then the surface was mirror-polished with abrasive cloths starting with MD-Dac (lubricated with 3 μm diamond suspension), to MD-Plus (lubricated with 1 μm diamond suspension), and finally MD-Chem (lubricated with OP-S colloidal silica suspension, 0.04 μm), all lubricants were supplied by Struers, UK. The sample was stored in a desiccator before use.

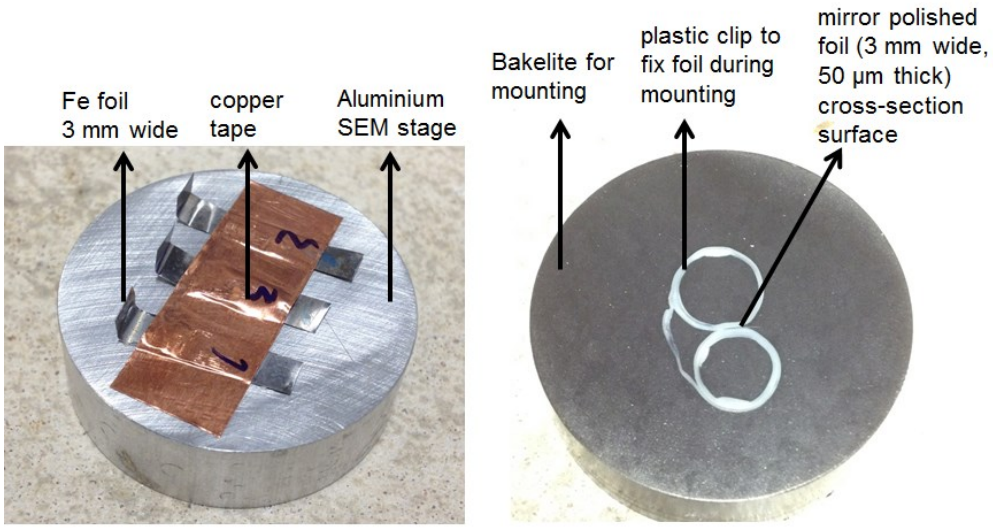

Figure 3-6. Pictures of samples for surface characterisation. (a) sample for SEM and EDX; (b) sample for EBSD

3.9 Raman spectroscopy

Ex-situ Raman spectroscopy was used to characterise the solid corrosion products formed in an artificial pit under certain conditions (details in Chapter 4). The instrument was a Renishaw RamaScope 2000 with a Leica microscope (50x objective), and a 633 nm HeNe laser. The spot size was ca. 1.5 µm.

The foil artificial pit electrochemical cell was similar to that described in Section 3.2.1. However, since the Araldite epoxy resin and Kapton tapes are both Raman-active, there had to be a "resin-free" and "Kapton-free" area for Raman measurement. The foil was embedded in Araldite epoxy resin except an area ca. 0.3×3 mm^2 near the upper edge of the foil, and then the foil was sandwiched by two glass cover slips (18×18 mm^2, Menzel-Glaser, Germany, Part No: MNJ-300-010W). The sandwiched foil was fixed under the cell with Kapton tapes, but the tapes at the "resin-free" area were cut off with a scalpel, thus the Raman laser could probe

the “resin-free” area directly through glass. The schematic diagram is shown in Figure 3-7.

Crevice formation between the foil and glass may take place, but it was ignored in this test.

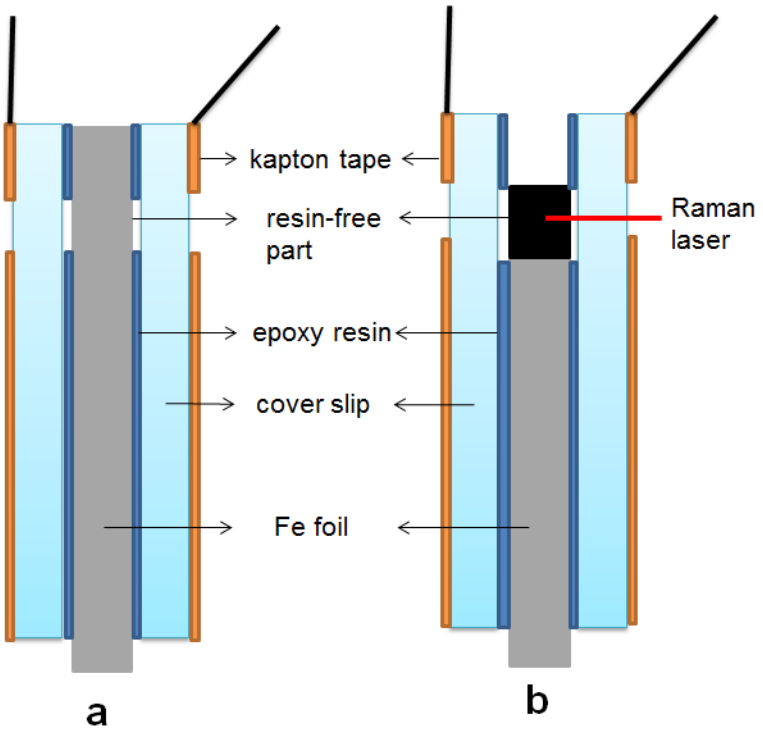

Figure 3-7. Schematic diagram of the Fe foil artificial pit electrochemical cell for Raman measurement (633 nm HeNe laser). (a) before experiment; (b) after experiment, top of the foil dissolved, black layer deposited at the “resin-free” part (foil thickness 50 µm, epoxy thickness <50 µm, cover slip thickness 80 to 120 µm, Kapton tape thickness 65 µm).

4. THE EFFECT OF CORROSION PRODUCTS IN ARTIFICIAL PITS OF IRON AND CARBON STEEL

4.1 Introduction

Solid corrosion products within the local sites have been reported in previous work, e.g. inside corrosion pits [62, 158] and cracks [159]. It has been reported that solid corrosion products within the local sites would lead to limitations of mass transport, thus promote local acidification and local attack [62]. Black corrosion products have also been observed inside artificial corrosion pits. For example, Kawaley [66] reported a black layer within iron artificial pits; Mi [67] found a black layer in stainless steel artificial pits, which slightly inhibited the diffusion of metal ions. Black precipitates have been observed even in an artificial pit grown in 99.99+% Ni in HCl [45], but detailed characterisation was not carried out. In addition, solid corrosion products on exposed metal surfaces have also been reported to inhibit the diffusion of metal ions and/or decrease their dissolution rate [59-65], but the effect has not been characterised quantitatively (see Section 2.4.2). In this study, the effect of solid corrosion products on mass transport and solution resistance has been studied quantitatively for an iron artificial pit in HCl.

4.2 Results

4.2.1 Formation of black layers in Fe artificial pits

Potentiodynamic and potentiostatic methods were applied to both Fe foil and wire artificial pits, which were monitored with an optical system as described in Section 3.4. The potentials in this chapter are all reported on the SCE scale.

4.2.1.1 Tests on Fe wire artificial pits

As described in Section 2.4.1, when the pit reaches a depth where the diffusion length of metal ions can be simply regarded as the depth of the artificial pit, the current density i is linear with the inverse pit depth $1/x$, which is characteristic of diffusion-limited dissolution (Equation 2-6). The effect of diffusion in the bulk solution outside the pit is negligible. This pit depth can be determined via a plot of current density vs. inverse pit depth [37].

A 250 µm thick commercial purity 99.5% Fe wire artificial pit (see Section 3.2.2) was dissolved in 1 M HCl at 0.6 V for pit growth, during which time the pit was free of any solid corrosion products. The current density i is plotted vs. inverse pit depth $1/x$ as shown in Figure 4-1. The plot became linear after pit was deeper than 600 µm, calculated using the charge passed (Equation 2-7). The pit depths measured directly with the optical system and calculated with Equation 2-7 agreed with each other within 5%. From this measurement, it was calculated that the pit has to be deeper than 600 µm to investigate diffusion within the pit using the linear approximation.

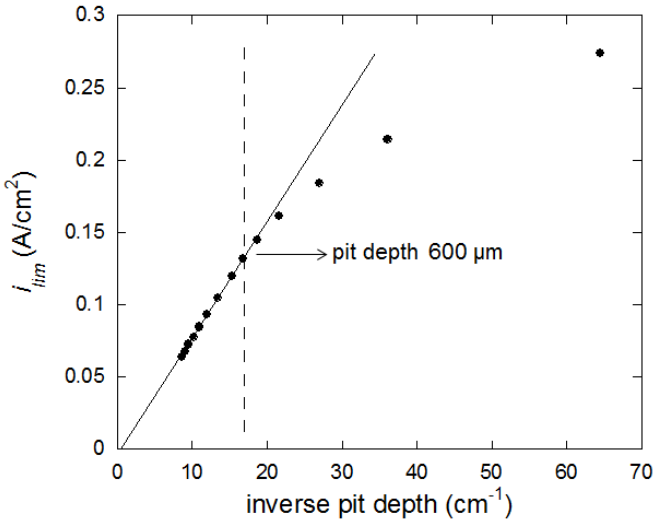

Figure 4-1. Diffusion-limited current density vs. inverse pit depth for a 250 µm diameter, 99.5% Fe wire artificial pit in 1 M HCl, potential at 0.6 V(SCE).

Figure 4-2 shows the results for a series of cyclic voltammetry measurements upon an Fe wire artificial pit (99.5%) which had been grown at 0.6 V until the pit was deeper than 1 mm. The potential was cycled between 0.6 V and -0.4 V at 2 mV/s starting from 0.6 V. The dissolution can be seen to be diffusion-limited between 0.6 V and -0.3 V. For each cycle, a black stripe precipitated on the metal surface when the potential was below 0.2 V. At the end of the 9th cycle at 0.6 V, there were nine stripes. The pit was flushed with a fine needle and syringe (Section 3.4), so that the black stripes were flushed out. After dissolution had reached the diffusion-limited current, the potential was restarted from 0.6 V and the 10th cycle was measured in the clean pit.

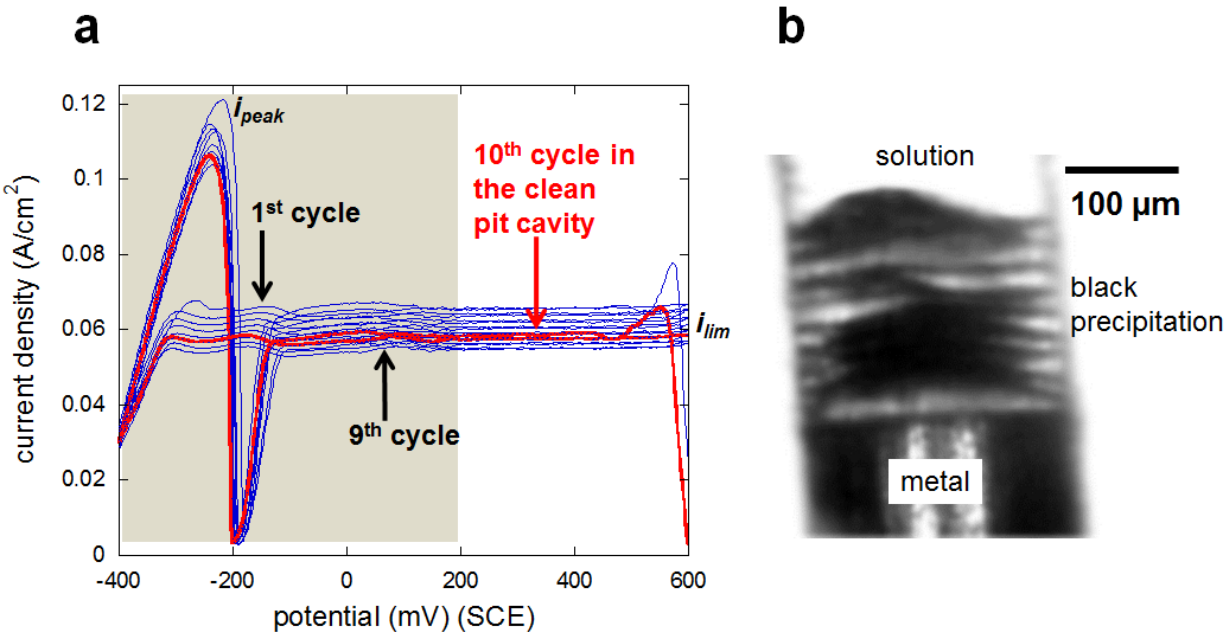

Figure 4-2. Potential cycles (2 mV/s) on a 99.5% Fe (carbon <0.1%wt.) wire (250 µm) artificial pit in 1 M HCl. The pit was deeper than 1 mm and was flushed just before the last (10th) cycle. (a) current-voltage characteristics of all cycles (2 mV/s); all cycles started at 600 mV(SCE), and the first and last cycles were both started by stepping to 600 mV(SCE) from open circuit, leading to an initial high current density; (b) a micrograph of the artificial pit taken just before flushing of the pit, black stripes formed below 200 mV(SCE). The potential range where black layers formed during potential cycles has been marked with grey shadow; the electrochemical behaviours are correlated with the changes on the electrode surface according to the description in Section 2.3.2.

Figure 4-2a shows the current-voltage characteristics. The micrograph shown in Figure 4-2b was taken just before flushing at the end of the 9th cycle. It can be seen that the current-voltage relationship in the artificial pit is similar to that described in Section 2.3.2. The gradual decrease of current density i_{lim} after each cycle was caused by the increase of pit depth [26, 32, 33]. However, the i_{lim} for the last (10th) cycle increased compared to the 9th cycle due to the removal of black stripes. This indicates that the stripes act as diffusion barriers in the pit, i.e. the i_{lim} in the 9th cycle (~55 mA/cm^2) increased to ~57 mA/cm^2 in the last cycle (by 3% to 4%). Figure 4-3 shows that the peak current density i_{peak} due to supersaturation followed a similar pattern of behaviour, i.e. a gradual decrease in cycle 1 to 9 followed by an increase for cycle 10 following the flushing away of the black stripes.

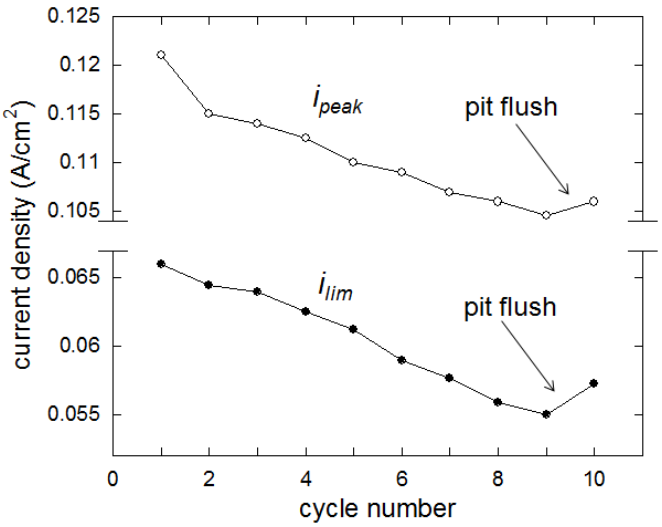

Figure 4-3. i_{peak} and i_{lim} in the potential cycles shown in Figure 4-2; the pit was flushed just before the last (10th) cycle.

A series of potentiostatic measurements was also made on a 99.5% Fe wire pit, which had been grown at 0.6 V until the depth was 600 µm. The potential was stepped down sequentially to 0.2 V, 0.1 V and 0 V, staying for 1 hour at each potential. The dissolution was still diffusion-limited, but a black layer was formed in each case as shown in Figure 4-4. The

black layers formed at 0.1 V and 0 V can be seen to be denser than that formed at 0.2 V. There was no black layer at 0.6 V, but some very small black precipitates were visible. The mechanism will be discussed in details in Chapter 5.

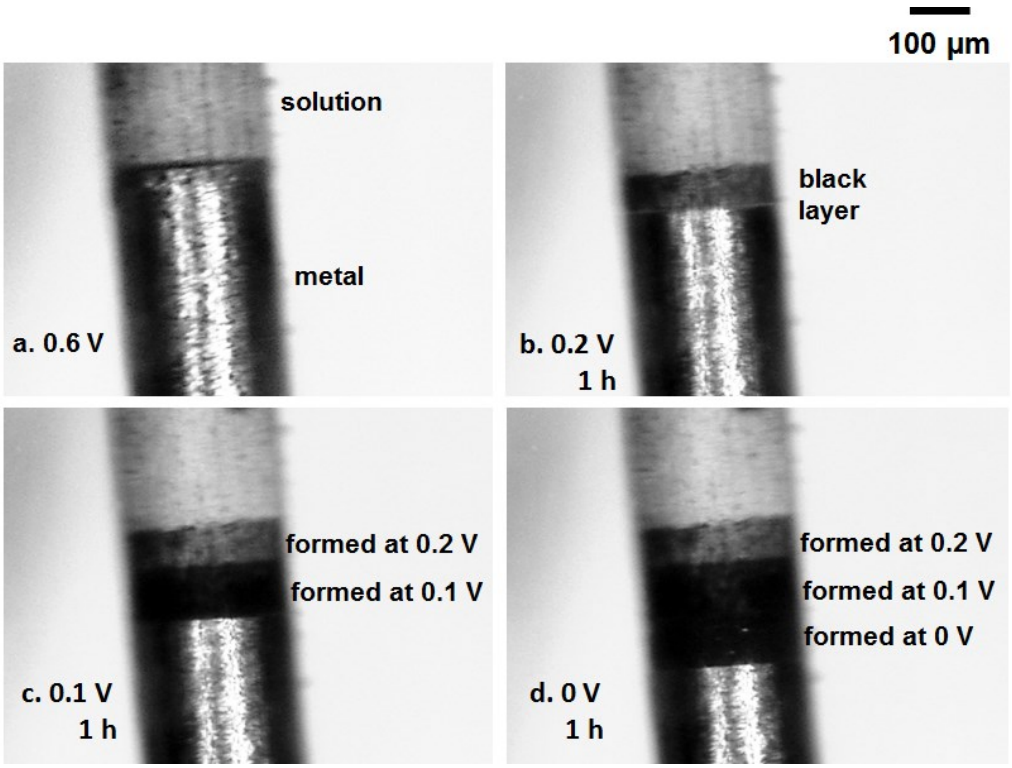

Figure 4-4. Micrographs of a 99.5% Fe (carbon <0.1%wt.) wire (250 µm) artificial pit in 1 M HCl. (a) at 0.6 V(SCE), clean pit, pit depth ~600 µm; (b) after at 0.2 V(SCE) for 1 hour; (c) after at 0.1 V(SCE) for 1 hour; (d) after at 0 V(SCE) for 1 hour.

4.2.1.2 Tests on Fe foil artificial pits

Foils with different carbon contents are compared, i.e. 99.99+% (75 µm thick), 99.5% Fe (100 µm thick, carbon ~0.08%wt.) and carbon steel (~130 µm thick, carbon ~0.75%wt.) foil artificial pits. All foil artificial pits (see Section 3.2.1) were prepared in 1 M HCl at 0.55 V until the pit depth was 700 µm (the pit depths measured directly with the optical system agreed well with those calculated from charge passed). Each of the artificial pits underwent three potential cycles between 0.55 V and -0.3 V (50 mV/min). Figure 4-5 shows the

micrographs for each foil in the end of the potential cycle experiments, and the current-voltage characteristics of the first potential cycle on each pit. The current/voltage characteristics were similar for 99.99+% and 99.5% Fe pits, but were very unstable for carbon steel. For the 99.5% Fe, a black stripe was formed below 0.2 V for each potential cycle, and the dissolution at 0.2 V was still in the diffusion limited region as shown in the current-voltage characteristics (Figure 4-5). However, the 99.99+% Fe pit was clean after three potential cycles. The carbon steel pit was covered by a thick black layer, which formed from the very beginning of dissolution.

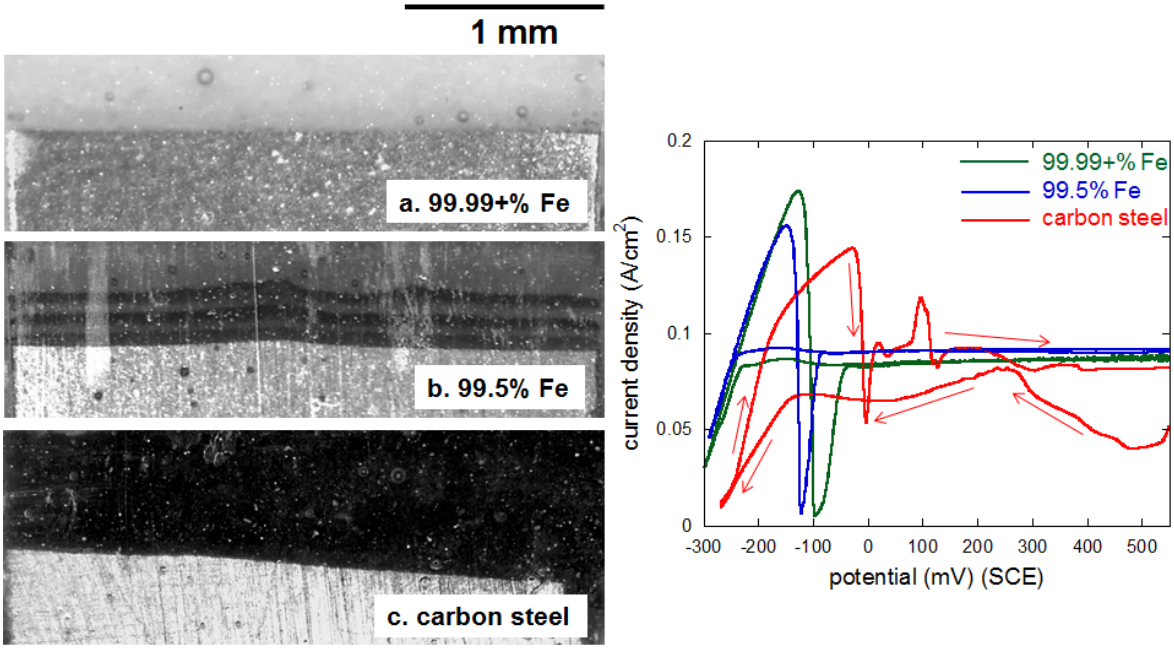

Figure 4-5. Micrographs of three artificial pits at the end of potential cycle experiments in 1 M HCl. Each pit was grown to a depth of ~700 µm, and then the potential was cycled between 0.55 V and -0.3 V(SCE) at 50 mV/min. (a) 99.99+% Fe foil (75 µm); (b) 99.5% Fe foil (100 µm), carbon ~0.08%wt., black stripes formed below 0.2 V(SCE); (c) carbon steel foil, ~130 µm thick, carbon ~0.75%wt. The current-voltage characteristics of the first potential cycle on each artificial pit are compared.

The black layers that formed in the 99.5% Fe foil pit could be easily flushed away, which means that it was very loose, consistent with [60], in which a “black film” on the surface of carburized steel was found to be not strongly adherent and easily removed by gentle rubbing.

However, the black layer formed in the carbon steel pit was not readily flushed, which indicates that the layer was more compact than that formed within the 99.5% Fe pit.

A series of potentiostatic tests was also carried out on a 99.5% Fe foil pit, which had been grown in 1 M HCl at 0.95 V to a depth of 600 µm. The potential was stepped down sequentially to 0.65 V, 0.45 V, 0.25 V and 0.05 V, remaining for 1 hour at each potential (Figure 4-6). It is known from the current-voltage characteristics in Figure 4-5 that the dissolution was diffusion-limited at all these voltages. The artificial pit was clean at 0.65 V and 0.45 V, but black layers precipitated at 0.25 V and 0.05 V, and it appeared denser at 0.05 V.

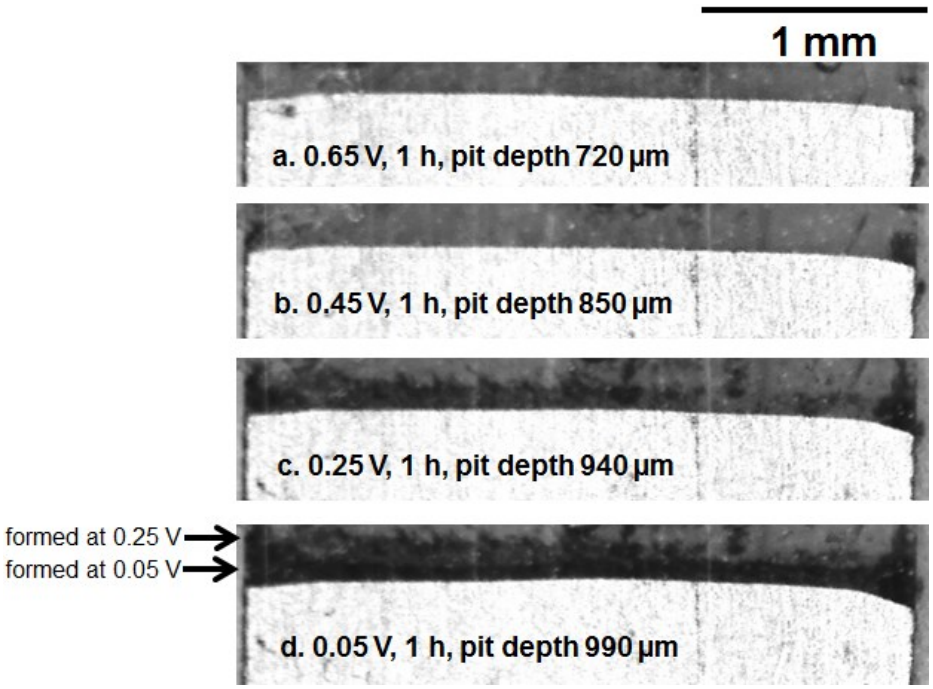

Figure 4-6. Micrographs of a 99.5% Fe foil artificial pit (100 µm thick, carbon ~0.08%wt.) in 1 M HCl. (a) at 0.65 V(SCE) for 1 hour; (b) at 0.45 V(SCE) for 1 hour; (c) at 0.25 V(SCE) for 1 hour; (d) at 0.05 V(SCE) for 1 hour.

4.2.2 The influence of a black layer on the dissolution of Fe wire artificial pits

4.2.2.1 Diffusion barriers

It has been shown earlier that the current density is linear with inverse pit depth when the pit is deeper than 600 μm (Figure 4-1), and that black stripes formed during potential cycles when potential was below 0.2 V, which acted as a diffusion barrier. This means that the current density would be affected by both the black layer precipitation and the pit depth. The influence of the black layers on diffusion has been characterised quantitatively with potentiostatic and potential step methods as described below.

The potential step procedure is described in Figure 4-7. For a 99.5% Fe pit, the potential step measurements started after the pit depth reached 800 μm at 0.6 V (see Figure 4-8a). A potential of 0.1 V was then applied and a black layer precipitated (see Figure 4-8b). The potential was then stepped up to 0.6 V again for 3 hours, during which time the pit was flushed after the first hour (Figure 4-8c shows the pit just before flushing), Figure 4-8d shows the pit at the end of 3 hours at 0.6 V. Then 0 V and 0.6 V were applied sequentially for 3 hours each. A black layer precipitated again after the 3 hours at 0 V (see Figure 4-8e), which still stayed within the pit at 0.6 V (see Figure 4-8f). For the sake of comparison, the sequence of "0.6 V (pit growth) – 0.1 V, 3 h – 0.6 V, 3 h" was also applied to a 99.99+% Fe pit, except that the pit was never flushed, because no black layer was formed. The corresponding micrographs for 99.99+% Fe pit are shown in Figure 4-9.

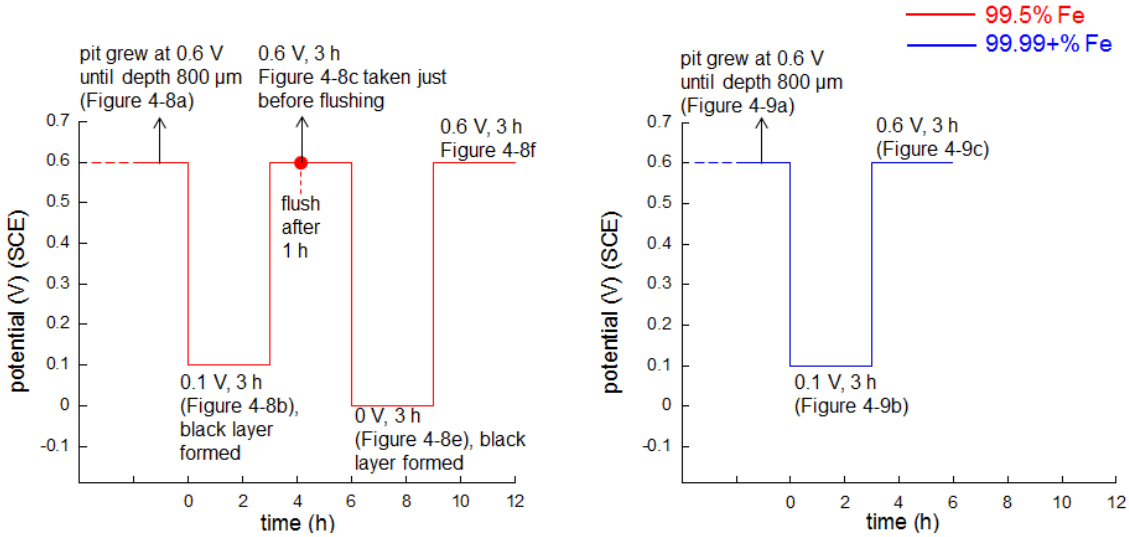

Figure 4-7. Potentiostatic and potential step procedures for 99.5% and 99.99+% Fe wire (250 µm) artificial pits, potentials on the SCE scale (Figure 4-8c was taken just before flushing the pit, the other figures were all taken at the end of each step).

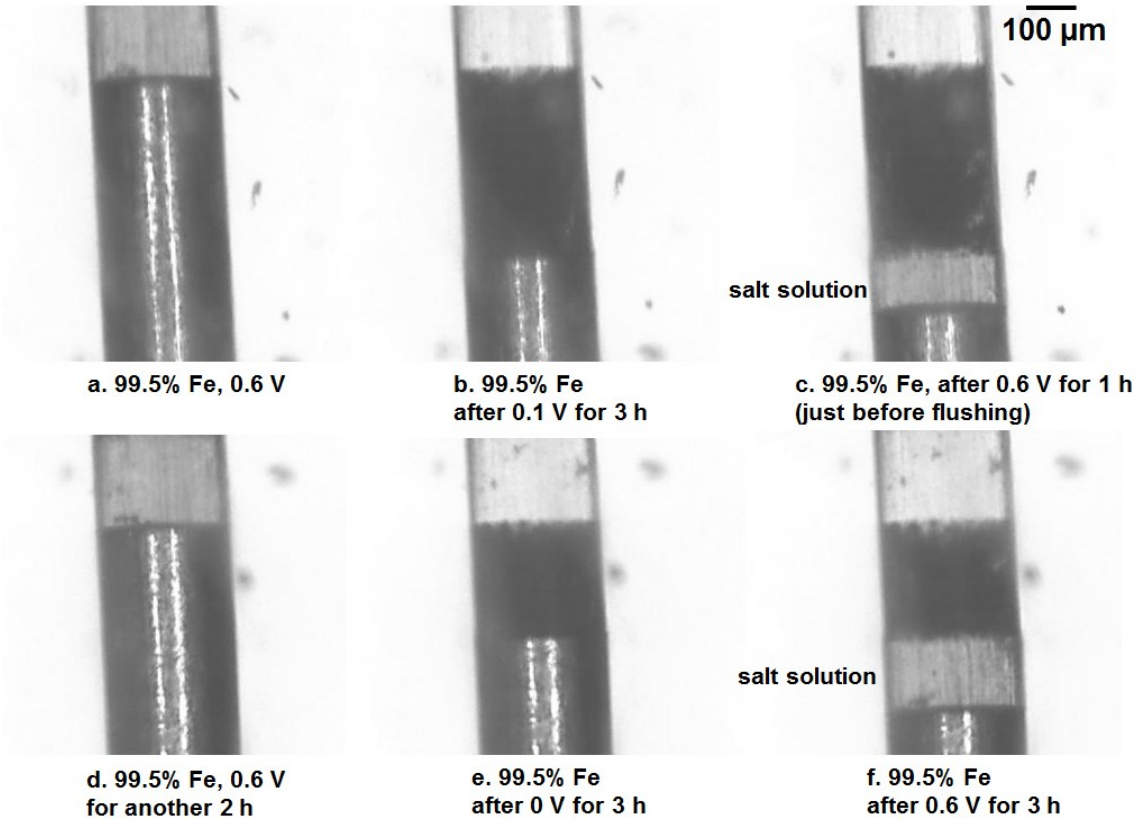

Figure 4-8. Micrographs of a 99.5% Fe (carbon <0.1%wt.) wire (250 µm) artificial pit in 1 M HCl. (a) a "clean" pit grew at 0.6 V(SCE), pit depth 800 µm; (b) 3 hours at 0.1 V(SCE), black layer precipitated; (c) 1 hour at 0.6 V(SCE) and just before flushing; (d) 2 hours at 0.6 V(SCE) after flushing; (e) 3 hours at 0 V(SCE), black layer precipitated; (f) 3 hours at 0.6 V(SCE), black layer stopped precipitating.

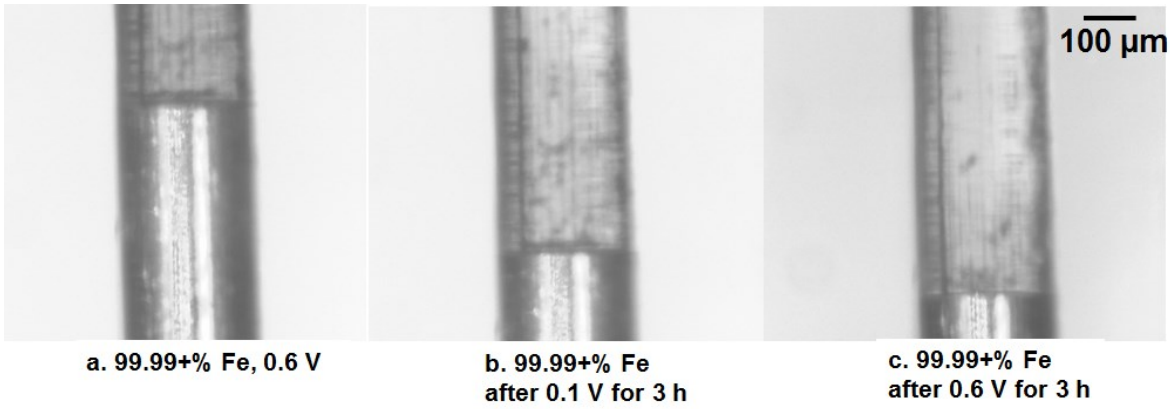

Figure 4-9. Micrographs of a 99.99+% Fe wire (250 µm) artificial pit in 1 M HCl. (a) a "clean" pit grown at 0.6 V(SCE), pit depth 800 µm; (b) 3 hours at 0.1 V(SCE); (c) 3 hours at 0.6 V(SCE).

In Figure 4-10a, the dependence of the diffusion-limited current density (i_{lim}) on the inverse pit depth ($1/x$) is plotted for the 99.5% Fe pit after the experimental procedure described in Figure 4-7. The dashed straight line is a fit to the data at 0.6 V (marked with a bracket in Figure 4-10a) obtained after reaching a pit depth of 650 µm but before the potential step to 0.1 V. This fit was used to predict the dependence of i_{lim} on $1/x$ for a clean pit, so that the "theoretical i_{lim}" at any pit depth in a clean pit could be obtained by extrapolation of the dashed straight line in Figure 4-10a.

In order to present more clearly the difference between the experimental and "theoretical data", the ratio of the experimental i_{lim} and "theoretical i_{lim}" is plotted vs. inverse pit depth as shown in Figure 4-10b. It was found that i_{lim} was decreased by 2% by a 350 µm thick black layer formed at 0.1 V (see Figure 4-8b), and decreased by 5% by a 250 µm thick black layer formed at 0 V (see Figure 4-8e).

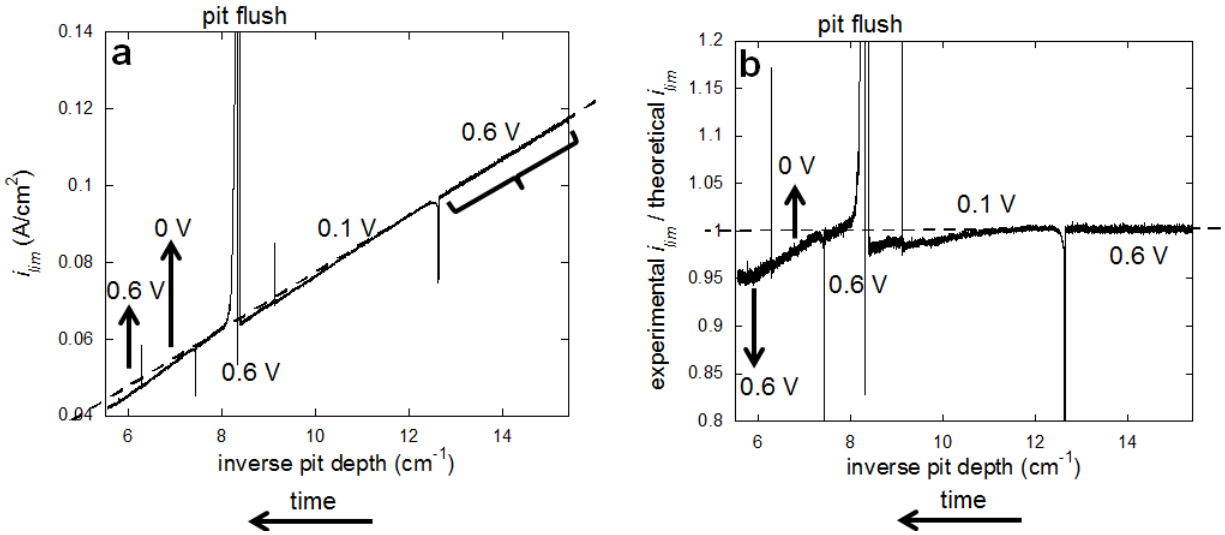

Figure 4-10. Potentiostatic and potential step methods applied on a 99.5% Fe (carbon <0.1%wt.) wire (250 µm) artificial pit in 1 M HCl; the procedure used was the sequence described in Figure 4-7. Potentials on the SCE scale. (a) i_{lim} vs. inverse pit depth; (b) ratio of the experimental i_{lim} and "theoretical i_{lim}" vs. inverse pit depth. The bracket in (a) shows the region used for the fitted dashed line, which was then used to obtain the "theoretical i_{lim}".

The same analysis was applied to the electrochemical data of a 99.99+% Fe pit (Figure 4-11). The difference between the experimental and "theoretical i_{lim}" was found to be negligible, even though there were some very small black precipitates visible within the pit (see Figure 4-9).

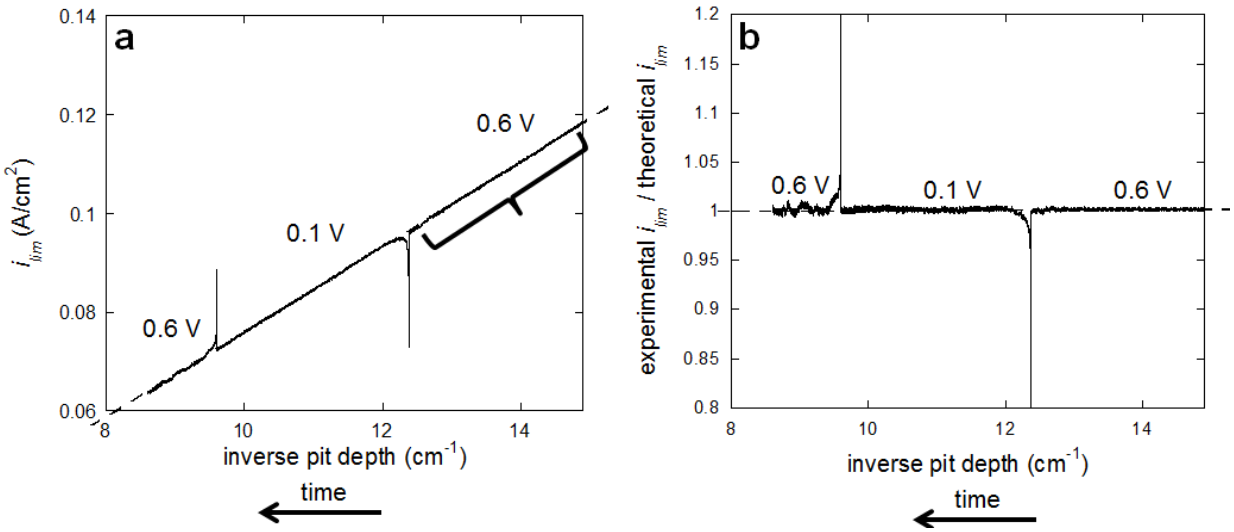

Figure 4-11. Potentiostatic and potential step experiments on a 99.99+% Fe wire (250 µm) artificial pit in 1 M HCl, the procedure used was the sequence described in Figure 4-7. Potentials on the SCE scale. (a) i_{lim} vs. inverse pit depth; (b) ratio of the experimental i_{lim} and "theoretical i_{lim}" vs. inverse pit depth. The bracket in (a) shows the region used for the fitted line, which was then used to obtain the "theoretical i_{lim}".

4.2.2.2 Measurements of pit solution resistance

As described in Section 3.4, resistance can be measured by imposing a constant frequency (30 kHz to 50 kHz) ac signal (amplitude 10 mV) on the applied potential when the effective ohmic resistance is less than 10 KΩ. Under the conditions in this chapter, the solution resistance is far less than 10 kΩ. Figure 4-12a shows an example of current-voltage and resistance-voltage characteristics obtained during a potential cycle (4 mV/s) on a 99.5% Fe wire artificial pit in 1 M HCl (pit depth ~900 µm).

During the negative scan, there should be a salt layer present on the metal whilst the potential is above E_T (the transition potential) [39], and the total resistance is the sum of the salt layer resistance and the solution resistance. The resistance decreased with potential because the salt layer was thinner at lower potentials [26, 32, 34], but the solution resistance is not expected to change. When the potential was below E_T, the salt layer dissolved, and iron dissolution was in the ohmic-control region, where the measured resistance was due to the solution resistance

only, which depends on pit depth and electrolyte concentration. Figure 4-12b shows both the applied potential and *IR*-corrected interfacial potential (the *IR* drop of the solution and the salt layer was subtracted from the applied potential) during the potential cycle. The region in which the black layer precipitates is marked (applied voltage lower than 0.2 V).

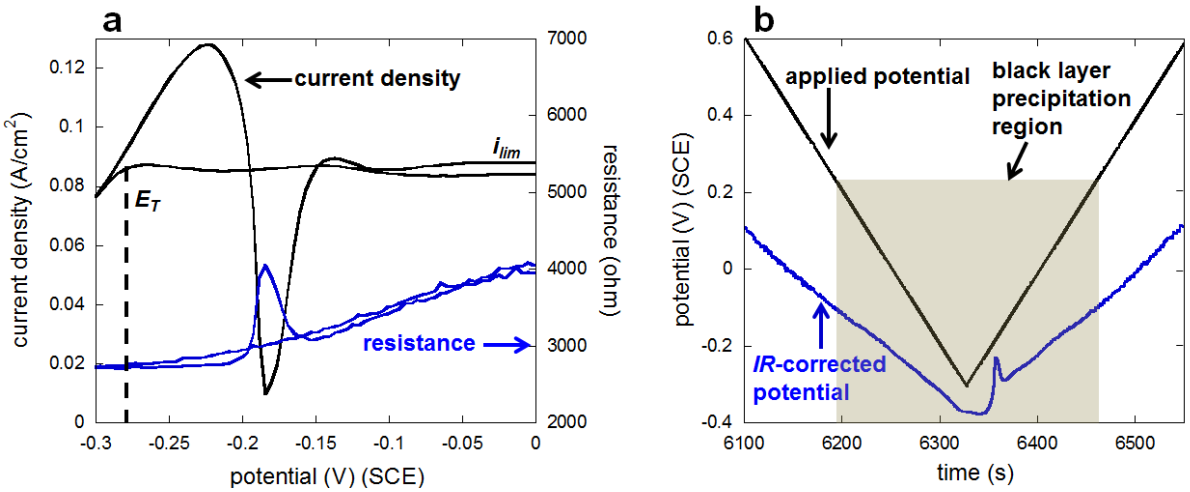

Figure 4-12. A potential cycle (4 mV/s) on a 99.5% Fe wire (250 µm) artificial pit in 1 M HCl, pit depth ~900 µm, resistance measured by imposing a 50 kHz ac signal, amplitude 10 mV. (a) current-voltage and resistance-voltage characteristics; (b) applied potential and the corresponding *IR*-corrected potential vs. time, the potential region for black layer precipitation is marked. Potentials on the SCE scale.

Potential step and potentiostatic methods coupled with an imposed ac signal (50 kHz, amplitude 10 mV) were used to investigate the contribution of the black layer to solution resistance (details of the impedance spectra are shown in Appendix, see Figure 9-1). The experimental procedures used here are described in Figure 4-13, and the letters "A" to "J" indicate the points at which the resistance was measured. The same experiments were carried out on both 99.5% and 99.99+% Fe pits for the sake of comparison, except that, the 99.5% pit was flushed after dissolution at 0.1 V for 3 hours, while the 99.99+% pit was not flushed because there was no black layer. Several micrographs corresponding to the time at points E, H and J are shown in Figure 4-14 (E, H and J for 99.5% Fe; E', H' and J' for 99.99+% Fe).

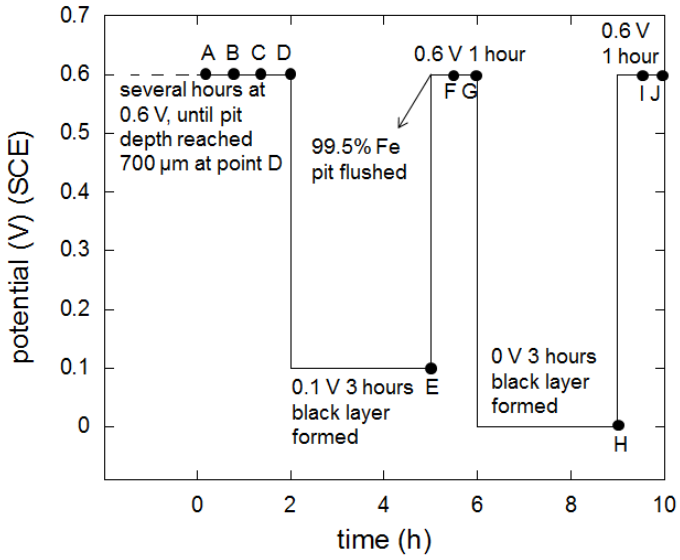

Figure 4-13. A schematic diagram of the potential step and potentiostatic procedures used for measurements on 99.5% and 99.99+% Fe wire (250 µm) artificial pits, "A" to "J" indicate the points at which the resistance was measured, the pit was flushed only for the 99.5% Fe artificial pit after 0.1 V applied for 3 hours (point E).

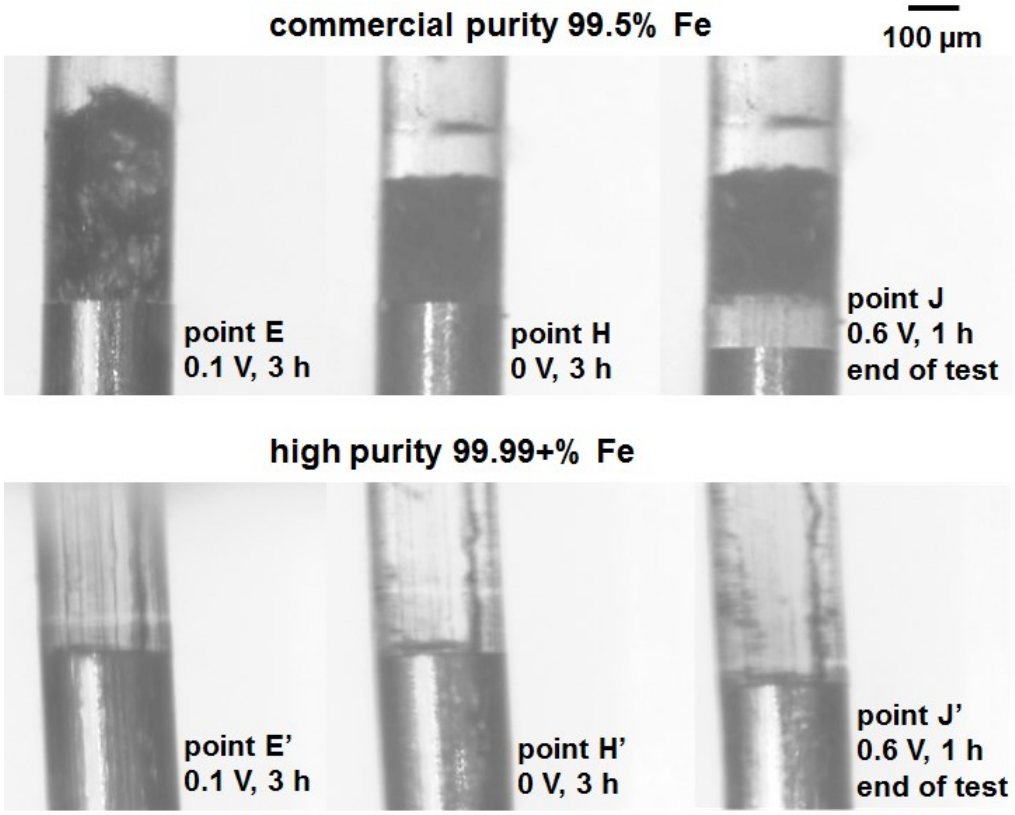

Figure 4-14. Micrographs of the 99.5% and 99.99+% Fe wire (250 µm) artificial pits in 1 M HCl at the times corresponding to points E, H and J in Figure 4-13 (E, H and J for 99.5% iron; E', H' and J' for 99.99+% iron). Potentials on the SCE scale.

Since the resistance of the salt layer has been reported to depend on both the potential and pit depth [32], the variation of the salt resistance at different voltages and pit depths has to be removed. This was accomplished by stepping the potential down to below E_T, thereby dissolving the salt layer for each resistance measurement from points A to J. The data for the resistance measurement for point D is shown in Figure 4-15 as an example. The current density was found to be diffusion-limited at both 0.6 V and 0.1 V, so the potential was stepped to a lower voltage, i.e. -0.4 V for 100 s in order to completely dissolve the salt layer. The resistance tended to level off and this value was regarded as the solution resistance.

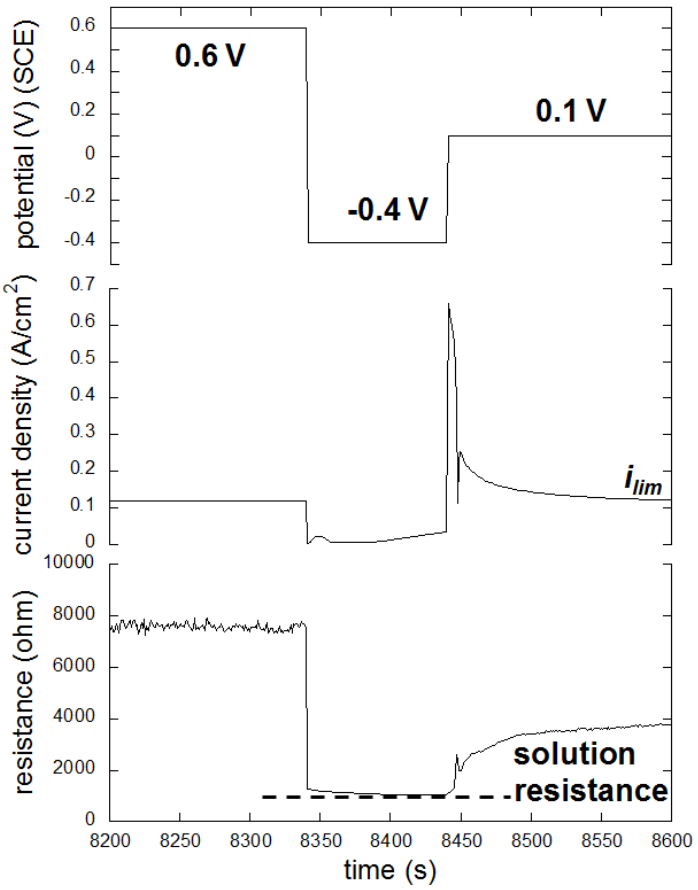

Figure 4-15. Potential, current density and resistance during the procedure of a measurement of pit solution resistance, potential stepped from 0.6 V to -0.4 V and back to 0.1 V on a 99.5% Fe wire (250 μm) artificial pit in 1 M HCl, pit depth ~700 μm, potentials on the SCE scale, resistance measured by an imposed ac signal with frequency 50 kHz, amplitude 10 mV.

Figure 4-16 shows the dependence of solution resistance R_s (pit solution and bulk solution resistance, in the absence of a salt layer) on pit depth for both Fe wires, the red dots represent data collected in a clean pit, and black dots represent those with a black layer. The solution resistance of the "clean" pit was found to depend approximately linearly on pit depth (red dots A, B, C, D, F, G for 99.5% iron, and all the dots for 99.99+% iron). Thus from the two regression lines which fit the red dots in Figure 4-16a and b, a "theoretical R_s" value of a "clean" pit could be obtained at any pit depth.

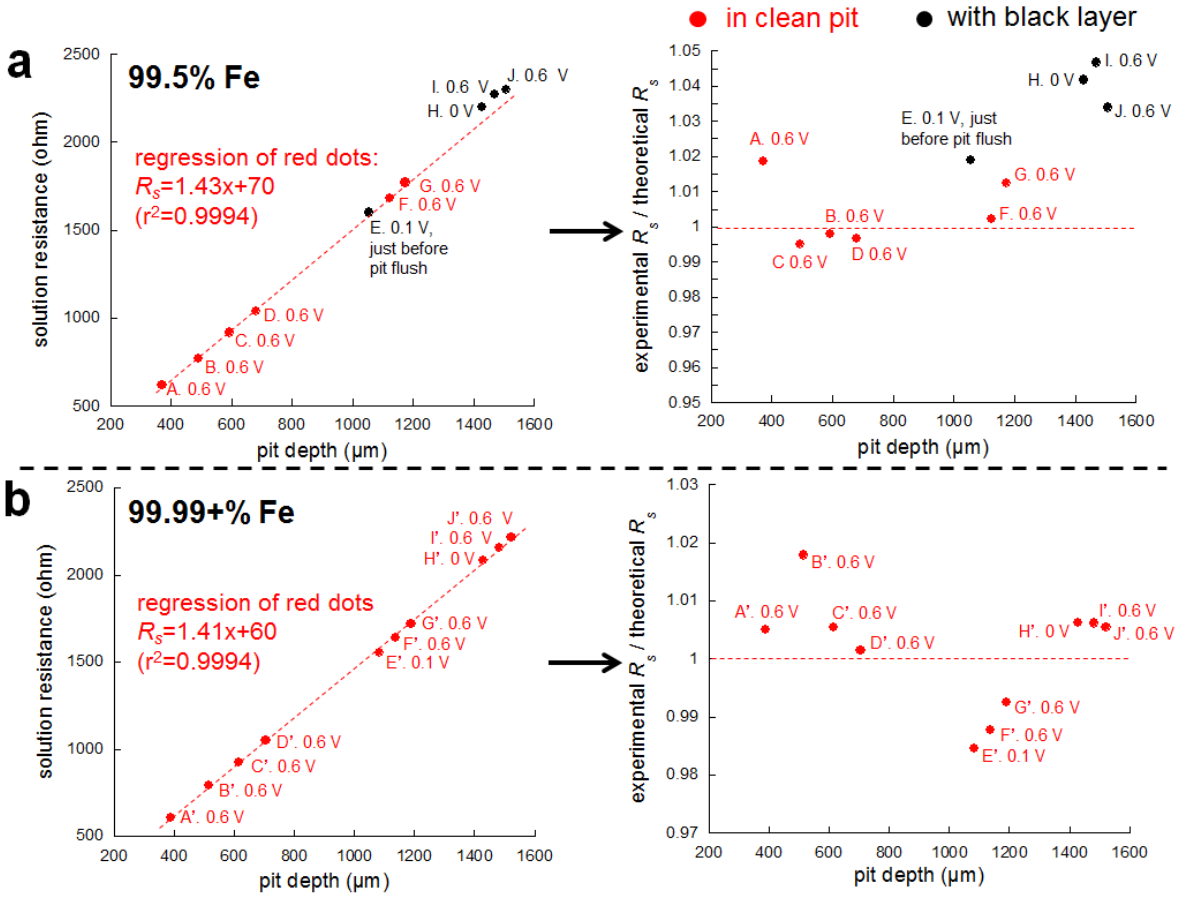

Figure 4-16. Dependence of R_s and "experimental R_s / theoretical R_s" on pit depth for (a) 99.5% and (b) 99.99+% Fe wire (250 μm) artificial pits in 1 M HCl, diameter 250 μm, the "theoretical R_s" at each pit depth was obtained from the regression lines which linear-fit the red dots, resistance at red dots and black dots were obtained from clean pits and the pits with black layer respectively, potentials on the SCE scale, resistance measured with an imposed 50 kHz ac signal, amplitude 10 mV.

To present more clearly the difference between the experimental and "theoretical R_s", the ratio of "experimental R_s / theoretical R_s" was plotted vs. pit depth for both purities of Fe wires. For the points of the 99.5% and 99.99+% iron pits where no black layer formed (the red dots), the experimental R_s and "theoretical R_s" agree within 2%. The experimental R_s at point E of the 99.5% iron pit (black layer formed at 0.1 V/SCE) is less than 2% higher than the "theoretical R_s", which indicates that the measurement at point E may be in an error range of this resistance measurement. However, for the points H, I and J of the 99.5% iron pit (black layer formed at 0 V/SCE), the experimental R_s values are 3% to 5% higher (i.e. ~100 Ω) than the "theoretical R_s", which indicates that the black layer induced a small extra resistance.

4.3 Discussion

4.3.1 Mass transport

For the 99.5% Fe pits shown in Figure 4-2 and Figure 4-10, the mass transport was found to be inhibited, indicating that the black layers act as diffusion barriers and hinder the transport of metal ions inside the pit, but the diffusion in 99.99+% Fe pit shown in Figure 4-11 was not hindered. While in Figure 4-5, the diffusion barrier effect of the three black stripes in 99.5% Fe pit was negligible compared to the 99.99%+ Fe pit, which was because the black stripes were not thick enough. For the carbon steel artificial pit (Figure 4-5), the thick black layer provided a more compact diffusion barrier than that of 99.5% Fe, which provided evidence that the thick black layer on the carbon steel largely affected the mass transport.

The presence of solid corrosion products as diffusion barriers can favour continuing growth of localised corrosion [160], because the metal ion concentration is critical to maintain an aggressive solution in a growing pit [9-13, 37, 54]. This mechanism may delay passivation

when the dissolution rate is low. It has been reported that an active pit for stainless steel has to contain at least 60% saturation concentration of metal ions [37], and that passivation of Ni artificial pit occurred when the concentration of Ni(II)Cl was less than 17% of the saturation concentration [45]. Flis [62] suggested that transport limitations by carbon particles, which were the corrosion products of iron dissolution, would lead to local acidification and promote local attack. Zhang [160] reported that the removal of corrosion products noticeably decreased the pit growth rate due to the loss of both chloride and hydrogen ions. In addition, since it has been suggested that an oxide film cover would keep meta-stable pits alive [161], it is expected that the corrosion products would also increase the possibility for a meta-stable pit to survive.

It should be noted that the inhibition effect of black layers may depend on several factors, i.e. carbon content and black layer thickness. For example, the inhibition effect should increase if the black layer was allowed to grow thicker. The effects shown in Figure 4-10 were under one specific condition of study.

4.3.2 Resistance

The effect of solid corrosion products on the resistance inside copper artificial corrosion pits in sulphate, carbonate and chloride electrolytes has been previously characterised with ac impedance method. It was found that the effect was large enough to decrease the interfacial potential, and the current density was below 10^{-5} A/cm^2, so the surface eventually passivated [158]. In this work, the black layer formed at 0 V(SCE) has been found to induce an extra resistance ~100 Ω in the pit solution, however, since the solution resistance at 0 V(SCE) was more than 2200 Ω (see Figure 4-16), this effect was small.

In addition, the slopes of the dashed straight lines in the plots of solution resistance vs. pit depth in Figure 4-16 can be used to obtain the average resistivity of the pit solution according to Equation 4-1,

$$R_s = \rho_s \frac{x}{A} + R_{ext} \qquad \text{Equation 4-1}$$

where ρ_s is regarded as the average resistivity of pit solution, x is the pit depth, A is the area of the electrode, R_s is the total solution resistance and R_{ext} is the cell resistance in the bulk solution (constant). The average resistivity of the solution in a clean pit was calculated to be ca. 6.9 Ω·cm. The resistance values were measured when the pit was deeper than ~400 μm (see Figure 4-16), so the time for metal ions to completely diffuse out of the pit was more than 10^2 s, or even in 10^3 s according to $t \approx x^2/D$ (D as diffusivity of metal ions), which is much longer than the time at -0.4 V (below E_T) for R_s measurement (see Figure 4-15), so the measured R_s should be the resistance of the mixture of $FeCl_2$ and HCl. Based on the calculation of OLI Analyser Studio v9.0 (see Section 3.5), if the average resistivity of the pit solution is 6.9 Ω·cm at 25 °C, the composition of the pit solution is estimated to be 1 M HCl + ca. 2 M $FeCl_2$ (C_{sat} of $FeCl_2$ ca. 4.49 M at 25 °C in pure water).

4.4 Conclusions

- Corrosion products in pure Fe and steel artificial pits in 1 M HCl have been studied. A black layer has been found within the 99.5% Fe (carbon ~0.1%wt.) pit at voltages below ca. 0.2 V(SCE), but not within a high purity 99.99+% Fe pit. A black layer covered the pit surface at all voltages for carbon steel (carbon ~0.75%wt.).

- The black layer has been found to inhibit the metal ion diffusion, which keeps the aggressiveness inside an active pit.
- The black layer formed at 0 V(SCE) has been found to induce a small extra resistance in the solution.

5. *IN-SITU* SYNCHROTRON STUDIES OF THE EFFECT OF NITRATE ON IRON ARTIFICIAL PITS IN CHLORIDE SOLUTIONS

5.1 Introduction

It is well known that nitrate can influence the corrosion of ferrous alloys in a variety of applications, and the effect has been widely studied since the 1960s [7, 35, 97, 121, 162, 163]. Several models have been proposed, which include competitive adsorption between NO_3^- and Cl^- [97], nitrate electroreduction [35, 121] or redox reaction between NO_3^- and Fe^{2+} [7, 35].

Salt layers can form at the bottom of growing corrosion pits [23, 24, 26, 28], and the presence of salt layers is important for continued pit growth. However, the salt layers in nitrate-containing solutions have received scant attention except in electrochemical machining (ECM) studies (see Section 2.3.3).

Other solid products in addition to salt layers have also been found on corrosion sites both in chlorides and nitrates. Black corrosion products have been found on the surface of dissolving carbon steels in nitrates, which were believed to consist of carbon films [60] or carbides [61, 159, 164-166]. Indeed a preparation method for Fe_3C powder has been reported that involves dissolution of high carbon steel in HNO_3 [167], indicating that Fe_3C is stable in HNO_3.

A black coating has been observed on iron grains dissolving in deaerated HCl upon the addition of nitrate, but it was not possible to characterise the coating with *ex-situ* XRD as it did not remain stable during the treatment [109]. Black layers were also observed on the steels dissolving in pure chloride solutions [59, 61, 66, 67], which were assumed to be carbides in [59, 61].

In this work, the salt layer composition and structure in nitrate solutions have been characterised using *in-situ* X-ray diffraction combined with electrochemical measurements on artificial pits. The black layer has been observed in the iron artificial pit (see Chapter 4), which has been characterised using both *in-situ* synchrotron X-ray diffraction and *ex-situ* Raman spectroscopy. In the course of this work, current fluctuations have been observed for Fe artificial pits in chloride/nitrate mixed solutions. The morphology of the electrode surfaces of foil artificial pits in HCl has also been compared in the presence and absence of nitrate. In addition, *in-situ* synchrotron X-ray radiography has been used to investigate the dissolution behaviour of iron artificial pits in chloride and nitrate/chloride solutions.

5.2 Results

5.2.1 HCl solution with and without trace nitrate

5.2.1.1 Observations of black layers in artificial pits

Electrochemical experiments with optical monitoring were carried out using 1 M HCl with different concentrations of $NaNO_3$ as shown in Table 5-1.

Table 5-1. Stages of the electrochemical experiment in 1 M HCl solutions with and without traces of nitrate

	solution composition	applied potentials
stage 1	1 M HCl (20 ml)	1 V, 0.7 V, 0.4 V, 0.1 V(Ag/AgCl) applied in sequence for each concentration
stage 2	1 M HCl and 20 mM $NaNO_3$ (20 ml)	
stage 3	1 M HCl and 50 mM $NaNO_3$ (20 ml)	
stage 4	1 M HCl and 0.1 M $NaNO_3$ (20 ml)	

The 99.5% Fe foil artificial pit was grown in 20 ml 1 M HCl at voltages which ranged from 1.0 V to 0.1 V(Ag/AgCl). Figure 5-1 shows a selection of micrographs taken during the experiments. Figure 5-1a shows that no solid corrosion products were formed in pure 1 M HCl at the applied voltages of 1.0 to 0.4 V(Ag/AgCl), but a black layer appeared on the dissolving surface when 0.1 V(Ag/AgCl) was applied (Figure 5-1b). Upon the addition of nitrate, the black layer continued to grow at all voltages tested. Once formed, the black layers did not move, but thickened following the receding electrode surface. In addition, the black layer was neither compact nor strongly adherent as reported in [59, 60], since bubbles could pass through the layer, and it was easily flushed away with a needle and syringe after potential had been switched off at the conclusion of the experiment (Figure 5-1f).

The appearance of significant numbers of bubbles is usually associated with nitrate addition, but in this case they were not very clearly observed (in 20 mM nitrate in Figure 5-1c) until the nitrate concentration increased to 50 mM (Figure 5-1d). The bubbles have also been reported in other Fe/NO_3^- systems [3, 66].

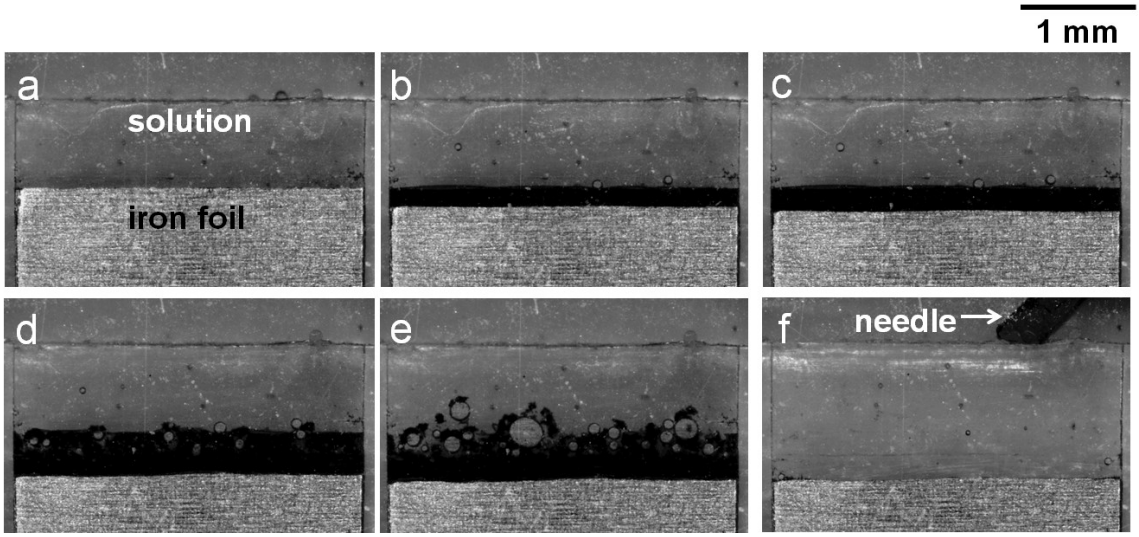

Figure 5-1. Micrographs taken at key points during the procedure in Table 5-1 for a 99.5% Fe foil artificial pit, (a) after sequential dissolution in 1 M HCl at 1 V, 0.7 V and 0.4 V, ca. 40 min for each voltage; (b) after further dissolution in 1 M HCl at 0.1 V for 2.2 hours; (c) after dissolution in 1 M HCl + 20 mM $NaNO_3$ at 1 V for 1 hour; (d) after dissolution in 1 M HCl + 50 mM $NaNO_3$ at 1 V for 1.2 hour; (e) after dissolution in 1 M HCl + 0.1 M $NaNO_3$ at 1 V (30 min), 0.7 V (25 min), 0.4 V (20 min) and 0.1 V (20 min) in sequence, and then the experiment ended; (f) after potential was switched off, black layer was flushed using a needle and syringe.

5.2.1.2 *In-situ* synchrotron tests

Before starting XRD measurements, an iron microelectrode was dissolved at 1 V(Ag/AgCl) until the artificial pit depth was ~500 μm (ca. 2 hours). *In-situ* synchrotron measurements were carried out using the conditions shown in Table 5-1. For each successive measurement, the artificial pit was deeper by at least 20 μm before starting X-ray measurements (as calculated with Faraday's law), and diffraction patterns were collected within a region less than 15 μm above the upper edge of the salt layer, so that the crystallites and black layers (if any) studied in each X-ray scan were generated exclusively under the corresponding condition.

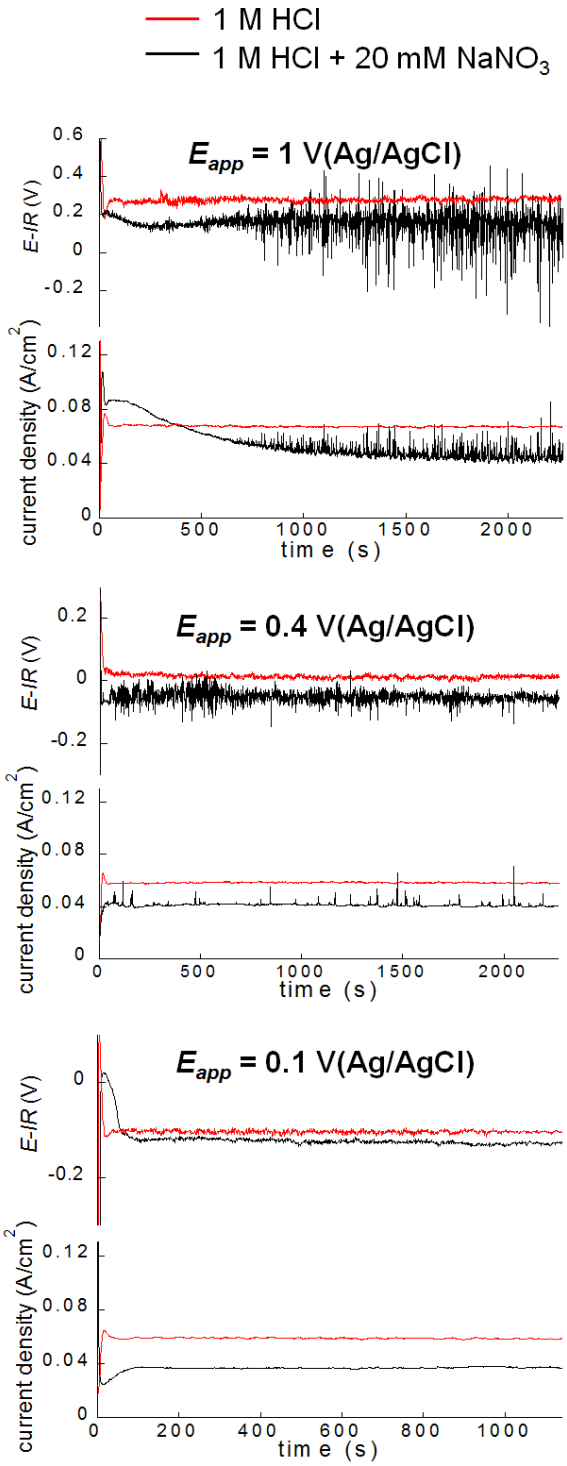

Figure 5-2. Interfacial potential and current density of the same Fe foil artificial pit at 1 V, 0.4 V, 0.1 V(Ag/AgCl) in pure 1 M HCl (in red, stage 1 in Table 5-1) and 1 M HCl + 20 mM $NaNO_3$ (in black, stage 2 in Table 5-1) during the XRD measurement, pit depth ca. 1 mm and 1.2 mm for 1 M HCl and 1 M HCl + 20 mM $NaNO_3$ respectively. All the measurements in 1 M HCl were made before the addition of nitrate. The resistance used for *IR*-correction of potential was measured using an imposed ac signal (f=50 kHz, amplitude 10 mV).

Figure 5-2 shows the current density and interfacial potential during X-ray measurements. Full ac impedance spectra between 0.1 V and 1 V(Ag/AgCl) have determined that the capacitance of the system is close to zero at frequency 30 to 50 kHz (see Figure 9-2 and Figure 9-3), so the total resistance was measured using an ac signal at 50 kHz (amplitude 10 mV) imposed on the applied potential. Both the current and interfacial potential were stable in pure 1 M HCl at all voltages studied. However, current fluctuations were observed after the addition of 20 mM $NaNO_3$ at 1 V and 0.4 V(Ag/AgCl). The higher current density at 1 V(Ag/AgCl) visible at the start of the plot was due to stirring after nitrate addition. The current fluctuation became smaller at 0.4 V(Ag/AgCl), and was not observed at 0.1 V(Ag/AgCl). The current density was consistently lower in 1 M HCl + 20 mM $NaNO_3$, since the pit was deeper in stage 2 of the measurement sequence (Table 5-1).

A typical stack plot of X-ray diffraction patterns in pure 1 M HCl at 1 V(Ag/AgCl) is shown in Figure 5-3. In the solution above the salt layer, a few very weak peaks were visible, but not possible to characterise. Within the salt layer, the patterns conform to the $FeCl_2.4H_2O$ standard [168], consistent with Rayment et al. [51]. Since the interval of the scan is 2 μm (see Section 3.6), the patterns of the salt layer extend essentially for ~10 μm. The very strong peak around 2Θ=29° is due to metallic iron from the foil. The same diffraction patterns were observed in salt layer at 0.7 V and 0.4 V(Ag/AgCl), and the layer was thinner (~6 μm) at both voltages.

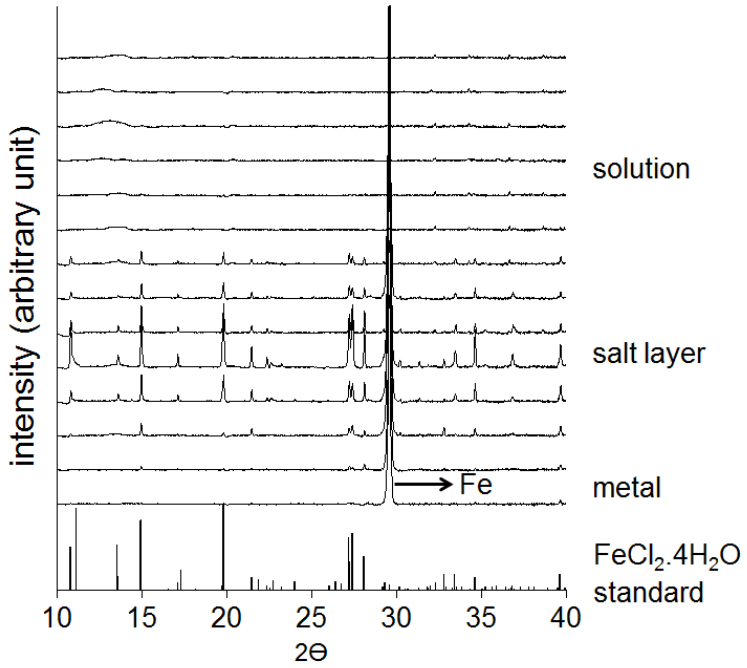

Figure 5-3. A stack plot of diffraction patterns collected at 2 μm intervals from one X-ray scan in an Fe artificial pit in pure 1 M HCl at 1 V(Ag/AgCl); diffraction patterns were collected in a sequence from the solution to the metal. The standard pattern of $FeCl_2.4H_2O$ [168] is shown at the bottom of the figure.

After the potential was stepped down to 0.1 V(Ag/AgCl) in 1 M HCl, the extent of the diffraction patterns of the salt layer decreases to ~4 μm (see Figure 5-4a). Much stronger diffraction patterns appear above the salt layer which conform to the standard pattern for Fe_3C [169] (Figure 5-4b) and which also correlate with formation of the black layer in Figure 5-1b. It is also noticeable that a few weak peaks in the pattern collected within the salt layer may be correlated with Fe_3C (very strong peaks of $FeCl_2.4H_2O$ have been cropped).

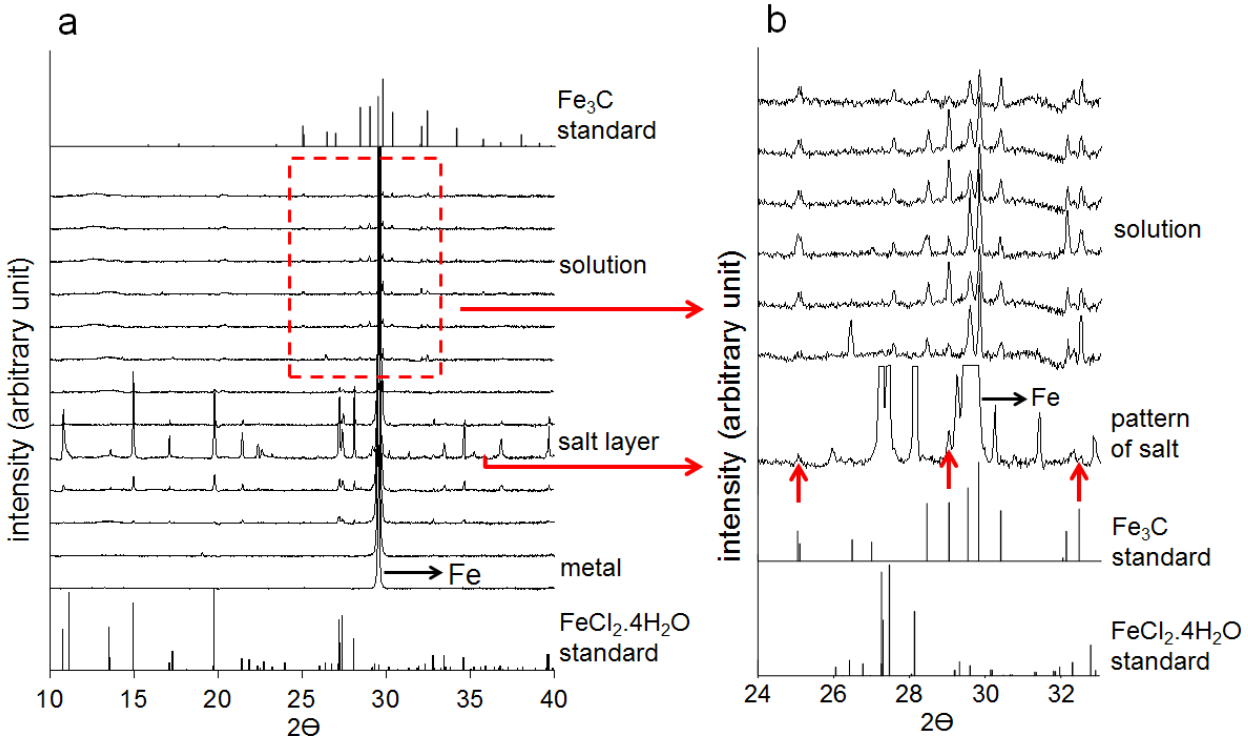

Figure 5-4. A stack plot of diffraction patterns collected at 2 µm intervals from one X-ray scan in an Fe artificial pit in pure 1 M HCl at 0.1 V(Ag/AgCl): (a) diffraction patterns collected in a sequence from the solution to the metal; (b) details of patterns collected ca. 2 to 12 µm above the salt layer, and a pattern collected in the salt layer; the arrows indicate weak peaks that correlate with Fe_3C. Standard patterns for $FeCl_2.4H_2O$ [168] and Fe_3C [169] are shown for reference.

After a trace of $NaNO_3$ (20 mM, 50 mM or 0.1 M) was added into 1 M HCl, the salt layer was still $FeCl_2.4H_2O$ and no nitrate phases were detected. Fe_3C was found to be present above the salt layer under all nitrate-containing conditions, i.e. at all voltages between 0.1 V and 1 V, which correlates with the black layer visible in Figure 5-1c-e. A stack plot of one X-ray scan in 1 M HCl and 20 mM $NaNO_3$ at 1 V(Ag/AgCl) is shown in Figure 5-5a as an example. The diffraction patterns of the salt layer extend for ~12 µm. Fe_3C has been detected in the solution above the salt layer, and a few weak peaks are also present in the pattern collected within the salt layer (see Figure 5-5b), which may be correlated with Fe_3C (very strong peaks of $FeCl_2.4H_2O$ have been cropped).

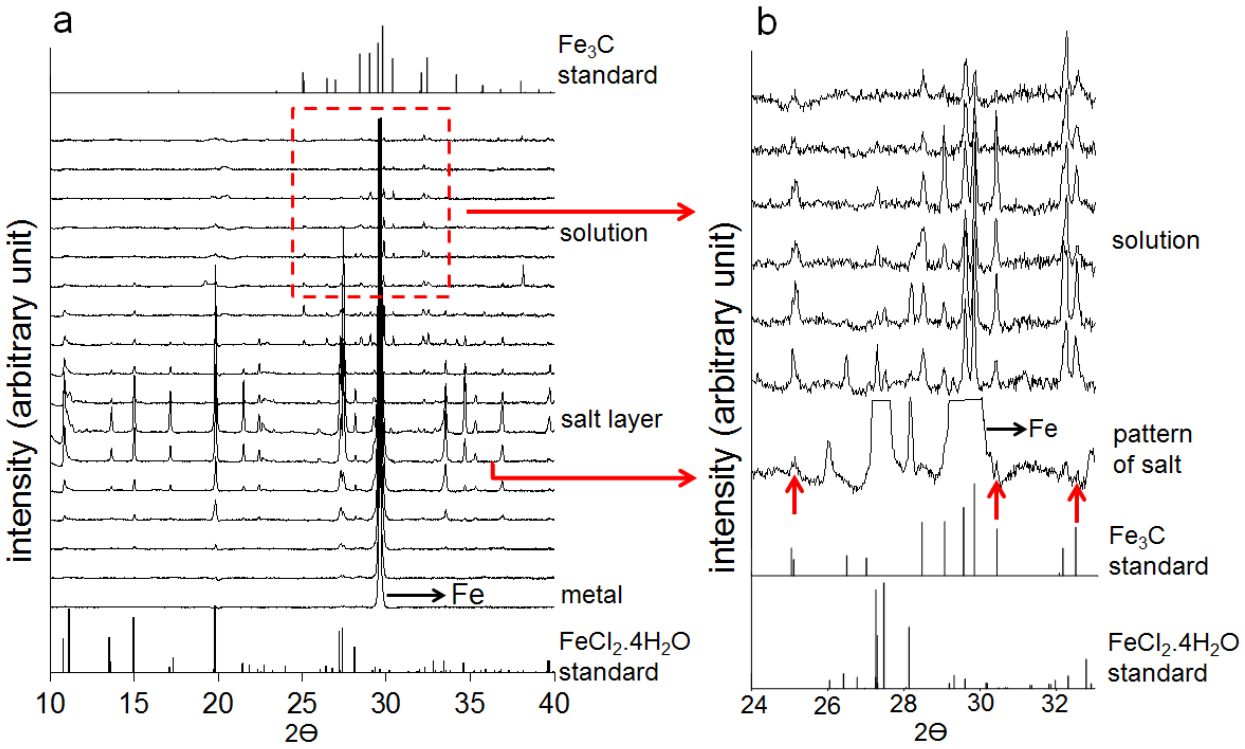

Figure 5-5. A stack plot of diffraction patterns collected at 2 µm intervals from one X-ray scan in an Fe artificial pit in 1 M HCl + 20 mM $NaNO_3$ at 1 V(Ag/AgCl): (a) diffraction patterns collected in a sequence from the solution to the metal; (b) details of patterns collected ca. 2 to 12 µm above the salt layer, and a pattern collected in the salt layer; the arrows indicate weak peaks that correlate with Fe_3C. Standard patterns for $FeCl_2.4H_2O$ [168] and Fe_3C [169] are shown for reference.

Figure 5-6 shows diffraction patterns calculated by averaging the data from all scans collected above the salt layers (i.e. where no $FeCl_2.4H_2O$ was visible) for three conditions: 1 M HCl at 1 V, 1 M HCl at 0.1 V and 1 M HCl + 20 mM $NaNO_3$ at 1 V(Ag/AgCl). This procedure makes the diffraction patterns of Fe_3C collected in the solution more clearly visible. It indicates that, in 1 M HCl at 0.1 V and in 1 M HCl + 20 mM $NaNO_3$ at 1 V, a significant amount of Fe_3C did not dissolve, and was thus left above the electrode as the surface of the iron electrode receded. In 1 M HCl at 1 V, a few very weak peaks in the averaged pattern may also be correlated with Fe_3C, which indicates that most but perhaps not all of the Fe_3C was dissolved, since a black layer was not observed in 1 M HCl at 1 V (see Figure 5-1a). In

addition, there are also a few weak peaks in these averaged patterns, which may be correlated with the salt $FeCl_2.4H_2O$, since the beam may be diffracted at the upper edge of the salt layer. The Fe_3C was clearly detected whenever the black layer was present, i.e. at 0.1 V(Ag/AgCl) in HCl and all voltages in the presence of trace nitrate, so it may be concluded from Figure 5-6 that crystalline component of the black layer observed in Figure 5-1 consisted of Fe_3C. The diffraction images for this region (not shown) indicate that the scattering arises from individual crystallites of Fe_3C, which means that they are few in number and have a relatively large particle size.

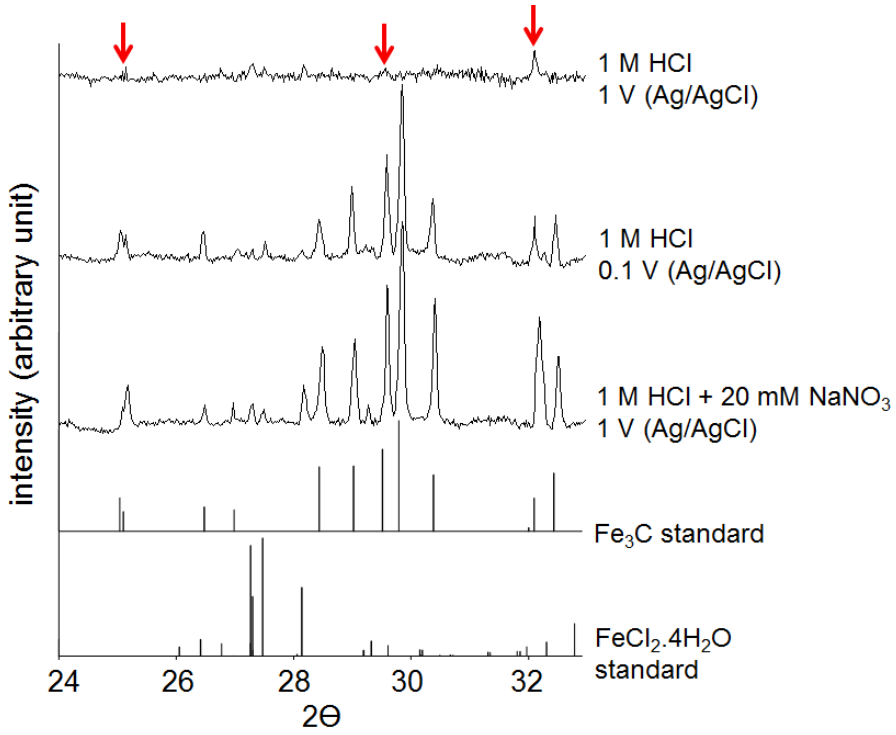

Figure 5-6. Averaged diffraction patterns collected above salt layers on an Fe artificial pit dissolving under three conditions: 1 M HCl at 1 V, 1 M HCl at 0.1 V and 1 M HCl + 20 mM $NaNO_3$ at 1 V(Ag/AgCl); the Fe_3C [169] and $FeCl_2.4H_2O$ [168] standard patterns are shown at the bottom of the figure. The arrows indicate the few weak peaks in the averaged pattern collected in 1 M HCl at 1 V(Ag/AgCl), which may be correlated with Fe_3C.

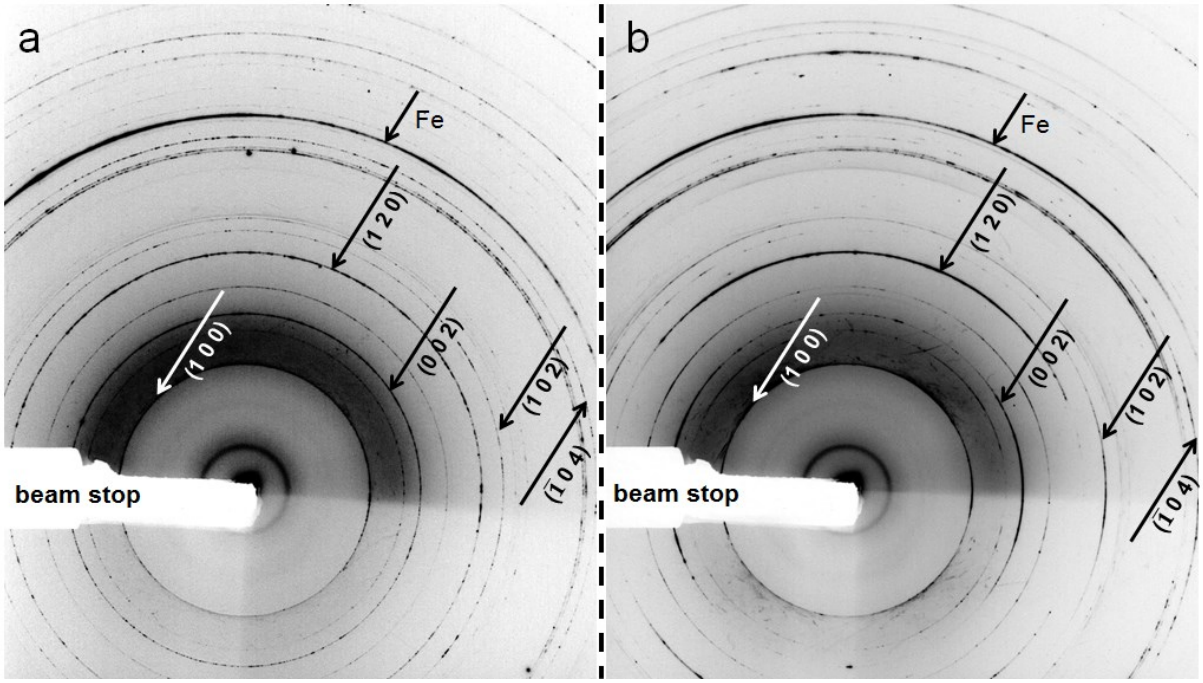

Figure 5-7. Averaged diffraction patterns of salt layers on an Fe artificial pit in (a) pure 1 M HCl and (b) 1 M HCl + 20 mM $NaNO_3$ at 1 V(Ag/AgCl); several diffraction rings showing nitrate-induced anisotropy of the crystals growth morphology are labelled.

Figure 5-7 shows two averaged diffraction images of salt layers grown in 1 M HCl in the absence (a) and presence (b) of nitrate. In the absence of nitrate, the rings are continuous, indicating that the crystallites are isotropic. Following the addition of nitrate, anisotropic scattering is seen on (1 2 0) reflections (which diffract predominantly vertically) and (0 0 2), (1 0 2) and ($\bar{1}$ 0 4) reflections, which show stronger diffraction horizontally (parallel to the iron surface). For the monoclinic lattice of $FeCl_2.4H_2O$ [168], the angle between (0 0 2) and (1 2 0) planes is 79°, but it is less than 28° between (0 0 2) planes and the other two anisotropic planes (1 0 2) and ($\bar{1}$ 0 4). In addition, the isotropic planes, e.g. (1 0 0), lie in the direction other than (0 0 2) and (1 2 0) planes. This suggests that the crystallites may form platelets with (1 2 0) lying horizontally. The anisotropy of the salt layer in the presence of trace nitrate was consistent at all voltages studied, while it was all isotropic in pure HCl. It

should be noted that the bottom part of the image is lighter, since the diffracted beam at the bottom half will penetrate through the metal.

5.2.2 Dissolution of iron in nitric acid with trace chloride

Since Fe undergoes spontaneous passivation in concentrated nitrate solutions [88, 130], a nitrate concentration of 0.1 M HNO_3 was used, and 10 mM HCl was added so dissolution could be easily initiated. An iron foil artificial pit was dissolved in this mixed solution at an applied voltage of 0.55 V(Ag/AgCl). The current density and interfacial potential are shown in Figure 5-8. The resistance for *IR*-correction of potential was also measured using an imposed ac signal (f= 50 kHz, amplitude 10 mV).

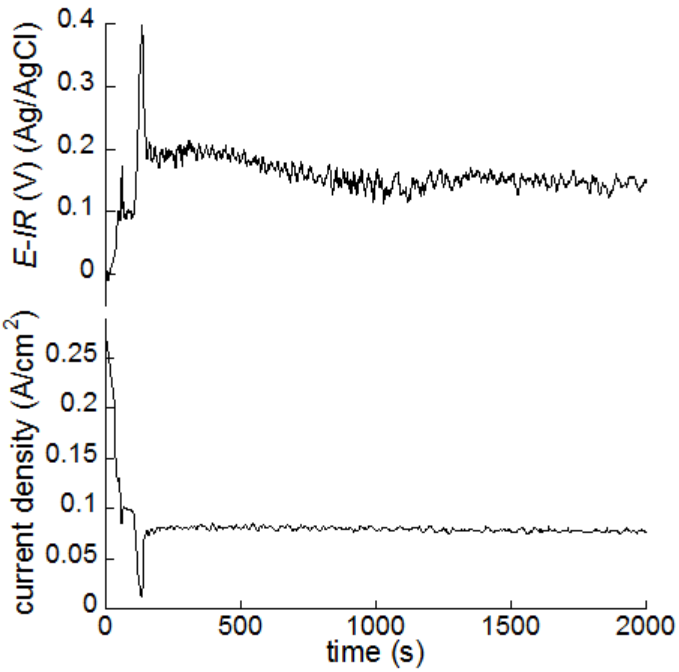

Figure 5-8. Interfacial potential and current density during X-ray measurements on an Fe artificial pit in 0.1 M HNO_3 + 10 mM HCl at 0.55 V(Ag/AgCl) applied directly from open circuit, pit depth ca. 0.9 mm. The resistance for *IR*-correction of potential was measured using an imposed ac signal (f= 50 kHz, amplitude 10 mV).

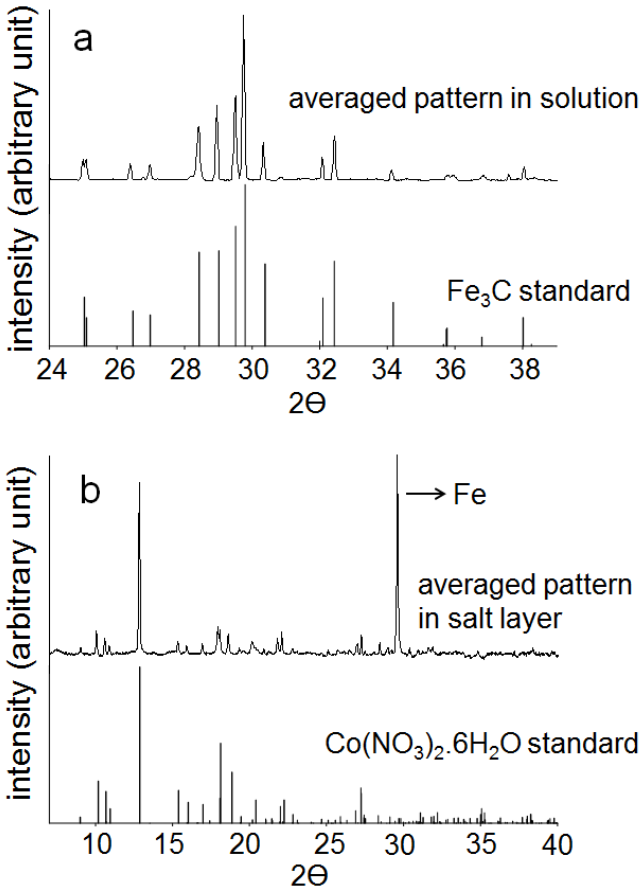

Figure 5-9. Averaged patterns of all patterns collected (a) in the solution above salt layer, and (b) within salt layer of an Fe artificial pit in 0.1 M HNO_3 + 10 mM HCl at 0.55 V(Ag/AgCl), compared with Fe_3C [169] and $Co(NO_3)_2.6H_2O$ [170] standard patterns, respectively.

Figure 5-9 shows the averaged diffraction patterns for the solution above the salt layer and also within the salt layer. As before, Fe_3C was detected in the solution (Figure 5-9a). The averaged pattern of the salt layer is a good match to the known pattern of $Co(NO_3)_2.6H_2O$ [170] and iron chloride is not observed (Figure 5-9b). The diffraction pattern for iron (II) nitrate has not been recorded in standard databases since the material may undergo spontaneous decomposition [46]. However, Fe^{2+} has a very similar ionic size to Co^{2+} (crystal ionic radius of Fe^{2+} ~1.06 Å, Co^{2+} ~1.04 Å [171]), so it is reasonable to assume that the phase observed is $Fe(NO_3)_2.6H_2O$, which is expected to be isostructural with $Co(NO_3)_2.6H_2O$ [170], according to which the cell parameters of the detected crystallites were peak-fitted (Table 5-2),

and the crystal system is monoclinic (I12/c1). As expected from the ionic radii for iron (II) and cobalt (II), the cell parameters derived for $Fe(NO_3)_2.6H_2O$ are slightly larger than those for $Co(NO_3)_2.6H_2O$.

Table 5-2. Peak-fitted cell parameters of the salt in an Fe artificial pit in 0.1 M HNO_3 and 10 mM HCl at 0.55 V(Ag/AgCl) according to cell parameters of $Co(NO_3)_2.6H_2O$ [170]

salt	a (Å)	b (Å)	c (Å)	α	β	γ
$Co(NO_3)_2.6H_2O$ [170]	14.960	6.112	12.632	90˚	118.45˚	90˚
detected salt	14.995±0.002	6.163±0.002	12.823±0.002	90˚	118.55±0.02˚	90˚

5.2.3 *Ex-situ* Raman spectroscopy on the black layer formed in HCl

In addition to the XRD characterisation of the black layer, *ex-situ* Raman spectroscopy has been applied to investigate the black layer formed in 1 M HCl.

Ex-situ Raman spectroscopy studies were carried out using the electrochemical cell described in Chapter 3.9. Since the black layers forms at an applied voltage of 0.1 V(Ag/AgCl), a commercial purity (99.5%) iron foil had been dissolved in a foil artificial pit in 1 M HCl at 1 V(Ag/AgCl) until the metal surface reached the glass window at the “resin-free” area of the cell. Then 0.1 V(Ag/AgCl) was applied for 2 hours to grow a black layer until the layer filled the window region ca. 0.3 mm (v)×3 mm (h). At this point the applied potential was switched off, the solution was removed, and the electrochemical cell was dried with warm air. The Raman spectrum obtained from the black layer in the iron artificial pit is shown in Figure 5-10.

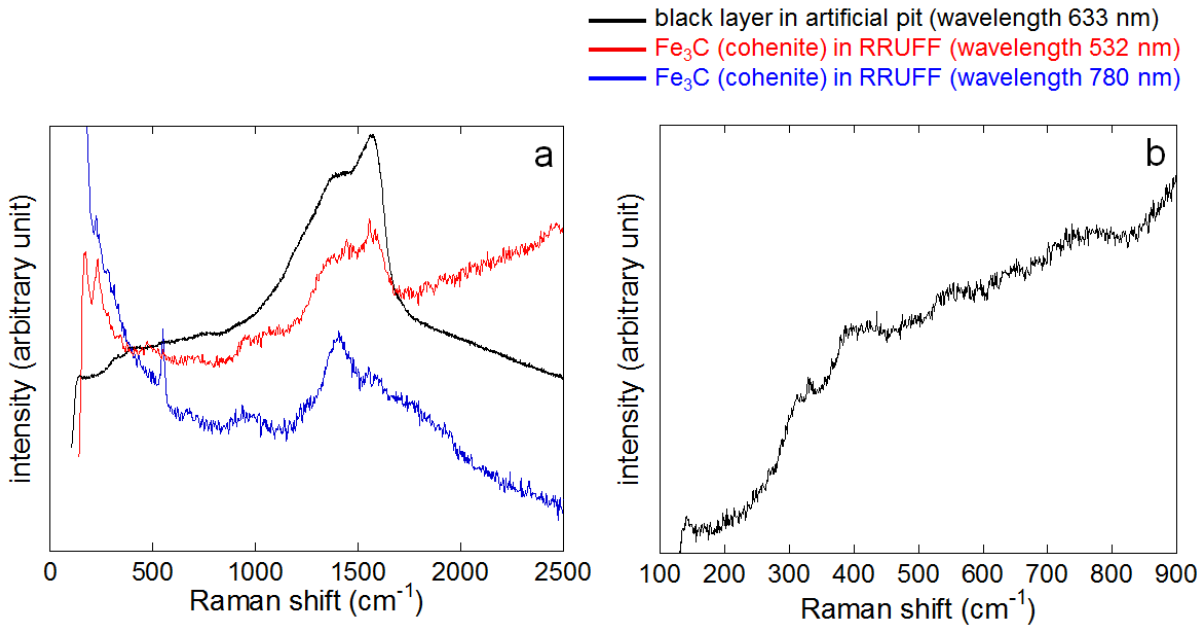

Figure 5-10. (a) A Raman spectrum (633 nm HeNe laser) of the black layer formed at 0.1 V(Ag/AgCl) in a 99.5% Fe foil artificial pit in 1 M HCl, compared with the Fe_3C (cohenite) sample reported in RRUFF database (with wavelengths 532 nm and 780 nm) [172]; (b) details of the Raman spectrum of black layer in the region between 100 cm^{-1} and 900 cm^{-1}

A Raman spectrum of iron carbide has been reported in [173], but it has not been confirmed to be Fe_3C by any technique, and the method for sample preparation was not clear. The Raman spectrum of Fe_3C has only been reported in the RRUFF database [172]. The sample is a piece of polished cohenite (same as cementite) and the identification has been confirmed by chemical analysis and X-ray diffraction (the diffraction pattern of the cohenite mineral agrees well with the pattern of Fe_3C reported in this work). The Raman spectrum of the black layer is compared with the data reported by RRUFF in Figure 5-10a. It can be seen that the two sharp peaks correlate with the Fe_3C (cohenite) reported in RRUFF database [172].

It is also reported that disordered carbon shows two sharp modes, the "G peak" at 1580 to 1600 cm^{-1} and "D peak" at ~1350 cm^{-1}, which are both due to sp^2 sites of disordered carbon [174, 175]. The D peak is characteristic of "amorphous state" or "nanocrystalline state" carbon [176], and the ratio of D peak and G peak intensity "I_D/I_G" at 0.9 or higher indicates an

"amorphous state" [177]. For example, the I_D/I_G for sputtered amorphous carbon (very large disorder) has been found to be ca. 1.5 [175]. Also, since amorphous carbon can contain a mixture of sp^3, sp^2 and even sp^1 sites, it may only display a single broad and asymmetrical Raman band centred at 1520 cm^{-1} [174, 178]. So the two strong peaks in Figure 5-10a also correlate with the G peak and D peak, and the ratio of I_D/I_G is ~0.9.

Furthermore, the Raman spectra of disordered carbon may also present a "T peak", which corresponds to sp^3 sites [175]. However, visible Raman spectroscopy (used in this study) is much more sensitive to sp^2 than to sp^3 sites [179, 180], so only G peak and D peak were found. The sp^3 sites (T peak), if exists in the black layer, might be detected by use of high energy UV Raman [181, 182].

As described in Section 5.2.1.2, the diffraction from Fe_3C is very weak, and the scattering of X-ray in the pit solution arises from individual crystallites of Fe_3C, the number of which is small. A small amount of Fe_3C in the pit solution is unlikely to form a thick black layer, so it is reasonably concluded that the black layer in the iron artificial pits consist of both Fe_3C and disordered carbon.

In addition, the Raman band positions of some other iron-containing corrosion products are shown in Table 5-3, the positions with less than 5 cm^{-1} difference are regarded as the same. The Raman bands of none of these iron corrosion products match the two sharp peaks in the spectrum of the black layer (Figure 5-10a). However, a few very weak peak can be seen between 200 cm^{-1} and 800 cm^{-1} (see Figure 5-10b), e.g. around 330 cm^{-1}, 410 cm^{-1}, 550 cm^{-1}, 770 cm^{-1}, which may match the bands of α-FeOOH, δ- FeOOH and α-Fe_2O_3. It is difficult to identify these conclusively, but trace iron oxides formed during sample treatment may be detectable.

Table 5-3. Raman band positions of iron-containing corrosion products

iron-containing compound	Raman band position (cm^{-1})
α-FeOOH, goethite [183, 184]	243, 298, 385, 414, 474, 550, 685, 993
γ-FeOOH, lepidocrocite [183, 184]	252, 380, 493, 522, 650, 719, 1303
δ- FeOOH, feroxyhyte [183, 185]	296, 400, 680, 1160, 1314
amorphous FeOOH [185]	700
FeO, wustite [183, 184, 186]	616, 663
Fe_3O_4, magnetite [183, 184, 186]	300, 532, 616, 663
α-Fe_2O_3, hematite [183, 184, 186]	227, 245, 293, 298, 414, 501, 612
γ- Fe_2O_3, maghemite [183]	350, 500, 700

5.2.4 Morphology of the iron surface in an "artificial pit"

In the laboratory, two 99.5% Fe foil artificial pits were grown to 500 μm in 1 M HCl at 1 V(Ag/AgCl), then 50 mM nitrate was added to one of the pits and both were grown for an additional 2 hours at the same voltage 1 V(Ag/AgCl). Nitrate induced the same current fluctuations as those shown in Figure 5-2. The SEM micrographs of the two artificial pit surfaces are shown in Figure 5-11. It can be seen that in the absence of nitrate, the surface is slightly roughened with some small cavities. In contrast, in the presence of 50 mM $NaNO_3$, the surface is very rough. The morphology of artificial pit surfaces along the rolling and transverse directions was compared. For the nitrate-containing solution, it can be seen that the metal surface has been crystallographically etched, since the morphology correlates well with the EBSD map (see Figure 5-11).

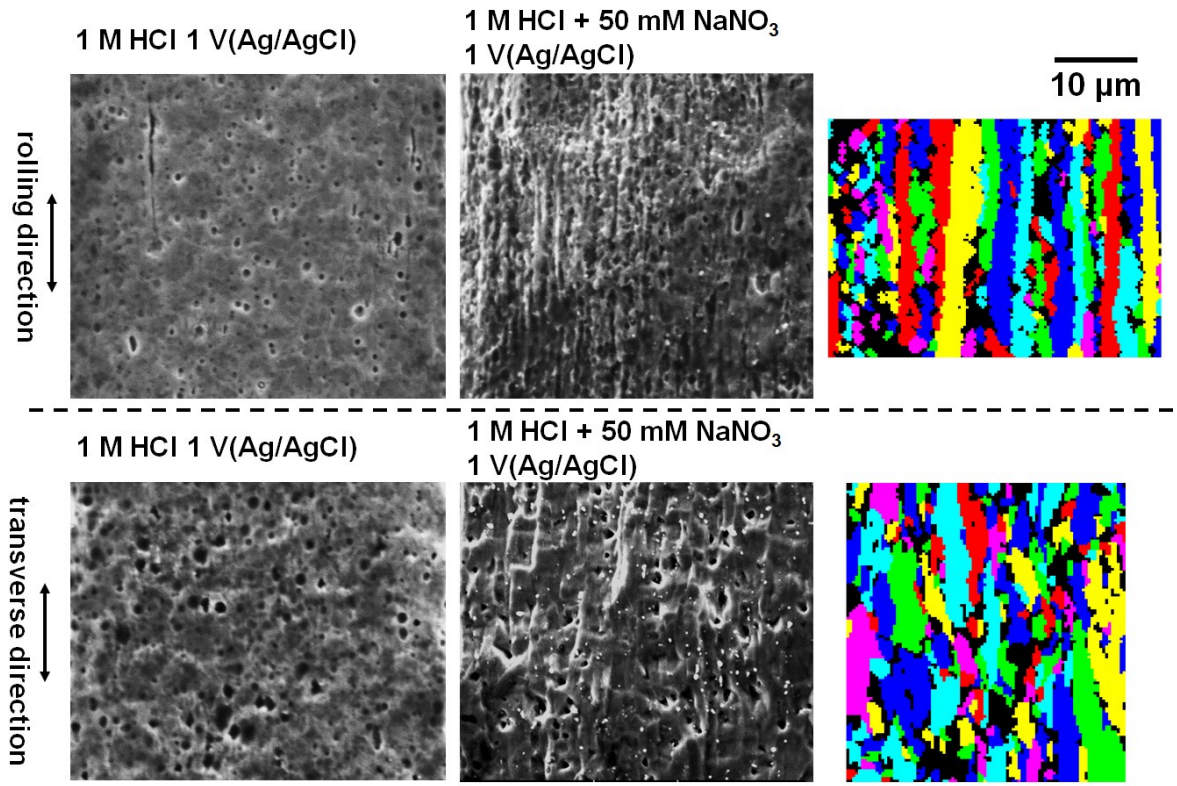

Figure 5-11. SEM micrographs of 99.5% Fe foil artificial pit surfaces after dissolution in pure 1 M HCl and 1 M HCl + 50 mM $NaNO_3$ at 1 V(Ag/AgCl) for 2 hours respectively (after both pit depths reached ca. 500µm in 1 M HCl at 1 V), compared with EBSD maps of mirror-polished cross sections of as-received foil strips. All the foils have been ultrasonically cleaned before SEM/EBSD measurement.

There are bright particles on the artificial pit surface after dissolution in 1 M HCl + 50 mM $NaNO_3$, even after ultrasonic cleaning (visualised in the SEM images in Figure 5-11 as small white dots). However, the bright particles are not observed after dissolution in pure 1 M HCl. These particles show elevated carbon levels (see Figure 5-12), consistent with the presence of Fe_3C and/or disordered carbon, although the use of SEM/EDX for accurate measurement of carbon levels is not practical.

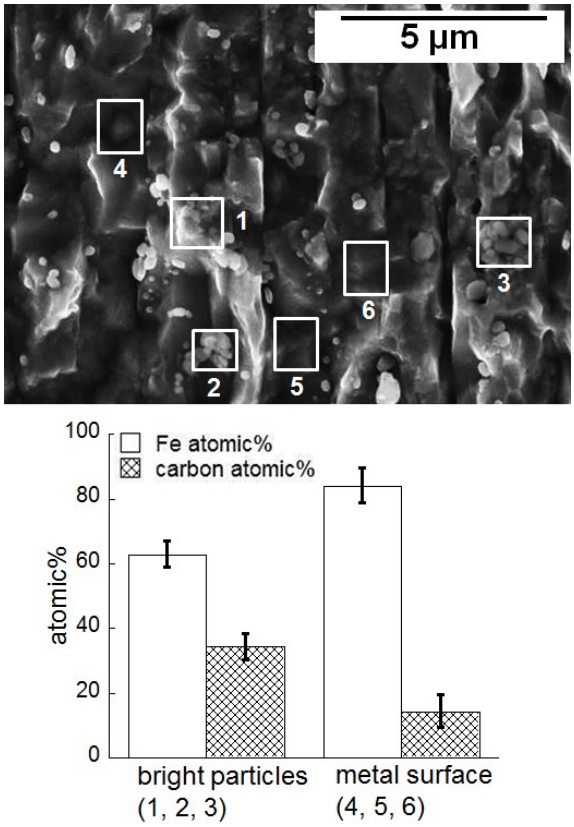

Figure 5-12. EDX measurements on the bright particles and bare metal surface of a 99.5% Fe foil artificial pit electrode after dissolution in 1 M HCl and 50 mM $NaNO_3$ at 1 V(Ag/AgCl) for 2 hours (after pit depth reached ca. 500 µm in 1 M HCl at 1 V).

In addition, another two 99.5% Fe pits were also grown in 1 M HCl at 1 V(Ag/AgCl) and pit depths reached 500 µm. Then 50 mM $NaNO_3$ was added to one of the pits and both were grown for an additional 2 hours at the same voltage 0.1 V(Ag/AgCl). The electrode surface was also slightly roughened in pure 1 M HCl and crystallographically etched in 1 M HCl + 50 mM $NaNO_3$ (Figure 5-13). It is known from the XRD and Raman measurements that Fe_3C/carbon were present under both conditions, so the crystallographic etching of the iron surface is influenced by the presence of nitrate instead of Fe_3C/carbon.

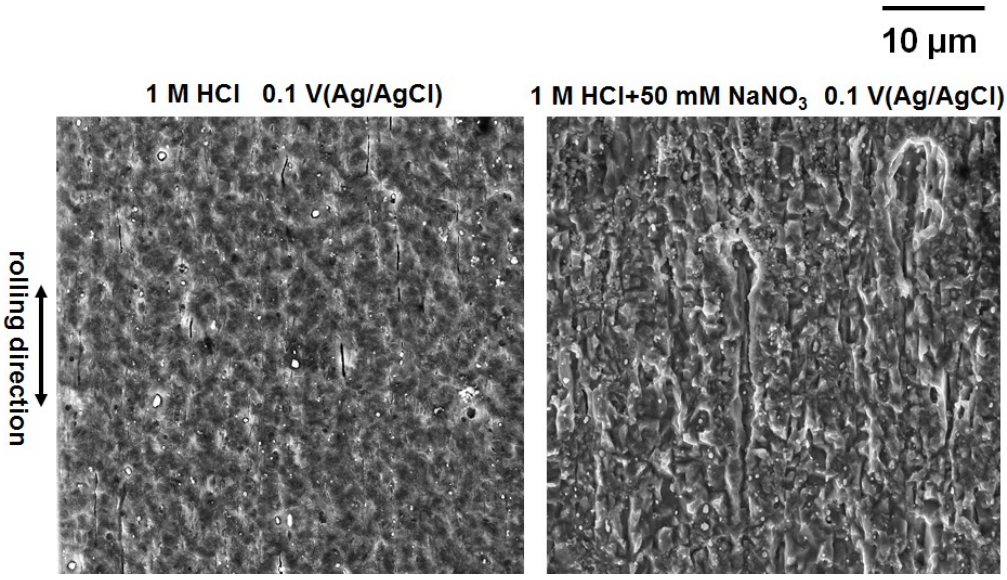

Figure 5-13. SEM micrographs of 99.5% Fe foil artificial pit surfaces after dissolution in pure 1 M HCl and 1 M HCl + 50 mM $NaNO_3$ at 0.1 V(Ag/AgCl) for 2 hours respectively (after both pit depths reached 500 µm in 1 M HCl at 1 V). Both foils have been ultrasonically cleaned before SEM measurement.

5.2.5 *In-situ* radiography experiments on iron foil artificial pits

5.2.5.1 Dissolution behaviour of iron in 1 M HCl

A high purity iron (99.99+%) foil (25 µm) artificial pit was grown for 1.5 hours in 1 M HCl at 1 V(Ag/AgCl) and the pit depth was ca. 400 µm before the electrochemical cell was moved to the beam for the radiography experiment (see Section 3.7). Then the artificial pit was further grown at 1 V(Ag/AgCl) for ca. 20 min and the dissolution was at a steady-state. A series of potential cyclic sweeps (at 10 mV/s and 2 mV/s in sequence) between 1 V and -0.25 V(Ag/AgCl) were carried out on the artificial pit, starting from 1 V(Ag/AgCl).

The current-voltage characteristics of a 2 mV/s sweep are shown in Figure 5-14 as an example. Points A to E are the key points for the comparison of corresponding images. Point A is the start of the cyclic sweep, point B is near the transition potential [39] where the salt layer dissolves, point C is at the reversing potential, point D is the peak current density during the

supersaturation process, after which a salt layer precipitates on the metal surface, and point E is the end of the cyclic sweep at 1 V(Ag/AgCl). In addition, it needs to be clarified that the hysteresis of the reversing of current at the potential reversing point (point C) is not observed for the experiments carried out under the same condition in laboratory, and it could be an effect of beam damage.

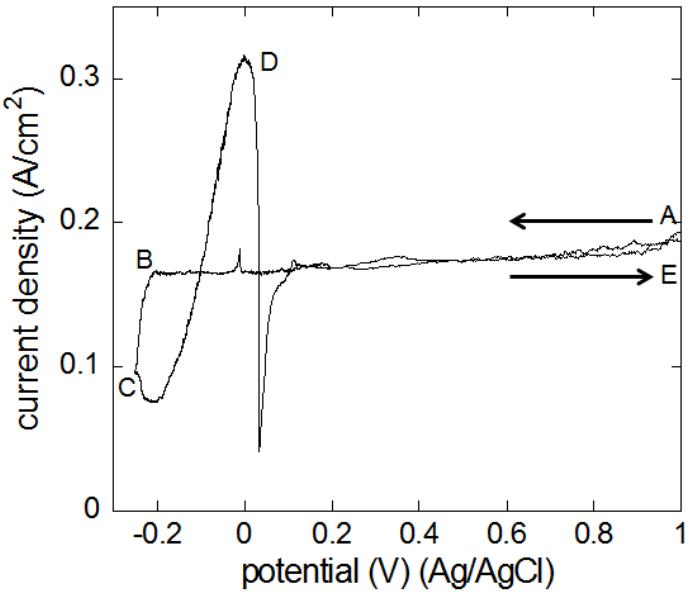

Figure 5-14. A plot of current density vs. applied potential for a potential cyclic sweep (2 mV/s) on a high purity iron (99.99+%) foil (25 µm) artificial pit in 1 M HCl during *in-situ* X-ray radiography experiments, potential swept between 1 V and -0.25 V(Ag/AgCl) starting from 1 V(Ag/AgCl), pit depth ca. 500 µm.

The radiographic images corresponding to points A to E on the current-voltage plot are shown in Figure 5-15a. To make the progress of corrosion more evidently clear, image calculation procedure was carried out, i.e. an image was subtracted by another image taken at a later stage to manifest the difference between the two. The "difference" images derived from calculation of "B-A", "C-B", "D-C" and "E-C" are shown in Figure 5-15b, where the white bands indicate the dissolved part between the two points. The greyscale value in each image in Figure 5-15b along a vertical red line through the dissolving interface is plotted as a function

of distance in pixels (Figure 5-15c). The high greyscale value corresponds to the region where the metal has dissolved, and the sharp drop in greyscale value corresponds to the top of the metal foil.

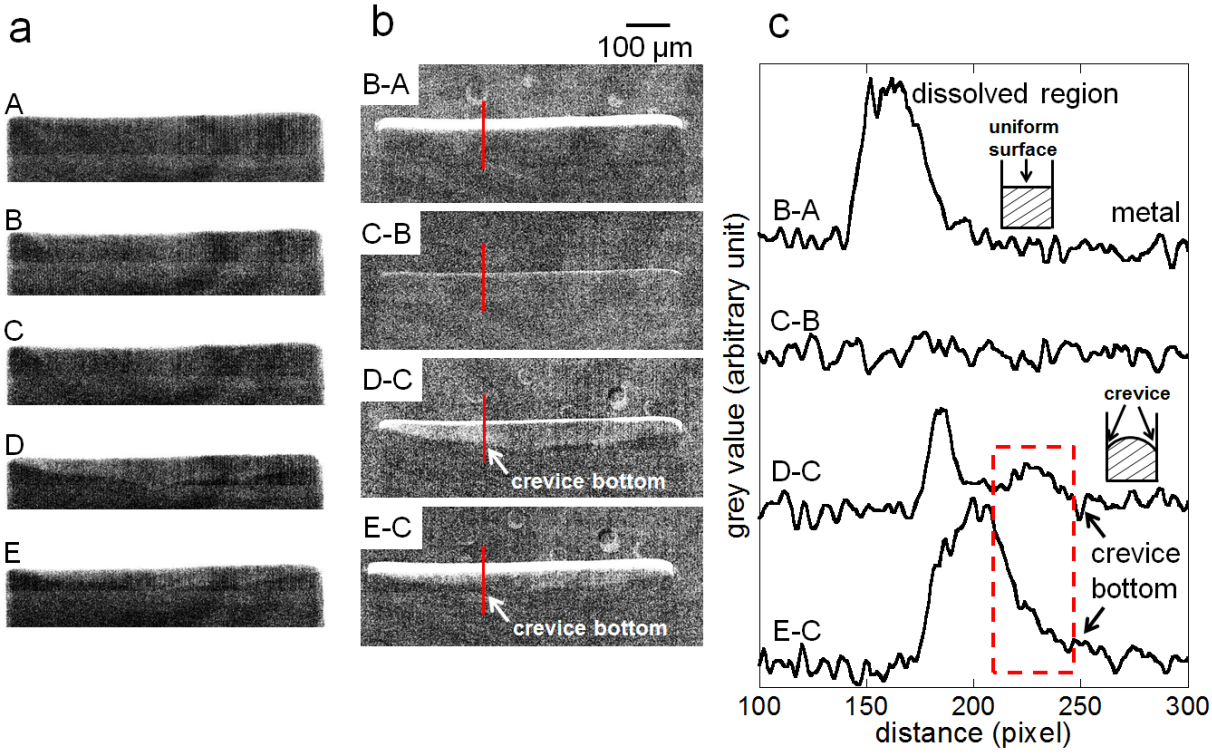

Figure 5-15. (a) The radiographic images corresponding to the points A to E in Figure 5-14; (b) "difference" images after the procedure of subtraction for related radiographic images in (a), the regions of metal dissolution appear bright. (c) Stack plots of pixel grey level vs. distance in pixels along each red line on the images in (b) (pixel size ~1 µm), the schematic diagrams describe the uniform metal surface and crevice formation. A high grey level in the plots corresponds to a lighter grey level in the images, indicating metal loss. The images were smoothed (replacing each pixel on the image with the average of its 3×3 neighbourhood) twice for noise reduction.

The "B-A" image shows that the surface of the metal foil has remained sharp from A to B, but has moved by ~20 µm during dissolution of the salt layer-covered surface, and that the top surface of the metal (bottom of the white band) is relatively smooth. From B to C, there is relatively little change in the profile as the current density has fallen over a very short time (~25 s), so the "C-B" image shows that the dissolution (white band) between points B and C

is negligible. From C to D, the "D-C" image shows that the position of the top of the foil for point D has not changed much compared to point C (only a very narrow bright band), but a curved grey region can be seen below the top of the foil, indicating the formation of a crevice, since there is a significant increase in the greyscale value near the metal surface (position in pixels 220 to 245, corresponding to a distance of ~25 μm). It suggests that the dissolution of a salt-free artificial pit may induce crevice formation between the foil and epoxy resin (metal thinning). When point E is compared with point C using the "E-C" image, it shows that the top surface of the foil has now become lower compared to "D-C" (the bright band above the top of the foil is thicker), but the corresponding greyscale value plot indicates that the position of the bottom of the crevice (at pixel ~245) has not changed (see Figure 5-15c). Since points D to E is dominated by dissolution of the surface under a salt layer (the top surface of the metal has dissolved by ~15 μm), the unchanged bottom of the crevice indicates that the diffusion-limited dissolution (salt-covered) tends to level the metal surface, so that the metal can dissolve uniformly. Similar plots for other positions on the metal surface (not shown) give results similar to Figure 5-15c.

The electrochemical experiment shown in Figure 5-14 has also been carried out in the laboratory (potential sweep rate 2 mV/s), but stopped during the course of supersaturation process in the potential forward sweep, equivalent to point D in Figure 5-14. The current-voltage characteristics and the SEM image taken after the experiment are shown in Figure 5-16a and b respectively. The hysteresis of the reversing of current at potential reversing point is not observed in Figure 5-16a. For the sake of comparison, another high purity (99.99+%) iron foil (25 μm) electrode was dissolved in 1 M HCl at 1 V(Ag/AgCl) for 2 hours (pit depth ca. 500 μm, diffusion-limited dissolution) without sweeping the potential,

and the SEM image of the electrode surface taken after the potentiostatic measurement is shown in Figure 5-16c.

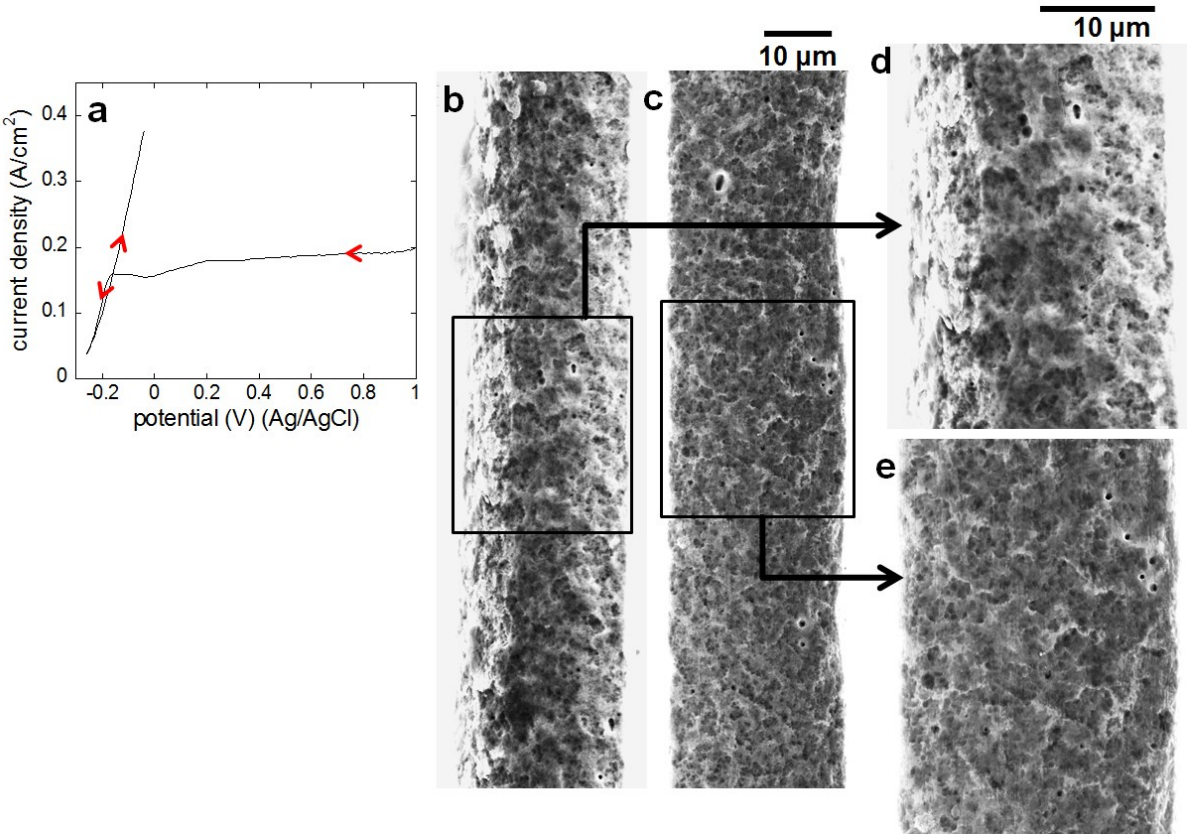

Figure 5-16. (a) A plot of current density vs. applied potential for a potential sweep (2 mV/s) on a high purity iron (99.99+%) foil (25 µm) artificial pit in 1 M HCl, the potential started from 1 V, reversed at -0.25 V(Ag/AgCl) and was switched off during the course of supersaturation process in the potential forward sweep, pit depth ca. 500 µm, the experiment was carried out in laboratory; (b) an SEM image of the artificial pit electrode surface after the potential sweep shown in (a); (c) an SEM image of another 99.99%+ iron foil (25 µm) artificial pit electrode surface after potentiostatic measurement at 1 V(Ag/AgCl) for 2 hours, pit depth ca. 500 µm. The insert (d) and (e) show details of (b) and (c), respectively.

It can be seen that the surface of the electrode in Figure 5-16b is slightly more roughened compared with Figure 5-16c. Furthermore, both sides of the foil in Figure 5-16b are lower compared to the centre, which indicates the crevice formation/metal thinning at the electrode surface.

5.2.5.2 Dissolution behaviour of iron in nitrate/chloride solutions

Kawaley [66] has found that, for the dissolution of iron in nitrate/chloride solutions, when the concentrations of nitrate and chloride are comparable, e.g. [Cl^-] 5 mM and [NO_3^-] 10 mM, there are a dissolution/passivation transition during the potential forward sweep where the dissolution suddenly stops, and a passivation/activation transition during the potential backward sweep where appears a burst of dissolution. This has been further studied in the present work using *in-situ* X-ray radiography.

A high purity iron (99.99+%) foil (25 μm) artificial pit was grown in 1 M HCl at 1 V(Ag/AgCl) for 1 hour and the pit depth was ca. 300 μm before the electrochemical cell was moved to the beam. Then the solution of 1 M HCl was removed from the electrochemical cell, and replaced with a solution of 0.1 M $NaNO_3$ + 0.05 M HCl (the same ratio of [NO_3^-]/[Cl^-] as used by Kawaley [66]). The potential swept between 0.9 V and -0.25 V(Ag/AgCl) at 10 mV/s starting from 0.9 V(Ag/AgCl), and the *in-situ* radiography measurement were started simultaneously.

Figure 5-17a shows the current-voltage characteristics of the potential sweep. Points A to E are the key points for the comparison of radiographic images. The potential cyclic sweep starts from the passivation region, and point A is at the transition from passivation to activation, point B is at the highest current density during the backward sweep, point C is at the reversing potential, point D is at the highest current density during the forward sweep, and point E is at the transition from dissolution to passivation. The corresponding images are shown in Figure 5-17b.

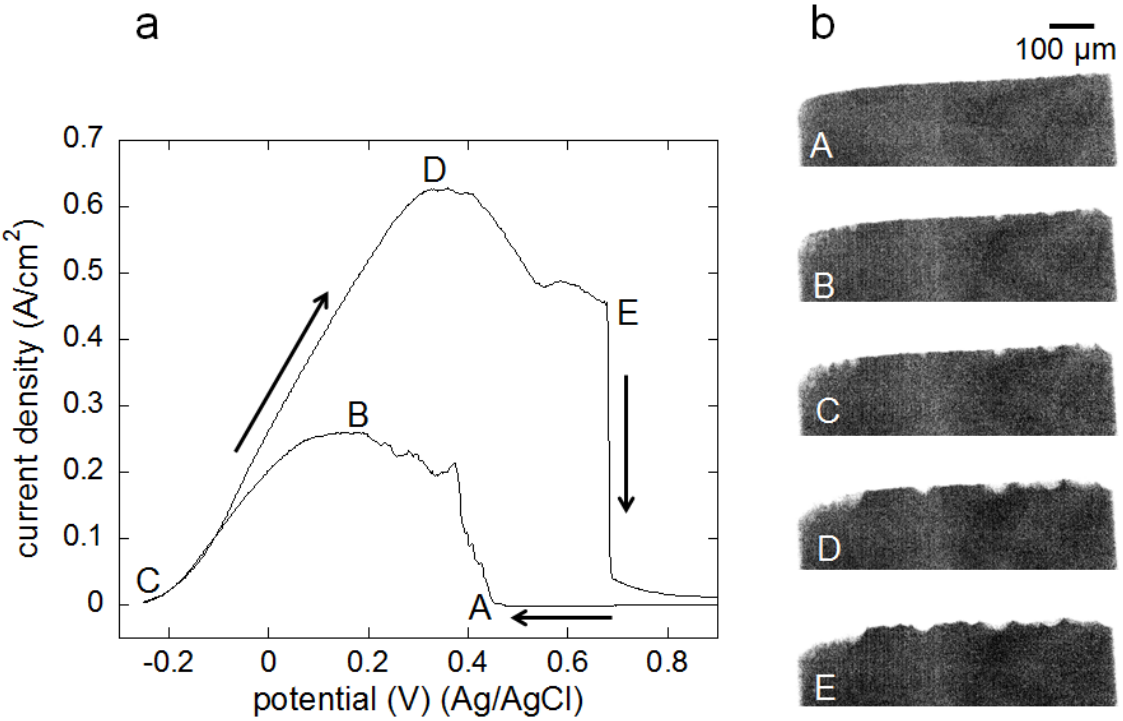

Figure 5-17. (a) A plot of current density vs. applied potential for a potential cyclic sweep (10 mV/s) on a high purity (99.99+%) iron foil (25 µm) artificial pit in 0.1 M $NaNO_3$+0.05 M HCl during *in-situ* X-ray radiography experiments, the potential was swept between 0.9 V and -0.25 V(Ag/AgCl) starting from 0.9 V(Ag/AgCl), pit depth ca. 300 µm; (b) The radiographic images corresponding to points A to E in (a).

As described above, an image calculation (subtraction) procedure can be carried out to manifest the difference between two points. All of the "difference" images have been calculated by subtracting the first image of the sweep taken at 0.9 V(Ag/AgCl) as shown in Figure 5-18a, and the images A to E correspond to the A to E in Figure 5-17b respectively. The greyscale value of the pixels along the blue line in Figure 5-18a is plotted as a function of distance in pixels in Figure 5-18b. The high greyscale value corresponds to the region where the metal has dissolved, and the drop in greyscale value corresponds to the metal surface.

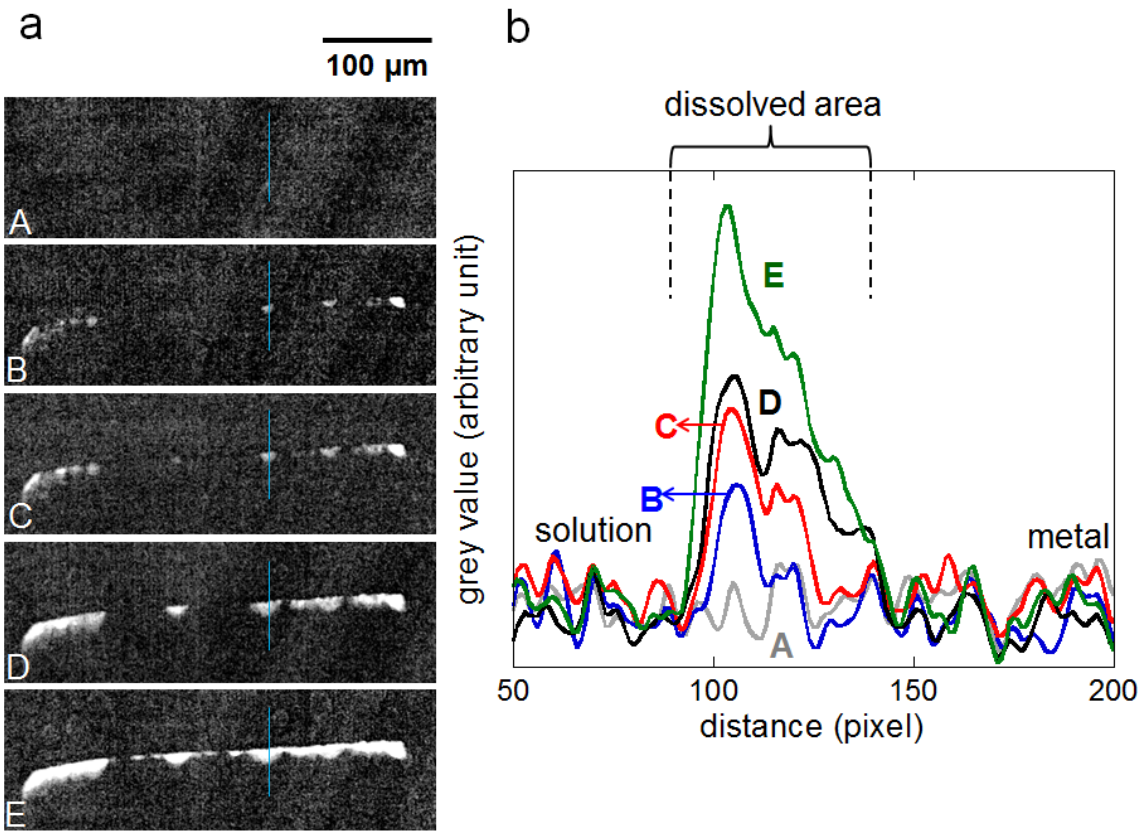

Figure 5-18. (a) "Difference" radiographs corresponding to points A to E in Figure 5-17: all the images have subtracted the first image taken at the beginning of the sweep at 0.9 V(Ag/AgCl), and the regions of metal dissolution appear bright; (b) plots of pixel grey level vs. distance in pixels along the vertical blue line on the radiographs in (a), plots A to E correspond to the images A to E in (a) respectively (pixel size ~1 µm). A high grey level in the plots corresponds to a lighter grey level in the images, indicating metal loss. The images were smoothed (replacing each pixel on the image with the average of its 3×3 neighbourhood) twice for noise reduction.

The bright regions indicate the metal dissolution since the start of the sweep. It can be seen that from point A (transition of passivation and activation) to B, the dissolution of certain parts of the metal surface have been activated, while other parts remain passivated. This phenomenon becomes more noticeable at point D (at the highest current density on the potential forward sweep), where more than half of the interface has been activated. Until point E, which is the transition from dissolution to passivation, some areas on the metal surface still remain passivated compared to the start of the cyclic sweep. Figure 5-18b indicates that the

thickness of the metal is not uniform along the blue line. Similar plots for other activated areas (not shown) give results similar to Figure 5-18b. It can be seen that the shape of attack is a crevice that gradually grows deeper and wider. The peak height increases during the scan, indicating that more of the metal is removed at the level of the top of the metal, and the greyscale value decreases deeper into the crevice as a lower fraction of the foil cross section has been dissolved.

Full ac impedance spectra (amplitude 10 mV) of the artificial pit measured at potentials of 0.2 V, 0.3 V, 0.4 V, 0.5 V and 0.6 V(Ag/AgCl) (before passivation) determined that the capacitive component of this system is close to zero at the frequency 30 to 50 kHz (see Figure 9-4). The electrochemical test described in Figure 5-17 was thus repeated with an ac signal at 50 kHz (amplitude 10 mV) imposed on the applied potential, so the resistance of the solution and salt layer (if any) were measured concurrently.

The current-voltage and resistance-voltage characteristics are shown in Figure 5-19a, and the plots of current density, resistance and *IR*-corrected potential vs. time are shown in Figure 5-19b. It can be seen that the *IR*-corrected potential is ca. 0.55 V(Ag/AgCl) at the transition of both passivation/activation and dissolution/passivation (see Figure 5-19b). It is also noted that the resistance starts to decrease before the dissolution/passivation transition on the potential forward sweep, which will be further studied in Section 5.2.6.

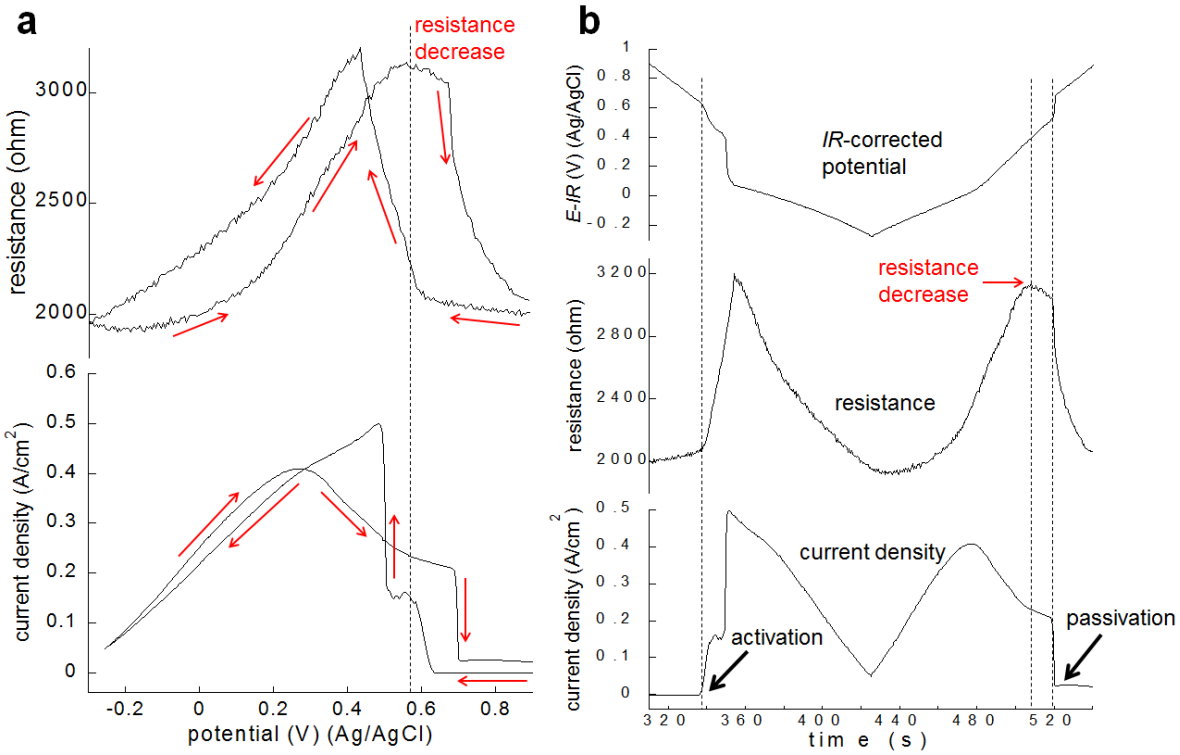

Figure 5-19. The plots of (a) current density and resistance vs. applied potential, and (b) current density, resistance and *IR*-corrected potential vs. time of a potential cyclic sweep (10 mV/s) on a high purity iron (99.99+%) foil (25μm) artificial pit in 0.1 M $NaNO_3$+0.05 M HCl, the potential swept between 0.9 V and -0.25 V(Ag/AgCl) starting from 0.9 V(Ag/AgCl), pit depth ca. 300 μm. The resistance of pit solution and salt layer (if any) were measured using an imposed ac signal (*f*= 50 kHz, amplitude 10 mV) on the applied potential.

In addition, SEM images of the electrode surface after the potential cyclic sweep are shown in Figure 5-20, where it can be seen that some very local areas of the electrode surface have been deeply attacked.

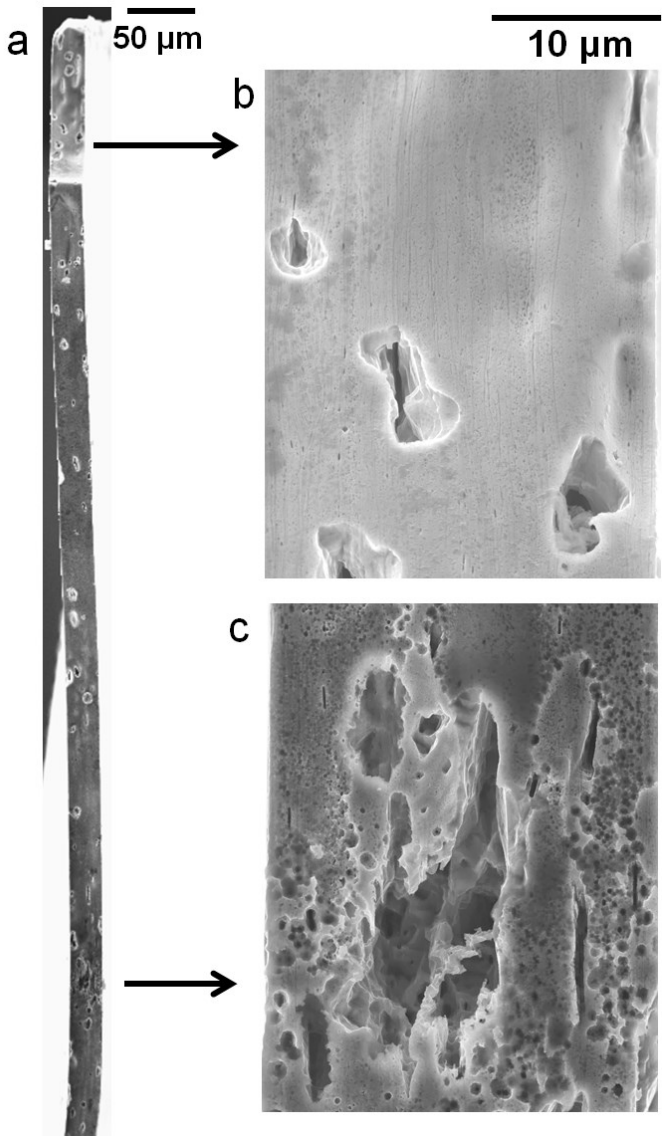

Figure 5-20. SEM images of the electrode surface of a high purity iron (99.99+%) foil (25 µm) artificial pit taken after the potential cyclic sweep described in Figure 5-19 in 0.1 M $NaNO_3$ + 0.05 M HCl. The insert (b) and (c) shows the details of (a).

5.2.6 Dissolution and passivation in nitrate/chloride solutions

To investigate the mechanism of the transition of dissolution/passivation of iron in nitrate/chloride mixed solutions (Section 5.2.5.2), a high purity (99.99+%) iron wire (250 µm) artificial pit has been used. The pit had been grown in 1 M HCl at 1 V(SCE) for 1 hour and the pit depth was ca. 300 µm. The HCl solution was then removed and replaced with 0.1 M $NaNO_3$ + 0.05 M HCl. The potential swept between 1 V and -0.2 V(SCE) at 2 mV/s, starting

from 1 V(SCE). Full ac impedance spectra (100 kHz to 10 Hz, amplitude 10 mV) of the artificial pit measured at potentials 0.2 V, 0.3 V, 0.4 V, 0.5 V and 0.55 V(SCE) determined that the capacitive component is close to zero at the frequency 10 kHz to 40 kHz (not shown). Thus a 30 kHz ac signal (amplitude 10 mV) was imposed on the applied potential to measure the resistance of solution and salt layer (if any). The current-voltage and resistance-voltage characteristics are shown in Figure 5-21a, and the plots of current, resistance and *IR*-corrected potential vs. time are shown in Figure 5-21b. It can be seen that the resistance also starts to decrease before the passivation (as shown in Figure 5-19). In addition, the *IR*-corrected potential is ca. 0.5 V(SCE) at the transition of both passivation to activation and dissolution to passivation, which is close to the results shown in Figure 5-19 (0.55 V vs. Ag/AgCl).

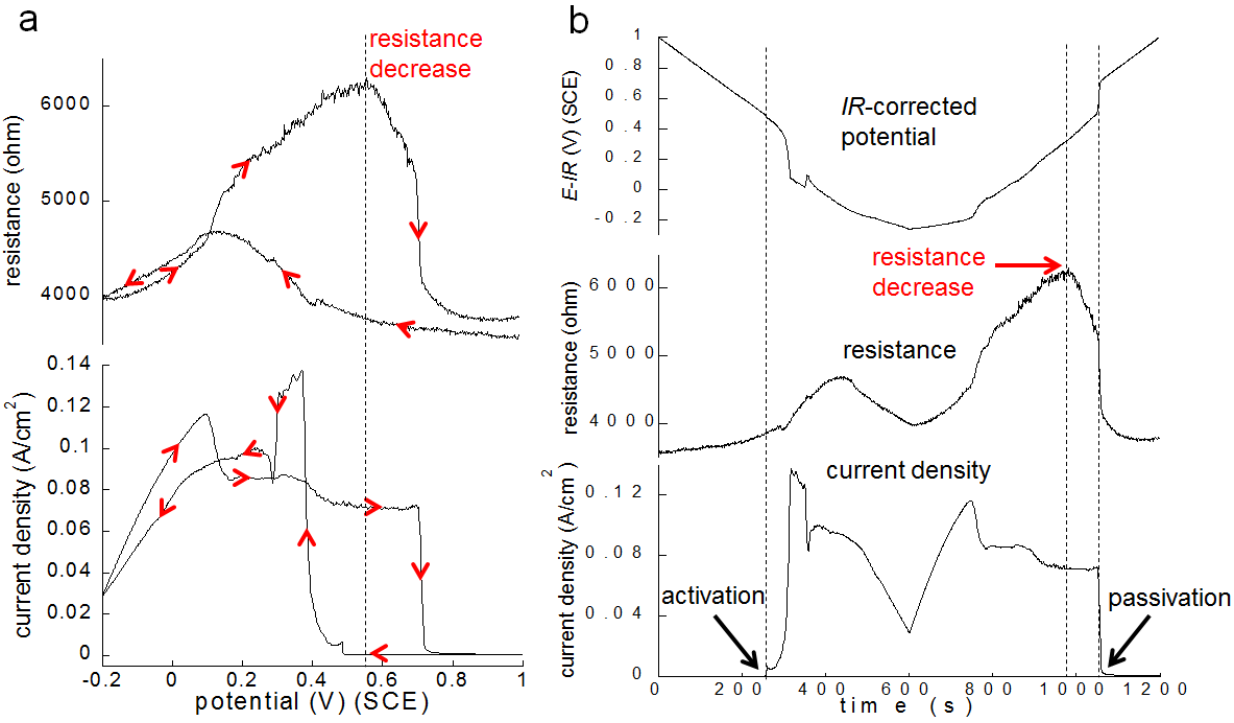

Figure 5-21. Plots of (a) current density and resistance vs. applied potential, and (b) current density, resistance and *IR*-corrected potential vs. time of a potential cyclic sweep (2 mV/s) on a high purity iron (99.99+%) wire (250 μm) artificial pit in 0.1 M $NaNO_3$+0.05 M HCl, the potential swept between 1 V and -0.2 V(SCE) starting from 1 V(SCE), pit depth ca. 300 μm. The resistance of solution and salt layer (if any) was measured using an imposed ac signal (*f*= 30 kHz, amplitude 10 mV).

Since it was noted that the transition from dissolution to passivation during the potential forward sweep is at the applied voltage ca. 0.7 V(SCE), but the resistance starts to decrease at the applied voltage ca. 0.55 V(SCE), potentiostatic measurements at voltages near the dissolution/passivation transition were carried out at 0.55 V and 0.6 V(SCE) in sequence. The experiment was carried out after the potentiodynamic sweep shown in Figure 5-21 with an initial step to 0.2 V(SCE) to reactivate the metal surface. The plots of current density, resistance (measured using an imposed ac signal at 30 kHz, amplitude 10 mV) and *IR*-corrected potential vs. time during the potentiostatic measurements are shown in Figure 5-22.

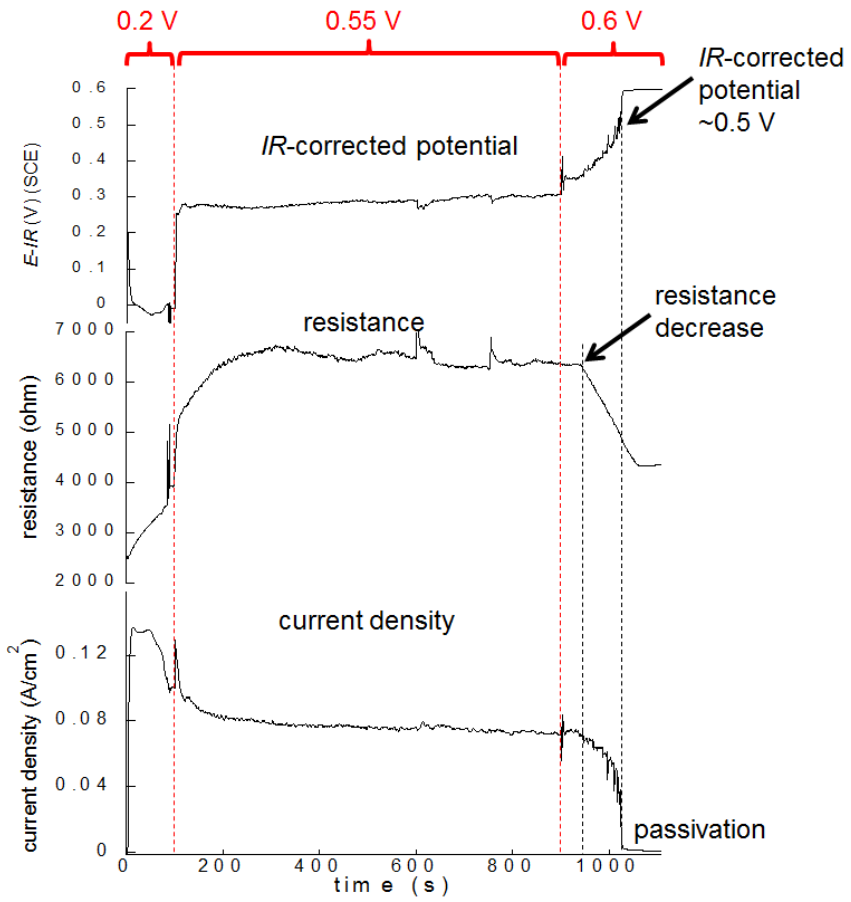

Figure 5-22. Plots of current density, resistance and *IR*-corrected potential vs. time during potentialstatic measurements on a high purity (99.99+%) Fe wire (250 μm) artificial pit in 0.1 M $NaNO_3$+0.05 M HCl at applied voltages of 0.55 V and 0.6 V(SCE). The resistance was measured using an imposed ac signal at 30 kHz (amplitude 10 mV) on the applied potential. The measurement followed the one shown in Figure 5-21, with an initial application of 0.2 V(SCE) for 100 s to initiate dissolution.

The dissolution was reactivated at 0.2 V(SCE) in the beginning, and potential was stepped to 0.55 V(SCE), at which the dissolution was stable at 0.08 A/cm^2 within ca. 14 min. However, when the applied potential was stepped up to 0.6 V(SCE), the iron surface passivated in 2 min, during which the current fluctuated before the complete passivation, and the metal surface completely passivated when the *IR*-corrected potential was ca. 0.5 V(SCE), which agrees with the potentiodynamic measurement described above (see Figure 5-21). In addition, the resistance also started to decrease before complete passivation.

5.3 Discussion

5.3.1 Effect of nitrate on salt layers

In 1 M HCl with and without the presence of trace $NaNO_3$, the salt layers have been found to be predominantly $FeCl_2.4H_2O$ with no evidence for a nitrate-containing phase. However, the addition of nitrate induced anisotropy within the salt layer. It is likely that nitrate affects the growth of the iron chloride phase by preferentially adsorbing on certain crystal planes which changes the crystal growth morphology. Thus diffracted X-ray from certain planes is weakened or even disappears at some regions of the diffraction rings, and the diffracted X-ray for other planes is enhanced.

5.3.2 Stability of carbon-containing species in artificial pits

Since the carbon content of the 99.5% Fe foils studied here is ca. 0.1%wt. (see Section 3.1), the carbon exists within the metal as interstitial carbon atoms and/or carbides. Table 5-4 compares the present work with previous work regarding the stability of carbides in chloride- or nitrate-containing electrolytes, and it agrees with [59, 159, 187], in which the *IR* drop

should be negligible. However, Cron [162] found different results on the same steel surface at -0.1 V(Ag/AgCl) in HNO_3 (pH 4).

Table 5-4. Comparison of the present work and previous work on the potential range for carbides dissolution or passivation (potentials all reported on the Ag/AgCl scale, the SCE scale was converted to the Ag/AgCl scale by adding 50 mV [17])

	in chlorides	in nitrate-containing solutions	comments
present work	-0.1 V, passive; 0 to 0.2 V, dissolved	-0.1 to 0.2 V, passive	99.5% Fe artificial pits in acidic chloride or nitrate/chloride mixed solutions (pH ~0), potential was *IR*-corrected. XRD technique.
Poulson [159]	-0.45 to -0.2 V passive	-0.4 to 1.2 V, passive	Little carbide dissolution appeared during carbon steel crack propagation in boiling solutions of 45%$MgCl_2$ or 4 M NH_4NO_3 at all voltages (voltages other than the values on the left were not studied). SEM images showed black products, assumed to be carbides.
Haisch [59]	-0.2 to 0.05 V passive; above 0.15 V, dissolved	no test	Fe_3C was anodically polarised in 20%NaCl, current density very low between -0.2 V and 0.05 V, but increased to 0.1 A/cm^2 above 0.15 V.
Hamelmann [187]	-0.4 to -0.1 V passive; above 0 V, dissolved	no test	Fe_3C microparticle (200 μm) on a gold sheet polarised in 20% NaCl. Current below 1 μA between -0.4 V and -0.1 V (negative current below -0.4 V), increased to >5 μA above 0 V.
Cron [162]	-0.4 V, -0.7 V passive; -0.1 V, dissolved	0.5 V, -0.7 V, passive; -0.1 V, passive or dissolved	Carbon steel in HCl or HNO_3 (pH=4). At -0.1 V in HNO_3, carbides were totally dissolved in one region but not in other regions on the same surface. SEM images showed black products, assumed to be carbides.

The equilibria of Fe_3C-water system at 25 °C have been determined (the Gibbs free energy of formation ΔG^0 of Fe_3C has been reported by Browning et al. [188], and the ΔG^0 of other iron

and carbon species has been reported by Pourbaix [189]) to compare with the equilibria of carbon and Fe [189]. The E-pH diagram has been constructed as shown in Figure 5-23, and the log terms, e.g. log[Fe^{2+}] and log[$P(CO_2)$], are assumed to be zero (the potentials in corresponding equilibrium equations are on the SHE scale; the potentials on the diagram are converted to the Ag/AgCl scale by subtracting 0.2 V from the SHE scale [17]).

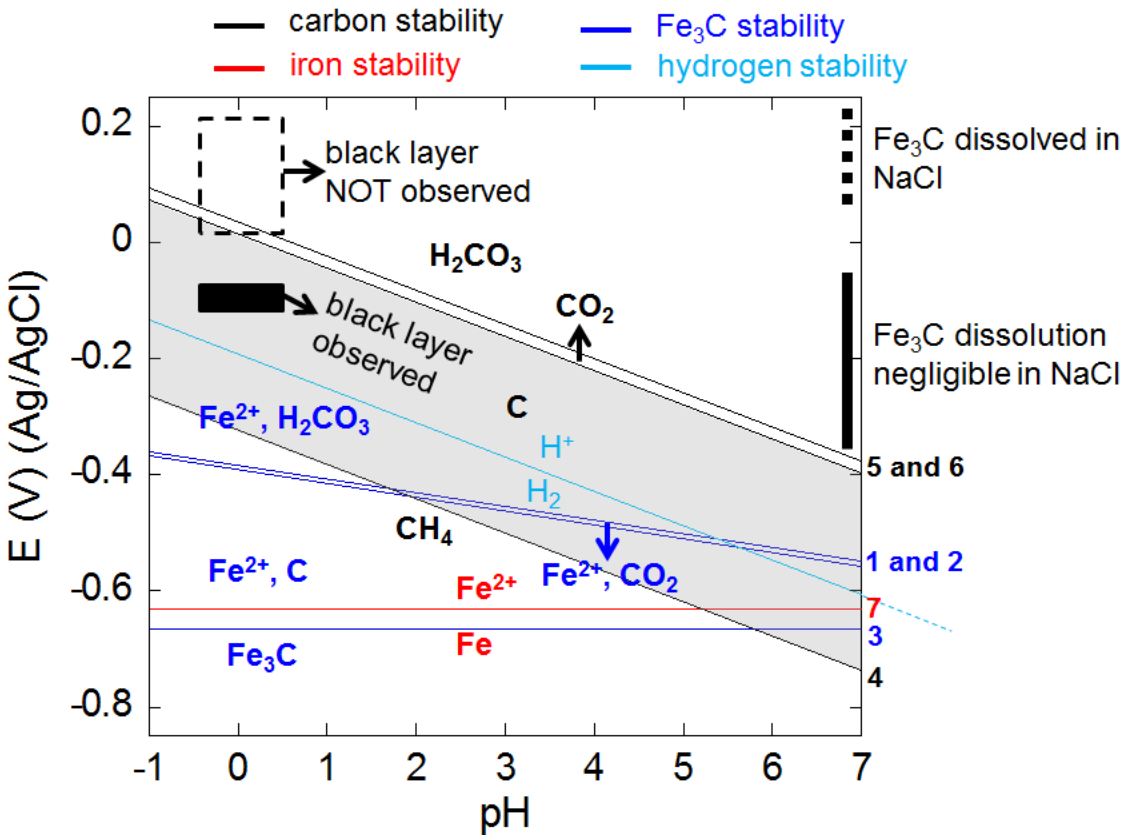

Figure 5-23. E-pH diagram for the Fe_3C-water, Fe-water and carbon-water system (pH between -1 and 7) at 25 °C derived from the Gibbs free energy ΔG^0 of Fe_3C [188] and the other iron and carbon species [189]. The black box represents the potential where black layer has been observed in the iron foil artificial pit in HCl, and the empty box represents the potentials where black layer has not been observed. The vertical black solid line and dashed line at pH 7 represent the potential regions where anodic dissolution of Fe_3C in NaCl was found negligible and noticeable respectively according to [59, 187]. The region where solid carbon is stable (according to Pourbaix [189]) is marked in grey shadow.

1. $Fe_3C + 3H_2O = 3Fe^{2+} + H_2CO_3 + 4H^+ + 10e^-$

$E = -0.192 - 0.0236pH + 0.0059\log[H_2CO_3] + 0.0177\log[Fe^{2+}]$,

2. $Fe_3C + 2H_2O = 3Fe^{2+} + CO_2 + 4H^+ + 10e^-$

$E = -0.200 – 0.0236pH + 0.0059\log[P(CO_2)] + 0.0177\log[Fe^{2+}]$,

3. $Fe_3C = 3Fe^{2+} + C(s) + 6e^-$ $E = -0.472 + 0.0295\log[Fe^{2+}]$,

4. $CH_4 = C + 4H^+ + 4e^-$ $E = -0.132 – 0.0591pH – 0.0148\log[P(CH_4)]$,

5. $C + 2H_2O = CO_2 + 4H^+ + 4e^-$ $E = 0.207 – 0.0591pH + 0.0148\log[P(CO_2)]$,

6. $C + 3H_2O = H_2CO_3 + 4H^+ + 4e^-$ $E = 0.228 – 0.0591pH + 0.0148\log[H_2CO_3]$,

7. $Fe = Fe^{2+} + 2e^-$ $E = -0.440 + 0.0295\log[Fe^{2+}]$.

The voltage at which the Fe_3C/carbon-containing black layer was observed in the iron artificial pit in HCl is marked in the E-pH diagram; it is assumed that the pH at the metal surface is between -0.5 and 0.5. From Figure 5-23, the dissolution of Fe_3C should take place near the voltage where iron dissolves. This does not correlate with the XRD results, which show Fe_3C at -0.1 V(Ag/AgCl) in HCl, or visual observations, which show black layers also at -0.1 V(Ag/AgCl). However, the dissolution of Fe_3C in NaCl has also been found to be negligible at voltages below ca. -0.05 V(Ag/AgCl), while the dissolution rate increases noticeably at voltages above ca. 0.05 V(Ag/AgCl) during the anodic polarisation of both Fe_3C substrate [59] and Fe_3C microparticles [187] (see Figure 5-23). Therefore it is likely that the dissolution of Fe_3C is controlled by a kinetic process, and the overvoltage has to be sufficiently positive so that the dissolution of Fe_3C is noticeable. When the overvoltage is not sufficient, the dissolution of Fe_3C is at such a low rate that it is not comparable to the dissolution rate of rapidly dissolving iron electrode, and Fe_3C will be detached from the metal surface before it is able to be completely dissolved, thus left in the solution. In contrast, Fe_3C will dissolve in a much higher rate at higher overvoltages, which agrees with the observation

that most but perhaps not all of Fe_3C were dissolved in 1 M HCl at applied voltage 1 V(Ag/AgCl) (*IR*-corrected potential ca. 0.2 $V_{Ag/AgCl}$), and only very few and weak peaks in the averaged pattern collected in solution may be correlated with Fe_3C (see Figure 5-6). It is interesting that detached particles of Fe_3C are observed in the electrolyte, and according to Figure 5-23, Fe_3C may dissolve slowly at a pH of 0, evolving hydrogen.

It has been proposed that the carbon layer outside Fe_3C may retard further dissolution of Fe_3C [162]. It can be seen from Figure 5-23 that the thermodynamic potentials of carbon oxidation (C/CO_2 and C/H_2CO_3) are consistently higher than that of Fe_3C oxidation (Fe_3C/CO_2 and Fe_3C/H_2CO_3) at pH ~0. Furthermore, carbon is stable between ca. -0.3 V and 0 V(Ag/AgCl) at pH of 0 (see Figure 5-23), which agrees with the potential range where the Fe_3C-containing black layer was observed. Since it has been reasonably concluded that the black layer is a mixture of disordered carbon and Fe_3C (see Section 5.2.3), a carbon layer may be protective to Fe_3C.

In the presence of nitrate, the dissolution of Fe_3C/carbon may be inhibited via competitive adsorption between nitrate and chloride [97], so Fe_3C is not attacked by chloride and has been found via *in-situ* synchrotron XRD at all voltages in this work.

In addition to the black corrosion products, bubbles are visible in the artificial pit in HCl (see Figure 5-1). Since the interfacial potential was less than 0.1 V(SHE) at the applied voltage 0.1 V(Ag/AgCl) (see Figure 5-2), which was close to the thermodynamic potential of hydrogen evolution reaction (HER) [189], the bubbles may be H_2. However, more bubbles have been observed after the addition of nitrate even at high voltages, which may also consist of NO_x: the products of nitrate reduction [91]. Li [3] also found bubbles in the vicinity of

anodically polarised steel at voltages above the HER potential and believed that it contained nitrogenous gases.

5.3.3 Effect of nitrate on electrochemistry

Figure 5-2 shows that nitrate ions induce current fluctuations during the dissolution of an Fe artificial corrosion pit, and the fluctuation is greater at higher voltages. The nitrate electroreduction reaction is feasible at all voltages in this work, which consumes protons and produces water, and may favour localised or partial passivation on the iron surface by increasing the pH. Newman and Ajjawi [35] and Kolman et al. [121] also ascribed the passivation of stainless steel to the nitrate reduction reaction. However, the protons, once consumed at some local sites, would be replenished from other areas if the reaction rate of nitrate reduction is low, so stable passivation is not observed for iron in mainly HCl solutions, instead, the "passivated" sites would be reactivated and covered by salt again.

At higher applied voltages, the salt layer is thicker [26, 34] and may be less acidic at the metal surface [28]. The diffusion length (within salt layer) for protons is greater, and they may need a longer time to diffuse to the "passivated" sites on the metal/salt interface and destroy the passivity. This local site then undergoes supersaturation and salt precipitation, resulting in current fluctuations. However, at lower applied voltages, the salt layer is thinner and protons are more able to prevent local passivation even though nitrate still tends to disfavour dissolution of local sites. Therefore the surrounding solution can remain saturated with metal ions, and salt can precipitate immediately at the sites once dissolution is reactivated, supersaturation may not be necessary, so the current fluctuations are not observed.

Ma [130] described nitrate as a "passivating agent" and has suggested that the competition between "passivating action" of nitrate and "depassivating action" of chloride resulted in the

formation/dissolution of ferrous salt layer and oxide film, which led to current oscillations during dissolution of iron. According to the mechanism described above, the current fluctuation in the present work should also involve the formation and dissolution of a salt layer and passive film at local sites.

5.3.4 Surface morphology of the "artificial pit"

Hoar [25] suggested that a film of high ionic conductivity suppressed crystallographic dissolution, because "asperities" dissolve faster and "valleys" dissolve more slowly (see Section 2.6). This appears to be the case for HCl in the absence of nitrate, which is independent of the microstructure of the metal. In the presence of nitrate, however, the pit surface was non-uniformly dissolved and crystallographically etched, which depends on the microstructure (see the EBSD maps in Figure 5-11). Various papers have reported crystallographic etching of iron alloys at relatively low potentials [72, 75, 76, 79], or during active dissolution which was not under mass transport control (i.e. salt-free) [10, 78, 85]. However, in this case, an ionically-conductive salt layer is clearly present for the dissolution in chloride/nitrate solutions, and crystallographic etching (see Figure 5-11) seems surprising. It has been reported that certain crystallographic planes may dissolve preferentially [87] or in a higher rate than other planes [86], which implies that some planes may be more active/inactive. So it is possible that the dissolution of certain crystallographic planes is disfavoured more easily as a result of the local/partial passivation in the presence of nitrate.

5.3.5 Dissolution behaviour of iron artificial pits

5.3.5.1 In pure HCl

It is shown that both the surface roughening of iron and crevice formation between iron and epoxy resin take place during active dissolution under salt-free conditions, especially for high-rate dissolution (see Section 5.2.5.1).

Surface roughening during the active dissolution (salt-free) has been reported on stainless steel [37] and Ni [52] artificial pits in chloride solutions, which can be ascribed to the absence of an ionically conductive film (see Section 2.6). The surface morphology (see Figure 5-16) may be correlated with the microstructure of metals.

For crevice formation, it is seen that the current density is ~60%i_{lim} at the reversing potential (see Figure 5-14). According to Fick's first law (Equation 2-6), the current density i is proportional to $D\Delta C$ at a fixed pit depth x, where D is the diffusivity of metal ions and ΔC is the difference in metal ion concentration between the pit bottom and the pit mouth. In fact, a decrease of i results in a decrease of C. When the current density decreased to ~60%i_{lim}, the pit solution was diluted, and the diffusivity D increased, so the metal ion concentration at the pit bottom decreased to below 60%C_{sat}, at which condition a pit may not remain active, and partial passivation may take place. Thus, when potential was reversed/increased, the dissolution was driven to a high rate, and the crevice formation may have to contribute to the dissolution if the partially passivated surface could not.

In contrast, when the potential was raised to return the dissolution to the diffusion-limited region, the crevice was dissolved gradually, because the dissolution is faster at "asperities" and slower at "valleys" [70] and the metal surface tends to dissolve uniformly. The effect of the microstructure on the surface morphology is negligible. In addition, since the hysteresis of

reversing of current at the potential reversing point in Figure 5-14 was not observed in Figure 5-16a, less obvious partial passivation is expected for the work shown in Figure 5-16a, and the effect of metal thinning should also be less compared to Figure 5-15b.

5.3.5.2 In nitrate/chloride

In the case of iron dissolution in nitrate/chloride mixed solutions, the resistance started to decrease before the complete passivation of iron surface. Since a salt layer has been detected in mainly nitrate solutions, which has been characterised to be composed of $Fe(NO_3)_2.6H_2O$ at an applied voltage of 0.55 V(Ag/AgCl) (see Section 5.2.2), the passivation was very likely to take place under the salt layer. Some of the areas that have been activated during the cyclic sweep (other areas remain passivated during the course of the cyclic sweep) may start to partially repassivate under the salt layer from the point where the resistance started to gradually decrease (in the potential forward sweep). The passivation of iron under a salt layer has been reported in H_2SO_4 and $HClO_4$ solutions [28], which is ascribed to the decreasing acidity with the increasing potential or increasing thickness of a salt layer, because protons are transported away (by electric field) from the metal surface via the pores within the salt layer. Furthermore, it was suggested that the change of pH increased proportionally with the increasing *IR* drop (electric field) across the salt layer. It is proposed in this work that the similar passivation behaviour of iron under a salt layer may also take place in nitrate/chloride solutions, and the decrease of acidity may also result from the proton-consuming nitrate reduction reaction [35] in addition to the proton transport. The passivation is very likely to be a gradual process, since the iron was not completely passivated until ca. 2 min after the potential was stepped from 0.55 V to 0.6 V(SCE) (see Figure 5-22). On the potential reverse sweep, the oxide film Fe_2O_3 would dissolve only below a certain potential (see the Pourbaix diagram of Fe [189]), which results in the passivation/dissolution transition.

In addition, it has also been found that the transition of dissolution/passivation during the potential forward sweep is at ca. 0.5 V(SCE) (see Figure 5-21 and Figure 5-22), which is close to the Fe^{2+}/Fe^{3+} redox potential [189], and a small amount of Fe^{3+} may be generated. As described in Section 2.7.3, it has been reported that a small amount of oxidising cations Fe^{3+} may catalyse the reduction of HNO_3 [91, 93, 133-135]. It is possible that a small amount of Fe^{3+} generated at ~0.5 V(SCE) is able to accelerate the nitrate reduction reaction, so that the pH is increased, which favours passivation on the metal surface. However, much more work has to be carried out to investigate the feasibility of this mechanism.

5.4 Conclusions

The effect of nitrate on dissolution of iron in artificial pits in chloride-containing solutions has been investigated with *in-situ* synchrotron X-ray diffraction and radiography, and *ex-situ* Raman spectroscopy.

- In 1 M HCl with and without trace nitrate, the salt layer is $FeCl_2.4H_2O$. However, in the presence of nitrate, the salt becomes anisotropic, consistent with the formation of plate-like (1 2 0) crystallites.
- In 1 M HCl at 0.1 V(Ag/AgCl), commercial purity iron undergoes dissolution with a layer of $FeCl_2.4H_2O$ on its surface, leaving a black layer that contains Fe_3C and disordered carbon further out in the electrolyte. Above 0.1 V(Ag/AgCl), no black layer is observed, and most of Fe_3C has been dissolved due to the increase of dissolution rate of Fe_3C at higher overvoltages.
- The addition of trace nitrate to 1 M HCl inhibits the dissolution of Fe_3C and carbon-containing black layer at all voltages.

- In 0.1 M HNO_3 with trace chloride, the salt layer is composed of $Fe(NO_3)_2.6H_2O$.
- In 1 M HCl with trace nitrate, current fluctuations develop, which increase with increasing potential.
- In 1 M HCl in the absence of nitrate, the electrode surface is slightly roughened, consistent with the dissolution under a salt layer; in the presence of trace nitrate, the electrode surface becomes crystallographically etched under a salt layer.
- Surface roughening and crevice formation between metal and epoxy resin of an iron artificial pit may take place during high-rate active dissolution in the absence of a salt layer, because iron may be partially passivated when the dissolution rate or concentration of metal ions is low, but the metal surface tends to level when dissolution is diffusion-controlled and a salt layer is present.
- In 0.1 M $NaNO_3$ + 0.05 M HCl, a dissolution/passivation transition appears when the potential is swept to ~0.7 V(Ag/AgCl) during a forward potentiodynamic sweep in an iron artificial pit, which is likely to be ascribed to the oxide passivation under a salt layer. The dissolution can be reactivated below a certain potential where the oxide film Fe_2O_3 cannot be stable. The partially passivated surface favoured very localised and deep attack on the electrode.

6. THE DIFFUSIVITY OF METAL IONS AND TAFEL KINETICS OF IRON ARTIFICIAL PITS

6.1 Introduction

The diffusivity of metal ions has been studied in artificial corrosion pits during diffusion-controlled dissolution, but most of the work in literature has only reported the diffusivity for chloride concentration of 1 M or less, and these values do not agree very well [20, 21, 33, 37, 58]. It describes the mass transport in pit solutions, which are a mixture of bulk solution components and metal salt electrolytes. In this study, the effective diffusion coefficient of metal ions in artificial pits in different concentrations of $MgCl_2$ has been calculated and compared with the self-diffusivity calculated via simulation software OLI Analyser Studio v9.0 (see Section 3.5).

The Tafel kinetics of iron artificial pit dissolution in chloride solution near metal ion saturation concentration have also been investigated using different methods: potential step/potentiostatic method [20, 37, 53, 54], transition potential method [39], and potentiodynamic method in ohmic-control region [67], the last two of which have been used in this study. This work also introduces a new method: the galvanodynamic method, which controls the current to maintain a near-saturation concentration. To minimise the effects of the corrosion products investigated in Chapter 4, high purity (99.99+%) Fe wire artificial pits were used for various chloride concentrations.

6.2 Results

6.2.1 Diffusivity of metal ions

Different diameters of high purity (99.99+%) iron wire (130 μm and 250 μm) artificial pits were prepared in six concentrations of $MgCl_2$ (0.01 M, 0.1 M, 0.5 M, 1 M, 2 M and 3 M) at 0.6 V(SCE), at which the dissolution was under diffusion-control. To simplify calculations, an average diffusivity was assumed for each chloride concentration [20, 30, 37, 58]. The pit depth was calculated via the charge passed (Equation 2-7), and was found to agree well with the optically measured pit depth.

6.2.1.1 "*ix*" value

As described in Chapter 4, the diffusion-limited current density is linear with inverse pit depth after the pit reaches a sufficient depth so that the diffusion of metal ions at the pit mouth is negligible; this pit depth is called the "appropriate pit depth" in this chapter. Figure 6-1 shows the dependence of current density on inverse pit depth for Fe wire artificial pits of two diameters (130 μm and 250 μm) in 0.5 M $MgCl_2$, and the "appropriate pit depth" is marked for each. Before this depth is reached, the diffusion around the pit mouth is significant.

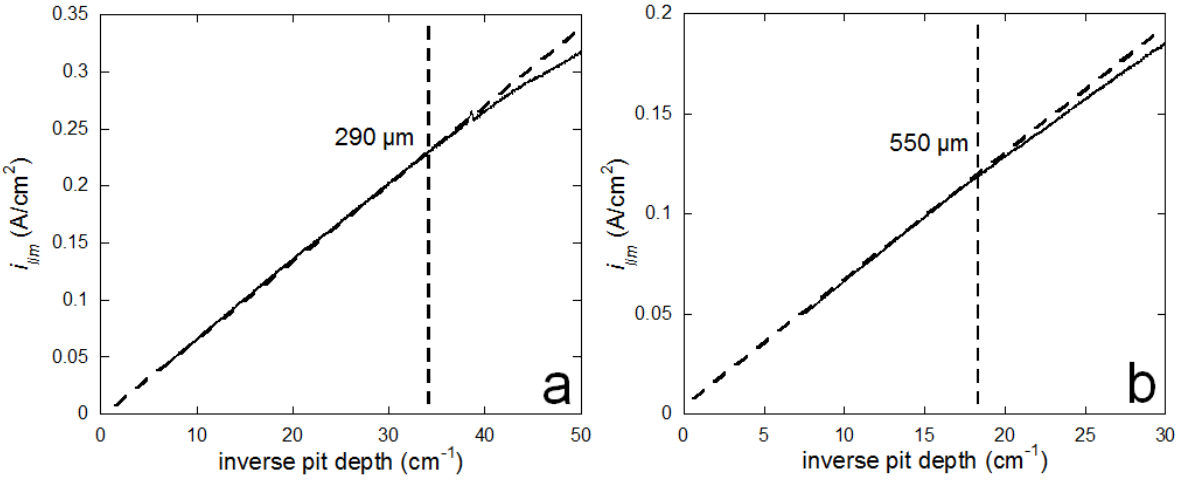

Figure 6-1. Diffusion-limited current density plotted vs. inverse pit depth for (a) 130 µm and (b) 250 µm diameter Fe wire artificial pits in 0.5 M $MgCl_2$, the "appropriate pit depth" is marked by vertical dashed line for each.

A more sensitive method is to plot "*ix*" vs. *x* (*i* is current density, *x* is pit depth) as shown in Figure 6-2. It can be seen that the "*ix*" value levels off after the pit reaches the "appropriate pit depths" 300 µm and 620 µm for the 130 µm and 250 µm diameter pits, respectively.

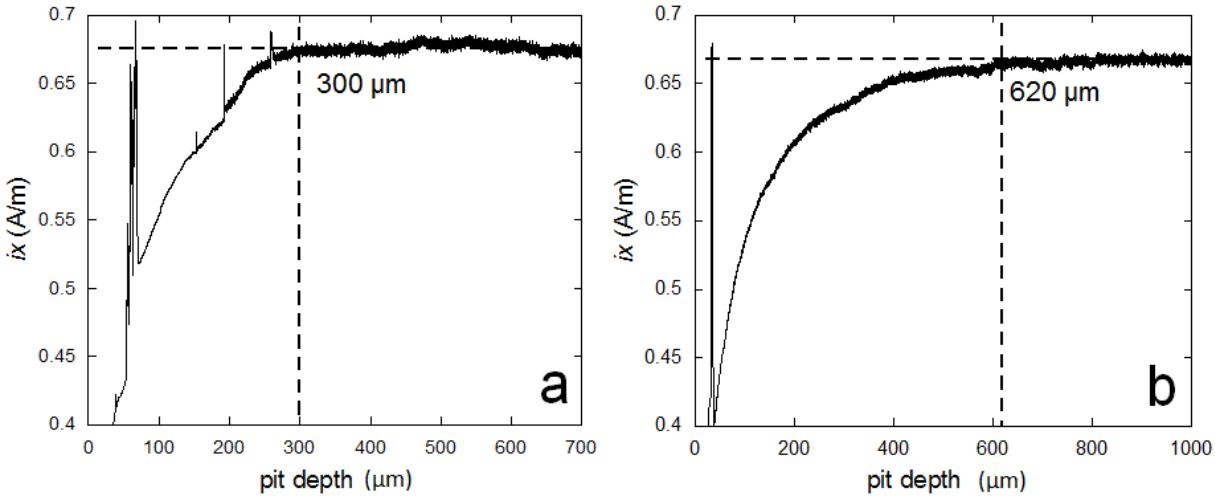

Figure 6-2. "*ix*" value plotted vs. pit depth for (a) 130 µm and (b) 250 µm diameter Fe wire artificial pits in 0.5 M $MgCl_2$. The "appropriate pit depth" is marked by vertical dashed lines for each.

The "*ix*" plateaux values can be used to obtain $D\Delta C$ values (D is the metal ion diffusivity, ΔC is the difference of metal ion concentration between pit bottom and pit mouth) via Equation 6-1, which is directly derived from Fick's first law (Equation 2-6). The $D\Delta C$ values after the pits reach the "appropriate pit depth" derived from Figure 6-2 are 3.50×10^{-8} mol·cm^{-1}·s^{-1} and 3.45×10^{-8} mol·cm^{-1}·s^{-1} for 130 μm and 250 μm diameter pits, respectively. This method gives $D\Delta C$ values at the steady-state, consistent with the pit stability product "*ix*" [55].

$$i = \frac{nFD\Delta C}{x} \qquad \text{Equation 6-1}$$

6.2.1.2 "x^2 vs. t"

A second method to obtain $D\Delta C$ values is via Equation 6-3, which is derived from Faraday's law (Equation 6-2) and Fick's first law (Equation 6-1),

$$m = (Q/F)(M/n) \qquad \text{Equation 6-2}$$

$$x^2 = (2M/\rho)D\Delta Ct \qquad \text{Equation 6-3}$$

where x is the artificial pit depth (which is calculated with the charge passed), M is the molar mass of Fe (56 g/mol), m is the mass of dissolved metal, ρ is the density of iron (7.87 g/cm^3), and t is the time for dissolution. Equation 6-1 and Equation 6-3 are consistent with the fact that a straight line of plot $t^{-1/2}$ vs. i indicates a diffusion control process [27].

Thus $D\Delta C$ values can be obtained from the slope of x^2 vs. t (see Equation 6-3). It should be noted that valid $D\Delta C$ values can only be obtained from the electrochemical data for pits deeper than the "appropriate pit depth". The slope of x^2 vs. t is a linear-fit as shown in

Figure 6-3. $D\Delta C$ values from the slopes in the figure are 3.50×10^{-8} mol·cm^{-1}·s^{-1} and 3.44×10^{-8} mol·cm^{-1}·s^{-1} for 130 μm and 250 μm pits, respectively.

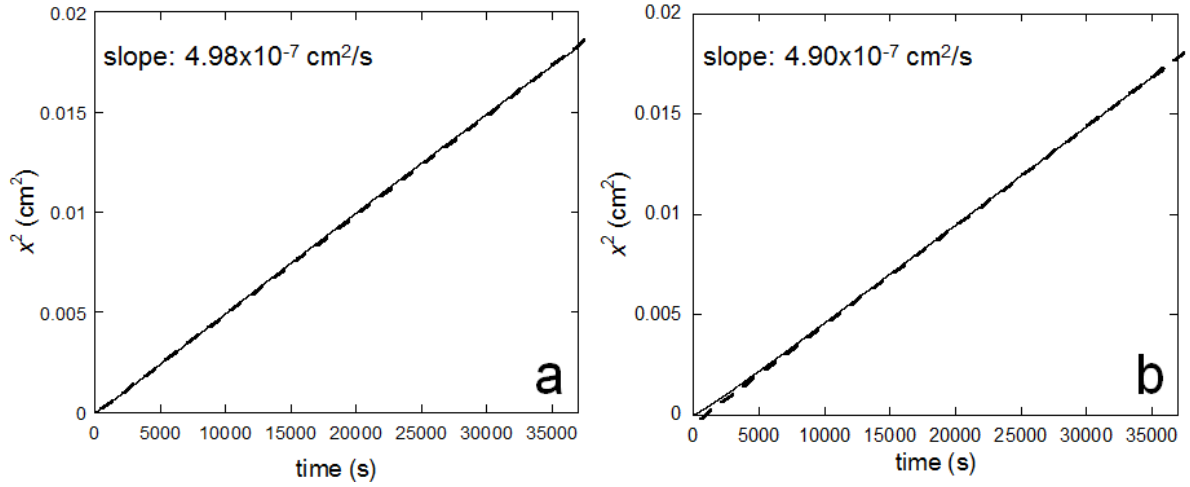

Figure 6-3. x^2 vs. t for (a) 130 μm and (b) 250 μm diameter Fe wire artificial pits in 0.5 M $MgCl_2$, the slope of x^2 vs. t is obtained with the electrochemical data after the pit reaches the "appropriate pit depth" (after ca. 3000 s and 7000 s for the 250 μm and 130 μm diameter pits, repectively).

The final pit depths in different $MgCl_2$ concentrations were all ca. 1.2 mm and each experiment was carried out three times. $D\Delta C$ values derived from the two pit diameters (130 μm and 250 μm) via the two methods are summarised in Table 6-1 and compared in Figure 6-4a. It can be seen that $D\Delta C$ values agreed well between the two methods (since the values are derived from the same electrochemical data) and two pit diameters. Chloride concentration is plotted on a linear scale in Figure 6-4b, and it is seen that $D\Delta C$ is approximately linear with chloride concentration, as found for stainless steel in [67, 190].

Table 6-1. $D\Delta C$ values of Fe wire artificial pits of 130 μm and 250 μm diameter in different $MgCl_2$ concentrations

[$MgCl_2$] (M)	$D\Delta C$ from "ix" value (10^{-8} mol·cm^{-1}·s^{-1})		$D\Delta C$ from "x^2 vs. t" (10^{-8} mol·cm^{-1}·s^{-1})	
	diameter 130 μm	diameter 250 μm	diameter 130 μm	diameter 250 μm
0.01	4.20±0.08	4.14±0.05	4.18±0.05	4.11±0.06
0.1	4.09±0.09	4.04±0.07	4.07±0.10	4.01±0.08
0.5	3.46±0.04	3.46±0.01	3.45±0.05	3.44±0.01
1	2.90±0.06	2.85±0.07	2.88±0.07	2.84±0.08
2	1.75±0.08	1.73±0.08	1.74±0.08	1.76±0.07
3	0.69±0.10	0.72±0.09	0.68±0.10	0.71±0.10

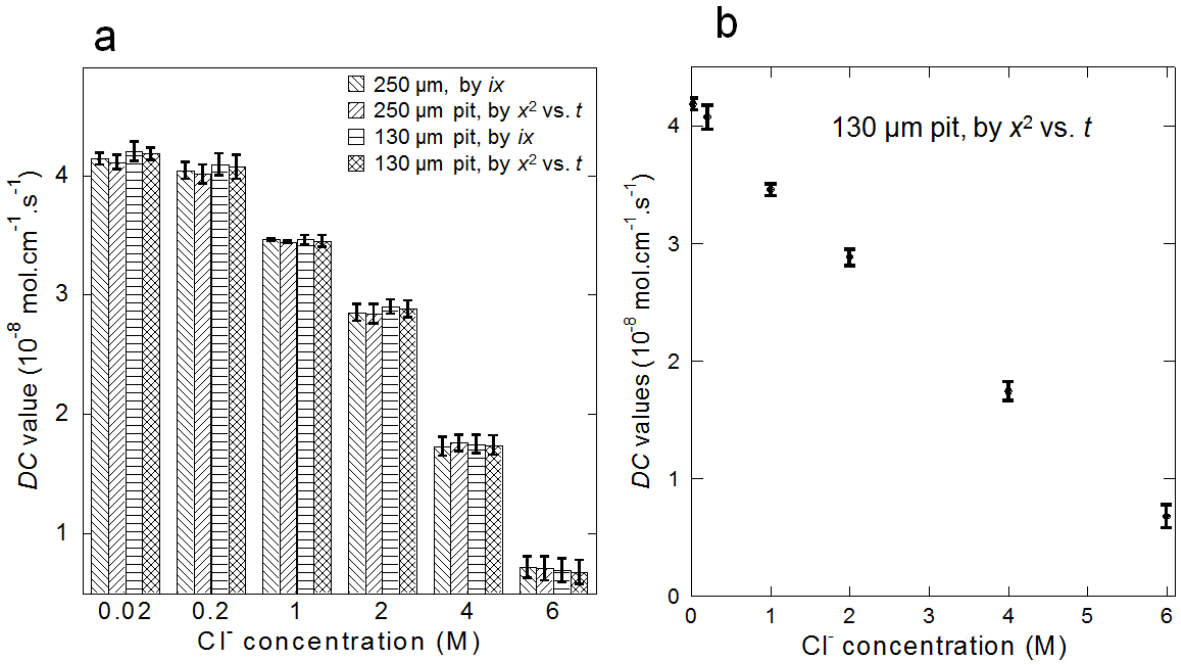

Figure 6-4. (a) Comparison of experimental data of 130 μm and 250 μm diameter Fe wire artificial pits measured with two methods in different concentrations of $MgCl_2$. (b) $D\Delta C$ values vs. chloride concentration of the bulk solution derived from the 130 μm pit via the "x^2 vs. t" method, chloride concentration on a linear scale.

For both methods, $D\Delta C$ can only be obtained as one parameter. ΔC can be regarded as the saturation concentration of metal ions (C_{sat}) if the concentration of metal ions at the pit mouth is assumed to be zero, and this assumption can only be valid after the pit reaches the "appropriate pit depth". The $FeCl_2$ saturation concentrations that have been used in literature is 4.2 M [30, 37, 53, 55, 58] and 5.0 M [21].

Figure 6-5a shows the decrease of $FeCl_2$ saturation concentration in $MgCl_2$ solution with increasing $MgCl_2$ concentration calculated using the OLI software. The $FeCl_2$ saturation concentration in pure water (when the concentration of $MgCl_2$ is zero) is 4.49 M (25 °C), which is in reasonable agreement with Kuo's measurement (4.25±0.05 M in water at 23±0.5 °C) [30].

According to Ernst and Newman [190], for concentrated $MgCl_2$ solutions with saturated $FeCl_2$, the concentration of Mg^{2+} is significant compared to the saturation concentration of $FeCl_2$, and Mg^{2+} "carries its own chloride". This is also shown in Figure 6-5b, which is derived from the same OLI calculation as Figure 6-5a. Figure 6-5b shows that the total chloride concentration includes the chloride from $MgCl_2$ solution and saturated $FeCl_2$ solution, and the value is between 8 M and 9 M for $MgCl_2$ concentration below 3 M.

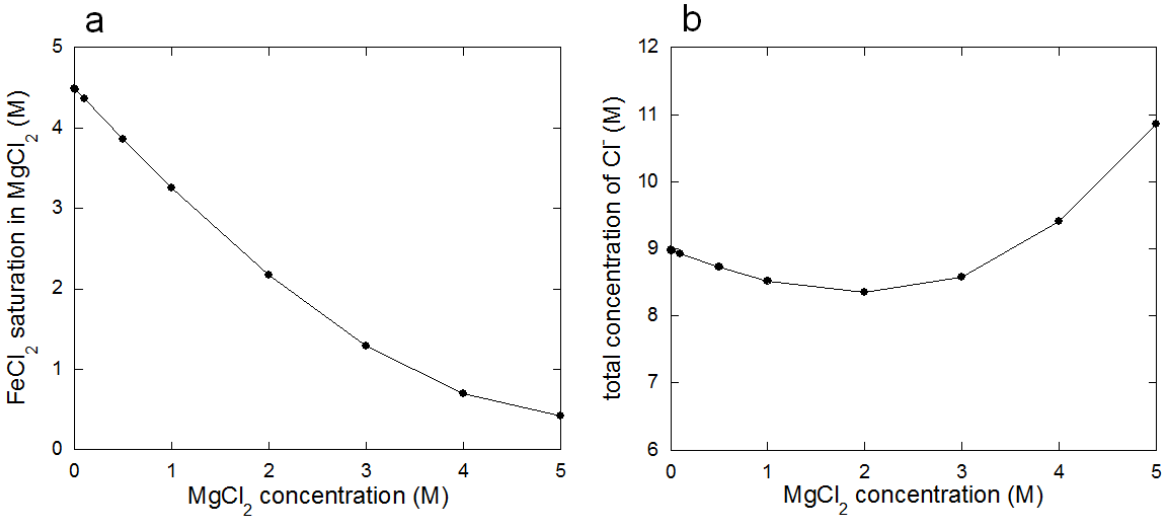

Figure 6-5. (a). Dependence of $FeCl_2$ saturation concentration in $MgCl_2$ on the $MgCl_2$ concentration calculated via OLI. (b) Dependence of total concentration of chloride (from $MgCl_2$ solution and saturated $FeCl_2$ solution) on $MgCl_2$ concentration calculated via OLI. The temperature is 25 °C.

6.2.1.3 A comparison of experimental and OLI-calculated $D\Delta C$

Since the $FeCl_2$ concentration can be regarded as saturated at the pit bottom and zero at the pit mouth after the pit reaches an "appropriate depth", ΔC equals C_{sat}. In this section, C_{sat} and D were separately obtained from OLI, and then DC_{sat} values were compared with the $D\Delta C$ values in Table 6-1. For the complex species between Fe^{2+} and Cl^-, OLI calculates the self-diffusivity of $FeCl^+$, so it is assumed that all the dissolved species are in a single form: either Fe^{2+} or $FeCl^+$, and the saturation concentration of Fe^{2+} or $FeCl^+$ is the same as the calculated saturation concentration of $FeCl_2$ (C_{sat}).

Firstly, it is assumed that the concentration of $MgCl_2$ in the pit solution is the same as in the bulk solution. The self-diffusivity of Fe^{2+} or $FeCl^+$ species was calculated via OLI based upon different approximations as follows.

Approximation (1): The pit solution is a mixture of $MgCl_2$ (with the same concentration as the bulk solution) and $FeCl_2$ with a concentration of $0.5C_{sat}$.

The diffusivity was calculated assuming that the average concentration of $FeCl_2$ in the pit solution is half-saturation (same assumption in [20]). The pit solution is assumed to be a mixture of bulk $MgCl_2$ and half-saturated $FeCl_2$ for the OLI calculation.

Since the $D\Delta C$ values obtained from the two methods for the two pit diameters agree well, Figure 6-6 compares the OLI calculation only with the $D\Delta C$ values obtained from "x^2 vs. t" for the 130 μm pit, based on the assumption that all the dissolved species are in a single form: either Fe^{2+} (Figure 6-6a) or $FeCl^+$ (Figure 6-6b). The consistently higher values found in experiments are caused by the effect of electrical migration [30, 32, 34], which becomes more significant with increasing chloride concentrations. The self-diffusion accounts for ca. 50% of the effective diffusion in 0.01 M $MgCl_2$, decreasing to less than 40% in 3 M $MgCl_2$. In

addition, it is found from the ratio between the OLI calculation and the experimental data that the effect of self-diffusion for $FeCl^+$ is slightly less than for Fe^{2+}. Since C_{sat} is the same for both species, the difference is due to that the diffusivity of $FeCl^+$ is smaller than that of Fe^{2+}. This is reasonable if it is assumed that the volume of a complex equals the sum of volumes of its constituent components [151], so the species with a larger size diffuses more slowly.

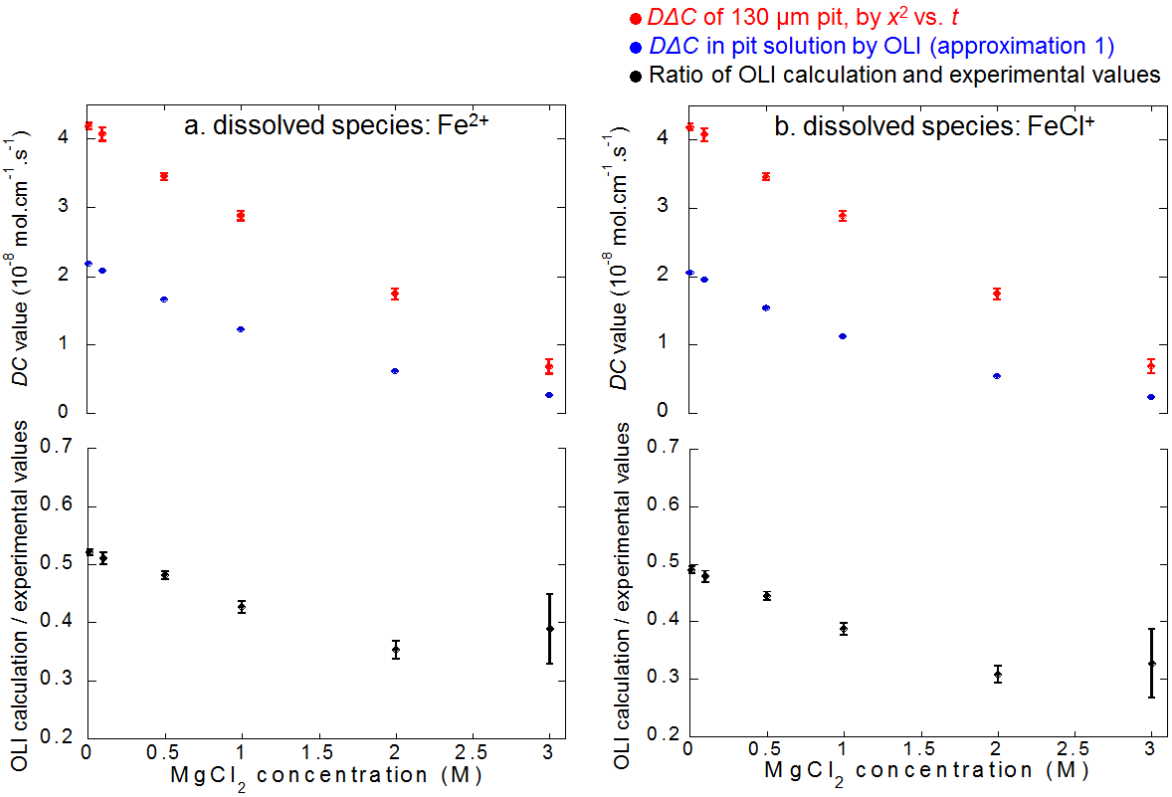

Figure 6-6. Comparison of $D\Delta C$ values calculated via OLI (based on approximation 1) and $D\Delta C$ values obtained from "x^2 vs. t" of 130 μm diameter Fe wire artificial pit. It is assumed that all the dissolved species is (a) Fe^{2+} or (b) $FeCl^+$ respectively. The average component of the pit solution is assumed to be a mixture of $MgCl_2$ (with the same concentration as bulk solution) and half-saturated $FeCl_2$, temperature 25 °C.

Approximation (2): Self-diffusivity of Fe^{2+} or $FeCl^+$ is the average of that in $MgCl_2$ (at the pit mouth) and $MgCl_2$ + saturated $FeCl_2$ (at pit bottom).

In [32], the average diffusivity of metal ions was assumed to be the average of that at the pit bottom and pit mouth, but the effect of bulk solution (0.5 M HCl) was neglected. A similar

assumption is made in this work, but the bulk solution is also taken into account, i.e. the diffusivity of Fe^{2+} or $FeCl^{+}$ is the average of that at the pit bottom (in saturated $FeCl_2$ + $MgCl_2$ with the same concentration as bulk solution) and pit mouth (in $MgCl_2$ bulk solution with no $FeCl_2$). The results are shown in

Figure 6-7. It is found that the difference is insignificant between averaging concentration (Figure 6-6) and averaging diffusivity (Figure 6-7), because the self-diffusivity of Fe^{2+} or $FeCl^{+}$ varies approximately linearly with the concentration of pure $MgCl_2$ or pure $FeCl_2$ (see Figure 6-8).

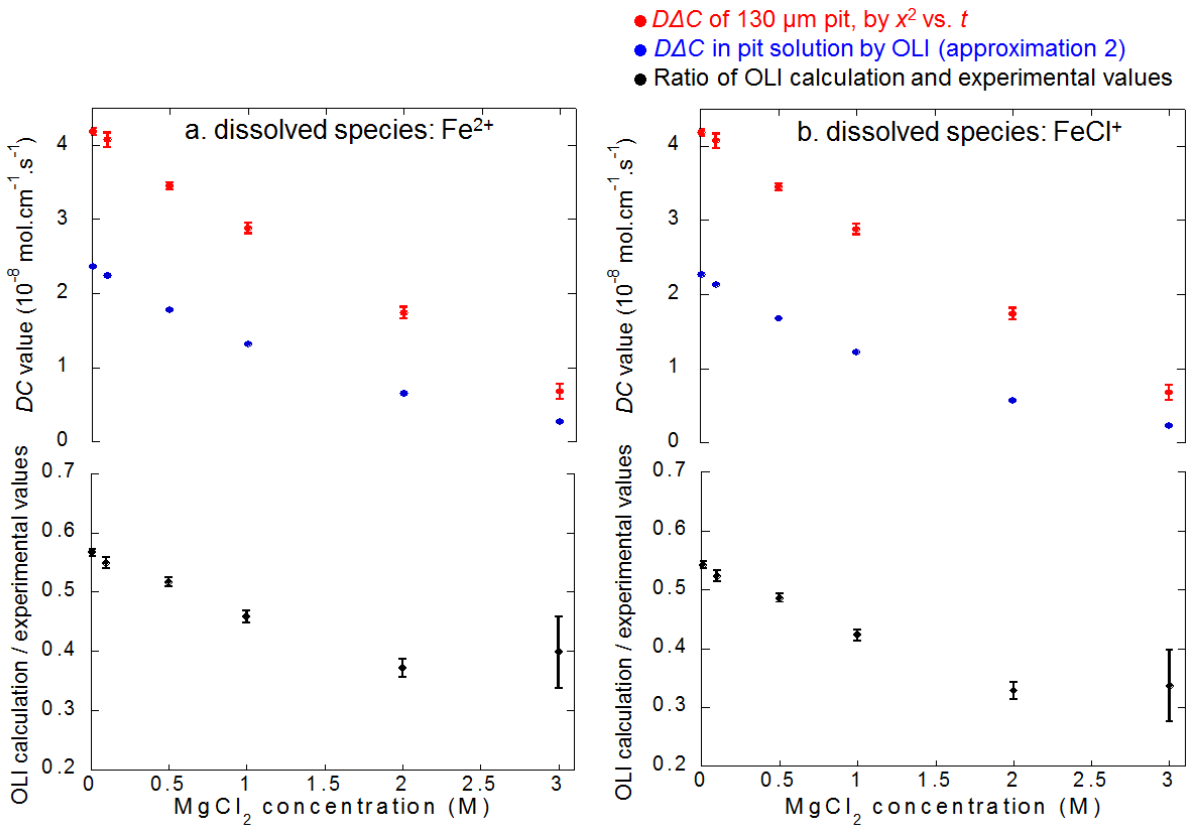

Figure 6-7. Comparison of *DΔC* values calculated via OLI (based on approximation 2) and *DΔC* values obtained from "x^2 vs. t" of 130 μm diameter Fe wire artificial pit. It is assumed that all the dissolved species is (a) Fe^{2+} or (b) $FeCl^{+}$ respectively. The self-diffusivity was assumed to be the average of that at the pit bottom ($FeCl_2$ with saturation concentration and $MgCl_2$ with the same concentration as in bulk solution) and pit mouth ($MgCl_2$ with the same concentration as bulk solution), temperature 25 °C.

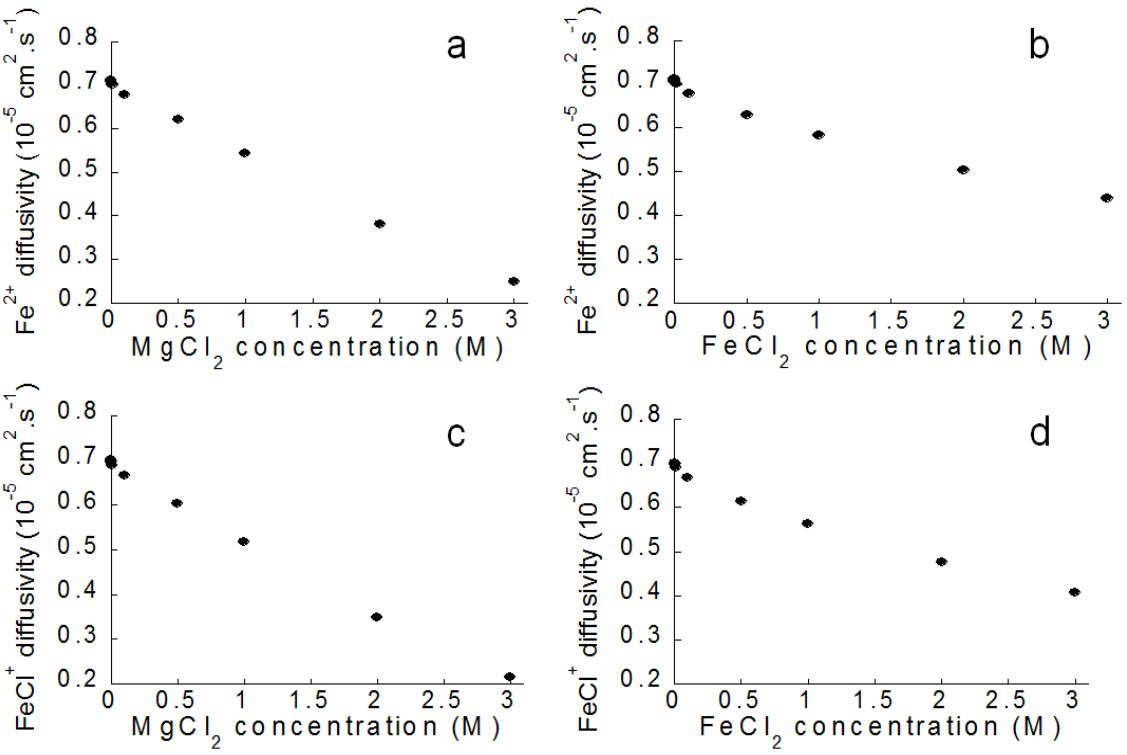

Figure 6-8. The approximately linear relationship between Fe^{2+} self-diffusivity and the concentration of solution (a) pure $MgCl_2$ and (b) pure $FeCl_2$, and between $FeCl^+$ self-diffusivity and the concentration of solution (c) pure $MgCl_2$ and (d) pure $FeCl_2$. The self-diffusivities were calculated via OLI, temperature 25 °C.

Secondly, according to Tester and Isaacs [34], the electric field across the axis of an artificial pit is resistant to the diffusion of cations of the bulk solution into the pit cavity. Ernst and Newman [190] have taken into account both the depletion of cations and the enrichment of anions of bulk solution, since they migrate in the opposite direction in the pit. Therefore, for the present work, there may be a decrease of Mg^{2+} concentration at the pit bottom compared to the bulk solution, which alters the saturation concentration of $FeCl_2$ (ΔC) compared to the approximations (1) and (2) described above. Galvele [13] has reported a model to calculate the concentration of ions (non-reacting species from bulk solution) at the pit bottom, which is a function of *IR* drop in the pit solution (Equation 6-4),

$$C_p = C_b \exp(-nF\Phi / RT) \qquad \text{Equation 6-4}$$

where C_p is the ion concentration at the pit bottom, C_b is the ion concentration in bulk solution, n is the valence of the ion, F is the Faraday's constant (96500 C/mol), T is the absolute temperature, R is the gas constant and Φ is the IR drop across pit solution.

Both depletion of Mg^{2+} and enrichment of Cl^- are taken into account as

$$[Mg^{2+}]_p = [Mg^{2+}]_b \exp(-2F\Phi / RT) \qquad \text{Equation 6-5}$$

$$[Cl^-]_p = [Cl^-]_b \exp(F\Phi / RT) \qquad \text{Equation 6-6}$$

where "p" and "b" mean pit solution and bulk solution respectively, from which Equation 6-7 may be derived,

$$\frac{[Mg^{2+}]_b}{[Mg^{2+}]_p} = \frac{[Cl^-]_p^2}{[Cl^-]_b^2} \qquad \text{Equation 6-7}$$

Since the total chloride concentration (same as $[Cl^-]_p$) is ca. 8.5 M for $MgCl_2$ concentration below 3 M (see Figure 6-5b), the concentration of Mg^{2+} or $MgCl_2$ at the pit bottom can be estimated from the concentrations of $MgCl_2$ bulk solutions. For example, if $[Mg^{2+}]_b$=0.01 M, $[Mg^{2+}]_p$ is ~0, and the saturation concentration of $FeCl_2$ is the same as in pure water (4.49 M); if $[Mg^{2+}]_b$=3 M, $[Mg^{2+}]_p$ is 1.5 M, and the saturation concentration of $FeCl_2$ is 2.7 M. Since the concentration of $MgCl_2$ in the bulk solution no longer equals that at the pit bottom, approximations (3) and (4) are used as follows.

Approximation (3): The pit solution is a mixture of $MgCl_2$ solution with a concentration of $([Mg^{2+}]_p+[Mg^{2+}]_b)/2$ and $FeCl_2$ with a concentration of $0.5C_{sat}$.

The saturation concentration of $FeCl_2$ was calculated via OLI according to $[Mg^{2+}]_p$ instead of $[Mg^{2+}]_b$. The results are shown in Figure 6-9. It is seen that self-diffusion accounts for ca. 50%

of the effective diffusion in low concentrations of $MgCl_2$ (similar as approximations 1 and 2), however, the effect of self-diffusion is found to be more significant with increasing $MgCl_2$ concentration, which is very different from the results based on approximations (1) and (2). In addition, it is also found from the ratio between OLI calculation and experimental data that the effect of self-diffusion for $FeCl^+$ is slightly less than for Fe^{2+}, which is due to the larger size of $FeCl^+$ compared to Fe^{2+} as described in the results based on approximation (1).

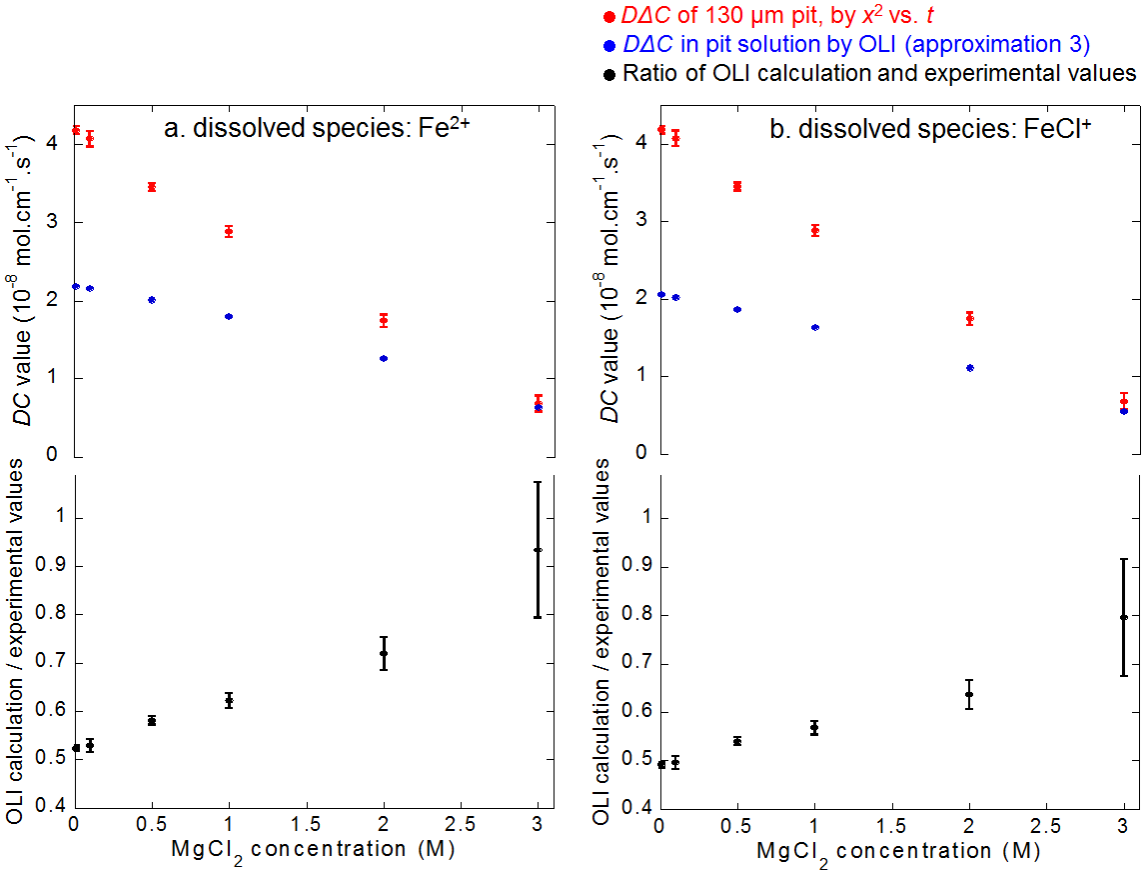

Figure 6-9. Comparison of $D\Delta C$ values calculated via OLI (based on approximation 3) and $D\Delta C$ values obtained from "x^2 vs. t" of 130 μm diameter Fe wire artificial pit. It is assumed that all the dissolved species is (a) Fe^{2+} or (b) $FeCl^+$ respectively. The average component of the pit solution is assumed to be a mixture of $MgCl_2$ solution in $([Mg^{2+}]_p+[Mg^{2+}]_b)/2$ and half-saturated $FeCl_2$, temperature 25 °C.

Approximation (4): Self-diffusivity of Fe^{2+} or $FeCl^{+}$ is the average of that in $MgCl_2$ (pit mouth, concentration is $[Mg^{2+}]_b$) and $MgCl_2$ + saturated $FeCl_2$ (pit bottom, concentration of $MgCl_2$ is $[Mg^{2+}]_p$).

The solution at the pit bottom is composed of $MgCl_2$ + saturated $FeCl_2$ (concentration of $MgCl_2$ is $[Mg^{2+}]_p$), and the solution at the pit mouth is the $MgCl_2$ bulk solution. The results based on approximation (4) are shown in

Figure 6-10, which are similar to the results shown in Figure 6-9, since the difference between averaging diffusivity and averaging concentration is insignificant as described above.

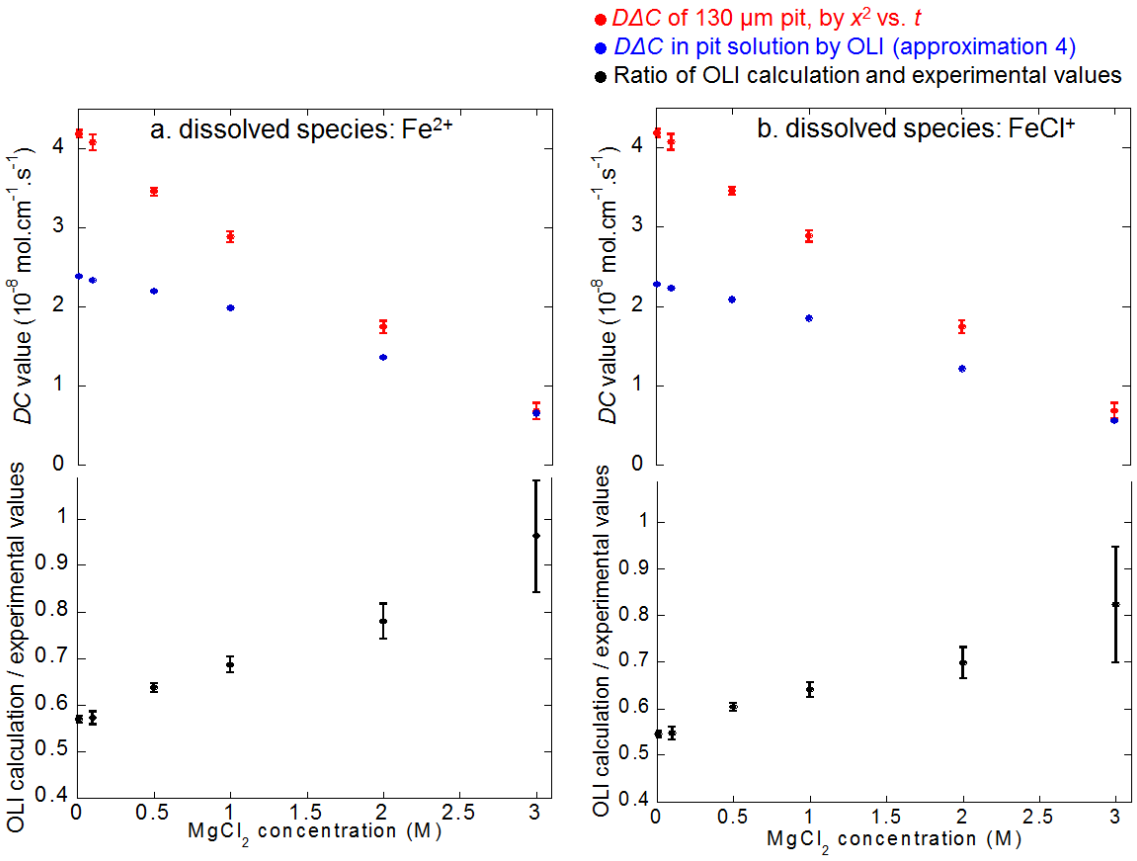

Figure 6-10. Comparison of $D\Delta C$ values calculated via OLI (based on approximation 4) and $D\Delta C$ values obtained from "x^2 vs. t" of 130 μm diameter Fe wire artificial pit. It is assumed that all the dissolved species is (a) Fe^{2+} or (b) $FeCl^{+}$ respectively. The self-diffusivity was assumed to be the average of that at the pit bottom ($FeCl_2$ with saturation concentration and $MgCl_2$ with the concentration of $[Mg^{2+}]_p$) and pit mouth ($MgCl_2$ with the same concentration as bulk solution), temperature 25 °C.

According to C_{sat} calculated via OLI, effective diffusion coefficient (D_{eff}) of the diffusion species (assumed to be Fe^{2+} or $FeCl^{+}$ in this work) is obtained from the experimental data, which are summarised in Table 6-2. It can be seen that the effective diffusion coefficient decreases with increasing solution concentration; the depletion of Mg^{2+} at pit bottom increases the saturation concentration of $FeCl_2$ by a factor of ~2 for 2 M and 3 M $MgCl_2$, so the *IR* drop across the pit solution is significant for the diffusion of metal ions, especially for relatively concentrated solutions.

Table 6-2. A summary of C_{sat} calculated via OLI and D_{eff} obtained from experimental data (the 130 μm pit, by x^2 vs $.t$) in different concentrations of $MgCl_2$

[$MgCl_2$] (M)	no depletion of Mg^{2+} in pit		with depletion of Mg^{2+} in pit	
	ΔC (C_{sat}) (M)	D_{eff} (10^{-5} cm^2/s)	ΔC (C_{sat}) (M)	D_{eff} (10^{-5} cm^2/s)
0.01	4.48	0.93±0.01	4.49	0.93±0.01
0.1	4.36	0.93±0.02	4.49	0.91±0.02
0.5	3.86	0.89±0.01	4.49	0.77±0.01
1	3.26	0.88±0.02	4.42	0.65±0.02
2	2.17	0.80±0.04	3.93	0.44±0.02
3	1.29	0.53±0.08	2.70	0.25±0.04

6.2.2 Tafel kinetics

Anodic Tafel slope shows the kinetics of metal dissolution in certain electrolytes under near-equilibrium conditions, and provides information on the dissolution mechanism (charge transfer process) (see Section 2.5). In this study, the Fe wire (130 μm) artificial pits were prepared in 0.01 M, 0.1 M, 0.5 M, 1 M, 2 M and 3 M $MgCl_2$. Three methods were applied to study the Tafel kinetics of iron dissolution in metal ion saturated or near-saturated solutions.

6.2.2.1 Potentiodynamic method in ohmic-control region

Pits were allowed to dissolve in different concentrations of $MgCl_2$ at 0.6 V(SCE), at which dissolution was under diffusion-control, until reaching a certain pit depth. The potential was

decreased to below E_T (transition potential) [39] to dissolve the salt layer and such that dissolution was under ohmic-control. The potential was then swept forwards to 0.6 V(SCE) again. A small ac signal (frequency 100 kHz, amplitude 10 mV) was imposed on the applied potential in order to make resistance measurements (in ohmic-control region), because the effect of capacitive component is negligible at high frequencies (see Figure 9-1). For example, Figure 6-11a shows the current-voltage and resistance-voltage characteristics of an Fe artificial pit (5 mV/s) in 2 M $MgCl_2$. In the ohmic-control region, the metal ion concentration may be below saturation, at saturation or supersaturation depending on the ratio of current density over i_{lim}. After *IR*-correction of the potential, a Tafel slope was obtained from the linear part of current vs. *IR*-corrected potential (Figure 6-11b). There are three parameters to be considered: sweep rate, reverse potential and pit depth.

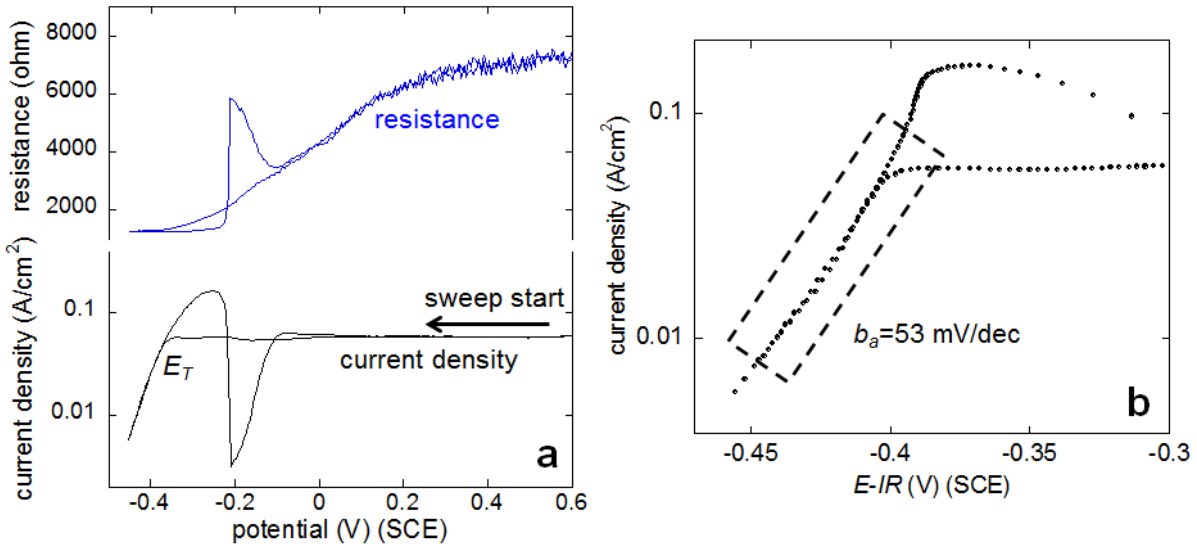

Figure 6-11. A potential sweep for an Fe artificial pit in 2 M $MgCl_2$ starting from 0.6 V and reversing at -0.45 V(SCE) at 5 mV/s, pit depth ca. 550 µm. (a) current-voltage and resistance-voltage characteristics of the potential sweep; (b) current density vs. *IR*-corrected potential in the ohmic-control region, Tafel slope obtained from the linear region, resistance measured by imposed ac signal (f=100 kHz, amplitude 10 mV)

(1). Sweep rate. Figure 6-12 shows current-voltage characteristics of an Fe artificial pit at 1 mV/s and 5 mV/s in 2 M $MgCl_2$ (pit depth ca. 500 µm), both potential sweeps were reversed at -0.45 V(SCE). The current of the slower forward sweep was found to increase compared to the faster sweep at for the same voltage in the ohmic-control region, because crevice formation between the metal and epoxy resin and/or surface roughening [37] may be prone to take place during active dissolution (salt-free), which has been shown in Section 5.2.5.1, and the period of active dissolution for slower sweep rate is longer. Furthermore, a longer period of active dissolution in low concentrations of metal ions may cause partial passivation on the electrode surface, which also leads to noticeable crevice formation and/or surface roughening when potential sweeps forwards for higher rate active dissolution (see Section 5.3.5.1). The Tafel slope obtained from the faster sweep is 53 mV/decade.

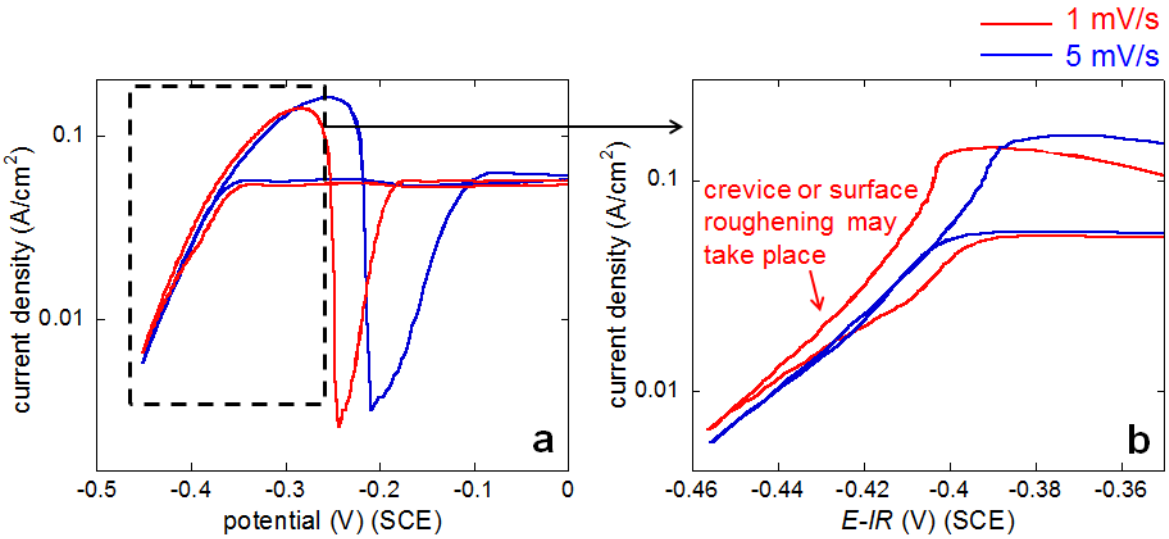

Figure 6-12. The current-voltage characteristics of an Fe artificial pit (1 mV/s and 5 mV/s) in 2 M $MgCl_2$, pit depth ca. 550 µm. (a) current density vs. applied potential; (b) current density vs. *IR*-corrected potential, resistance measured by imposed ac signal (f=100 kHz, amplitude 10 mV)

(2). Reverse potential. Figure 6-13 shows current-voltage characteristics of an Fe artificial pit at 5 mV/s in 1 M $MgCl_2$, potentials reversed at -0.35 V and -0.4 V(SCE), and the pit depth

was ca. 550 µm. For the sweep reversing at -0.4 V(SCE), the period available for active-dissolution was longer and the metal ion concentration was much lower for the region close to reverse potential. Accordingly, noticeable crevice formation and/or surface roughening [37] may also take place, and the current during the forward sweep increased compared to the backwards sweep at a same voltage in the ohmic-control region. The Tafel slope is 52 mV/decade for the sweep reversing at -0.35 V(SCE).

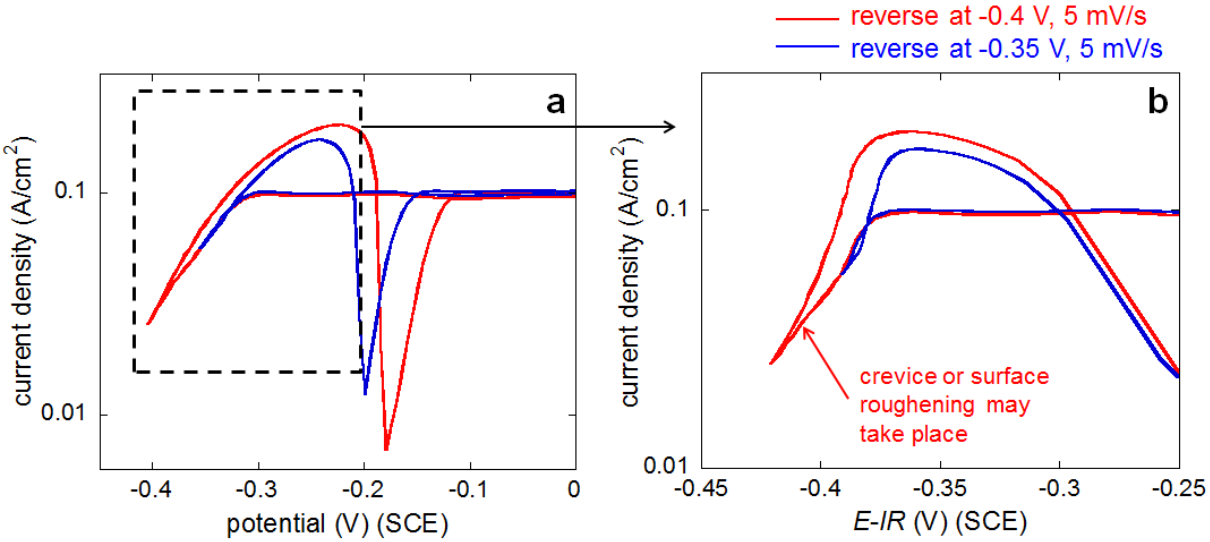

Figure 6-13. The current-voltage characteristics of an Fe artificial pit (5 mV/s) in 1 M $MgCl_2$, potential reversing at -0.4 V and -0.35 V(SCE), pit depth ca. 550 µm. (a) current density vs. applied potential; (b) current density vs. *IR*-corrected potential, resistance measured by imposed ac signal (f=100 kHz, amplitude 10 mV)

(3). Pit depth. Results from two different pit depths (550 µm and 850 µm) have been compared. It has been found that E_T is lower for a deeper pit [39], so potential has to reverse at a lower value for a deeper pit to dissolve the salt. Figure 6-14a shows the current-voltage characteristics of an Fe artificial pit (5 mV/s) in 0.5 M $MgCl_2$ at two different depths, and the Tafel slope is independent of pit depth, ca. 56 mV/decade (Figure 6-14b).

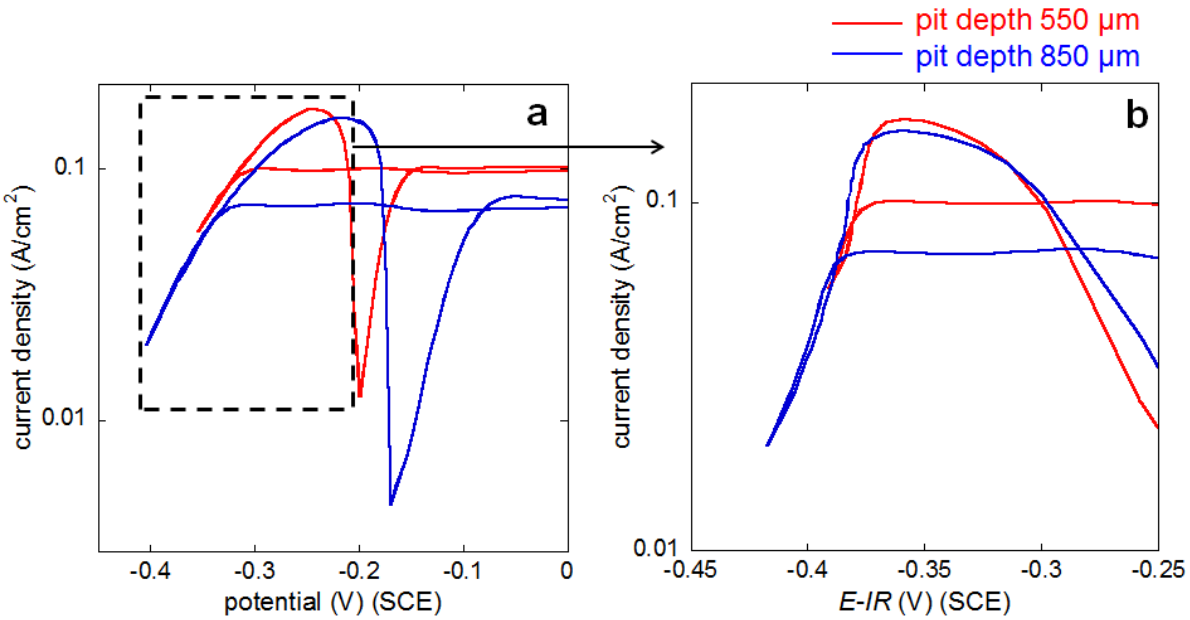

Figure 6-14. The current-voltage characteristics of an Fe artificial pit (5 mV/s) in 0.5 M $MgCl_2$, pit depth ca. 550 µm and 850 µm. (a) current density vs. applied potential; (B) current density vs. *IR*-corrected potential, resistance measured by imposed ac signal (f=100 kHz, amplitude 10 mV)

Figure 6-15 describes the current-voltage characteristics of potential sweeps on Fe artificial pits in different concentrations of $MgCl_2$ at the same pit depth, and it shows that E_T also decreases with increasing chloride concentration at a fixed pit depth. Since the reverse potential has to be lower than E_T in order to ensure complete dissolution of the salt layer, deeper pits and more concentrated chloride solutions both require a lower reverse potential. However, the potential cannot be too low in order to avoid noticeable surface roughening and/or crevice formation (e.g. see Figure 6-13).

In addition, in dilute chloride solutions, e.g. 0.01 M or 0.1 M $MgCl_2$, metal ions diffuse faster and the salt layer dissolves more quickly than in concentrated chloride solutions, so that the solution of metal ions dilutes quickly, which may also favour crevice formation and/or surface roughening [37]. Therefore a very fast sweep rate (15 mV/s) had to be used for 0.01 M $MgCl_2$. It indicates that the appropriate reverse potential and sweep rate both depend on the chloride

concentration. Table 6-3 summarises the Tafel slope of Fe artificial pits in different chloride concentrations, each experiment was carried out three times (at different pit depths). Tafel slope is independent of sweep rates used in Table 6-3.

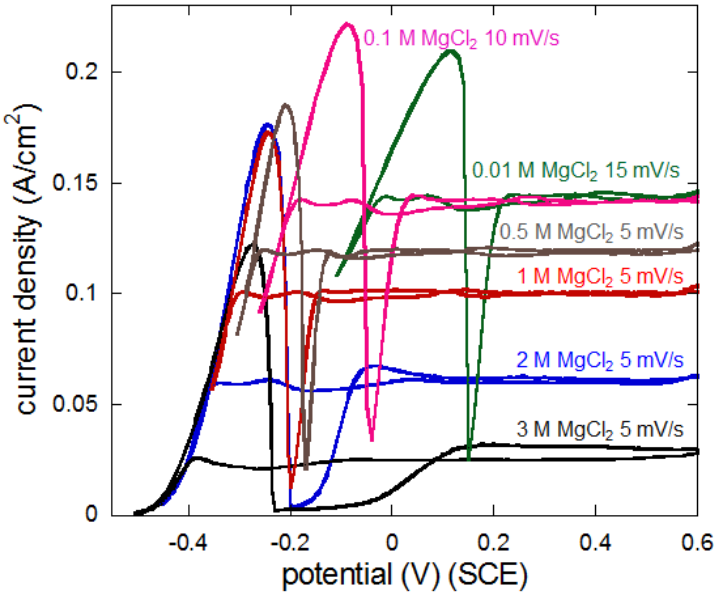

Figure 6-15. Current-voltage characteristics of Fe artificial pits in different $MgCl_2$ concentrations, pit depth ca. 550 µm for all

Table 6-3. Tafel slopes of Fe artificial pits in different chloride concentrations ($MgCl_2$) measured via the potentiodynamic method in ohmic-control region

$[Cl^-]$ (M)	sweep rate (mV/s)	Tafel slope (mV/decade)
0.02	15	60±5
0.2	10	57±7
1	4, 5, 10	56±6
2	4, 5, 10	60±7
4	4, 5, 10	56±8
6	4, 5, 10	59±7

6.2.2.2 Transition potential method

The method used is similar to that described by Laycock and Newman [39]. The transition potential E_T is the transition from diffusion-control to ohmic-control dissolution, at which point current equals diffusion-limited current I_{lim}, but starts to decrease with decreasing

potential in the reverse sweep (see Figure 2-6), so the metal ion is saturated and salt layer dissolves. The aim of measuring E_T is to obtain the saturation concentration of metal ions for Tafel kinetics study, since I_{lim} is proportional to inverse pit depth, different pit depths have to be used to obtain a series of I_{lim}.

Fe pits were prepared in different chloride concentrations at 0.4 V(SCE). For the E_T measurement, the potential was swept from 0.4 V(SCE) to below E_T, and then stepped back directly to 0.4 V(SCE) instead of sweeping, since E_T was measured during the backward sweep. The same sweep rate 5 mV/s was applied for all $MgCl_2$ concentrations, including 0.01 M and 0.1 M, for which noticeable crevice formation and/or surface roughening may take place, but which would not affect the value of E_T obtained, and creviced/roughened surface would be dissolved during diffusion-limited dissolution (described in Section 5.2.5.1). Figure 6-16 shows the current response for several potential sweeps/steps in 0.5 M $MgCl_2$, 27 potential sweeps were carried out in total, during which i_{lim} decreased by one decade due to the increase of pit depth.

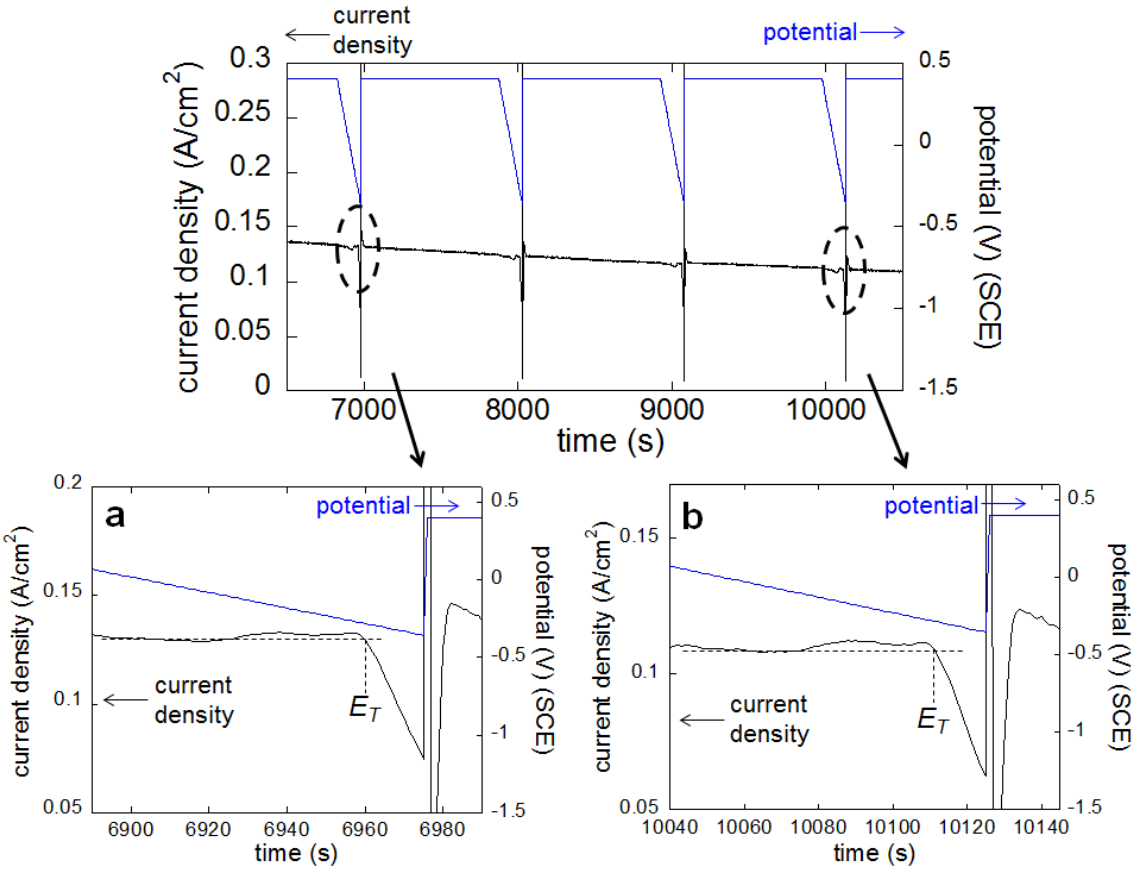

Figure 6-16. Current response for several potential sweeps/steps applied on an Fe artificial pit in 0.5 M $MgCl_2$ for the transition potential measurement, potential swept at 5 mV/s from 0.4 V(SCE) to below E_T and then stepped back directly to 0.4 V(SCE). The insert (a) and (b) show details of the current response.

Thus a series of i_{lim} and corresponding E_T was obtained as shown in Figure 6-17a. E_T was then *IR*-corrected using the simultaneously measured resistance (using the imposed ac signal) and plotted versus the corresponding i_{lim} to obtain a Tafel slope as shown in Figure 6-17b.

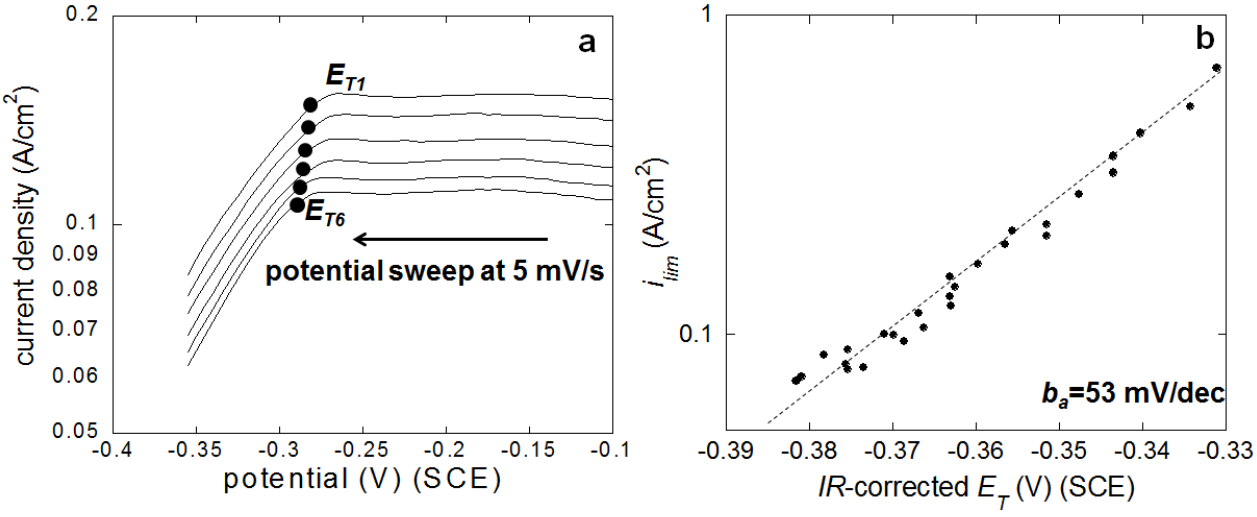

Figure 6-17. Tafel slope obtained from a series of i_{lim} and E_T of an Fe artificial pit in 0.5 M $MgCl_2$. (a) a series of potential sweeps in 5 mV/s to measure E_T; (b) i_{lim} vs. *IR*-corrected E_T, resistance measured by imposed ac signal (f=100 kHz, amplitude 10 mV)

Table 6-4 summarises the value of the Tafel slope measured in six chloride concentrations, and each experiment was carried out three times.

Table 6-4. Tafel slopes of Fe artificial pits in different chloride concentrations ($MgCl_2$) via the transition potential method

[Cl^-] (M)	Tafel slope (mV/decade)
0.02	63±10
0.2	66±8
1	58±8
2	68±9
4	64±10
6	64±8

6.2.2.3 Galvanodynamic method

For diffusion-controlled dissolution, current is limited at I_{lim}. The bottom of the artificial pit is salt-covered, which means that the solution is saturated. When the current is held at the value of I_{lim} (galvanostatic condition), the concentration is expected to remain at saturation. This is the idea upon which the galvanodynamic method is based, which can be described in several steps.

Step 1. An Fe artificial pit was prepared in $MgCl_2$ at 0.6 V(SCE) until the pit depth reached a certain value where the dissolution was diffusion-limited. Then the potential was swept back (5 mV/s) to below E_T to dissolve the salt layer while the resistance was measured simultaneously using the imposed ac signal. Figure 6-18a shows an example of a typical potential sweep to below E_T in 0.5 M $MgCl_2$, it can be seen that the resistance tends to level off after salt layer has dissolved.

Step 2. After the salt layer has dissolved completely, the control-mode was switched to current-control, and the current was cyclically swept up and down around the value of I_{lim} with increasing amplitude until limits were reached (discussed as follows), so the average of current was always at I_{lim}. During these sweeps the potential was recorded. Figure 6-18b shows an experiment during which a current sweep rate of 50 μA/s was used as an example. The potential was found to change approximately linearly with time and current since the dissolution was ohmic-controlled. During the current sweep, the increase of pit depth was negligible because the total elapsed time was short (< 30 s). Since the ac signal could not be applied for the current-control mode, the pit solution resistance was assumed to be the value measured after dissolution of the salt layer in step 1 (~2950 Ω).

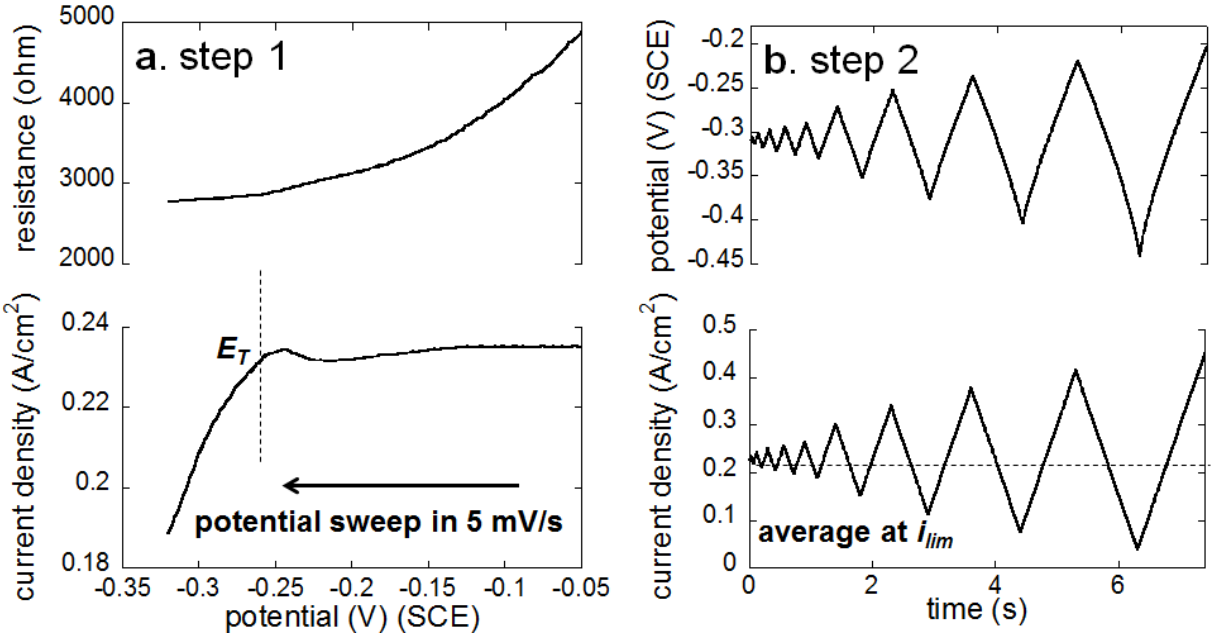

Figure 6-18. An illustration of the galvanodynamic method for an Fe artificial pit in 0.5 M $MgCl_2$, pit depth ca. 300 µm. (a) step 1: potential swept back at 5 mV/s to below E_T to dissolve salt layer, resistance measured simultaneously by imposed ac signal (f=100 kHz, amplitude 10 mV); (b) step 2: current swept around I_{lim} in 50 µA/s, potential was recorded.

Step 3. Since resistance and potential have been recorded in step 1 and step 2 respectively, the applied current and *IR*-corrected potential are plotted in Figure 6-19, in which the Tafel slope is obtained (63 mV/decade).

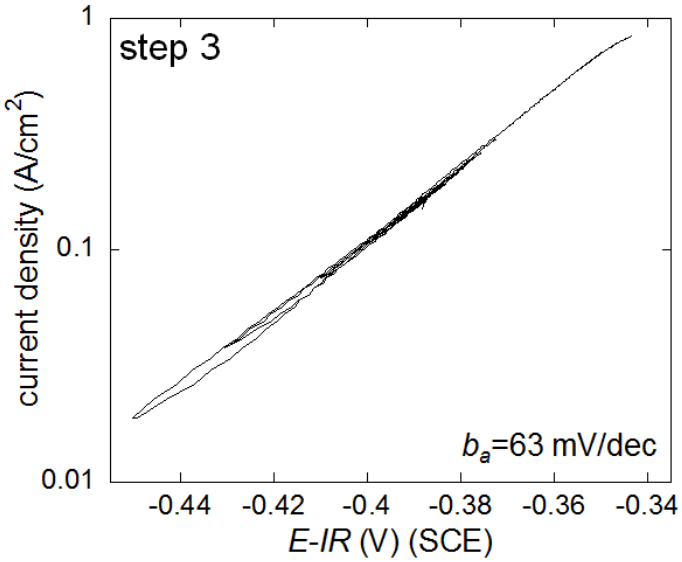

Figure 6-19. A semi-log plot of the current density vs. *IR*-corrected potential measured via galvanodynamic method (after step 1 and 2 in Figure 6-18) on an Fe artificial pit in 0.5 M $MgCl_2$, pit depth ca. 300 μm

There are several parameters to be considered: the upper and lower limits of sweep, the sweep rate and the pit depth, which are discussed as follows.

(1). Upper and lower limits of sweep. The limit means the highest or lowest current value between which log *i* is approximately linear with *IR*-corrected potential. The limits varied with sweep rates (1, 10, 50 μA/s) as shown in Figure 6-20, which describes galvanodynamic measurements of Fe artificial pits in 0.5 M $MgCl_2$. The lower limit could be below 0.01 A/cm^2 for all scan rates, but the upper limit was much higher for 50 μA/s (ca. 1 A/cm^2). The lower limit would drive *IR*-corrected potential back to around open circuit potential, the upper limit could lead to supersaturation and salt precipitation, which if occurred, would have resulted in a marked increase of potential (where the assumed solution resistance is no longer valid) similar to the potential transient of the galvanostatic experiment reported by Kuo and Landolt [27]. Based on the linear region in the insert of Figure 6-20, the Tafel slopes for the three scan rates are all ca. 64 mV/decade.

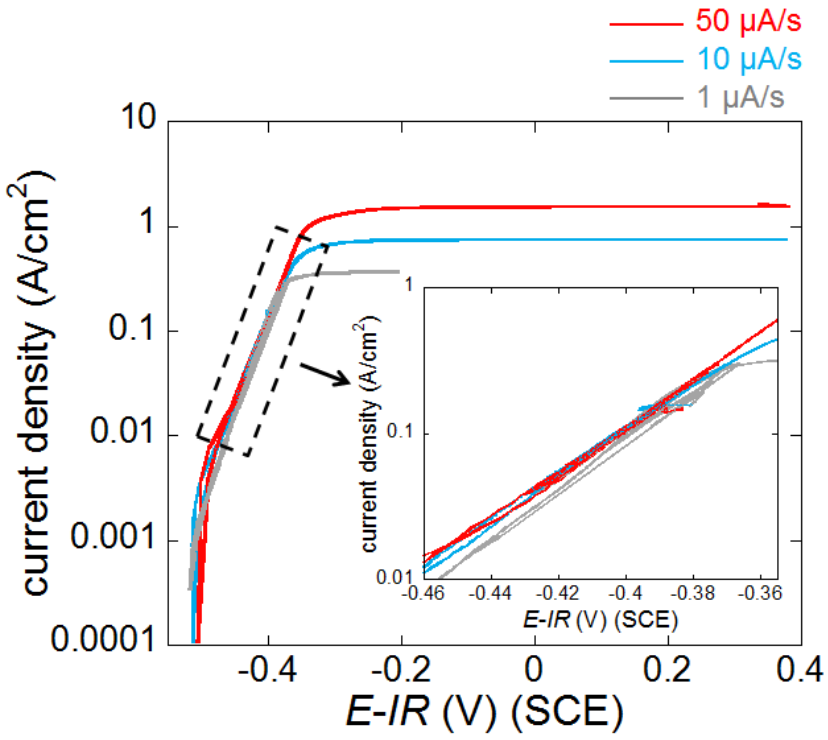

Figure 6-20. Plots of applied current vs. *IR*-corrected potential measured via galvanodynamic method on an Fe artificial pit in 0.5 M $MgCl_2$ at sweep rates 1 µA/s, 10 µA/s and 50 µA/s, pit depths ca. 500 µm, i_{lim} ca. 0.14 A/cm^2, the insert shows details of the linear region.

(2). Pit depth. The galvanodynamic measurements described above were carried out at different pit depths in 0.5 M $MgCl_2$, the same sweep rate 50 µA/s was used, and the linear regions were extracted for each pit depth as shown in Figure 6-21, in which the Tafel slopes at the three pit depths are all ca. 62 mV/decade, indicating that the Tafel slope is independent of pit depth.

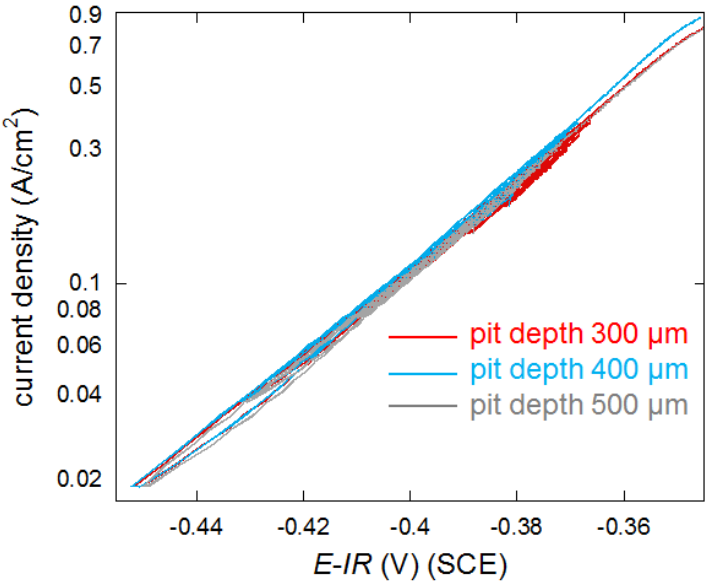

Figure 6-21. Plots of applied current vs. *IR*-corrected potential measured via galvanodynamic method on an Fe artificial pit in 0.5 M $MgCl_2$ at pit depths 300 µm, 400 µm and 500 µm, sweep rate 50 µA/s

(3). Sweep rate. The resistance of pit solution has been assumed to be constant, however, the actual resistance is expected to change due to "current-controlled" supersaturation and dilution, since the resistivity varies with solution concentration. Figure 6-22 shows the resistivity of 0.5 M $MgCl_2$ with different concentrations of $FeCl_2$ (derived from OLI). When the $FeCl_2$ concentration is near the saturation concentration (C_{sat} = 3.86 M in 0.5 M $MgCl_2$), the resistivity increases with the $FeCl_2$ concentration. The calculation for other concentrations of $MgCl_2$ (0 to 3 M) also shows that the resistivity of the mixed solution ($FeCl_2$ + $MgCl_2$) increases with the concentration of $FeCl_2$ at near saturation concentration of $FeCl_2$ (not shown).

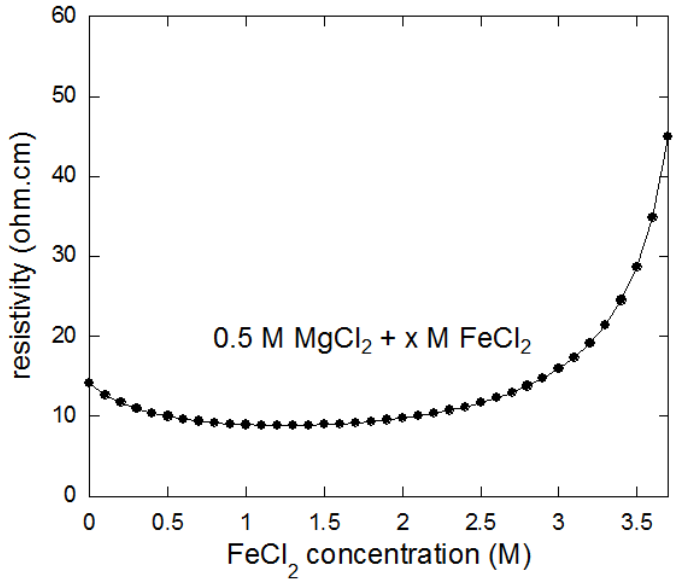

Figure 6-22. Resistivity of mixed solution of 0.5 M $MgCl_2$ with various concentrations of $FeCl_2$ derived from OLI, temperature 25 °C

Figure 6-20 has shown that the Tafel slopes are the same for the scan rates 1 μA/s, 10 μA/s and 50 μA/s. Furthermore, Figure 6-23 compares the result from a 50 μA/s scan with an even slower scan rate of 0.2 μA/s in 0.5 M $MgCl_2$ at the same pit depth as Figure 6-20. It can be seen that the slope for 0.2 μA/s is 81 mV/decade. The approximation of constant resistance of pit solution is more likely to be valid for a faster sweep, since the "current-controlled" supersaturation and dilution process is very quick and would only alter the concentration at the pit bottom, which should not affect the mean resistivity of the whole pit solution. However, for a very slow sweep, the supersaturation and dilution process are given enough time for the diffusion of metal ions, which affects the mean resistivity of pit solution. So the mean resistance is no longer constant. Therefore, for the sweep at 0.2 μA/s, the *IR*-correction was excessive at dilution and insufficient at supersaturation, as shown in Figure 6-23. The validity of the approximation is shown to rely upon the use of a scan fast enough so that the change of average resistance of pit solution is negligible. Galvanodynamic measurements

with a wide range of scan rates were carried out three times each (different pit depths) in 0.5 M $MgCl_2$, the Tafel slope values are shown in Figure 6-24.

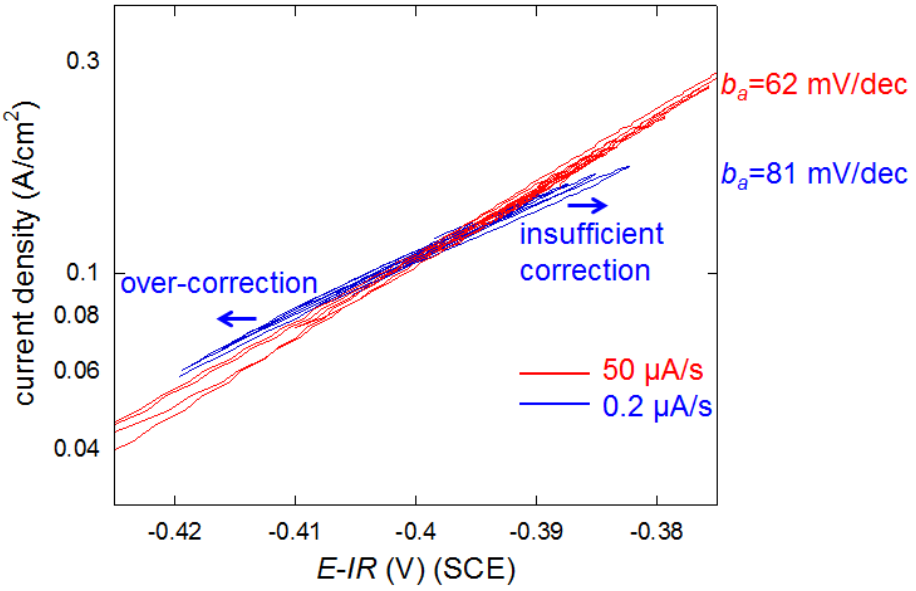

Figure 6-23. Comparison of applied current vs. *IR*-corrected potential measured via galvanodynamic method in 50 µA/s and 0.2 µA/s on an Fe artificial pit in 0.5 M $MgCl_2$, pit depth ca. 500 µm

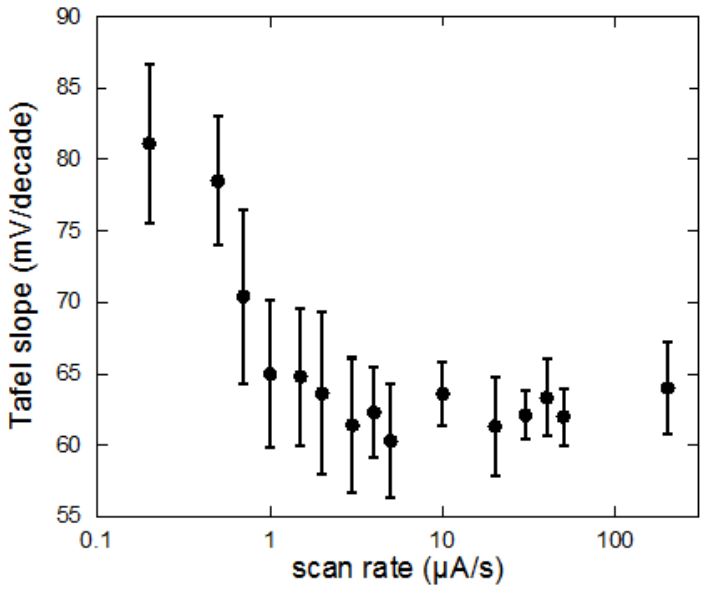

Figure 6-24. Dependence of Tafel slope on scan rate, derived from galvanodynamic measurements on Fe artificial pits in 0.5 M $MgCl_2$, pit depth ca. 500 µm

Table 6-5 summarises the Tafel slopes derived for different chloride concentrations using the galvanodynamic method. A scan rate of 50 µA/s was applied for all chloride concentrations and each experiment was carried out three times (different pit depths).

Table 6-5. Tafel slopes of Fe artificial pits in different chloride concentrations ($MgCl_2$) measured using galvanodynamic method (current scan rate 50 µA/s)

[Cl^-] (M)	Tafel slope (mV/decade)
0.02	72±9
0.2	67±6
1	63±3
2	65±5
4	64±6
6	66±7

Tafel slopes from all the methods are compared in Figure 6-25a, the plots of current density vs. *IR*-corrected potential for three methods in 0.5 M $MgCl_2$ are compared in Figure 6-25b.

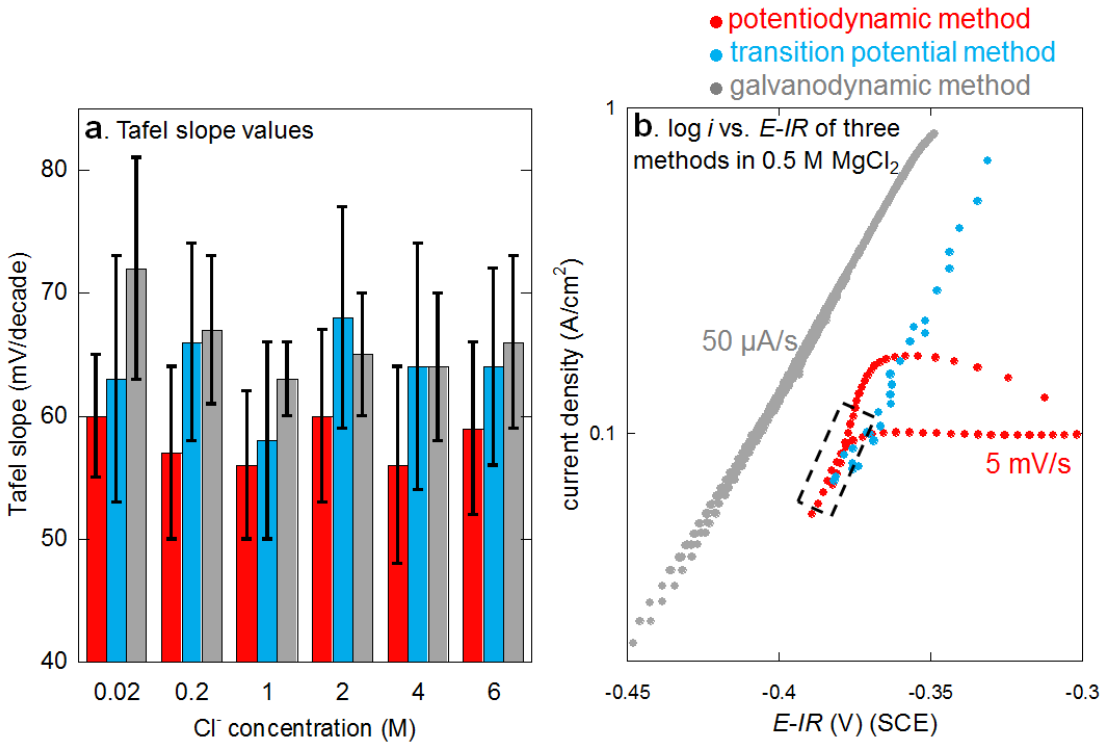

Figure 6-25. Comparison of the Tafel slopes derived from the potentiodynamic, transition potential and galvanodynamic methods. (a) Tafel slope values vs. chloride concentration; (b) applied current vs. *IR*-corrected potential in 0.5 M $MgCl_2$, sweep rates were 5 mV/s and 50 µA/s for potentiodynamic and galvanodynamic methods respectively.

6.3 Discussion

6.3.1 Diffusivity of metal ions

Previous work has been carried out to investigate the mass transport within a corrosion pit, which is significant for the study of pit stability. There is a concentration gradient across the pit depth, and the ionic diffusivity varies with solution concentrations, so the diffusivity should also vary along the pit cavity. However, approximations have been made that an average diffusivity can be used to describe the mass transport within a corrosion pit [20, 30, 37, 58], which has also been used in this work.

Isaacs [33] assumed the diffusivity of metal ions as 0.5×10^{-5} cm^2/s for a stainless steel artificial pit in 1 M NaCl, and calculated the metal ion saturation concentration as 6 M (according to Equation 2-6). While another work of Tester and Isaacs [34] suggested that the mass transport in the artificial pit should be the combination of diffusion and electrical migration (see Equation 2-8). The "effective diffusion coefficient", including both diffusion and electrical migration, has been determined for iron dissolution [30], for artificial pits of stainless steel [21, 37, 58] and Fe-17.4Cr alloy [20] in 1 M chloride, and Ni artificial pit in 0.5 M HCl [32], and the diffusivity was regarded as a constant in the solution.

Based on the approximations (1) to (4) in the present work, the diffusion accounts for ca. 50% of the effective diffusion for dilute $MgCl_2$ (0.01 M and 0.1 M), and it decreases to ca. 35% in 3 M $MgCl_2$ if the depletion of Mg^{2+} is ignored, while it increases to more than 90% (for Fe^{2+}) and 80% (for $FeCl^+$) if the depletion of Mg^{2+} is taken into account. The difference can be essentially ascribed to the change of ΔC or C_{sat}. The depletion of Mg^{2+} at the pit bottom increases ΔC (the driving force of diffusion [34]) by a factor of ~2 for 2 M and 3 M $MgCl_2$ (see Table 6-2), for which the effect of diffusion due to the concentration gradient across the

pit solution is significant compared to the approximations ignoring the Mg^{2+} depletion. In contrast, for very dilute $MgCl_2$ solutions, C_{sat} is very close to that in pure water, and the depletion of Mg^{2+} cannot noticeably change the C_{sat}, so the effect of dilute $MgCl_2$ on diffusivity calculation is negligible and the difference between the results of approximations (1)(2) and (3)(4) are insignificant. Since the electrical migration of Fe^{2+} or $FeCl^+$ is considered as shown in Section 6.2.1.3, it is sensible to take into account the migration of Mg^{2+}, which results in the depletion of Mg^{2+} at the pit bottom. The results based on approximations (3) and (4) are expected to be more practical. The C_{sat} of Fe^{2+} or $FeCl^+$ in different concentrations of NaCl has been calculated by Ernst and Newman [190], however, the applied model assumes that the solubility product of $FeCl_2$ (derived from the saturation concentration of $FeCl_2$ in pure water) is independent of chloride concentration of bulk solutions ($K_{sp}=[Fe^{2+}][Cl^-]^2$, or $K_{sp}=[FeCl^+][Cl^-]$), which indicates that an ideal solution (activity coefficient is assumed to be 1 for all species) has been assumed. In comparison, the OLI model has taken into account the dependence of activity coefficient on concentrations and has been extensively validated via experimental data [153], so the saturation concentration of $FeCl_2$ used in the present work is expected to be practical.

According to Kuo and Landolt [30], the Fe^{2+} diffusivity was ~70% of the effective diffusion coefficient, however, they regarded diffusivity as a constant for all chloride concentrations. Danielson [32] calculated the diffusivity of Ni^{2+} as the average of diffusivity in infinite dilution and 5 M $NiCl_2$ (C_{sat} of $NiCl_2$) and found that the diffusion also accounted for 70% of the effective diffusion, and the effect of bulk solution (0.5 M HCl) was ignored. Since the bulk solution is not concentrated, ignoring the effect of bulk solution may be reasonable.

For diffusion-limited dissolution in 1 M chloride (0.5 M $MgCl_2$ for the present work), the effective diffusion coefficient of the dissolving species (Fe^{2+} or $FeCl^+$) is 0.89×10^{-5} cm^2/s if

the depletion of Mg^{2+} is ignored, and 0.77×10^{-5} cm^2/s if the depletion of Mg^{2+} is considered. The effective diffusion coefficients within an Fe-alloy artificial pits in 1 M chloride have been previously reported by Kuo and Landolt [30] (0.85×10^{-5} cm^2/s), Gaudet et al. [37] (0.824×10^{-5} cm^2/s), Steinsmo and Isaacs [20] (1.02×10^{-5} cm^2/s) and Ghahari [58] (1.03×10^{-5} cm^2/s) (see Table 2-1). The difference amongst these studies and the present work could be attributed to the applied saturation concentrations and different Fe-alloys studied, e.g. Gaudet et al. [37] studied stainless steel 304 and assumed that the $FeCl_2$ saturation concentration in 1 M NaCl was the same as in water (4.2 M [30]), while Steinsmo and Isaacs [20] took into consideration the effect of $CrCl_3$ for Fe-17.4Cr alloy and used 3.5 M.

6.3.2 Tafel kinetics

6.3.2.1 Compare the three methods with the work in the literature

It has been found that the Tafel slope is independent of pit depth, which agrees with [20, 53]. The Tafel slope for iron obtained via the potentiodynamic method agrees well with [67], which used the same method for stainless steel 304 artificial pits in different $MgCl_2$ concentrations, and the comparison between Mi [67] and the present work is shown in Figure 6-26. The difference of Tafel slopes between iron and stainless steel for metal ion saturation concentration is negligible, which may be ascribed similar electron transfer numbers for the dissolution reaction , 2 for Fe and 2.2 (in average) for stainless steel 304. The dissolution mechanism for stainless steel may be dominated by the dissolution of Fe.

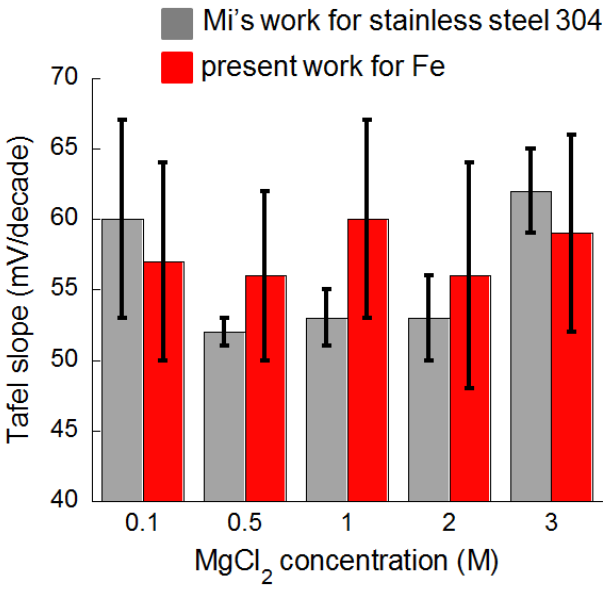

Figure 6-26. Comparision of Tafel slopes obtained for artificial pits of Fe (the present work) and stainless steel 304 (Mi [67]) via potentiodynamic method in different $MgCl_2$ concentrations

For the transition potential method, since the *IR*-correction used by Laycock and Newman [39] did not include the resistance of pit interior solution (see Section 2.5.2), the difference is significant compared to the present work. Mi [67] found that the Tafel slopes for stainless steel 304 derived from the transition potential method would be close to the values found by Laycock and Newman [39] if the pit interior resistance was also ignored and only the pit exterior resistance was considered, however, the Tafel slopes of stainless steel 304 reported by Mi [67] are 50 mV/decade in 0.5 M $MgCl_2$ and 48 mV/decade in 3 M $MgCl_2$ when "full *IR*-correction" was applied (also used in the present work), and which agrees with the present work (see Table 6-4).

The galvanodynamic method gives Tafel slope values similar to the other two methods, but it is shown in Figure 6-25b that, at a fixed current value, the *IR*-corrected potential measured via the galvanodynamic method was 20 to 30 mV lower. The *in-situ* X-ray radiography and SEM measurements in Section 5.2.5.1 show that the active dissolution (salt-free) of iron at high rate

may induce crevice formation and surface roughening (see Figure 5-15 and Figure 5-16). As in Figure 6-12 and Figure 6-13, crevice formation and/or surface roughening can move the potential to negative direction, which may account for the potential difference at a fixed current value between the forward and backward sweeps. During galvanodynamic control, dissolution was not diffusion-limited, and crevice formation and/or surface roughening may contribute to the overall dissolution, a small degree of which seems inevitable under the salt-free condition. When crevice formation and/or surface roughening take place, the dissolution area increases, so that the current density and metal ion concentration will be slightly lower at a fixed current value than a non-creviced pit, and the pit solution resistance would decrease (see Figure 6-22), causing the slight decrease of potential.

For the potentiodynamic method, the current range was relatively small (normally less than one decade), but it could be as large as two decades for the galvanodynamic method (see Figure 6-20). For the transition potential method, the current range could be more than one decade if measured with very deep pits, however, the data points are scattered (see Figure 6-17b) in the same way as [39], a large amount of data are required to ensure accuracy.

When $FeCl_2$ is saturated, although the saturation concentration of $FeCl_2$ decreases with increasing $MgCl_2$ concentration, the total chloride concentrations are identical (ca. 8.5 M) for $MgCl_2$ concentrations from 0.01 M to 3 M, although the saturation concentration of $FeCl_2$ varies between 1 M and 4.5 M (see Figure 6-5). The similar Tafel slope values for different $MgCl_2$ concentrations indicate that the slope may be independent of $MgCl_2$ concentration and $FeCl_2$ concentration when $FeCl_2$ is saturated.

Most studies of the dissolution mechanism of iron have been based on linear voltammetry on relatively large electrodes (0.2 to 1.2 cm^2), instead of a small diameter (1.3×10^{-4} cm^2 for the

130 μm pit) and deep pit geometry, and the effects of chloride and hydrogen ion concentrations on the anodic dissolution rate have been investigated by varying the components of solutions [191-201]. In these studies, the metal ion concentrations are insignificant, except for Kuo and Nobe [198], who studied "high polarisation" where iron may dissolve in relatively concentrated metal ions (current density ~0.1 A/cm^2). In Kuo and Nobe's study, for chloride concentration of 4.5 M, Tafel slope was found to be 40 mV/decade and 110 mV/decade when the concentration of hydrogen ions was 0.1 M and 4.5 M respectively (the effect of hydrolysis on pH was ignored), however, due to the difference on experimental geometry compared to the present work, the enrichment of chloride at the metal surface is not expected to be as significant as in the present work, so the concentration of chloride should be much less.

6.3.2.2 The applicability of galvanodynamic method

The transition potential method is assumed to measure the Tafel slope just at the metal ion saturation concentration (see [39]). The average of the metal ion concentration is near-saturation for both potentiodynamic and galvanodynamic methods in this study, but the concentration at current other than I_{lim} is unknown, since the concentration (ΔC) and diffusivity (D) change simultaneously, and it is only possible to obtain $D\Delta C$ as one parameter. However, for a fast current sweep in a short period, only the concentration of the pit bottom is cyclically altered, the average concentration of the pit solution can be assumed to be unchanged, so the diffusivity in pit solution is constant, and thus the value of ΔC can be estimated via current values. A fast galvanodynamic measurement can produce metal ion concentrations in a wide range, e.g. half saturation or twice supersaturation if the sweeping current averages at 50%i_{lim} or 200%i_{lim}, which cannot be obtained via the other two methods. Furthermore, since the metal ion concentration can be varied widely and metal ions are

critical to maintain the pH and chloride concentration at pit bottom, wide ranges of pH and chloride concentrations (both calculated via OLI) are also possible, which can be used to investigate the dissolution mechanism of a growing pit. However, more work has to be carried out to evaluate the extent of the effects of crevice formation and/or surface roughening. A correction on current density (according to the altered dissolution area) may be feasible.

6.4 Conclusions

- When making the approximation of averaging concentration/diffusivity in Fe artificial pits, the self-diffusivity of dissolving species (calculated via OLI as Fe^{2+} or $FeCl^{+}$) accounts for ~50% of the effective diffusion in 0.01 M $MgCl_2$, and this proportion decreases with increasing $MgCl_2$ concentration if the depletion of Mg^{2+} is ignored. While the proportion increases with increasing $MgCl_2$ concentration if the depletion of Mg^{2+} is considered. The other factor in the effective diffusion is electrical migration.
- Three methods have been used to calculate Tafel slope of iron dissolution in metal ion saturated solutions via iron artificial pits (total chloride concentration at the pit bottom ca. 8.5 M for $MgCl_2$ less than 3 M), the results range from 56 to 70 mV/decade for different $MgCl_2$ concentrations, which are independent of $MgCl_2$ and $FeCl_2$ concentration when $FeCl_2$ is saturated.
- The galvanodynamic method has been investigated in the present work. A small degree of crevice formation and/or surface roughening may be ascribed to the result that, at a fixed current value, the *IR*-corrected potential is consistently lower compared to the other two methods. The galvanodynamic method may be applicable for studies on the dissolution mechanism in a wide range of ion concentrations.

7. GENERAL DISCUSSION AND FUTURE WORK

7.1 General discussion

7.1.1 The presence of solid corrosion products in iron artificial pits

Black solid corrosion product layers have been observed in 99.5% iron (carbon ~0.1%wt.) artificial pits in HCl. These corrosion products have been characterised as a mixture of disordered carbon and cementite/cohenite (Fe_3C) via Raman and XRD measurements (Chapter 4), and their stability in HCl has been found to depend on the interfacial potential (passive at -0.15 V/SCE and mostly dissolving above -0.05 V/SCE). The dissolution of the corrosion products is likely to be controlled by a kinetic process, and consideration of the thermodynamic stability of Fe_3C and C suggests that the cementite (Fe_3C) is probably protected by the presence of a carbon layer. An addition of nitrate has also been found to be protective, since in the presence of nitrate, Fe_3C has been detected via *in-situ* synchrotron XRD at all voltages in this work.

7.1.2 The effects of black layers on the stability of corrosion sites

The effects of the black layers in an iron artificial pit have been quantitatively characterised. It has been found that the black layers act as both diffusion and resistive barriers: the diffusion of metal ions is inhibited and a small increase may be induced on the solution resistance. A thick black layer has been observed in the carbon steel (carbon ~0.75%wt.) artificial pit, which is also expected to consist of carbon and carbides, so the corrosion of carbon steel is expected to be affected by such deposits since they will affect both diffusion of metal ions and resistance within corrosion sites.

For a localised corrosion site to be stable in an otherwise passive surface, the rate of metal ion production needs to be at least as great as the rate of metal ion escape, since the metal ion is critical to maintain the aggressive solution in a growing pit [9-13, 37, 54]. The inhibitive effect on diffusion will decrease the rate of metal ion escape, but the resistance effect will tend to decrease the potential at the metal/solution interface, thereby decrease the rate of metal ion production, thus the relative size of these opposing effects will affect the stability of corrosion sites.

The diffusivity of metal ions determined in Chapter 5.2.5 is for a high purity (99.99+%) Fe pit. However, if any solid corrosion products are detected within a pit, a decrease of diffusivity is expected and has to be taken into account in models of pit growth. An investigation similar to Chapter 4 could be carried out to evaluate the extent of the effects of solid corrosion products as diffusion/resistive barriers.

Since the solid corrosion products inhibit the diffusion of metal ions (critical to maintaining the aggressive solution in a growing pit [9-13, 37, 54]), the pit stability product "*ix*" [55] in a pit with corrosion products would decrease compared to a clean pit, which supports the argument in Section 4.3.1 that the solid corrosion products may keep the pit growth stable at a low dissolution rate. Since the stability of corrosion products depends on interfacial potential, and nitrate may noticeably enlarge the passivation region of the corrosion products, the effects of diffusion/resistive barriers are expected to vary with potentials and solutes.

All these factors have to be taken into account in models of pit stability, which, if not considered properly, would induce significant differences from reality.

7.1.3 The effects of nitrate on iron artificial pits

The salt layer in pure HCl has been characterised as isotropic $FeCl_2.4H_2O$, and an addition of trace nitrate does not change the composition of the salt layer, but the salt crystals become anisotropic, and the crystallites may form platelets with (1 2 0) lying horizontally. It is possible that nitrate ions may preferentially adsorb on certain crystal planes and change the growth of crystals, which indicates that nitrate ions can interact with metal chloride salts within a growing corrosion pit.

In mainly nitrate solutions, evidence has been presented that the salt layer is composed of $Fe(NO_3)_2.6H_2O$, the structure of which has been characterised for the first time. Iron passivation in nitrate/chloride solutions involves passivation under a nitrate salt layer, which is thought to be due to the decreasing of acidity at the metal/salt interface, thereby leading to oxide passivation. It has also been found that nitrate can inhibit the dissolution of Fe_3C and induces the precipitation of a black layer on the iron surface at all voltages in this work.

7.1.4 Non-uniform dissolution in 1D artificial pits

1D artificial pit measurements in previous work are usually based on the assumption of uniform dissolution. In this work, the dissolution tends to be uniform under a salt layer (e.g. electropolishing) in chloride solutions, however, non-uniform dissolution has also been observed for some circumstances: active dissolution (salt-free) in chloride solutions; active and/or diffusion-limited dissolution (salt-covered) in nitrate solutions.

Thinning of the iron foil (crevice) was observed during active dissolution (salt-free) in HCl (see Figure 5-15). Surface roughening of electrode surfaces was also observed by SEM measurements after high rate active dissolution (see Figure 5-16). As described in Section 5.3.5.1, when the active dissolution rate (salt-free) is low, the concentration of metal

ions may be insufficient to keep the aggressiveness at the metal surface, so partial passivation can take place. If the dissolution is then driven to a high rate via a potentiodynamic or galvanodynamic control-mode, crevice formation may have to contribute to the dissolution.

In the chloride/nitrate solutions, transitions between dissolution and passivation have been observed during potentiodynamic measurements on an iron artificial pit in 0.1 M $NaNO_3$ + 0.05 M HCl. Bursts of dissolution took place at separate regions on the metal surface, while other regions remained passive. The transitions between passivation and bursts of dissolution induced deep and localised attack, which, once initiated, is an autocatalytic process, i.e. the local concentration of dissolved metal ions is sufficient to promote the attack and prevent passivation, resulting in highly non-uniform dissolution (see Figure 5-17, Figure 5-18, and Figure 5-20). The addition of trace nitrate in 1 M HCl also induced non-uniform dissolution of the metal surface (crystallographic etching) after diffusion-limited dissolution (see Figure 5-11 and Figure 5-13).

7.2 Future work

7.2.1 Effect of corrosion products within carbon steel pits

The influence of the corrosion products within an iron artificial pit in HCl has been characterised. The study can be extended to carbon steels, where more corrosion products and greater effects on the mass transport and resistance are expected. Since the corrosion products inhibit the diffusion of metal ions and may delay the passivation at a low dissolution rate, the repassivation potential of a carbon steel pit may be characterised as a function of carbon content.

7.2.2 Further studies on iron dissolution in chloride/nitrate solutions

The dissolution/passivation transition of iron in 0.1 M $NaNO_3$ and 0.05 M HCl has been ascribed to the passivation under a salt layer, which has been proposed earlier for iron passivation in $HClO_4$ and H_2SO_4 solutions [28]. However, the resolution of the *in-situ* X-ray radiography in this work was not high enough to provide strong evidence for this mechanism, i.e. the salt layer could not be visualised; the passivation under a salt layer could not be clearly observed via the "difference" images. Measurements with higher resolution radiography and thinner iron layers may make it possible to resolve the metal/salt interface.

7.2.3 The investigation of diffusivity as a function of solution chemistry in a growing pit

As described in Section 6.3.1, the studies on the calculations of diffusivity of metal ions are all based on an approximation that an average diffusivity (effective diffusion coefficient) can be used to describe the mass transport within a corrosion pit. However, since the solution concentration in the pit varies along the pit cavity, and the diffusivity varies with solution concentration, an average diffusivity is not sufficient to model the mass transport. Models for localised corrosion have to properly take into account the properties of concentrated solutions (which is very likely to be the case near the bottom of a growing pit), and the role of electrical migration (which has been found to be significant especially for dilute bulk solutions). Therefore it is important to input data on diffusivity and resistivity as a function of solution chemistry, which varies within a growing pit.

8. CONCLUSIONS

1. The influence of solid corrosion products within a corrosion pit has been investigated via an iron artificial pit in 1 M HCl. The corrosion products have been found to be composed of disordered carbon and Fe_3C, which are left on the iron surface during dissolution. The corrosion products form below applied voltage ~0.2 V(SCE), which is ascribed to the lack of dissolution of carbon/Fe_3C at low voltages. A carbon layer may also be protective to Fe_3C. The solid corrosion products act as diffusion/resistive barriers, and decrease the pit stability product "*ix*".
2. *In-situ* synchrotron XRD has been used to characterise the salt layer in iron artificial pits in chloride/nitrate solutions. The salt layer is $FeCl_2.4H_2O$ in 1 M HCl with and without trace nitrate. However, the salt becomes anisotropic in the presence of nitrate, consistent with the formation of plate-like (1 2 0) crystallite planes. In HNO_3 with trace chloride, the salt layer is composed of $Fe(NO_3)_2.6H_2O$.
3. Fe_3C is not dissolved in all the electrolytes containing nitrate at applied voltages between 0.1 V(Ag/AgCl) and 1 V(Ag/AgCl).
4. Addition of trace nitrate in 1 M HCl induces current fluctuations, which increase with increasing applied potential. It is believed to result from the nitrate reduction reaction on the metal surface, which inhibits the dissolution by consuming protons and producing water. The current fluctuations may involve the formation/dissolution of passive film and salt layer.
5. The surface of the iron electrode has been found to be slightly roughened in 1 M HCl in the absence of nitrate, consistent with the dissolution under a salt layer; in the presence of

trace nitrate, the electrode surface becomes crystallographically etched under a salt layer, which may be affected by partial passivation in the presence of nitrate.

6. Crevice formation between metal and epoxy resin for an iron artificial pit may take place during the high-rate active dissolution (salt-free), but the metal surface tends to level during the diffusion-controlled dissolution (salt-covered).
7. Abrupt transitions between dissolution and passivation of iron have been found during the potentiodynamic measurements in 0.1 M $NaNO_3$ and 0.05 M HCl solution, which may be ascribed to the mechanism of "iron passivation under a salt layer" and nitrate reduction reaction. The metal surface is partially passivated during the potentiodynamic measurements, which favour deep and localised attack.
8. The effective diffusion coefficient of metal ions is regarded as the combination of self-diffusion and electrical migration. It has been obtained from high purity iron artificial pits and compared with self-diffusivity of metal ions calculated via OLI. The effective diffusion coefficients of metal ions in an artificial pit in 0.5 M $MgCl_2$ are 0.77×10^{-5} cm^2/s and 0.89×10^{-5} cm^2/s with and without consideration of Mg^{2+} depletion at the pit bottom respectively.
9. Tafel kinetics of iron dissolution has been studied via three methods: potentiodynamic method, transition potential method and galvanodynamic method. The Tafel slope ranges from 56 to 70 mV/decade, which is independent of the $MgCl_2$ and $FeCl_2$ concentration when $FeCl_2$ is saturated. The galvanodynamic method may be applicable to studies on iron dissolution mechanism.

9. Appendix

Ac impedance measurements were carried out on iron wire and foil artificial pits to measure the resistance of solution and salt layer (if any) at a certain voltage, which value was applied for 2 minutes before frequency sweep until the current was stable. This approach is based on that described in previous work [36].

Figure 9-1 shows the Nyquist plots of a 99.5% iron wire (250 µm) artificial pit at different pit depths in pure 1 M HCl at an applied voltage of -0.4 V(SCE), at which the metal dissolved under salt-free conditions. The frequency was swept from 100 kHz to 10 Hz (amplitude 10 mV). It can be seen that the effect of the capacitive component of the system (represented by the imaginary part) is negligible between 100 kHz and 30 kHz, where the value of the real part is regarded as the solution resistance. Therefore, the solution resistance (in the absence of a salt layer) was measured using imposed 50 kHz and 100 kHz ac signals (amplitude 10 mV) in Section 4.2.2.2 and Section 6.2.2, respectively. The plots are consistent with the previous work [36, 45].

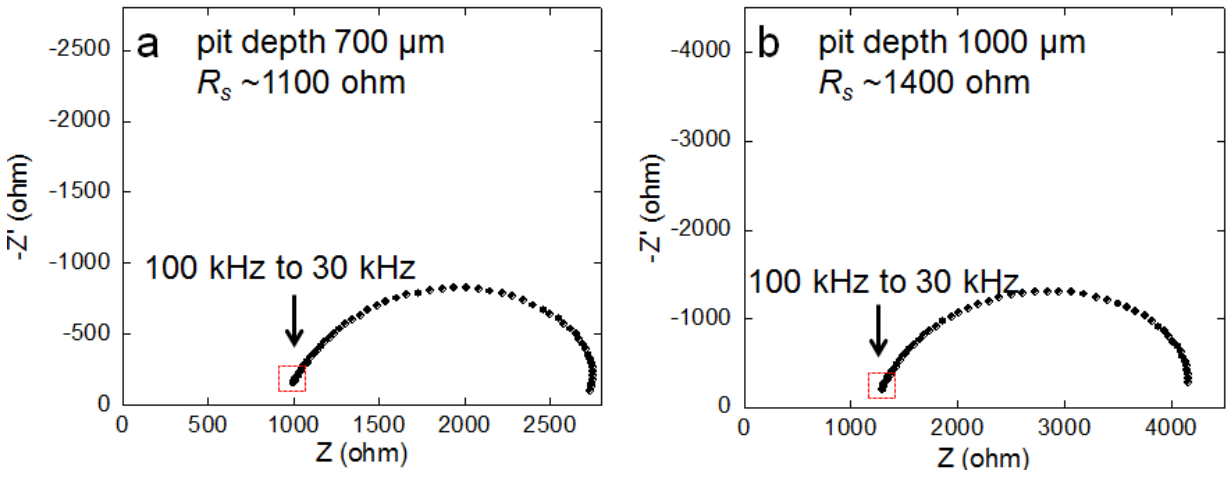

Figure 9-1. Nyquist plots of ac impedance method to measure the solution resistance of a 99.5% Fe wire (250 µm) artificial pit in 1 M HCl at -0.4 V(SCE) at pit depths (a) 700 µm and (b) 1000 µm. The frequency in the figure is between 100 kHz and 10 Hz (amplitude 10 mV).

Figure 9-2. shows the Nyquist plots of a 99.5% iron foil (3 mm wide, 50 μm thick) artificial pit in pure 1 M HCl at 0.1 V and 1 V(Ag/AgCl), at which the metal dissolved under salt-covered conditions. The plots are consistent with the previous work [36, 45]. Figure 9-3 shows the Nyquist plots of the same iron foil artificial pit in 1 M HCl and 20 mM $NaNO_3$ at 0.1 V and 1 V(Ag/AgCl). The data points are scattered, consistent with the current fluctuations observed in the presence of trace nitrate (see Figure 5-2). From both figures, it can be seen that the effect of the capacitive component is negligible between 50 kHz and 30 kHz, where the value of the real part is regarded as the resistance of solution and salt layer. Therefore, the resistance values of solution and salt layer of the artificial pit in 1 M HCl with and without 20 mM $NaNO_3$ were both measured using an imposed 50 kHz ac signal (amplitude 10 mV) in Section 5.2.1.2.

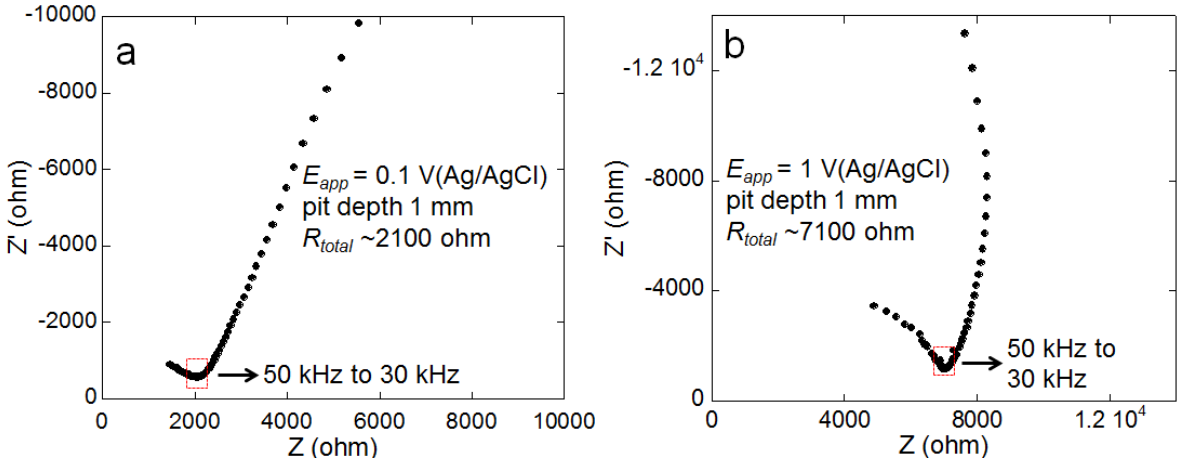

Figure 9-2. Nyquist plots of ac impedance method to measure the resistance of solution and salt layer of a 99.5% Fe foil (3 mm wide, 50 μm thick) artificial pit in 1 M HCl at (a) 0.1 V(Ag/AgCl) and (b) 1 V(Ag/AgCl). The frequency in the figure is between 100 kHz and 200 Hz (amplitude 10 mV). Pit depth ca. 1 mm.

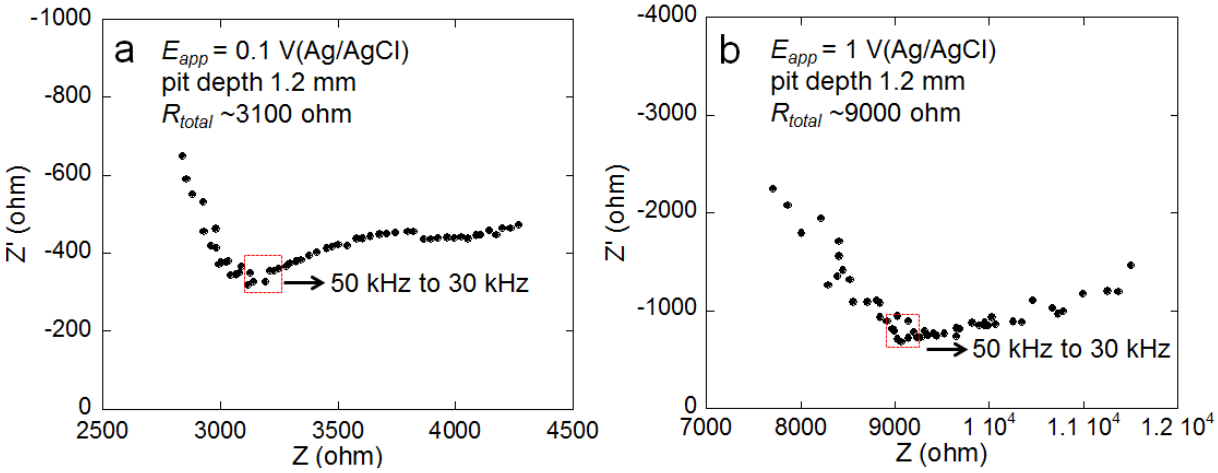

Figure 9-3. Nyquist plots of ac impedance method to measure the resistance of solution and salt layer of a 99.5% Fe foil (3 mm wide, 50 μm thick) artificial pit in 1 M HCl and 20 mM $NaNO_3$ at (a) 0.1 V(Ag/AgCl) and (b) 1 V(Ag/AgCl). The frequency in the figure is between 100 kHz and 200 Hz (amplitude 10 mV). Pit depth ca. 1.2 mm.

Figure 9-4 shows the Nyquist plots of a 99.99% iron foil (0.7 mm wide, 25 μm thick) artificial pit in 0.1 M HNO_3 and 0.05 M HCl at 0.2 V and 0.6 V(Ag/AgCl). It can be seen that the effect of the capacitive component is negligible between 50 kHz and 30 kHz, where the value of the real part is regarded as the resistance of solution and salt layer (if any). Therefore, the resistance values of the solution and salt layer (if any) in 0.1 M HNO_3 and 0.05 M HCl was measured using an imposed 50 kHz ac signal (amplitude 10 mV) in Section 5.2.5.2.

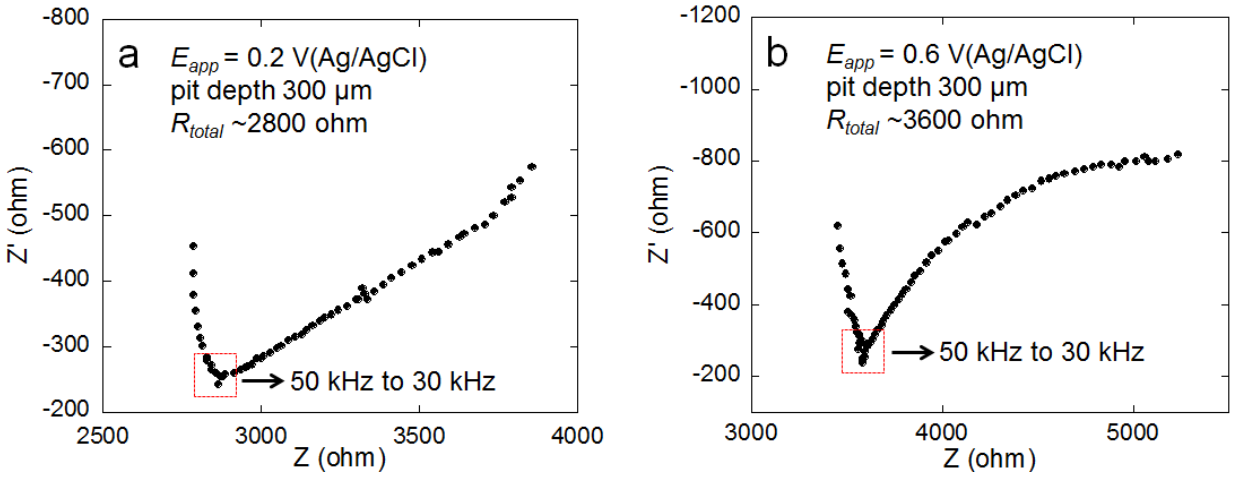

Figure 9-4. Nyquist plots of ac impedance method to measure the resistance of solution and salt layer (if any) of a 99.99% Fe foil (0.7 mm wide, 25 μm thick) artificial pit in 0.1 M HNO_3 and 0.05 M HCl at (a) 0.2 V(Ag/AgCl) and (b) 0.6 V(Ag/AgCl). The frequency in the figure is between 100 kHz and 100 Hz (amplitude 10 mV). Pit depth ca. 300 μm.

10. REFERENCES

1. NDA, *UK Radioactive Higher Activity Waste Storage Review (NDA Reports March 31 2009)*. 2009: http://www.nda.gov.uk/publication/uk-radioactive-higher-activity-waste-storage-review-march-2009/.
2. NDA, *Review of the corrosion performance of selected metals as canister materials for UK spent fuel and or HLW – Appendix B (carbon steel) (RWM Reports July 17 2010)*. 2010: http://www.nda.gov.uk/publication/review-of-the-corrosion-performance-of-selected-metals-as-canister-materials-for-uk-spent-fuel-and-or-hlw-appendix-b-carbon-steel/.
3. Li, X.J., *PhD Thesis: Understanding liquid-air interface corrosion of steel in simplified liquid nuclear waste solutions*, in *Materials Science and Engineering*. 2013, The Ohio State University: Ohio, USA.
4. Edgemon, G.L., V.S. Anda, H.S. Barman, M.E. Johnson, and K.D. Boomer, *History and operation of the Hanford high-level waste storage tanks.* Corrosion, 2009. **65**(3): p. 163-174.
5. Lillard, R.S., G. Vasquez, and D.F. Bahr, *Influence of nitrate on pit stability in austenitic stainless steel.* Corrosion, 2010. **66**(7).
6. Razygraev, V., M. Lebedeva, and I. Korchak, *A Method for determining safe concentrations of chloride ions in pitting corrosion of steels in nitrate media.* Protection of Metals, 2008. **44**(7): p. 743-749.
7. Sazou, D. and M. Pagitsas, *Nitrate ion effect on the passive film breakdown and current oscillations at iron surfaces polarized in chloride-containing sulfuric acid solutions.* Electrochimica Acta, 2002. **47**(10): p. 1567-1578.
8. King, F., *Overview of a carbon steel container corrosion model for a deep geological repository in sedimentary rock (Nuclear Waste Management Organization Technical Report)*. 2007, Integrity Corrosion Consulting Limited: http://www.nwmo.ca/uploads_managed/MediaFiles/5_NWMOTR-2007-01_CSteelModel_R0.pdf.
9. Davenport, A.J., *Second Year Corrosion Lecture Notes*. 2013, University of Birmingham.
10. Frankel, G.S., *Pitting corrosion*, in *ASM Handbook*, J. S. D. Cramer and B. S. Covino, Jr., Editor. 2003, ASM International: Materials Park, OH.
11. Revie, R.W., *Uhlig's Corrosion Handbook*. 3rd ed. 2011: John Wiley & Sons Ltd.
12. Frankel, G.S., *Pitting corrosion of metals - A review of the critical factors.* Journal of the Electrochemical Society, 1998. **145**(6): p. 2186-2198.
13. Galvele, J.R., *Transport processes and mechanism of pitting of metals.* Journal of the Electrochemical Society, 1976. **123**(4): p. 464-474.
14. Wilde, B.E. and E. Williams, *Use of current/voltage curves for study of localized corrosion and passivity breakdown on stainless steels in chloride media.* Electrochimica Acta, 1971. **16**(11): p. 1971-&.
15. Suzuki, T., M. Yamabe, and Y. Kitamura, *Composition of anolyte within pit anode of austenitic stainless-steels in chloride solution.* Corrosion, 1973. **29**(1): p. 18-22.
16. Mankowski, J. and Z. Szklarskasmialowska, *Studies on accumulation of chloride-ions in pits growing during anodic polarization.* Corrosion Science, 1975. **15**(8): p. 493-501.

17. Kelly, R.G., J.R. Scully, D. Shoesmith, and R.G. Buchheit, *Electrochemical Techniques in Corrosion Science and Engneering*. 2003, New York: Marcel Dekker Inc.
18. Frankel, G.S. and N. Sridhar, *Understanding localized corrosion.* Materials Today, 2008. **11**(10): p. 38-44.
19. Suzuki, T. and Y. Kitamura, *Critical potential for growth of localized corrosion of stainless-steel in chloride media.* Corrosion, 1972. **28**(1): p. 1-&.
20. Steinsmo, U. and H.S. Isaacs, *Dissolution and repassivation kinetics of Fe-Cr alloys in pit solutions. 1. Effect of the surface salt layer.* Journal of the Electrochemical Society, 1993. **140**(3): p. 643-653.
21. Isaacs, H.S., J.H. Cho, M.L. Rivers, and S.R. Sutton, *In-situ X-ray microprobe study of salt layers during anodic-dissolution of stainless-steel in chloride solution.* Journal of the Electrochemical Society, 1995. **142**(4): p. 1111-1118.
22. Beck, T.R., *Pitting of titanium. 2. one-dimensional pit experiments.* Journal of the Electrochemical Society, 1973. **120**(10): p. 1317-1324.
23. Alkire, R., D. Ernsberger, and T.R. Beck, *Occurrence of salt films during repassivation of newly generated metal-surfaces.* Journal of the Electrochemical Society, 1978. **125**(9): p. 1382-1388.
24. Hoar, T.P. and J.A.S. Mowat, *Mechanism of electro-polishing.* Nature, 1950. **165**(4185): p. 64-65.
25. Hoar, T.P., D.C. Mears, and G.P. Rothwell, *The relationships between anodic passivity, brightening and pitting.* Corrosion Science, 1965. **5**(4): p. 279-289.
26. Novakovs.Vm and A.N. Sorokina, *Model study of chloride pitting in 18-8 stainless steel.* Corrosion Science, 1966. **6**(5): p. 227-&.
27. Kuo, H.C. and D. Landolt, *Galvanostatic transient study of anodic film formation on iron in concentrated chloride media.* Corrosion Science, 1976. **16**(12): p. 915-922.
28. Beck, T.R., *Formation of salt films during passivation of iron.* Journal of the Electrochemical Society, 1982. **129**(11): p. 2412-2418.
29. Russell, P. and J. Newman, *Anodic-dissolution of iron in acidic sulfate electrolytes. 1. formation and growth of a porous salt film.* Journal of the Electrochemical Society, 1986. **133**(1): p. 59-69.
30. Kuo, H.C. and D. Landolt, *Rotating-disk electrode study of anodic dissolution of iron in concentrated chloride media.* Electrochimica Acta, 1975. **20**(5): p. 393-399.
31. Beck, T.R. and R.C. Alkire, *Occurrence of salt films during initiation and growth of corrosion pits.* Journal of the Electrochemical Society, 1979. **126**(10): p. 1662-1666.
32. Danielson, M.J., *Transport properties of salt films on nickel in 0.5 N HCl.* Journal of the Electrochemical Society, 1988. **135**(6): p. 1326-1332.
33. Isaacs, H.S., *Behavior of resistive layers in localized corrosion of stainless steel.* Journal of the Electrochemical Society, 1973. **120**(11): p. 1456-1462.
34. Tester, J.W. and H.S. Isaacs, *Diffusional effects in simulated localized corrosion.* Journal of the Electrochemical Society, 1975. **122**(11): p. 1438-1445.
35. Newman, R.C. and M.A.A. Ajjawi, *A microelectrode study of the nitrate effect on pitting of stainless steels.* Corrosion Science, 1986. **26**(12): p. 1057-1063.
36. Grimm, R.D., A.C. West, and D. Landolt, *AC impedance study of anodically formed salt films on iron in chloride solution.* Journal of the Electrochemical Society, 1992. **139**(6): p. 1622-1629.

37. Gaudet, G.T., W.T. Mo, T.A. Hatton, J.W. Tester, J. Tilly, H.S. Isaacs, and R.C. Newman, *Mass transfer and electrochemical kinetic interactions in localized pitting corrosion.* AIChE Journal, 1986. **32**(6): p. 949-958.
38. Tang, Y.C. and A.J. Davenport, *Magnetic field effects on the corrosion of artificial pit electrodes and pits in thin films.* Journal of the Electrochemical Society, 2007. **154**(7): p. C362-C370.
39. Laycock, N.J. and R.C. Newman, *Localised dissolution kinetics, salt films and pitting potentials.* Corrosion Science, 1997. **39**(10-11): p. 1771-1790.
40. Hunkeler, F., A. Krolikowski, and H. Bohni, *A study of the solid salt film on nickel and stainless-steel.* Electrochimica Acta, 1987. **32**(4): p. 615-620.
41. Vetter, K.J. and Strehblo.Hh, *Formation and shape of corrosion pits in localized corrosion on iron theoretical results pertaining to localized corrosion.* Berichte Der Bunsen-Gesellschaft Fur Physikalische Chemie, 1970. **74**(10): p. 1024-&.
42. West, A.C., R.D. Grimm, D. Landolt, C. Deslouis, and B. Tribollet, *Electrohydrodynamic impedance study of anodically formed salt films on iron in chloride solutions.* Journal of Electroanalytical Chemistry, 1992. **330**(1-2): p. 693-706.
43. Clerc, C. and D. Landolt, *Ac impedance study of anodic films on nickel in LiCl.* Electrochimica Acta, 1988. **33**(7): p. 859-871.
44. Grimm, R.D. and D. Landolt, *Salt films formed during mass-transport controlled dissolution of iron-chromium alloys in concentrated chloride media.* Corrosion Science, 1994. **36**(11): p. 1847-1868.
45. Sridhar, N. and D.S. Dunn, *In situ study of salt film stability in simulated pits of nickel by Raman and electrochemical impedance spectroscopies.* Journal of the Electrochemical Society, 1997. **144**(12): p. 4243-4253.
46. Lohrengel, M.M., I. Kluppel, C. Rosenkranz, H. Bettermann, and J.W. Schultze, *Microscopic investigations of electrochemical machining of Fe in NaNO3.* Electrochimica Acta, 2003. **48**(20-22): p. 3203-3211.
47. Lohrengel, M.M. and C. Rosenkranz, *Microelectrochemical surface and product investigations during electrochemical machining (ECM) in NaNO3.* Corrosion Science, 2005. **47**(3): p. 785-794.
48. Lohrengel, M.M., *Pulsed electrochemical machining of iron in NaNO3: Fundamentals and new aspects.* Materials and Manufacturing Processes, 2005. **20**(1): p. 1-8.
49. Rosenkranz, C., M.M. Lohrengel, and J.W. Schultze, *The surface structure during pulsed ECM of iron in NaNO3.* Electrochimica Acta, 2005. **50**(10): p. 2009-2016.
50. Isaacs, H.S. and S.M. Huang, *Behavior of dissolved molybdenum during localized corrosion of austenitic stainless steel.* Journal of the Electrochemical Society, 1996. **143**(12): p. L277-L279.
51. Rayment, T., A.J. Davenport, A.J. Dent, J.P. Tinnes, R.J.K. Wiltshire, C. Martin, G. Clark, P. Quinn, and J.F.W. Mosselmans, *Characterisation of salt films on dissolving metal surfaces in artificial corrosion pits via in situ synchrotron X-ray diffraction.* Electrochemistry Communications, 2008. **10**(6): p. 855-858.
52. Hammons, J.A., A.J. Davenport, S.M. Ghahari, M. Monir, J.-P. Tinnes, M. Amri, N. Terrill, F. Marone, R. Mokso, M. Stampanoni, and T. Rayment, *Interfacial Phenomena during Salt Layer Formation under High Rate Dissolution Conditions.* The journal of physical chemistry. B, 2013. **117**(22): p. 6724-32.
53. Enerhaug, J., U.M. Steinsmo, O. Grong, and L.R. Hellevik, *Dissolution and repassivation kinetics of a 12.3Cr-2.6Mo-6.5Ni super martensitic stainless steel - A*

comparative study. Journal of the Electrochemical Society, 2002. **149**(6): p. B256-B264.
54. Newman, R.C. and H.S. Isaacs, *Diffusion-coupled active dissolution in the localized corrosion of stainless-steels.* Journal of the Electrochemical Society, 1983. **130**(7): p. 1621-1624.
55. Pistorius, P.C. and G.T. Burstein, *Metastable pitting corrosion of stainless-steel and the transition to stability.* Philosophical Transactions of the Royal Society of London Series a-Mathematical Physical and Engineering Sciences, 1992. **341**(1662): p. 531-559.
56. Steinsmo, U. and H.S. Isaacs, *The dissolution and repassivation kinetics of Fe-Cr alloys in pit solutions.* Corrosion Science, 1993. **35**(1-4): p. 83-88.
57. Pickerin.Hw and Frankent.Rp, *Mechanism of localized corrosion of iron and stainless-steel. 1. electrochemical studies.* Journal of the Electrochemical Society, 1972. **119**(10): p. 1297-&.
58. Ghahari, S.M., *PhD thesis: In-situ synchrotron X-ray characterisation and modelling of pitting corrosion of stainless steel*, in *School of Metallurgy and Materials*. 2012, University of Birmingham: Birmingham, UK.
59. Haisch, T., E.J. Mittemeijer, and J.W. Schultze, *On the influence of microstructure and carbide content of steels on the electrochemical dissolution process in aqueous NaCl-electrolytes.* Materials and Corrosion-Werkstoffe Und Korrosion, 2002. **53**(10): p. 740-755.
60. Green, J.A.S. and R.N. Parkins, *Electrochemical properties of ferrite and cementite in relation to stress corrosion of mild steels in nitrate solutions.* Corrosion, 1968. **24**(3): p. 66-&.
61. Haisch, T., E. Mittemeijer, and J.W. Schultze, *Electrochemical machining of the steel 100Cr6 in aqueous NaCl and NaNO3 solutions: microstructure of surface films formed by carbides.* Electrochimica Acta, 2001. **47**(1-2): p. 235-241.
62. Flis, J., M. Ziomek-Moroz, and I. Flis-Kabulska, *Effect of carbon on corrosion and passivation of iron in hot concentrated NaOH solution in relation to caustic stress corrosion cracking.* Corrosion Science, 2009. **51**(8): p. 1696-1701.
63. Ingham, B., M. Ko, G. Kear, P. Kappen, N. Laycock, J.A. Kimpton, and D.E. Williams, *In situ synchrotron X-ray diffraction study of surface scale formation during CO(2) corrosion of carbon steel at temperatures up to 90 degrees C.* Corrosion Science, 2010. **52**(9): p. 3052-3061.
64. Nesic, S. and L. Lunde, *Carbon-dioxide corrosion of carbon-steel in 2-phase flow.* Corrosion, 1994. **50**(9): p. 717-727.
65. Raspini, I., E. Chung, and C. Saragovi, *Corrosion layers of low-alloy carbon steels in CO2(g)-saturated solutions by Mossbauer spectroscopy.* Corrosion, 2000. **56**(8): p. 832-838.
66. Kawaley, G., *PhD thesis: Localised corrosion of iron in food products*, in *School of Metallurgy and Materials*. 2008, University of Birmingham: Birmingham, UK.
67. Mi, N., *PhD thesis: Synchrotron X-ray Studies of Atmospheric Pitting Corrosion of Stainless Steel*, in *Metallurgy and Materials*. 2013, University of Birmingham: Birmingham, UK.
68. Trethewey, K.R. and J. Chamberlain, *Corrosion: for Science and Engineering*. 2nd ed. 1995: Longman Scientific&Technical.

69. Laycock, N.J. and S.P. White, *Computer simulation of single pit propagation in stainless steel under potentiostatic control.* Journal of the Electrochemical Society, 2001. **148**(7): p. B264-B275.
70. Hoar, T.P. and G.P. Rothwell, *The influence of solution flow on anodic polishing. Copper in aqueous o-phosphoric acid.* Electrochimica Acta, 1964. **9**(2): p. 135-150.
71. Hoar, T.P., *Production and breakdown of passivity of metals.* Corrosion Science, 1967. **7**(6): p. 341-&.
72. Sato, N., *The stability of pitting dissolution of metals in aqueous solution.* Journal of the Electrochemical Society, 1982. **129**(2): p. 260-264.
73. Sato, N., *An overview on the passivity of metals.* Corrosion Science, 1990. **31**: p. 1-19.
74. Sato, N., *The stability of localized corrossion.* Corrosion Science, 1995. **37**(12): p. 1947-1967.
75. Schwenk, W., *Theory of stainless steel pitting.* Corrosion, 1964. **20**(4): p. T129-&.
76. Ke, R.R. and R. Alkire, *Initiation of corrosion pits at inclusions on 304 stainless steel.* Journal of the Electrochemical Society, 1995. **142**(12): p. 4056-4062.
77. Beck, T.R., *Effect of hydrodynamics on pitting.* Corrosion, 1977. **33**(1): p. 9-13.
78. Frankent.Rp and Pickerin.Hw, *Mechanism of localized corrosion of iron and stainless steel. 2. Morphological studies.* Journal of the Electrochemical Society, 1972. **119**(10): p. 1304-&.
79. Sazou, D., A. Diamantopoulou, and M. Pagitsas, *Complex periodic and chaotic current oscillations related to different states of the localized corrosion of iron in chloride-containing sulfuric acid solutions.* Journal of Electroanalytical Chemistry, 2000. **489**(1-2): p. 1-16.
80. Sazou, D. and M. Pagitsas, *Non-linear dynamics of the passivity breakdown of iron in acidic solutions.* Chaos Solitons & Fractals, 2003. **17**(2-3): p. 505-522.
81. Sazou, D. and M. Pagitsas, *Electrochemical instabilities due to pitting corrosion of iron.* Russian Journal of Electrochemistry, 2006. **42**(5): p. 476-490.
82. Mao, K.W. and D.T. Chin, *Anodic behavior of mild-steel in NaClO3 at high-current densities.* Journal of the Electrochemical Society, 1974. **121**(2): p. 191-194.
83. Datta, M. and D. Landolt, *On the role of mass-transport in high-rate dissolution of iron and nickel in ECM electrolytes. 2. chlorate and nitrate solutions.* Electrochimica Acta, 1980. **25**(10): p. 1263-1271.
84. Mao, K.W., M.A. Laboda, and J.P. Hoare, *Anodic film studies on steel in nitrate-based electrolytes for electrochemical machining.* Journal of the Electrochemical Society, 1972. **119**(4): p. 419-&.
85. Landolt, D., *Fundamental aspects of electropolishing.* Electrochimica Acta, 1987. **32**(1): p. 1-11.
86. Leidheiser, H. and A.T. Gwathmey, *The influence of crystal face on the electrochemical properties of a single crystal of copper.* Transactions of the Electrochemical Society, 1947. **91**: p. 95-110.
87. Datta, M. and D. Landolt, *On the role of mass-transport in high-rate dissolution of iron and nickel in ECM electrolytes. 1. chloride solutions.* Electrochimica Acta, 1980. **25**(10): p. 1255-1262.
88. Evans, U.R., *Behaviour of metals in nitric acid.* Transactions of the Faraday Society, 1944. **40**: p. 0120-0129.
89. Balbaud, F., G. Sanchez, G. Santarini, and G. Picard, *Cathodic reactions involved in corrosion processes occurring in concentrated nitric acid at 100 degrees C.* European Journal of Inorganic Chemistry, 2000(4): p. 665-674.

90. Balbaud, F., G. Sanchez, G. Santarini, and G. Picard, *Equilibria between gas and liquid phases for concentrated aqueous solutions of nitric acid.* European Journal of Inorganic Chemistry, 1999(2): p. 277-285.
91. Balbaud, F., G. Sanchez, P. Fauvet, G. Santarini, and G. Picard, *Mechanism of corrosion of AISI 304L stainless steel in the presence of nitric acid condensates.* Corrosion Science, 2000. **42**(10): p. 1685-1707.
92. Armstrong, R.D., G.E. Cleland, and G.O.H. Whillock, *Effect of dissolved chromium species on the corrosion of stainless steel in nitric acid.* Journal of Applied Electrochemistry, 1998. **28**(11): p. 1205-1211.
93. Takeuchi, M. and G.O.H. Whillock, *Effect of NOx gases on corrosion of stainless steel in hot nitric acid solutions.* British Corrosion Journal, 2002. **37**(3): p. 199-205.
94. Fauvet, P., F. Balbaud, R. Robin, Q.T. Tran, A. Mugnier, and D. Espinoux, *Corrosion mechanisms of austenitic stainless steels in nitric media used in reprocessing plants.* Journal of Nuclear Materials, 2008. **375**(1): p. 52-64.
95. Podestá, J.J. and A.J. Arvía, *Kinetics of the anodic dissolution of iron in concentrated ionic media: galvanostatic and potentiostatic measurements.* Electrochimica Acta, 1965. **10**(2): p. 171-182.
96. Uhlig, H.H. and J.R. Gilman, *Pitting of 18-8 stainless steel in ferric chloride inhibited by nitrates.* Corrosion, 1964. **20**(9): p. T289-&.
97. Leckie, H.P. and H.H. Uhlig, *Environmental factors affecting critical potential for pitting in 18-8 stainless steel.* Journal of the Electrochemical Society, 1966. **113**(12): p. 1262-&.
98. Toshima, Y., T. Hashimoto, K. Naitoh, E. Yamamoto, and Y. Kogawa, *Influence of nitrate on pitting of type-316L stainless-steel in FGD processes.* Journal of Chemical Engineering of Japan, 1982. **15**(1): p. 11-16.
99. Yang, S.F. and D.D. Macdonald, *Theoretical and experimental studies of the pitting of type 316L stainless steel in borate buffer solution containing nitrate ion.* Electrochimica Acta, 2007. **52**(5): p. 1871-1879.
100. Macdonald, D.D., *Passivity - the key to our metals-based civilization.* Pure and Applied Chemistry, 1999. **71**(6): p. 951-978.
101. Anderko, A., N. Sridhar, and D.S. Dunn, *A general model for the repassivation potential as a function of multiple aqueous solution species.* Corrosion Science, 2004. **46**(7): p. 1583-1612.
102. Ramya, S., T. Anita, H. Shaikh, and R.K. Dayal, *Laser Raman microscopic studies of passive films formed on type 316LN stainless steels during pitting in chloride solution.* Corrosion Science, 2010. **52**(6): p. 2114-2121.
103. Bandy, R. and D. Vanrooyen, *Properties of nitrogen-containing stainless alloy designed for high-resistance to pitting.* Corrosion, 1985. **41**(4): p. 228-233.
104. Siantar, D.P., C.G. Schreier, C.S. Chou, and M. Reinhard, *Treatment of 1,2-dibromo-3-chloropropane and nitrate-contaminated water with zero-valent iron or hydrogen/palladium catalysts.* Water Research, 1996. **30**(10): p. 2315-2322.
105. Cheng, I.F., R. Muftikian, Q. Fernando, and N. Korte, *Reduction of nitrate to ammonia by zero-valent iron.* Chemosphere, 1997. **35**(11): p. 2689-2695.
106. Huang, C.P., H.W. Wang, and P.C. Chiu, *Nitrate reduction by metallic iron.* Water Research, 1998. **32**(8): p. 2257-2264.
107. Zawaideh, L.L. and T.C. Zhang, *The effects of pH and addition of an organic buffer (HEPES) on nitrate transformation in Fe-0-water systems.* Water Science and Technology, 1998. **38**(7): p. 107-115.

108. Alowitz, M.J. and M.M. Scherer, *Kinetics of nitrate, nitrite, and Cr(VI) reduction by iron metal.* Environmental Science & Technology, 2002. **36**(3): p. 299-306.
109. Huang, Y.H. and T.C. Zhang, *Effects of low pH on nitrate reduction by iron powder.* Water Research, 2004. **38**(11): p. 2631-2642.
110. Alexander, B.J. and R.T. Foley, *Corrosion products of iron dissolution-dependence on anions in solution.* Corrosion, 1976. **32**(7): p. 297-302.
111. Buresh, R.J. and J.T. Moraghan, *Chemical reduction of nitrate by ferrous iron.* Journal of Environmental Quality, 1976. **5**(3): p. 320-325.
112. Huang, Y.H., T.C. Zhang, P.J. Shea, and S.D. Comfort, *Effects of oxide coating and selected cations on nitrate reduction by iron metal.* Journal of Environmental Quality, 2003. **32**(4): p. 1306-1315.
113. Brossia, C.S. and R.G. Kelly, *Influence of alloy sulfur content and bulk electrolyte composition on crevice corrosion initiation of austenitic stainless steel.* Corrosion, 1998. **54**(2): p. 145-154.
114. Newman, R.C. and T. Shahrabi, *The effect of alloyed nitrogen or dissolved nitrate ions on the anodic behavior of austenitic stainless-steel in hydrochloric-acid.* Corrosion Science, 1987. **27**(8): p. 827-838.
115. Ortiz, M.R., M.A. Rodriguez, R.M. Carranza, and R.B. Rebak, *Oxyanions as inhibitors of chloride-induced crevice corrosion of Alloy 22.* Corrosion Science, 2013. **68**: p. 72-83.
116. Wexler, S.B.D. and J.R. Galvele, *Anodic behavior of aluminium straining and a mechanism for pitting.* Journal of the Electrochemical Society, 1974. **121**(10): p. 1271-1276.
117. Grabke, H.J., *The role of nitrogen in the corrosion of iron and steels.* Isij International, 1996. **36**(7): p. 777-786.
118. Misawa, T. and H. Tanabe, *In-situ observation of dynamic reacting species at pit precursors of nitrogen-bearing austenitic stainless steels.* Isij International, 1996. **36**(7): p. 787-792.
119. Yashiro, H., D. Hirayasu, and N. Kumagai, *Effect of nitrogen alloying on the pitting of type 310 stainless steel.* Isij International, 2002. **42**(12): p. 1477-1482.
120. Uhlig, H.H. and E.W. Cook, *Mechanism of inhibiting stress corrosion cracking of 18-8 stainless steel in MgCl2 by acetates and nitrates.* Journal of the Electrochemical Society, 1969. **116**(2): p. 173-&.
121. Kolman, D.G., D.K. Ford, D.P. Butt, and T.O. Nelson, *Corrosion of 304 stainless steel exposed to nitric acid-chloride environments.* Corrosion Science, 1997. **39**(12): p. 2067-2093.
122. Suresh, G., V.R. Raju, U.K. Mudali, and R.K. Dayal, *Corrosion assessment of type 304L stainless steel in nitric acid.* Corrosion Engineering Science and Technology, 2003. **38**(4): p. 309-312.
123. Tomashov, N.D., G.P. Chernova, and M.Y. Rutten, *Electrochemical-behavior of stainless-steel in nitric-acid solutions with added ferric-chloride and hydrochloric-acid.* Protection of Metals, 1982. **18**(6): p. 671-678.
124. Gray, J.J., J.R. Hayes, G.E. Gdowski, and C.A. Orme, *Inhibiting effects of nitrates on the passive film breakdown of alloy 22 in chloride environments.* Journal of the Electrochemical Society, 2006. **153**(5): p. B156-B161.
125. Gray, J.J. and C.A. Orme, *Electrochemical impedance spectroscopy study of the passive films of alloy 22 in low pH nitrate and chloride environments.* Electrochimica Acta, 2007. **52**(7): p. 2370-2375.

126. Matsuda, S. and H.H. Uhlig, *Effect of pH, sulfates, and chlorides on behavior of sodium chromate and nitrite as passivators for steel.* Journal of the Electrochemical Society, 1964. **111**(2): p. 156-161.
127. Chou, Y.L., J.W. Yeh, and H.C. Shih, *Pitting Corrosion of Co(1.5)CrFeNi(1.5)Ti(0.5)Mo(0.1) in Chloride-Containing Nitrate Solutions.* Corrosion, 2011. **67**(6).
128. Galvez, J.L., J. Dufour, C. Negro, and F. Lopez-Mateos, *Determination of iron and chromium fluorides solubility for the treatment of wastes from stainless steel mills.* Chemical Engineering Journal, 2008. **136**(2-3): p. 116-125.
129. Zakeri, M. and M.H. Moayed, *Investigation on the effect of nitrate ion on the critical pitting temperature of 2205 duplex stainless steel along a mechanistic approach using pencil electrode.* Corrosion Science, 2014. **85**(0): p. 222-231.
130. Ma, H.Y., C. Yang, G.Y. Li, W.J. Guo, S.H. Chen, and J.L. Luo, *Influence of nitrate and chloride ions on the corrosion of iron.* Corrosion, 2003. **59**(12): p. 1112-1119.
131. Li, W.H., X.L. Wang, and K. Nobe, *Electrodissolution kinetics of iron in chloride solutions. 7. experimental potential curret oscillations.* Journal of the Electrochemical Society, 1990. **137**(4): p. 1184-1188.
132. Li, W.H., K. Nobe, and A.J. Pearlstein, *Electrodissolution kinetics of iron in chloride solutions. 8. chaos in potential current oscillations.* Journal of the Electrochemical Society, 1993. **140**(3): p. 721-728.
133. Arai, Y.M., K.; Honda, T.; Takahashi, H., *Effects of Iron (III) Ions on Corrosion of Stainless Steel in Concentrated Nitric Acid Solutions at High Temperature.* Zairyo-to-kankyo, 2002. **51**(1): p. 23-29.
134. Priya, R., S. Ningshen, and U.K. Mudali, *Influence of Oxidizing Ion Concentration on the Corrosion Resistance of Type 304L Stainless Steel in Nitric Acid Medium.* Corrosion, 2013. **69**(4): p. 335-344.
135. Ningshen, S., U.K. Mudali, S. Ramya, and B. Raj, *Corrosion behaviour of AISI type 304L stainless steel in nitric acid media containing oxidizing species.* Corrosion Science, 2011. **53**(1): p. 64-70.
136. Willmott, P., *An Introduction to Synchrotron Radiation: Techniques and Applications*. 2011: John Wiley & Sons, Ltd.
137. Diamond Light Source. *About Synchrotrons*. 2014 (cited 03/2014); Available from: http://www.diamond.ac.uk/Home/About/FAQs/About-Synchrotrons.
138. ESRF. *What is a synchrotron?* 2014 (cited 03/2014); Available from: http://www.esrf.eu/about/synchrotron-science/synchrotron.
139. Lightsources. *What Is a Light Source*. 2014 (cited 03/2014); Available from: http://www.lightsources.org/what-light-source.
140. Dowsett, M., A. Adriaens, C. Martin, and L. Bouchenoire, *The Use of Synchrotron X-rays To Observe Copper Corrosion in Real Time.* Analytical Chemistry, 2012. **84**(11): p. 4866-4872.
141. Jin, Y., X.S. Sun, and Q. Xue, *X-ray Diffraction Analysis Techniques*. 2008: National Defense Industry Press, Beijing.
142. Ghahari, S.M., D.P. Krouse, N.J. Laycock, T. Rayment, C. Padovani, T. Suter, R. Mokso, F. Marone, M. Stampanoni, M. Monir, and A.J. Davenport, *Pitting corrosion of stainless steel: measuring and modelling pit propagation in support of damage prediction for radioactive waste containers.* Corrosion Engineering Science and Technology, 2011. **46**(2): p. 205-211.

143. Laycock, N.J., D.P. Krouse, S.M. Ghahari, A.J. Davenport, T. Rayment, and C. Padovani, *Localised dissolution kinetics from fast in-situ radiograhy of propagating pits in stainless steel and implications for modeling pitting corrosion over long time-scales*, in *Critical Factors in Localized Corrosion 7*, J.R. Kish, G.S. Frankel, A.J. Davenport, N. Birbilis, and K. Zavadil, Editors. 2012, Electrochemical Soc Inc: Pennington. p. 3-16.
144. Nagy, Z. and H. You, *Radiolytic effects on the in-situ investigation of buried interfaces with synchrotron X-ray techniques.* Journal of Electroanalytical Chemistry, 1995. **381**(1-2): p. 275-279.
145. Nagy, Z. and H. You, *Applications of surface X-ray scattering to electrochemistry problems.* Electrochimica Acta, 2002. **47**(19): p. 3037-3055.
146. Mesu, J.G., A.M. Beale, F.M.F. de Groot, and B.M. Weckhuysen, *Observing the influence of X-rays on aqueous copper solutions by in-situ combined video/XAFS/UV-Vis spectroscopy*, in *X-ray Absorption Fine Structure-XAFS13*, B. Hedman and P. Painetta, Editors. 2007, Amer Inst Physics: Melville. p. 818-820.
147. Pastina, B., J.A. LaVerne, and S.M. Pimblott, *Dependence of molecular hydrogen formation in water on scavengers of the precursor to the hydrated electron.* Journal of Physical Chemistry A, 1999. **103**(29): p. 5841-5846.
148. Advent Rearch Materials. *Product information Tempers*. 2014 (cited 10/2014); Available from: http://www.advent-rm.com/information/glossary.aspx?definition=tempers.
149. OLI Systems. *An electrolyte chemistry laboratory on your PC*. 2014 (cited 04/2014); Available from: http://www.olisystems.com/new-streamanalyzer.
150. Wang, P.M., A. Anderko, and R.D. Young, *Modeling electrical conductivity in concentrated and mixed-solvent electrolyte solutions.* Industrial & Engineering Chemistry Research, 2004. **43**(25): p. 8083-8092.
151. Anderko, A. and M.M. Lencka, *Modeling self-diffusion in multicomponent aqueous electrolyte systems in wide concentration ranges.* Industrial & Engineering Chemistry Research, 1998. **37**(7): p. 2878-2888.
152. Wang, P.M. and A. Anderko, *Modeling self-diffusion in mixed-solvent electrolyte solutions.* Industrial & Engineering Chemistry Research, 2003. **42**(14): p. 3495-3504.
153. Wang, P.M., A. Anderko, and R.D. Young, *A speciation-based model for mixed-solvent electrolyte systems.* Fluid Phase Equilibria, 2002. **203**(1-2): p. 141-176.
154. OLI Systems. *A Guide to Using OLI Analyzer Studio version 3.2*. 2011 (cited 04/2014); Available from: http://support.olisystems.com/Documents.
155. Mosselmans, J.F.W., P.D. Quinn, A.J. Dent, S.A. Cavill, S.D. Moreno, A. Peach, P.J. Leicester, S.J. Keylock, S.R. Gregory, K.D. Atkinson, and J.R. Rosell, *I18-the microfocus spectroscopy beamline at the Diamond Light Source.* Journal of Synchrotron Radiation, 2009. **16**: p. 818-824.
156. De Nolf, W., F. Vanmeert, and K. Janssens, *XRDUA: crystalline phase distribution maps by two-dimensional scanning and tomographic (micro) X-ray powder diffraction.* Journal of Applied Crystallography, 2014. **47**: p. 1107-1117.
157. Roisnel, T. and J. Rodriguez-Carvajal, *WinPLOTR: A Windows tool for powder diffraction pattern analysis*, in *Epdic 7: European Powder Diffraction, Pts 1 and 2*, R. Delhez and E.J. Mittemeijer, Editors. 2001, Trans Tech Publications Ltd: Zurich-Uetikon. p. 118-123.

158. Ha, H., C. Taxen, K. Williams, and J. Scully, *Effects of selected water chemistry variables on copper pitting propagation in potable water.* Electrochimica Acta, 2011. **56**(17): p. 6165-6183.
159. Poulson, B., *Fractography of stress corrosion cracking in carbon steels.* Corrosion Science, 1975. **15**(8): p. 469-&.
160. Zhang, Q.L., R.G. Wang, M. Kato, and K. Nakasa, *Observation by atomic force microscope of corrosion product during pitting corrosion on SUS304 stainless steel.* Scripta Materialia, 2005. **52**(3): p. 227-230.
161. Frankel, G.S., L. Stockert, F. Hunkeler, and H. Boehni, *Metastable pitting of stainless-steel.* Corrosion, 1987. **43**(7): p. 429-436.
162. Cron, C.J., J.H. Payer, and R.W. Staehle, *Dissolution behavior of Fe-Fe3 structures as a function of pH, potential, and anion - an electron microscopic study.* Corrosion, 1971. **27**(1): p. 1-&.
163. Lillard, R.S., G. Vasquez, and D.F. Bahr, *The kinetics of anodic dissolution and repassivation on stainless steel 304L in solutions containing nitrate.* Journal of the Electrochemical Society, 2011. **158**(6): p. C194-C201.
164. Henthorne, M.P., R. N., *Some aspects of the influence of structure upon stress-corrosion cracking and grain boundary corrosion in mild steels.* British Corrosion Journal, 1967. **2**(5): p. 186-192.
165. Flis, J. and J.C. Scully, *Transmission electron microscopical study of corrosion and stress corrosion of mild steel in nitrate solution.* Corrosion Science, 1968. **8**(4): p. 235-&.
166. Parkins, R.N., *Mechanistic aspects of intergranular stress corrosion cracking of ferritic steels.* Corrosion, 1996. **52**(5): p. 363-374.
167. Flis, J., *Effect of C on corrosion of Fe in NH4NO3 solution within a wide potential range.* Corrosion Science, 1970. **10**(10): p. 745-&.
168. Verbist, J.J., T.F. Koetzle, M.S. Lehmann, and W.C. Hamilton, *Neutron-diffraction study of iron (II) chloride tetrahydrate, FeCl2.4H2O.* Journal of Chemical Physics, 1972. **56**(7): p. 3257-&.
169. Wood, I.G., L. Vocadlo, K.S. Knight, D.P. Dobson, W.G. Marshall, G.D. Price, and J. Brodholt, *Thermal expansion and crystal structure of cementite, Fe(3)C, between 4 and 600 K determined by time-of-flight neutron powder diffraction.* Journal of Applied Crystallography, 2004. **37**: p. 82-90.
170. Prelesnik, P.V., F. Gabela, B. Ribar, and I. Krstanovic, *Hexaquacobalt(II) dinitrate (V).* Crystal Structure Communications, 1973. **2**: p. 581.
171. Shannon, R.D., *Revised effective ionic radii and systematic studies of interatomic distances in halides and chalcogenides.* Acta Crystallographica Section A, 1976. **32**(SEP1): p. 751-767.
172. RRUFF. *R100076 - RRUFF database: Raman, X-ray, Infrared, and Chemistry*. 2014 (cited 08/2014); Available from: http://rruff.info/chem=C/notchem=O,N,Cl,P/display=default/R100076.
173. Pradhan, S.K., B.B. Nayak, B.K. Mohapatra, and B.K. Mishra, *Micro Raman spectroscopy and electron probe microanalysis of graphite spherulites and flakes in cast iron.* Metallurgical and Materials Transactions a-Physical Metallurgy and Materials Science, 2007. **38A**(10): p. 2363-2370.
174. Ferrari, A.C. and J. Robertson, *Interpretation of Raman spectra of disordered and amorphous carbon.* Physical Review B, 2000. **61**(20): p. 14095-14107.

175. Ferrari, A.C. and J. Robertson, *Resonant Raman spectroscopy of disordered, amorphous, and diamondlike carbon.* Physical Review B, 2001. **64**(7).
176. Kim, J.H., J. Kim, J.H. Park, C.K. Kim, C.S. Yoon, and Y. Shon, *Synthesis of carbon-encapsulated iron carbide nanoparticles on a polyimide thin film.* Nanotechnology, 2007. **18**(11).
177. Dimovski, S., A. Nikitin, H.H. Ye, and Y. Gogotsi, *Synthesis of graphite by chlorination of iron carbide at moderate temperatures.* Journal of Materials Chemistry, 2004. **14**(2): p. 238-243.
178. Charon, E., J.N. Rouzaud, and J. Aleon, *Graphitization at low temperatures (600-1200 degrees C) in the presence of iron implications in planetology.* Carbon, 2014. **66**: p. 178-190.
179. Sails, S.R., D.J. Gardiner, M. Bowden, J. Savage, and D. Rodway, *Monitoring the quality of diamond films using Raman spectra excited at 514.5 nm and 633 nm.* Diamond and Related Materials, 1996. **5**(6-8): p. 589-591.
180. Wada, N., P.J. Gaczi, and S.A. Solin, *Diamond-like 3-fold coordinated amorphous-carbon.* Journal of Non-Crystalline Solids, 1980. **35-6**(JAN-): p. 543-548.
181. Gilkes, K.W.R., H.S. Sands, D.N. Batchelder, J. Robertson, and W.I. Milne, *Direct observation of sp(3) bonding in tetrahedral amorphous carbon using ultraviolet Raman spectroscopy.* Applied Physics Letters, 1997. **70**(15): p. 1980-1982.
182. Merkulov, V.I., J.S. Lannin, C.H. Munro, S.A. Asher, V.S. Veerasamy, and W.I. Milne, *UV studies of tetrahedral bonding in diamondlike amorphous carbon.* Physical Review Letters, 1997. **78**(25): p. 4869-4872.
183. deFaria, D.L.A., S.V. Silva, and M.T. deOliveira, *Raman microspectroscopy of some iron oxides and oxyhydroxides.* Journal of Raman Spectroscopy, 1997. **28**(11): p. 873-878.
184. Thibeau, R.J., C.W. Brown, and R.H. Heidersbach, *Raman-spectra of possible corrosion products of iron.* Applied Spectroscopy, 1978. **32**(6): p. 532-535.
185. Keiser, J.T., C.W. Brown, and R.H. Heidersbach, *Characterization of the passive film formed on weathering steels.* Corrosion Science, 1983. **23**(3): p. 251-259.
186. Park, E., J.Q. Zhang, S. Thomson, O. Ostrovski, and R. Howe, *Characterization of phases formed in the iron carbide process by X-ray diffraction, Mossbauer, X-ray photoelectron spectroscopy, and Raman spectroscopy analyses.* Metallurgical and Materials Transactions B-Process Metallurgy and Materials Processing Science, 2001. **32**(5): p. 839-845.
187. Hamelmann, T. and M.M. Lohrengel, *Electrochemical investigations of single microparticles.* Electrochimica Acta, 2001. **47**(1-2): p. 117-120.
188. Browning, L.C., T.W. Dewitt, and P.H. Emmett, *Equilibria in the systems Fe2C-Fe-CH4-H2 and Fe3C-Fe-CH4-H2.* Journal of the American Chemical Society, 1950. **72**(9): p. 4211-4217.
189. Pourbaix, M., *Atlas of electrochemical equilibria in aqueous solutions*. 1974: Houston, TX.: NACE.
190. Ernst, P. and R.C. Newman, *Explanation of the effect of high chloride concentration on the critical pitting temperature of stainless steel.* Corrosion Science, 2007. **49**(9): p. 3705-3715.
191. Darwish, N.A., F. Hilbert, W.J. Lorenz, and H. Rosswag, *Influence of chloride-ions on kinetics of iron dissolution.* Electrochimica Acta, 1973. **18**(6): p. 421-425.
192. McCaffer.E and Hackerma.N, *Kinetics of iron corrosion in concentrated acidic chloride solutions.* Journal of the Electrochemical Society, 1972. **119**(8): p. 999-&.

193. Tzinmann, M., A. Kriaa, and C. Fiaud, *The Hammett acidity functions and their use for metallic corrosion in hydrooganic solutions.* Electrochimica Acta, 1987. **32**(6): p. 887-890.
194. Kriaa, A., N. Hamdi, K. Jbali, and M. Tzinmann, *Kinetics study of iron dissolution in highly concentrated acidic media using Hammett acidity function.* Corrosion Science, 2008. **50**(12): p. 3487-3493.
195. Cavallaro, L., L. Felloni, G. Trabanelli, and F. Pulidori, *The anodic dissolution of iron and the behaviour of some corrosion inhibitors investigated by the potentiodynamic method.* Electrochimica Acta, 1964. **9**(5): p. 485-494.
196. Eichkorn, G., W.J. Lorenz, L. Albert, and H. Fischer, *Influence of surface activity on anode dissolution mechanisms of iron in acid solutions.* Electrochimica Acta, 1968. **13**(2): p. 183-&.
197. Felloni, L., *Effect of pH on electrochemical behaviour of iron in hydrochloric acid.* Corrosion Science, 1968. **8**(3): p. 133-&.
198. Kuo, H.C. and K. Nobe, *Electrodissolution kinetics of iron in chloride solution. 6. concentrated acidic solutions.* Journal of the Electrochemical Society, 1978. **125**(6): p. 853-860.
199. Chin, R.J. and K. Nobe, *Electrodissolution kinetics of iron in chloride solutions. 1. acidic solutions.* Journal of the Electrochemical Society, 1972. **119**(11): p. 1457-&.
200. Ogle, K. and S. Weber, *Anodic dissolution of 304 stainless steel using atomic emission spectroelectrochemistry.* Journal of the Electrochemical Society, 2000. **147**(5): p. 1770-1780.
201. Smart, N.G., M. Gamboaaldeco, and J.O. Bockris, *Corrosion mechanisms of iron in concentrated acidic zinc-chloride media.* Corrosion Science, 1993. **34**(5): p. 759-777.